& MICROWAVE
ANTENNA AMS SYSTEMS

2010

Bulk Acoustic Wave Resonators and their Application to Microwave Devices

Jordi Verdú Tirado

Bulk Acoustic Wave Resonators and their Application to Microwave Devices

Ph.D. Dissertation by:

Jordi Verdú Tirado

Advisors:

Prof. Pedro de Paco Sánchez

Prof. Óscar Menéndez Nadal

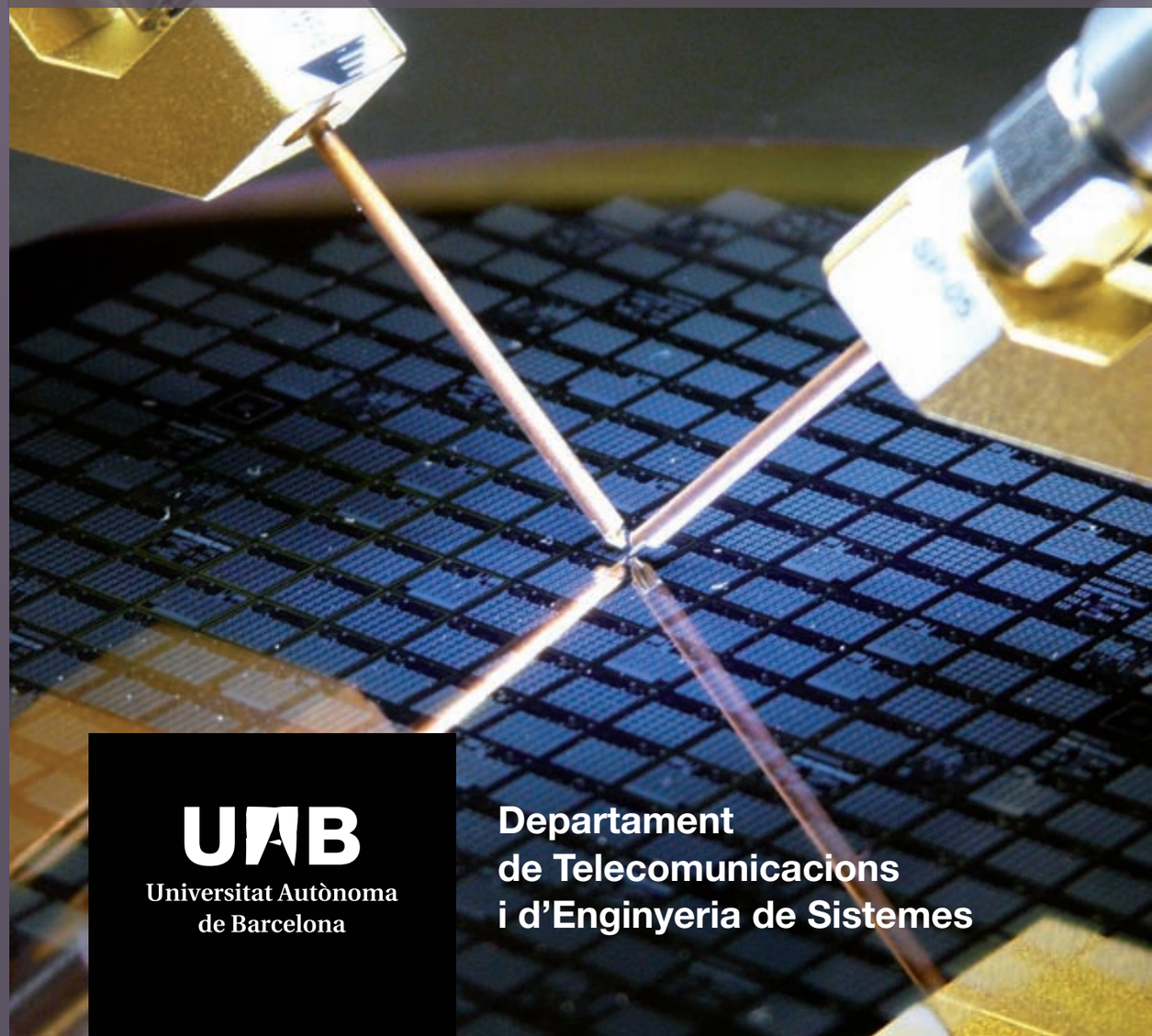

UAB

Universitat Autònoma de Barcelona

Departament de Telecomunicacions i d'Enginyeria de Sistemes

"La ciencia se compone de errores,
que, a su vez,
son los pasos hacia la verdad"
(Julio Cortázar)

Abstract

The exponential growth in wireless communication systems in recent years has been due to the requirements of small high performance microwave devices. The main limitation of microwave devices based on traditional technologies is that these technologies are not compatible with the manufacturing process of standard integrated circuits (IC). Microwave devices based on acoustic resonators, and bulk acoustic wave (BAW) resonators in particular, overcome this limitation since this technology is compatible with standard IC technologies. Furthermore, acoustic resonators are excited by means of an acoustic wave with a propagation velocity around four or five times lower than the propagation velocity of electromagnetic waves, and the resulting size of the device is therefore also lower in the same proportion. This is the incentive behind this study.

The study is basically divided into two blocks. The first block comprises the chapters number 2, 3 and 4, and is devoted to the study of the BAW resonator. First, the BAW resonator is studied in its one-dimensional form, i.e. considering that only a mechanical wave is propagated in the thickness dimension, in order to obtain the equivalent circuits which enable the electrical characterization of the BAW resonator. However, these models do not take into account effects due to lateral waves. The need for a 3D simulator tool therefore becomes evident. Using the 3D simulator, the electrical behaviour of the BAW resonator can be completely characterized, and the boundary conditions required as well as the origin of lateral standing waves can therefore be stated. The presence of lateral standing waves entails the degradation of the electrical performance of the BAW resonator, mainly in terms of the quality factor and the effective electromechanical coupling constant.The improvement in the electrical performance of the BAW resonator is therefore mainly based on its ability to minimize the presence of unwanted lateral modes. Two different solutions are proposed to that end: apodization and the presence of a perimetric ring on the top of the metal electrode. The former solution consists of designing the top electrode in such a way that non-parallel edges are found. The resonant paths thereby become larger and the resonant modes thus become more attenuated due to the material losses. However, although the strength of these modes is lower, more resonant modes are present since there are more possible resonant paths. This finally leads to the degradation of the quality factor of the BAW resonator. The latter solution consists of including a thickened edge load on the top of the metal electrode, which leads to boundary conditions in which lateral waves cannot propagate through the structure. By doing this, the electrical response of the BAW resonator is spurious-free and the quality factor obtained is thus higher than if the apodization solution is used.

The second block of this thesis is devoted to the application of BAW resonator to the microwave filter design, and particularly to filters based on electrically connected BAW resonators, as in the case of ladder-type filters. This type of filter presents a very high selectivity due to the presence

of a pair of transmission zeros, but a poor out-of-band rejection due to the natural capacitor divider.The design procedure using closed-form expressions is therefore presented first, with the effect of the metal electrodes considered negligible, and this procedure subsequently modified in order to include these effects. In order to improve the filter performance out-of-band, the proposed solution consists of modifying the BAW resonators with the presence of reactive elements (capacitors and inductances) in series or a shunt configuration. By doing so, the modification is directly related with the allocation of the resonant frequencies. The modified and non-modified BAW resonators are therefore connected in a ladder-type topology including a new pair of transmission zeros, making the out-of-band rejection higher.

The final chapter of this study focuses on the design of a dual-band filter based on BAW resonators. The proposed topology is based on the conventional ladder-type topology but instead of having an elemental cell comprising a single BAW resonator in series and a shunt configuration, two series and two shunt BAW resonators are now present. By doing this, one of the transmission bands is related with one series and shunt BAW resonator and the second transmission band is due to the other pair of resonators. With the proposed design procedure, each of the transmission bands can be allocated to the desired frequencies. Finally, the design procedure is applied to the GPS L1/L5 and Galileo E5a/E5b applications.

Resumen

El crecimiento exponencial que han experimentado los sistemas de comunicaciones inalámbricos actuales durante los últimos años, ha dado lugar a la necesidad de disponer dispositivos de microondas de tamaño reducido y, a su vez, de altas prestaciones. El principal obstáculo con el que se encuentran los dispositivos basados en las tecnologías clásicas, es que dichas tecnologías no son compatibles con los procesos estándar de fabricación de circuitos integrados (IC). En este sentido, dispositivos de microondas basados en resonadores acústicos, en concreto resonadores BAW, ofrecen una solución a dicha limitación ya que son compatibles con los procesos estándar de fabricación de circuitos integrados. Por otro lado, dichos resonadores son excitados mediante una onda acústica cuya velocidad de propagación es alrededor de cuatro o cinco órdenes de magnitud menor que las ondas electromagnéticas, con lo que el tamaño del dispositivo también será menor en la misma proporción. La motivación de este trabajo viene dada por el escenario que se plantea.

El documento está básicamente dividido en dos grandes bloques. El primer bloque que consta de los capítulos 2, 3 y 4 está dedicado al estudio de un resonador BAW. En primer lugar, el estudio se realiza para una estructura unidimensional, es decir, teniendo en cuenta que en el resonador solamente se propaga una onda acústica en la dirección longitudinal, con el objetivo de extraer los modelos circuitales que permiten la caracterización eléctrica de dicho resonador. Sin embargo, estos modelos no son capaces de predecir con exactitud el comportamiento eléctrico del resonador acústico ya que no contemplan efectos derivados de la propagación de ondas laterales. Así, la necesidad de incorporar una herramienta de simulación 3D se hace necesaria. Mediante el simulador 3D, el resonador se puede caracterizar por completo, así, el origen y las condiciones necesarias para la presencia de ondas laterales estacionarias pueden ser establecidas. La presencia de las ondas laterales generan efectos no deseados en la respuesta eléctrica del resonador básicamente en forma de degradación del factor de calidad y de la constante de acoplo electromecánico efectiva. Así pues, la mejora del comportamiento eléctrico del resonador se basa principalmente, en la minimización de la presencia de las ondas laterales no deseadas. Para ello se proponen dos soluciones diferentes: el apodizado y la inclusión de un anillo en el perímetro del electrodo superior. La primera solución consiste en diseñar el electrodo superior de manera que no existan caras paralelas. Con ello, los patrones de resonancia que se generan hacen que la onda deba viajar una distancia mayor con la correspondiente atenuación debida a las pérdidas del material. Sin embargo, aunque la amplitud de dichas ondas se ve claramente decrementada, el número de patrones resonantes aumenta respecto al caso convencional, y también el número de modos no deseados. Esto finalmente se traduce en una degradación del factor de calidad del resonador. La segunda solución consiste en forzar unas condiciones de contorno determinadas que hacen que las ondas laterales no puedan propagarse. Con esto, la respuesta del resonador aparece libre de modos no deseados con lo que el factor de calidad del resonador es mucho mayor

que lo que se puede conseguir mediante el apodizado.
El segundo gran bloque de este trabajo está dedicado a la aplicación de los resonadores acústicos al diseño de filtros. Este bloque se ha centrado básicamente en topologías en las que los resonadores acústicos están conectados eléctricamente, y en particular en topologías tipo "ladder". Este tipo de filtros presenta una selectividad alta debido a la presencia de un par de ceros de transmisión, pero a su vez un pobre rechazo fuera de banda debido al comportamiento capacitivo de dichos resonadores. Así, en primer lugar se propone una metodología de diseño con expresiones cerradas, en un primer lugar considerando negligible la presencia de los electrodos metálicos, y realizando alguna modificación en el proceso de diseño para incluir dichos efectos. Por otro lado, con el objetivo de mejorar las prestaciones del filtro fuera de banda, se propone como solución modificar los resonadores acústicos mediante la presencia de elementos reactivos (capacidades y bobinas) ya sea en serie o en paralelo. La modificación de dichos resonadores se da principalmente en la posición de las frecuencias de resonancia. Así, si en una topología ladder se incluyen resonadores modificados y no modificados, se genera un nuevo par de ceros de transmisión en la respuesta que hacen que el rechazo fuera de banda sea mayor.
El último capítulo de este trabajo está dedicado al diseño de un filtro con una respuesta en transmisión que presenta dos bandas de paso. La topología está basada en la topología ladder clásica con la diferencia que, en lugar de tener una celda elemental formada por un resonador serie y paralelo, se tiene una celda elemental formada por dos resonadores serie y dos paralelos. Con esto, una banda de transmisión viene dada por la interacción de un resonador serie y uno paralelo, mientras que la segunda banda se da por la interacción del segundo par de resonadores. Con el método de diseño que se propone, cada una de las bandas puede ser diseñada a la frecuencia que se desee. Finalmente, se muestra el diseño de un filtro dual para la aplicación de GPS L1/L5 y Galileo E5a/E5b.

Acknowledgements

Many people have contributed to this work, and I would like to thank each one for their support, collaboration and guidance. I would like to start by mentioning various people, not colleagues but previous teachers who are partly responsible for making me what I am today. I would also like to thank my friends on this adventure, Edén, Joan, Jordi, Mónica and Toni, for their support and never ending discussions. This has been very helpful in several fields in my research. Humberto from CNM must also be included here, because he gave me a better understanding of the fabrication process.

The most important reason for writing this section is of course Eulàlia. She has been my inspiration every day, as well as much-needed support at difficult times. I would also like to mention my family, my parents Ramón and Maria José, Judith, to my other "parents" and friends Santi and Lluïsa, Arnau and of course Olívia and forthcoming sons. Finally, thanks to all my friends, and especially all who have undertaken this adventure before me.

Finally, I would like to give a special mention to my supervisors Pedro and Óscar. Thank you for your infinite patience with me, and for teaching me everything I know. Without their help, I certainly wouldn't be here right now. Thank you for teaching me the meaning of research, and for teaching me to move beyond the obvious. Thank you for trusting me to carry out this work.

June 2010,

Contents

List of Figures

List of Tables

Acronyms

SoC	System on chip.
GPS	Global positioning system.
BAW	Bulk acoustic wave.
WLAN	Wireless local area network.
CDMA	Code division multiple access.
UMTS	Universal mobile telecommunication system.
GSM	Group special mobile.
RF	Radio frequency.
DCS	Digital communication system.
PCS	Personal communication system.
MEMS	Microelectronic mechanical system.
SMR	Solidly mounted resonator.
WiMAX	Worldwide interoperatibility for microwave access.
SAW	Surface acoustic wave.
IDT	Interdigital transducer.
FBAR	Film bulk acoustic resonator.
TCF	Temperature coefficient of frequency.
CMOS	Complementary metal oxide semiconductor.
IC	Integrated circuit.
RIE	Reactive ion etching.
OoB	Out of band.
SCF	Stacked crystal filter.
CRF	Coupled resonator filter.
BVD	Butterworth-Van Dyke.
KLM	Krimholtz-Leedom-Matthaei.
FEM	Finite element method.
TEM	Transversal electro-magnetic.
TS	Thickness shear.
TE	Thickness extensional.
FDTD	Finite difference time domain.
PML	Perfectly matched layer.
GNSS	Global navigation satellite system.
SIR	Stepped impedance resonator.

CHAPTER 1

Introduction

The use of microwave resonators can be extended to a very large number of devices such filters, oscillators, frequency meters and tuned amplifiers. In this sense, the development of the microwave devices and systems are in most cases led by the development of contained resonators. The common characteristic among most microwave resonators is that the excitation is by means of an electromagnetic wave. Meanwhile, the size of the devices is usually directly related to the wavelength of the electromagnetic wave at a certain frequency, which at the same time is directly related to the propagation velocity of the electromagnetic wave.

In recent years, there has been an exponential growth in wireless applications systems. The goals of the designers of these systems are mainly focused on obtaining small high performance devices, and integration of the different devices in one chip (SoC). The resulting size of electromagnetic resonators at RF/Microwave frequencies is a limitation from the point of view of integration, since at these frequencies the size of microwave resonators is usually much greater than some other integrated components. This also means that the resulting device is large, which is a limitation in portable communication systems.

Acoustic resonators have become consolidated as a key technology in overcoming the limitations mentioned above. First, the propagation velocity of acoustic waves is around four or five times lower than that of electromagnetic waves. Second, the resulting size of the device is also four or five times lower compared to the electromagnetic case. Acoustic resonators, and specifically bulk acoustic wave (BAW) resonators are compatible with standard integrated circuits (IC) technology. Overcoming these limitations has increased exponentially growing in the recent history of wireless communication applications.

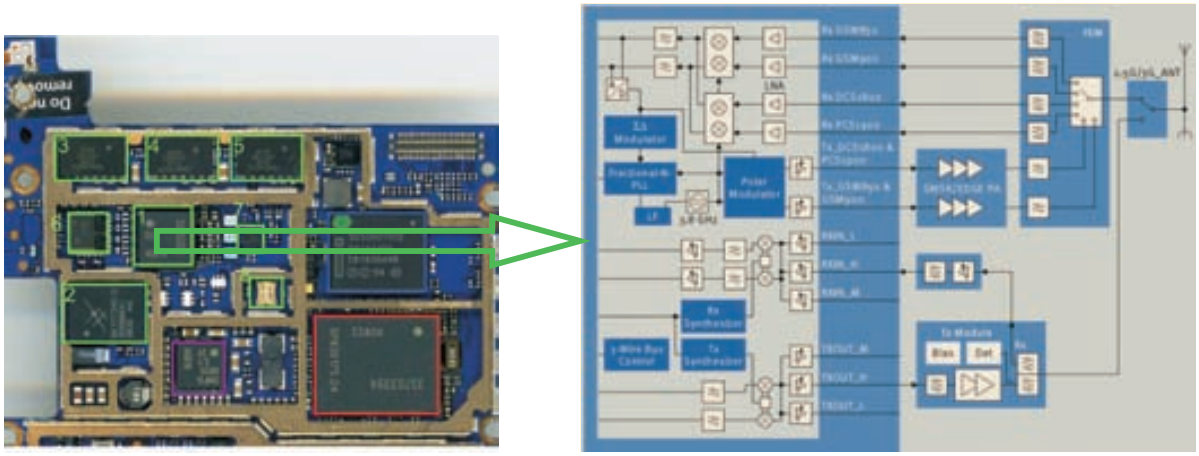

Figure 1.1: Iphone wireless modem (left side) and Infineon PMB6952 Dual mode W-CDMA/Edge chip (right side).

There are several applications in which acoustic resonators can be found such as global positioning systems (GPS, Galileo), data transfer (WLAN, Bluetooth), cellular mobile systems (CDMA, UMTS, GSM), satellite communications and other applications such as military applications [1]. In a basic architecture for a microwave front-end, a bandpass filter at the input of the transceiver path is required. Figure 1.1 shows the Iphone wireless modem layout where, the green chips numbered from 1 to 8 are the RF parts of the modem, while the other marked parts are active parts. The block diagram for chip number 1 is on the right of Figure 1.1. As mentioned above, at the input of the transceiver path, i.e. after the antenna, there are four different bandpass filters for the GSM850/900, DCS1800 and PCS1900 signals. There are bandpass filters also found in the transmission module. Various oscillators and tuned amplifiers are also included in this architecture. Figure 1.2(a) shows the expected evolution of the 3G/4G RF Front-End from 2007 to 2013, with a significant increase in the number of filters making up the system. This is consistent with the business market of BAW devices, in which there is an increase of almost 50% from 2004 to 2009, as shown in Figure 1.2(b).

The driving forces of technology could therefore be summarized as cost, performance, and device size, with all being closely related. High performance is required mainly in order to obtain bandpass filters with the necessary system bandwidths with low loss. However, not only cost, but also the increased battery requirements are a concern when inefficient filters are present in the system. Finally, size is crucial in handset units, but decreasing the size of the devices leads to more of them in each wafer, and thus, a reduction of the cost per unit. As usually discussed by the scientific community working in these areas, the items above were the driving forces in applying BAW technology to these applications, and are still the goals today.

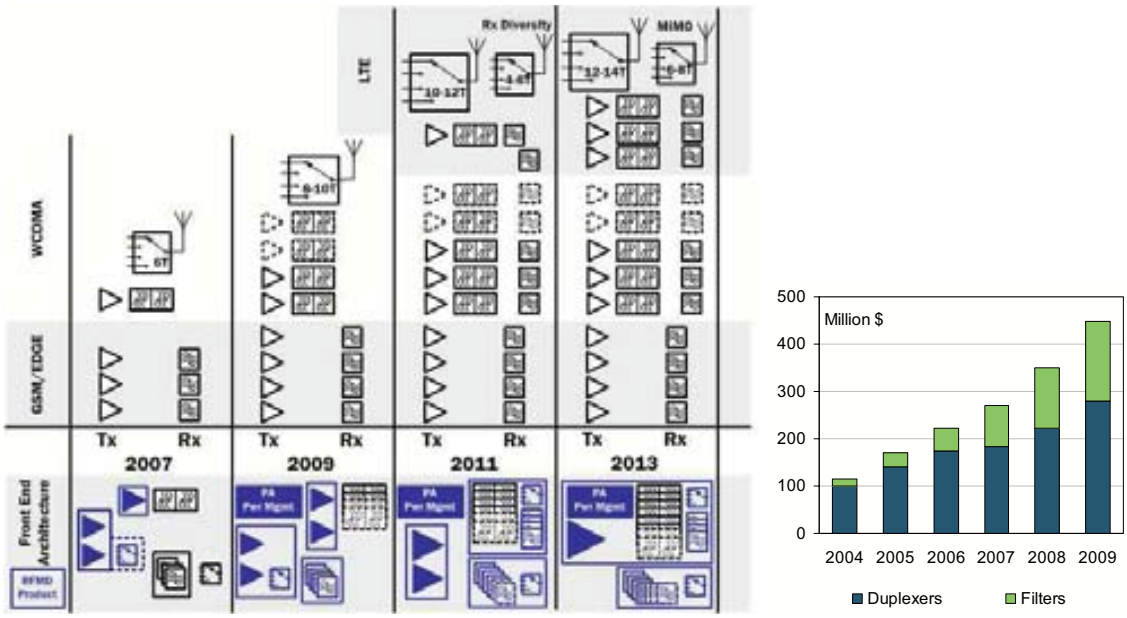

(a) (b)

Figure 1.2: (a) 3G/4G RF Front End Evolution [3G/4G Multimode Cellular Front End Challenges]. (b) market for BAW devices in the last 5 years [World-wide MEMS Markets 2006].

1.1 From Piezoelectric Crystals to Thin Films

The underlying physical phenomena operating in acoustic devices is piezoelectricity. The etymological meaning of piezoelectricity comes from *Piezos* and *Electro*, which means pressure and electricity. Piezoelectricity is the characteristic of some materials in which after a force (or pressure) is applied, an electrical field in the material is generated. This is called the direct piezoelectric effect. The inverse piezoelectric effect also occurs when stresses and strains occur in the material structure when some voltage is applied. Piezoelectricity involves the coupling between the mechanical (stress and strain) and the electrical properties of a piezoelectric material.

The use of piezoelectric materials for different applications begins in the early 1960's at Bell Telephone Laboratories [2], where the first approach was to accomplish electronic functions using the properties of some piezoelectric crystals. Most of the devices developed were amplifiers and oscillators at frequencies below 100 MHz. The drawback of using piezoelectric crystals is that commercially available crystals have a thickness around 25 μm, which is equivalent to a fundamental frequency of 60 MHz. In order to operate at higher frequencies, the crystal should therefore be thinned, with the limitation of the need to mechanically support the thin-plate resonator afterwards.

Later, in the early 1970's, the desire to have devices operating at higher frequencies arose. The way to achieve this was to grow the piezoelectric layer on the substrate instead of thinning piezoelectric crystal for higher frequencies. One of the studies on how to achieve this was the work done by Sliker and Roberts in 1967 [3], when CdS was evaporated on a resonant piece of bulk quartz crystal which served as a transducer in 1967. The resonator working at 279 MHz had a Quality factor of $Q = 5000$ at the resonance frequency. In 1968, Page replaced a piece of quartz with a thin substrate of single crystal silicon [4]. After this, numerous applications were developed in the fields of signal processing [5, 6], frequency generation [7], control and filtering [8], and some others that are mentioned in [9].

In the early 1980's, Lakin and Wang [10, 11] manufactured a composite resonator, in which a film of ZnO was deposited over a single crystal membrane. In this case, the resonator was designed at 500 MHz, and this frequency presented a quality factor of $Q = 9000$. At the same time, Grudkowski also designed a high-Q resonator based on ZnO over a silicon substrate, and obtained promising results between 200 and 500 MHz [12]. Later, in the mid-1990's, the first BAW resonators over a Bragg reflector, solidly mounted resonators (SMR), began to be developed, and this structure provides a more robust solution in terms of mechanical cracking. In 1995 Lakin applied the SMR to the design of filters working at 1.6 GHz based on AlN piezoelectric films [13].

Although there was some interest in acoustic technology among the scientific community, the evolution of devices based on acoustic wave resonators in the industry began with Lakin at TFR Technologies in 1989. They were the pioneers of FBAR and subsequently SMR technology. Afterwards, Agilent started to developed the same technology in 1994, with Ruby and Merchant as mentioned in [14]. In 2000, they reported a production run for FBAR duplexers at 1.9 GHz with 1/10 the volume of commercial units [15]. Since then, some entrepreneurs have tried to develop this technology, such as NXP, which has developed a 2.3 GHz filter for satellite radio application in a mobile phone or a duplexer for the 1.9 GHz band; Skyworks, who are marketing power amplifier modules with an integrated BAW filter for WLAN applications, and Front-End modules for LTE/EUTRAN (Tx 2500-2570 MHz), (Rx 2620-2690 MHz) with a BAW Inter-Stage Filter and Duplexer; Triquint, whose process for BAW technology using the SMR solution has been optimized for applications at 1900 and 2400 MHz for mobile handsets, 3G/4G cellular base station, WLAN, WiMAX, GPS and defence and aerospace applications; AVAGO, whose solution for BAW technology is the air-gap cavity, unlike the SMR at Triquint; and EPCOS, who also provide a miniaturized BAW duplexer for CDMA mobile phone systems.

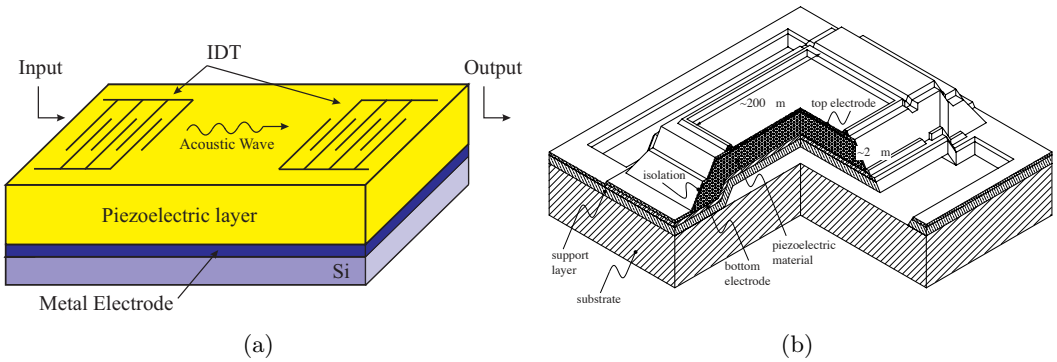

Figure 1.3: Schematic view of: (a) Surface Acoustic Wave Resonator. (b) Bulk Acoustic Wave Resonator.

1.2 Acoustic Resonators: Surface Acoustic Wave and Bulk Acoustic Wave

Two different technologies can be distinguished depending on how the acoustic wave propagates through the piezoelectric slab: Surface Acoustic Wave (SAW) and Bulk Acoustic Wave (BAW) devices. Figure 1.3(a) shows the schematic view for a SAW resonator. In this case, as its name suggest, the acoustic wave propagates parallel to the piezoelectric slab in the interdigital transducer (IDT) along the surface of the resonator [16, 17]. SAW resonators are limited in their achievable operating frequency since this is due to the separation of the each finger in the IDT. The limit is therefore around 2.5 GHz. Meanwhile, SAW devices are generally manufactured on a LiTaO3 or LiNbO3 crystal substrates [18], which are not compatible with the standard IC technology processes. However, the advantage over the BAW technology is the simplicity in the manufacturing process, in which only three masks are needed. This work has focused on BAW resonators, however, some of the details differentiating the two technologies are worthy of consideration. It will thus be easier to understand the decision to use BAW resonators in this work.

Figure 1.3(b) shows the schematic view for a BAW resonator in which the acoustic wave propagates through the piezoelectric slab in the thickness direction [20, 21, 22]. The operating frequency limit of BAW resonators is around 10 GHz [23]. This is an approximate limit and it is due to the fragility of layers above this frequency, i.e. layers below 500 nm, although some works mention resonators operating at higher frequencies [24]. Various works can be found in the literature for applications above 5 GHz [25, 26]. Regarding with the compatibility with the standard IC technology process, BAW technology is compatible with any wafer processing such as silicon and gallium arsenide (GaAs).

As for their power handling capability, BAW resonators present a better performance than SAW. This is due to the fact that in an SAW resonator, major stress is applied to the narrow

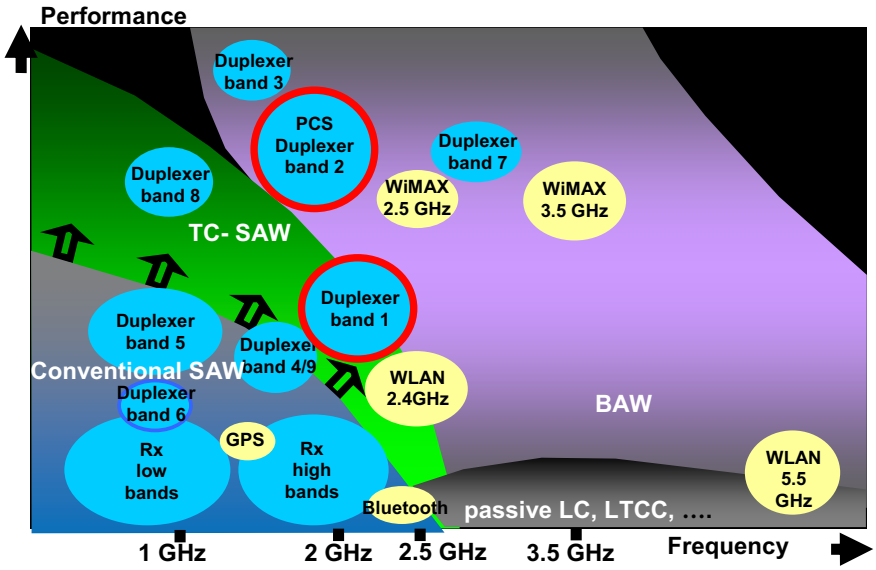

Figure 1.4: Mobile commercial applications mapped to SAW, temperature compensated SAW and BAW technologies [19].

Table 1.1: Comparison of SAW and BAW technology.

	SAW	BAW
Frequency range	up to 2.5 GHz	up to 10 GHz
Power Handling	$\sim$ 31 dBm	$\sim$ 36 dBm
Temperature Coefficient of Frequency (TCF)	-45 ppm/°C	-20 ppm/°C
Quality factor	$\sim$ 700	$\sim$ 2000
Compatibility with IC process	No	Yes

fingers under high-power conditions. As a result, stress migration occurs, and in addition, the high resistance of the electrode causes Joule heat, which accelerates the migration. This effect also contributes to greater dependence of the resonant frequencies with temperature. In a BAW resonator, the stress on the electrode is not as high as in SAW, and therefore more power handling is allowed and there is less dependence on temperature. This can be easily understood considering that BAW resonators are based on a parallel plate capacitor instead of the long, narrow and thin interdigital fingers used in SAW.

The quality factor in BAW resonators becomes much higher than in SAW resonators as it is demonstrated in [27], where the achieved quality factor is $Q = 5000$ at 800 MHz, however, the obtained values are generally around $Q = 2000$ at 2 GHz. This is due to the fact that the cavity size is only $\lambda/2$, while SAW is trapped on the surface where the cavity is many wavelengths long which can be understood as an overmode acoustic resonator.

A comparison of the main characteristics of the two technologies is shown in Table 1.1. Both SAW and BAW have specific strengths and limitations, and in the most of the cases they complement each other. This means that the number of applications in which they compete against each other is very limited. This can be seen in Figure 1.4, where the applications space for SAW and BAW are shown. BAW will expand the ability to serve high frequency and power applications due to its ability to satisfy the requirements of high performance devices. At the same time, due to the inherent cost advantage, it seems that SAW will retain the market for the applications that they are currently serving. Taking into account the projection of BAW resonators in the application to microwave devices, this thesis therefore focuses mainly on this type of acoustic resonator

1.3 Bulk Acoustic Wave Resonators

The most basic configuration of a BAW resonator consists of a piezoelectric layer sandwiched between two metal electrodes, as in a parallel plate capacitor, where the electric field is generated in the direction of the thickness, thereby exciting the acoustic wave . At the same time, in order to have a resonating mode in the structure, the acoustic wave must be confined in the acoustic cavity created by the piezoelectric layer. There are several ways to confine the acoustic wave which basically results in two different types of BAW resonators: film bulk acoustic resonators (FBAR) and solidly mounted resonators (SMR). In the former, the idea is to create an air-gap cavity below the bottom metal electrode. The electrical behavior of the air is a short-circuit forcing the acoustic wave to reflect between the top and bottom surfaces, and therefore to generate the resonant mode. In the SMR configuration, a Bragg reflector is placed below the bottom metal electrode. The Bragg reflector consists of an alternating low and high acoustic impedances layer which confines the acoustic wave to certain conditions.

It must be taken into account that the electrical performance of BAW resonators depends on the piezoelectric layers, and also on the way in which the acoustic wave is confined in the structure. A brief discussion about the piezoelectric materials available, with their intrinsic properties, as well as the various ways to confine the acoustic wave is therefore included in this section.

1.3.1 Piezoelectric materials

The most common piezoelectric materials used for the development of BAW devices are Zinc Oxide (ZnO) [28, 29] and Aluminum Nitride (AlN) [30, 31], but resonators based on Cadmium Sulfide (CdS) can also be found in the literature [29, 32]. All these materials have the same crystallographic structure, which is an hexagonal 6mm class [28, 33]. In this case, all these materials

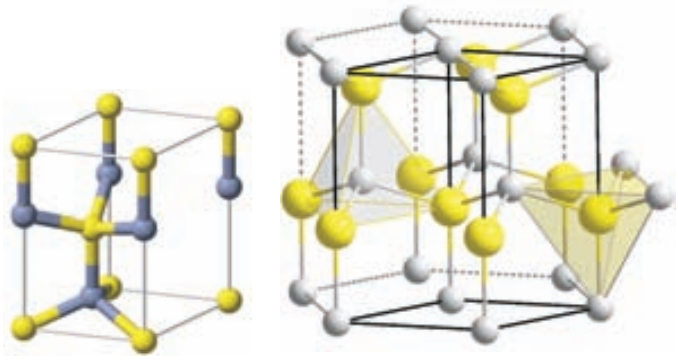

(a) (b)

Figure 1.5: Atomic structure of: (a) Wurtzite single cell. (b) Wurtzite full structure.

Table 1.2: Mechanical and electrical properties reference values for the different piezoelectric materials.

Material	c_{33}[N/m^2]	ρ[Kg/m^3]	e_{33}[C/m^2]	ϵ_r	V_p[m/s]	Z_a[Kg/m^2s]	k_t^2
AlN	395	3260	1.5	10.5	11340	3.70e7	$\sim 6.1\%$
ZnO	211	5680	1.32	10.2	6370	3.61e7	$\sim 9.1\%$
CdS	94	4820	0.44	9.5	4500	2.15e7	$\sim 2.4\%$

are classified as a Wurtzite crystals since each one is comprised of binary compounds. The single cell and the full atomic structure are shown in Figure 1.5. One of the characteristics of these materials is their strong orientation in one direction, generally [001] which corresponds to the thickness dimension. One one hand, this is an advantage since the value of the electromechanical coupling coefficient becomes greater. The electromechanical coupling coefficient is an intrinsic property of piezoelectric materials which relates the amount of converted electrical energy into mechanical energy or viceversa. On the other hand, in the manufacturing process, there is a problem with controlling the film texture, as well as the physical properties [34].

Among the available piezoelectric materials, AlN and ZnO seem to be the most suitable for microwave applications due to their inherent properties, mainly the high acoustic propagation velocity and electromechanical coupling coefficient compared with CdS. Table 1.2 shows the main mechanical and electrical parameters of some of the piezoelectric materials used, which will be the reference parameters in this study. AlN is maybe where the most of the efforts have been put on due to the high acoustic velocity and high reliability. Furthermore, AlN is compatible with the standard CMOS process, which must be taken into account from the point of view of On-Chip integration. ZnO presents a higher electromechanical coupling coefficient, but also a higher TCF and lower acoustic velocity. In terms of integration, ZnO is limited due to the CMOS contamination requirement [35]. The use of CdS has not been recently exploited due to the low value of k_t^2.

1.3.2 Mechanisms for the confinement of the acoustic wave

The BAW technology is mainly characterized, among others, by high values of the quality factor Q which lead to very good performance by the BAW resonators. The quality factor is directly related with the ratio of the total energy in the structure to the power lost in a half-cycle. There are some losses mechanisms related with the degradation of the quality factor of the BAW resonator, and one of these is related to the confinement of the acoustic wave in the BAW resonator. This section considers the various ways of confining the acoustic wave. These can be classified into two groups: air-gap cavity and Bragg reflector. The former consists of making the BAW resonator structure float on air. Due to the mechanical properties of this medium, the acoustic wave reflects the top and bottom electrode surfaces and resonance is thereby achieved. The latter solution consists of the Bragg reflector, which is a set of alternating low and high acoustic impedance located below the bottom electrode.

The most used techniques to create the air-gap cavity to confine the acoustic wave are: through-the-hole, bridge supported and backside edge. Figure 1.6(a) shows the first of these techniques. In this case, the idea is to create several holes in the structure in order to introduce an etching material to release the material under the bottom metal electrode and then, to create the air-gap cavity. The drawback with using this kind of solution is related to its manufacturability. Creating the etch holes weakens the structure mechanically, and makes it susceptible to breakage.

The next technique is called bridge supported. In this case, a sacrificial layer is deposited under the bottom electrode. When the structure is complete, the layer is removed and the air-gap cavity is created. This process is shown in Figure 1.6(b). This is the same as in the work in [36] in which the bar-shape shown was manufactured achieving a quality factor of $Q = 1400$. In this case, the drawback is related with the etching time. For resonators with very different areas, there is a trade-off between the etching time and the size of the device, i.e. devices with large areas will need much more etching time than devices with small areas. In this case, small devices can be damaged due to excess etching time. However, the work in [24], which presents a ladder-type filter working at 19.8 GHz, leading to extremely thin film layers. This involves having a sacrificial layer to make a very thin air-gap cavity in order to prevent the resonator from cracking, and to maintain the air-gap cavity when the resonator is deformed.

Finally, the idea of the backside etch consists of creating an air-gap cavity by removing the material under the BAW resonator from the back side of the wafer. This process can be wet, i.e. using etching solutions, or dry, by using reactive ion etching (RIE). Figure 1.6(c) shows a resonator in which the removed material can be clearly seen below the bottom metal electrode. There are other works, such as [37]. In this case, two ladder-type filters are shown, where the composing resonators were manufactured using the silicon bulk micromachining technique in order to obtain the air-gap cavity. In comparison with the previous techniques, in [38] a FBAR

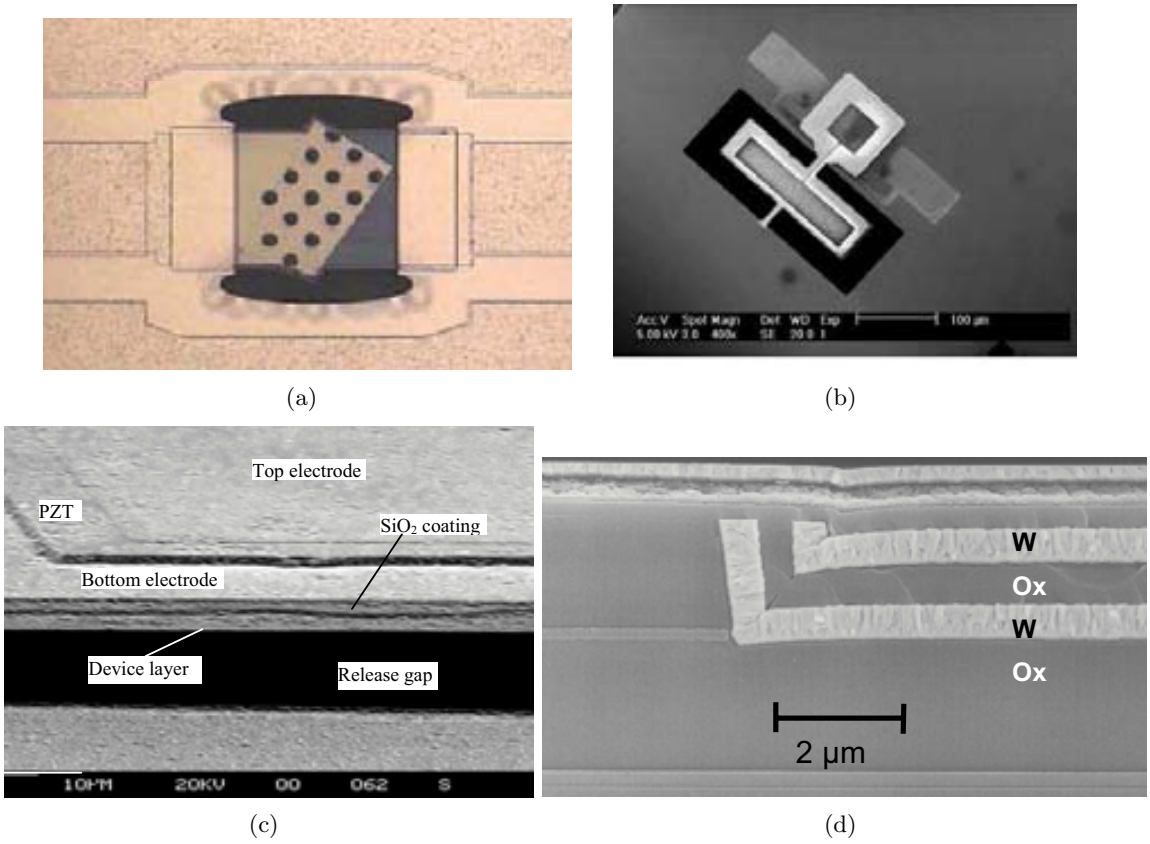

Figure 1.6: Different mechanisms to confine the acoustic wave: (a) Through-the-hole under-cut FBAR. (b) Air-gap or bridge under-cut FBAR. (c) Edge-supported FBAR. (d) Solidly Mounted Resonator (SMR) [39].

resonator was manufactured without using any sacrificial layer. In this case, the whole resonator structure is suspended by itself in the air, achieving a quality factor of between three and five times that achieved with the solution using a sacrificial layer.

The techniques mentioned above for confining the acoustic wave present a very good performance, although in some cases the resulting structures are mechanically weak and fragile. A Solidly Mounted Resonator (SMR) is another way of confining the acoustic wave. In this case, instead of forming an air-gap cavity, a Bragg reflector is placed between the substrate and the bottom electrode of the BAW resonator.

The Bragg reflector, as seen in Figure 1.6(d) [39] is formed by a succession of low and high impedance layers with thickness $\lambda/4$ in which the typical values of the quality factor for these resonators are in the range of 500-800 [40, 41, 42]. The confinement of the acoustic wave will depend on the ratio between the high and low impedance layers: the bigger the ratio, the better performance of the Bragg reflector. The number of layers in the Bragg reflector is also an important parameter in the design of such a structure.

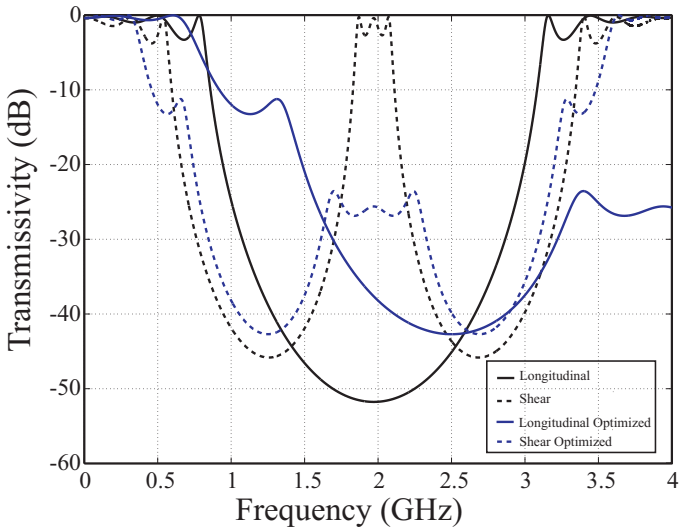

Figure 1.7: Comparison of the transmissivity response for a $\lambda/4$ and optimized Bragg reflector at 2 GHz.

Using the conventional solution for the design of the reflector entails a consideration: the propagation of thickness shear waves through the reflector. Unlike the fundamental mode, in which the propagation direction and the particle displacement are the same, shear waves are all those in which the propagation direction and the particle displacement are orthogonal. The propagation velocity of these is usually close to half of the thickness propagation velocity. In this case, the thickness of the layers at these propagation velocities will be very close to $\lambda/2$, leading to these waves travelling through the reflector and leaking to the substrate, with the corresponding degradation of the quality factor of the BAW resonator. The most common solution to this problem is the optimization of the layers for both the thickness and shear modes, as in [43, 44]. In Figure 1.7, the transmissivity and return losses using the conventional $\lambda/4$ (black line) and the optimized (blue line) solution are shown for the longitudinal and shear waves. Using the conventional solution, the transmissivity for the longitudinal mode is below 20 dB, but for the shear wave it is not less than 2 dB. In the optimized case, both longitudinal and shear transmissivity is below 20 dB, providing a very good performance at 2 GHz.

1.3.3 Electrical performance of BAW resonators

The input electrical impedance of a BAW resonator is characterized by the presence of two resonances at the resonance frequency f_r where the magnitude of the electrical impedance tends to its minimum value, and the antiresonance frequency f_a where the magnitude of the electrical impedance tends to infinity. The input electrical impedance for a certain BAW resonator is shown in Figure 1.8. This figure also shows that the phase between resonant frequencies is 90° behaving as an inductor, while outside these frequencies it is -90° with a pure capacitive behavior.

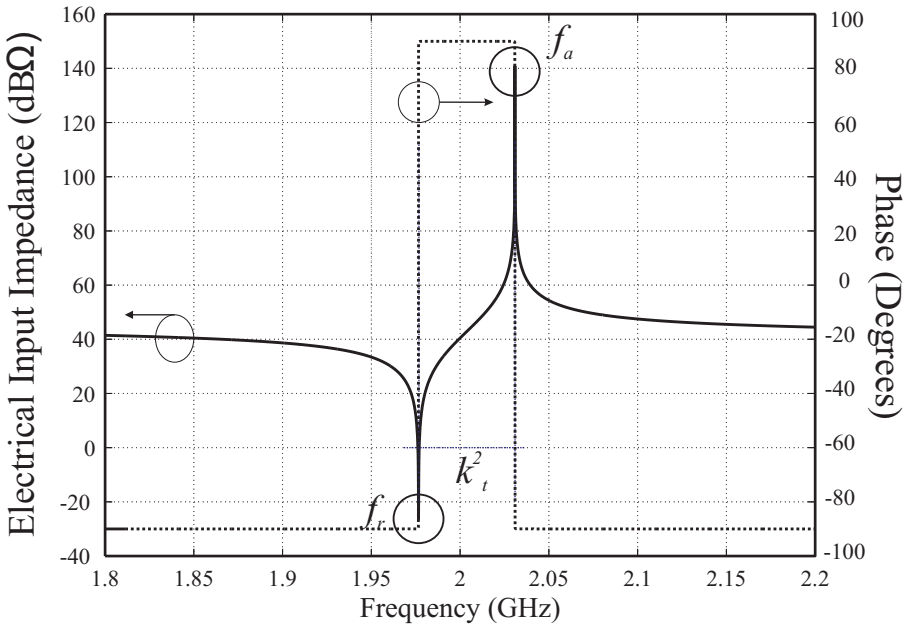

Figure 1.8: Electrical input impedance of a BAW resonator.

There are some one-dimensional models that allow the electrical characterization of the BAW resonator in terms of allocation of the resonant frequencies and the static capacitance C_0, with the most important being the well-known Mason model [45]. They are one-dimensional since lateral dimensions are considered to be infinite. However, due to the finite lateral dimension of the resonator structure, lateral acoustic waves, and generally Lamb waves, can also propagate [46]. Lateral standing waves become evident in the electrical behaviour of the BAW resonator in the form of spurious or unwanted resonances. In recent years, some of the efforts devoted to this technology have focused on finding the way to minimize their presence. The presence of lateral standing waves is related with the concept of energy trapping, which was studied in the early 1960s by Mindlin [47], Shockley [48] and Curran [49]. In this case, the area of the resonator which comprises all the layers of the stack acts as an acoustic cavity in which the modes which fulfil the boundary conditions propagate along the structure, and reflect at the boundaries leading to the lateral standing waves. From the point of view of multilayer structures, these modes have been seen to be a combination of thickness and shear waves, and an analytical solution can be developed for this kind of structure [50, 51].

The degradation of the performance of the BAW resonator due to these spurious modes is widely discussed in [52]. This is basically due to the fact that part of the energy contained in the fundamental thickness mode leaks to the lateral modes which results in the degradation of the quality factor of the resonator, but it is more evident when the BAW resonators are in a filter configuration leading to a strong ripple in the transmission bandpass. The presence of the lateral modes can be studied from the point of view of the acoustic dispersion which relates the

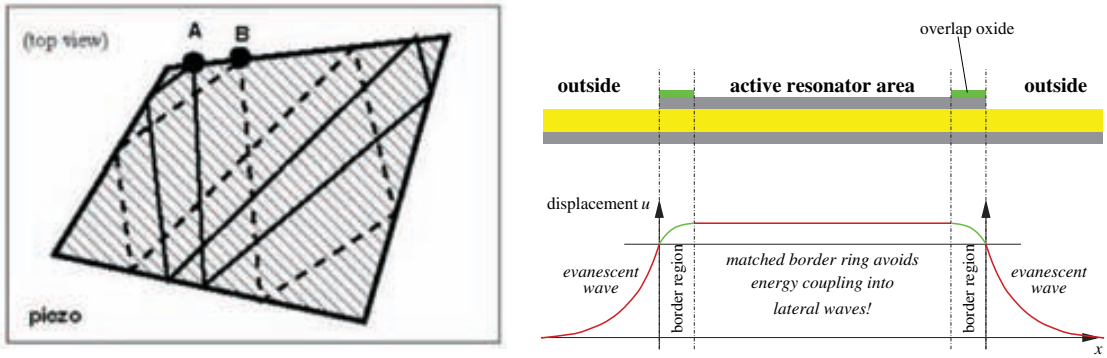

(a) Top view of an apodized BAW resonator [57] (b) Cross-sectional view of a BAW resonator with the thickened edge load [58]

Figure 1.9: Differente techniques to improve the electrical behavior of a BAW resonator.

wave number of the lateral wave with the frequency using the techniques described by Telschow in [53], or using laser interferometry as shown in [54, 55, 56].

Two different techniques has been proposed to improve the performance of the BAW resonators: apodization and thickened edge load, which are shown schematically in Figure 1.9. The first technique consists of designing the top electrode with non-parallel edges. By doing so, the resonant paths becomes much longer than for a squared electrode, making the standing waves to be more attenuated as proposed in [59]. But also circular shapes are also valid for this purpose as seen in [60, 61]. However, as will discussed further in this work, this solution entails a higher number of resonant paths that are now present in the structure, i.e. a higher number of spurious resonances. Although these are more attenuated, more energy leaks to these resonances giving cause to the degradation of the quality factor of the BAW resonator.

The second technique was discussed by Kaitila in [62]. Since the BAW resonator can be understood as an acoustic waveguide [28], the idea is to create a region with specific boundary conditions in which lateral acoustic modes cannot propagate. For type I resonators this is done by including a thickened edge load in the perimeter of the structure. The Smith Chart representation of the electrical input impedance of a BAW resonator with dispersion type I (ZnO) can be seen in Figure 1.10(a), where the presence of the unwanted modes is between resonances. For Type II resonators (AlN), as seen in Figure 1.10(b), the presence of unwanted modes is mainly given below the resonance frequency, thus in this case the solution is to create a region with a higher cut-off frequency, and this is only achieved by removing material in the perimeter of the structure. Since this solution is not evident from the technological point of view, Fattinger in [63], proposed a solution in which the idea was to include a Bragg reflector with as much dispersion type I material as possible forcing the whole stack to have a type I dispersion behavior. Different experimental results using this technique on type I resonators, generally ZnO, can be found in

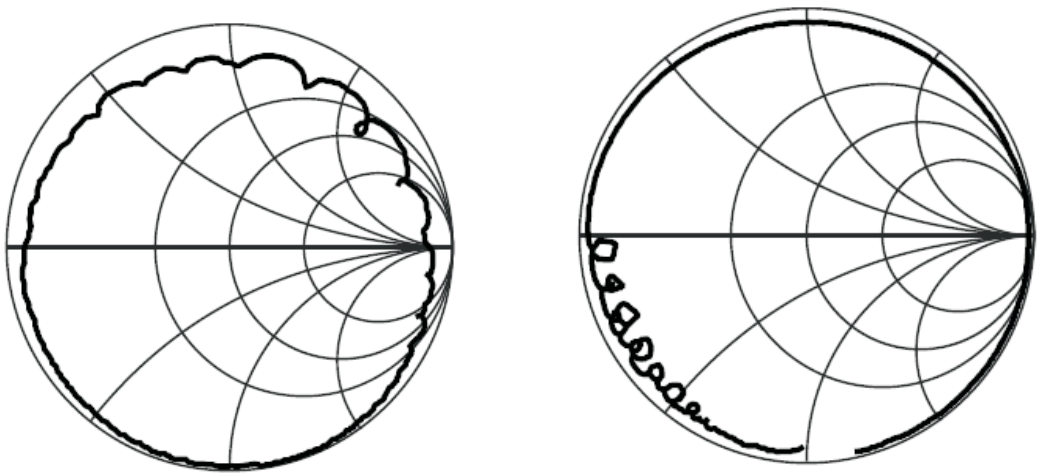

(a) (b)

Figure 1.10: Spurious modes in (a) type I resonator and (b) type II resonator [67].

[58, 64, 65, 66]. Looking at the Smith chart representation also gives a qualitative idea of the obtained Q-value. This is given by the radious of the main loop. For dispersion type I resonators, the radius is not as high between resonant frequencies as in dispersion type II. This is due to the fact that in this case, part of the energy of the fundamental mode leaks to the spurious modes which present a higher Q-value since they are allocated between resonant frequencies.

What has become obvious is that analysis of a BAW resonator demands accurate and reliable modelling, i.e. going beyond the one-dimensional model, to complete characterization of the electrical behaviour of the BAW resonator. Several analysis methods have been proposed in this regard. In 1974, Kagawa proposed a two-dimensional analysis method based on finite elements [68]. Boucher proposed a mixed method combining finite elements with the perturbation method [69]. In 1990, Lerch performed a comparison between the two- and three-dimensional method based on finite elements [70] in which the three-dimensional simulation clearly offers a higher agreement and prediction compared to the two-dimensional method, with the extra cost of the computation time. Although there are several ways of carrying out simulation and analysis of BAW resonators for the complete characterization of the electrical behaviour, the finite element method has been consolidated as the most commonly used analysis method, and achieves very high levels of agreement between the simulation and experimental results, and sometimes uses two-dimensional models since the degree of accuracy does not require three-dimensional models [71, 72], or the use of three-dimensional models as can be seen in [61, 73].

1.4 Filters Based on BAW Resonators

As mentioned above, the most common architecture for a wireless system is the classical heterodyne circuit block diagram, like the one shown in Figure 1.1. In the receiving path, the needs are generally based on the amplification or only the detection of the bandwidth of the desired signal, and to the exclusion of all other interfering ones. In conversion schemes, the intermediate frequency (IF) chosen is dependent on the available filter technology, in order to produce the required fractional bandwidth of the signal [74]. The particular features of the various technologies available define their range of applicability, such as achievable resonator Q, size and manufacturability. From this point of view, filters based on BAW resonators seem to be able to meet the requirements of modern communication systems, as high selectivity, high frequency operating range and compatibility with standard IC technologies.

Depending on how the BAW resonators are interconnected, there are two main groups of filter topologies [75]: Ladder and Lattice, in which the BAW resonators are electrically connected, and Stacked Crystal Filters and Coupled Resonator Filters, in which the BAW resonators are acoustically coupled. The main features of the different types of filters will be discussed in this section, with the advantages and drawbacks in each case.

1.4.1 Filters based on electrically connected BAW resonators

Considering BAW resonators as circuit elements, networks of resonators can be designed to implement various filter characteristics. In this section we are going to deal with topologies in which the BAW resonators are electrically connected between them in a balanced and unbalanced configuration. Lattice-type filters belongs to the balanced while ladder belongs to the unbalanced topology.

The conventional Ladder topology is composed of consecutive series and shunt BAW resonators, as seen in Figure 1.11(a). This type of filter presents a transmission response shown in Figure 1.11(b), which is characterized by its high selectivity due to the presence of two notches. The transmission zeros are due to the resonance and antiresonance frequency of the shunt and series resonators respectively. The drawback of this type of filter is their poor out-of-band (OoB) rejection, which is due to the natural capacitor voltage divider. Improvement of the OoB rejection entails increasing the order of the filter [76, 77]. However, at the same time, increasing the order of the filter entails increasing the in-band insertion loss [78] and the ripple, and also entails the presence of a pair of spikes at the limits of the bandpass. As will be discussed in detail, this is related with the image impedance and the required condition for bandpass and stopband in a network cascade configuration [79]. The achievable relative bandwidth can be written in terms of the effective electromechanical coupling as $W(\%) \simeq k_{eff}^2/2$ [35]. In order to obtain reasonable

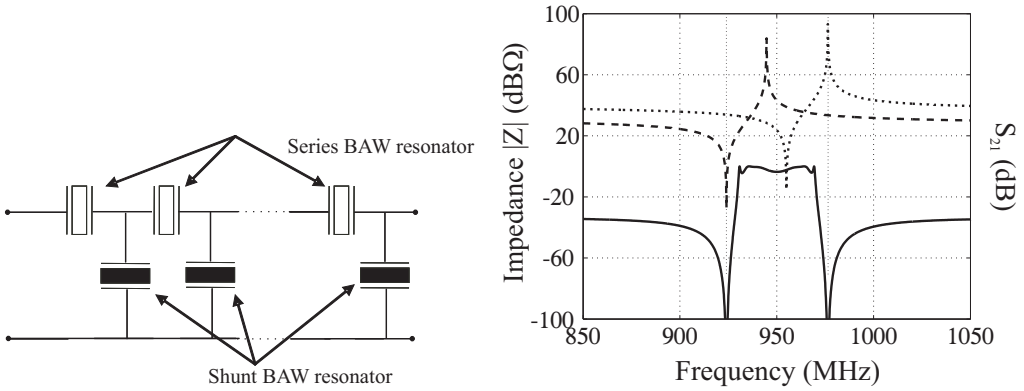

(a) Ladder-type filter configuration (b) Ladder-type filter transmission response

Figure 1.11: Ladder-type filter configuration and transmission response [77]

bandwidth, the shunt resonators must be slightly untuned from the series resonators. To do this entails some difficulties in the fabrication process which requires of some special techniques like frequency trimming [80].

Ladder-type filters based on ZnO or AlN can be found since the early 1990s, such as the work in [81], which mentions a Ladder-type filter with order $N = 6$. In this case, the central frequency is around 1 GHz, achieving an OoB rejection higher than 100 dB, and an insertion loss of around 3.8 dB. However, the presence of spurious modes leads to in a ripple in the bandpass. In this case, the solution was to include grounded inductors between the building blocks in order to move these spurious upwards towards the bandpass. In [82], Lakin designed various filters for GPS applications, such as 3/2[1], 4/3 and 6/6 structures. The 6/6 structure shows a transmission band centred on 1.48 GHz with an insertion loss of 6.8 dB, and an OoB rejection higher than 40 dB. Later, in 1995, Mang designed a Ladder-type filter based on ZnO with order $N = 3$ and $N = 5$, achieving an insertion loss of 2.2 dB and selectivity of 15 dB for the former, and an insertion loss of 5 and selectivity of 32 dB for the latter, and showed the relation between the order of the filter N, the insertion loss L and the OoB rejection with experimental results [83]. In this case, the selectivity was calculated as the difference in dB between the minimum insertion loss of the bandpass and the minimum OoB rejection.

Very narrow bandpass ladder-filters can also be designed without the corresponding degradation of the effective electromechanical coupling constant. In [84], Lakin proposed overmoded BAW resonators applied to Ladder filters. Since the effective electromechanical coupling coefficient of higher fundamental harmonics is lower, this achieves very narrowband filters , with bandwidths of $B_w = 76$ KHz at a central frequency of 1.6 GHz. However, in this case, having a very low $k^2_{eff} = 0.019\%$ value leads to a high insertion loss of $L = 7.3$ dB.

[1] N/M where N refers to the number of series resonators and M to the number of shunt resonators.

From the frequency operation point of view, as mentioned above, filters based on BAW resonators overcome the limitation with SAW resonators. Applications above 5 GHz can be found in [26], in which a 5/3 Ladder filter with doubled resonators is manufactured at 5.2 GHz, with a 4 dB relative bandwidth of $W = 3.2\%$, exhibiting a minimum insertion loss of $L = 2.0$ dB, and an OoB rejection of more than 24 dB. The prototype manufactured and its frequency transmission response are found in Figure 1.12. [24], even discusses a Ladder-filter for K-band. Here, the central frequency is at 19.8 GHz and the insertion loss $L = 4.1$ dB for a relative bandwidth of $W = 2\%$. However, such a high frequency entails very thin layers, which are mechanically weak and fragile.

Afterwards, efforts were focussed on the improvement of the performance of the transmission response, basically with the inclusion of reactive elements in the filter topology. In [78], in order to improve the OoB rejection for a narrowband filter, the parasitic elements due to the package are used, with the inductor specifically associated with the wire-bonded package, achieving a filter response with relative bandwidth $W \simeq 2.5\%$, and insertion losses $L = 1.2$ dB, OoB=50 dB and N=8, or $L = 0.8$ dB, OoB=30 dB and N=6; making the capacitance ratio to be more relaxed to fulfil the OoB specification. Also in [77], external reactive elements are used in order to add transmission zeros to the transmission response which leads to an increase in the OoB rejection without increasing the order of the filter.

With the aim of trying to systematize the design procedure of this type of filter, in [85] Shirakawa presents a synthesis methodology which enables the placement of asymmetric transmission zeros, as well as the exact determination of the transfer function poles. However, in order to determine the final parameters, i.e. the geometrical definition of the BAW resonators, an optimization process is necessary. This drawback is overcome in the work by Menéndez in [76], which includes the closed-form expressions for the design of a Ladder-type filter, showing a very good agreement between transmission response and the designed Ladder-type filter for the GPS application in [86], without any optimization process. Further on, in [87], the design

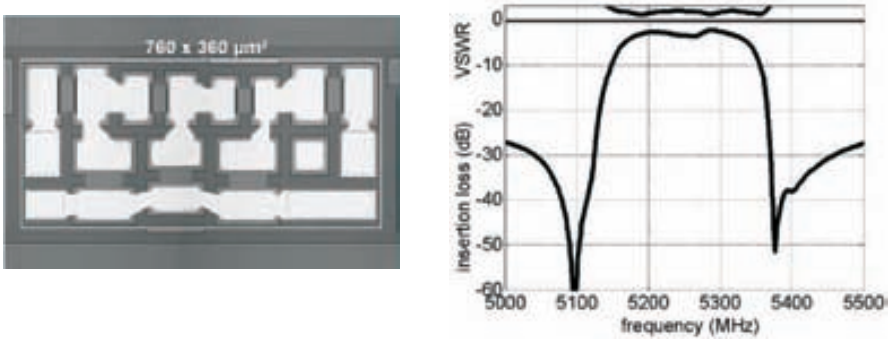

Figure 1.12: Manufactured prototype and transmission response for a Ladder-filter at 5.2 GHz [26].

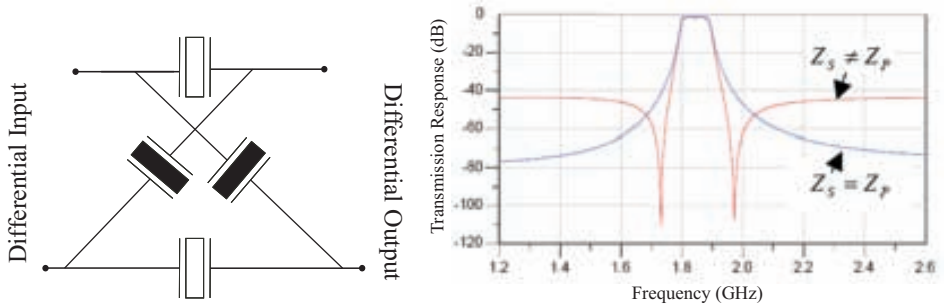

(a) Lattice-type filter configuration (b) Lattice-type filter transmission response

Figure 1.13: Lattice-type filter configuration and transmission response [89]

procedure for Ladder-type filters is expanded to take the effect of the electrodes into account.

Finally, some works are also related to mass volume production, such as [88], in which the different features for the volume manufacturing are discussed. As it is described in that study, the challenges are focused on the quality of the piezoelectric material on a regular basis, and the right frequency on more than just a few spots on a wafer. Similarly, Infineon's trimming method corrects run-to-run deviations as well as uniformity problems achieving satisfactory yields $> 80\%$.

Lattice-type filters are the other configuration included in the large family of electrically connected BAW resonators filters. This is an interesting configuration for applications wherein the direct connection with RF integrated circuits is best made using balanced networks. The basic configuration of this type of filter is shown in Figure 1.13, where balanced input and output are found. In this configuration, the normal pole-zero response of a resonator is suppressed to give a more conventional multi-pole response. This configuration therefore usually exhibits a higher bandwidth than ladder-type filters without the presence of the transmission zeros, unless the electrical impedance of the BAW resonators $Z_s \neq Z_p$, as shown in Figure 1.13(b). Furthermore, unlike Ladder-type filters, Lattice-type filters present a better OoB rejection due to the fact that if the series and cross capacitors are chosen equal, this leads in a voltage cancellation across the two pairs of resonators. The drawback is that they cannot perform balanced to unbalanced transitions if these are required [90].

Finally, some hybrid configurations have been developed as a combination of ladder- and lattice-type filters. [91], presents a combination of the Ladder and Lattice topology in which the best performance of both topologies is obtained, i.e. the high selectivity of the Ladder-type filters and the good OoB rejection of the Lattice-type filters as seen in Figure 1.14. The results obtained show a transmission response centered on 2.15 GHz, with an insertion loss of $L = 3.55$ dB, and an OoB rejection higher than 40 dB. Other references and achievements for the Lattice-type filter topology can be found in [92].

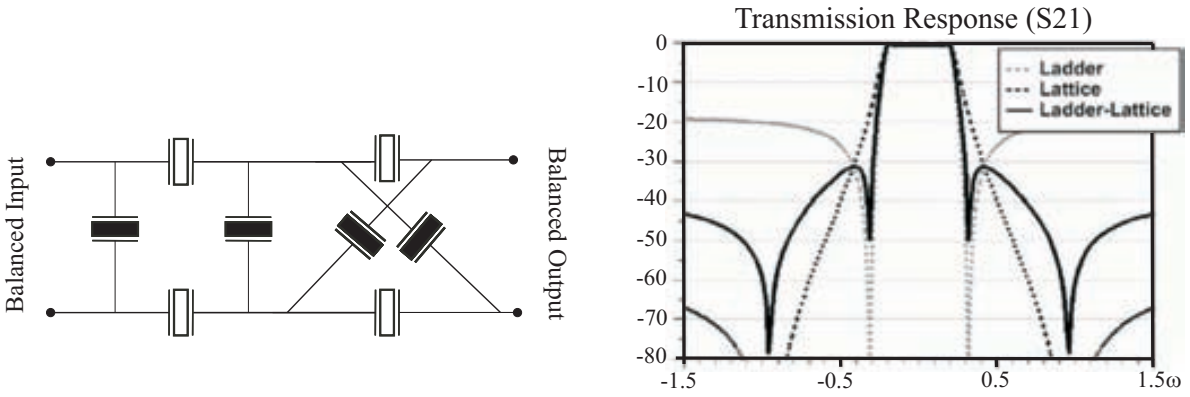

Figure 1.14: Ladder-Lattice topology and its transmission response S_{21} [91].

1.4.2 Filters based on acoustically coupled BAW resonators

One of the most important drawbacks in the filters based on electrically connected BAW resonators is related to the limited achievable bandwidth, which mainly arises in the ladder-type filters. This is due to the finite value of the effective electromechanical coupling constant. The solution to this limitation consists of newer filter configurations, and particularly, filters based on acoustically coupled resonators. They key to wide bandwidth multipole filters without using of external reactive elements, is in acoustic loading and resonance splitting due to propagating effects, rather than just the electrical interactions of resonators as circuit elements [94].

The simplest configuration of a filter based on acoustically coupled resonators is the stacked crystal filter (SCF) which is shown in Figure 1.15(a) [93]. The structure consists of two stacked BAW resonators in which the central electrodes are electrically grounded. When an electric field is applied to the top resonator, the mechanical deformations in this resonator induce mechanical

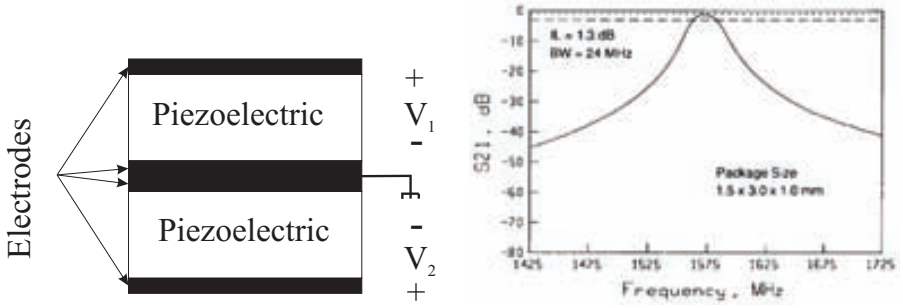

(a) Stacked Crystal Filter configuration (b) Stacked Crystal Filter transmission response

Figure 1.15: Stacked Crystal Filter configuration and transmission response [93]

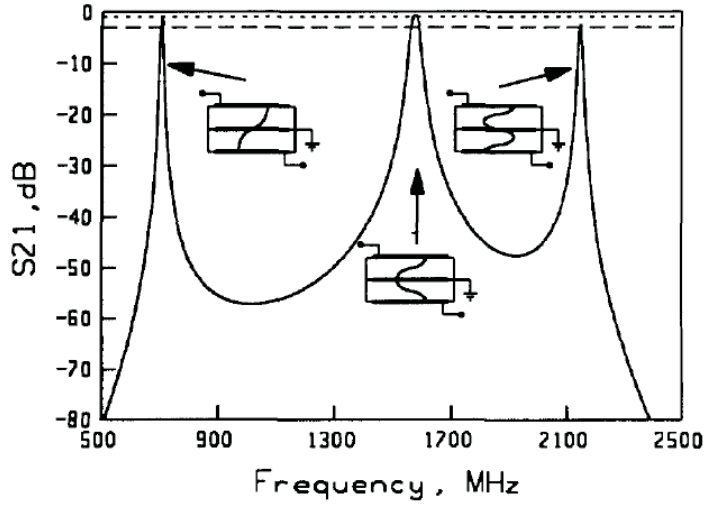

Figure 1.16: Wide frequency range SCF transmission response [94].

deformations in the bottom resonator with the corresponding electric field. In this structure, the BAW resonators are so strongly coupled that the structure acts as a single resonator. The frequency response of this type of filter is shown in Figure 1.15(b). This topology presents a complex frequency response, as shown in Figure 1.16 where different resonances are present at approximate multiples of the frequency, corresponding to the half wavelength across the whole structure [94]. The resonance with the wider bandwidth is where there is a half wavelength across each of the BAW resonators. The lower band occurs when there is approximately half of the wavelength across the whole structure, and the higher band when there are three half wavelengths.

The first filter based on SCF was presented by Ballato in 1973 [95]. In this case, the filter response showed a relative bandwidth of 4.2%, and an insertion losses of $L = 8$ dB. Later, Lakin proposed the equivalent circuit for the SCF in [96], which has been very useful in the design of this filter and other configurations. In [97], more experimental results are shown for different configurations, connecting two SCF sections in series in order to obtain more selectivity in the transmission response, or SCF which uses the highest resonance which present a high Q-value, exhibiting insertion losses below 1.5 dB. Two-pole or two SCF sections connected in series can be also found in [98], with the aim in this case being to manufacture filters above 2 GHz. In this case, several transmission bands are found at 8.2, and 12.4 GHz, with the former achieving an insertion losses of $L = 6$ dB, and the latter $L = 3.3$ dB. In order to improve the performance of the SCF filter, Lakin proposed manufacturing the SCF over a narrowband SMR [93], forcing the lower and higher resonances to be attenuated due to the poor confinement of the acoustic wave at these frequencies.

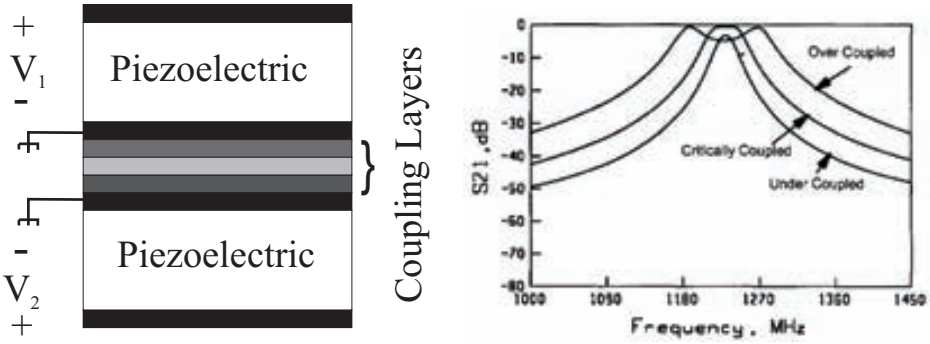

(a) Coupled Resonator Filter configuration

(b) Coupled Resonator Filter transmission response

Figure 1.17: Coupled Resonator Filter configuration and transmission response [94]

The design of SCF filters has been traditionally based on an optimization process using the equivalent circuit model proposed by Lakin in [96]. In order to overcome this limitation, and with the aim to provide more control over the transmission response of the filter, in [99] Menéndez presents the methodology for designing SCF filters with a Butterworth/Chebyshev response, giving closed-form expressions to that end. Here, two SCF sections are presented which are connected by means of a coupling element, a reactive element, with the drawback of adding losses to the filter response, and increasing its size. As a design example, two different filters are presented for narrow- and wideband transmission response ($W = 0.7\%$ and $W = 3\%$ respectively), using a capacitor as a coupling element in the former, and using an inductor in the latter.

However, the SCF filter can be considered as a particular case of the Coupled Resonator Filter (CRF) structure in which wider bandwidths in the transmission response can be achieved by reducing the coupling between both BAW resonators. The general configuration is shown in Figure 1.17 where the structure consists of a pair of BAW resonators that are acoustically coupled by means of a set of coupling layers. After the set of coupling layers is removed from the structure, there is a SCF case in which the whole structure behaves like a single overmoded resonator. Depending on the configuration of the coupling layers, different situations may arise, as shown in Figure 1.17(b) in which the composing BAW resonators may be under-coupled, critically-coupled or over-coupled. The coupling layers thus control the filter bandwidth. Unlike the SCF case, the typical transmission response for an over coupled CRF clearly shows two different poles. The CRF is designed so that the bandwidth is determined by the degree of coupling between the resonators and not by the inherent bandwidth of the coupling mechanism [94]. In [100], a four-pole CRF is designed at 1960 MHz, achieving a 3 dB relative bandwidth of $W = 3.6\%$ and an insertion losses of $L = 2.8$ dB. The topology of the structure allows it to be used as a mode conversion structure. In [101], a single-to-single CRF structure has been

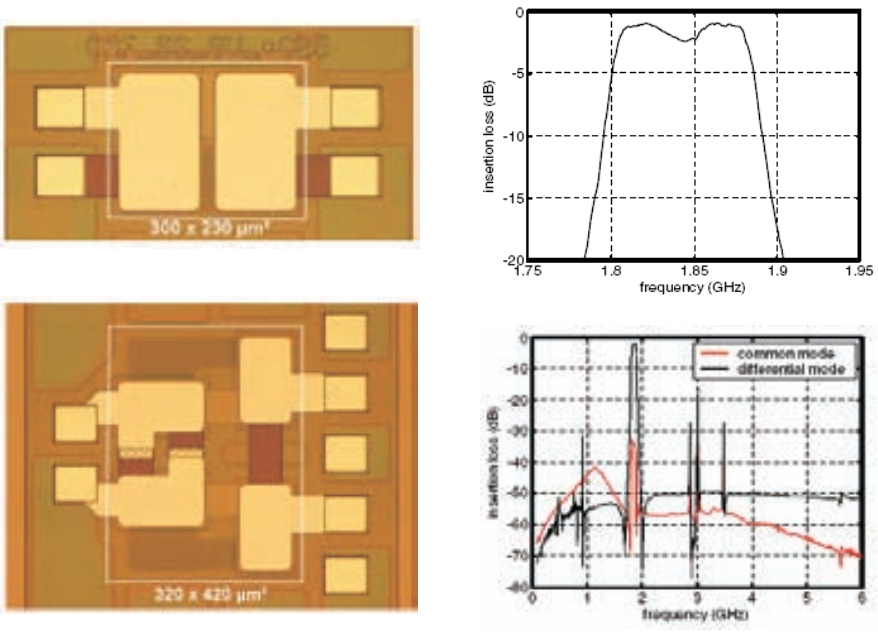

Figure 1.18: Manufactured single-to-single and single-to-balanced CRF filter [101].

manufactured at 1.8 GHz, with a bandwidth of $B_w = 79.7$ MHz with a minimum insertion losses of $L = 1$ dB. This work also includes a single-to-balanced mode conversion structure featuring an impedance transformation from 50 Ω to 200 Ω. The common mode suppression achieved is in the range of -40 to -60 dB. The results for the single-to-single and the single-to-balanced structures can be found in Figure 1.18 (top view and bottom view respectively).

Using the proposed equivalent circuit for the SCF structure, in [102], the equivalent circuit for the CRF structure was developed, which allows it to be linked to the classical filter synthesis techniques based on the coupling control to this structure. Very importantly, by using quarter-wavelength thick layers for the coupling layer, and taking into account that the value of the coupling is directly related with the acoustic impedance and the area of the comprising layers, only a discrete number of achievable coupling values are possible. In order to overcome this limitation, in [103], each of the coupling layers are designed to have a different quarter-wavelength thick. However, this requires an optimization process to achieve the desired purpose. Corrales proposes a set of closed-form expressions for the design of the set of coupling layers, which enable the structure to be designed without time-consuming optimization costs [104]. Furthermore, the proposal by Fattinger in [101] is to use some organic materials with a very low acoustic impedance, with the advantage that only one layer is required to decouple both resonators. However, the drawback of this solution is that this kind of material is usually relatively lossy (1000-2000 dB/cm) [67].

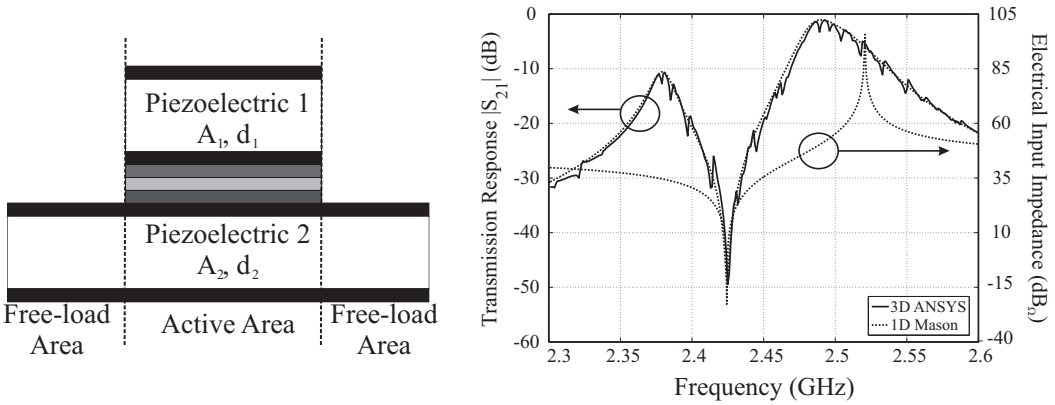

Figure 1.19: Asymmetric CRF structure and its transmission response with the electrical input impedance corresponding to the free-load area [105].

All the proposed CRF structures are formed in such a way that the whole stack presents the same area, which has been called symmetric CRF. In [106], a synthesis methodology is proposed for a CRF structure in which the bottom resonator has a bigger area than the top one, which has been called asymmetric CRF. In this case, the authors model the structure by means of the Mason model, cascading the resonators and coupling layers, and assuming a different area in the bottom electrode. This is partially correct, as demonstrated in [105]. Taking into account the various boundary conditions in the structure, using the one-dimensional model is not a valid approach for modelling the whole structure. The free-load area of the asymmetric CRF must be modelled as an independent BAW resonator that is electrically connected to the active CRF structure. By doing so, a deep notch is achieved in the transmission response of the structure which was not possible with filters based on acoustical coupled resonators. The structure and the transmission response of the asymmetrical CRF structure and the electrical input impedance of the free-load area are shown in Figure 1.19 in order to illustrate this phenomenon [105]. This configuration also enables stop-band filters to be obtained with the proper allocation of the transmission zeros and the proper allocation of both transmission bands.

1.5 Motivation and Purpose of the Thesis

The revision and the state of the art of the current achievements related with the BAW technology shows that the application of BAW technology to microwave devices is mainly due to advances in the microelectronic manufacturing process. The efforts in the development of technology have therefore focused on improving the performance of the BAW resonator and on the application of BAW resonators to the design of microwave devices, and particularly RF filters. Taking this into account, different features can be emphasised regarding BAW technology and its application to RF filters:

1. The validity of the one-dimensional Mason model to represent the electrical behavior of BAW resonators has been highlighted in the numerous works related to it. Derived models such the Butterworth-Van Dyke or the KLM model are also very good approaches to the electrical behavior of the BAW resonator at fundamental modes and in higher harmonics. However, effects due to the three-dimensional nature of the structure are evident in the form of the degradation of the electrical performance of the BAW resonator due to the presence of spurious modes at the frequencies of interest, which cannot be predicted by the one-dimensional approach.

2. Various solutions have been developed in order to minimize or avoid the presence of unwanted modes. The apodization technique only requires a change in the geometry of the top electrode, which does not imply any complication in the manufacturing process. However, when using this solution the quality factor obtained is not optimum, since unwanted modes are minimized but are still present. The materials used also play a very important role in this technique. Meanwhile, the inclusion of a thickened edge load provides a more robust solution, since in this case the lateral modes cannot propagate through the structure, achieving very good Q-values. However, the side-effects arising from this solution could affect the electrical behavior of the BAW resonator.

3. Filters based on BAW resonators are becoming consolidated as the key to overcoming the limitations presented by filters based on other technologies in modern communication systems, such as size, operation frequency range and compatibility with standard integrated circuit technology. Filters based on electrically connected resonators, and particularly Ladder-type filters, consist of a very simple topology, with high selectivity and low insertion loss. However, the main drawback is the poor OoB rejection. Filters based on acoustically coupled resonators overcome the limitation of ladder-type filters, but the drawback in this case is the optimization process needed for the design of the coupling layers, and the complex manufacturing process

Taking into account the above, the work of this thesis has focused on the use of the three-dimensional analysis for a full understanding of the BAW resonator from the electrical and mechanical point of view. A more specific study on the different proposed mechanisms to improve the performance of BAW resonators, and the application of the BAW technology to the design of microwave filters will be carried out. The aim is to try to move beyond simple electrical behavior and to try to obtain additional information from the physics underlying the working principle of acoustic devices. By doing so, the mechanical effects can be electrically modelled and we can thus have better predictions of the performance of the BAW resonator. The main reasons for beginning this thesis can therefore be summarized as follows:

1. A complete analysis and understanding of the various mechanisms in the electrical and mechanical plane that govern the piezoelectric effect, to obtain a better understanding of the different ways to model the BAW resonator in one dimension. This will be very useful in stating the limitations of such a model and the mechanisms that can be used to overcome them. The dependence of the geometry with the electric properties of BAW resonators can be related to most cases.

2. To use the available methods of analysis of BAW resonators to obtain the complete characterization of their electrical behavior. For this purpose, ANSYS has been chosen as software that is very suitable for carrying out the different simulations. Since the mechanical behavior of the BAW resonator can also be extracted with ANSYS, the aim of this thesis is to try to move beyond electrical models and to have a better understanding of the phenomena underlying the working principle of BAW resonators. To that end, and taking into account the allocation of the spurious modes depending on the dispersion type material, BAW resonators based on Zinc Oxide and air-gap cavity have been chosen for carrying out the three-dimensional study.

3. Using three-dimensional simulations, a more in-depth study of the proposed techniques for the optimization of the BAW resonator performance can therefore be carried out. For the apodization technique, the aim is to analyze the relationship between the performance of the BAW resonator with the different available metal electrodes and the shape of the top electrode. Meanwhile, the side effects of the thickened edge load solution will be characterized and modelled using the one-dimensional equivalent circuits, and the results validated with the three-dimensional analysis.

4. Regarding the filters based on electrically connected resonators, the aim is to try to improve the performance, particularly of Ladder-type filters. Efforts must be made to improve the poor out-of-band presented by this type of filters.

5. Finally, all the presented filter topologies present a single transmission band. There are efforts devoted to the design of multi-frequency microwave devices in order to improve the

performance of the systems where they are included. In the European project Mobilis[2], one of the goals was to try to develop a multi-band/multi-standard transmitter and its implementation for the application of DCS-Edge/WCDMA. One of the works that must by highlighted in this thesis is the development of a dual-band filter based on BAW resonators which is very similar to the conventional ladder-type filter. This has to be highlighted because: by one hand, a dual-band transmission response can be achieved using BAW resonators, which is not until this moment known; on the other hand, the simplicity and the similarity with the conventional ladder-type filter topology makes a very suitable device to be manufactured. Therefore, this new topology has become an objective of this thesis.

1.5.1 Thesis outline

In this chapter, we have reviewed the development of the BAW technology from the point of view of performance of BAW resonators, as well as the application of these resonators to the design of microwave devices. The reason for the thesis has also been discussed, as well as the objectives.

Chapter 2 includes an analysis of the acoustic wave propagating through non-piezoelectric material. The circuital representation obtained shows a series of analogies between the mechanical and electrical plane that is very useful for further developments. This development is then expanded to the piezoelectric slab by obtaining the well-known Mason model. By using this model, the mass loading effect can be extensively considered and the effects of the presence of metal electrodes can be described. After this, various one-dimensional approaches such the Butterworth-Van Dyke and the KLM model are also discussed. By doing so, the limitations of the one-dimensional models and the needs of the three-dimensional simulations can be justified.

In chapter 3, BAW resonators are studied using the three-dimensional analysis. First, the mechanical wave solution will be extrapolated from the one- to the three-dimensional case. After this, the propagation of lateral waves is studied in order to obtain the boundary condition requirements and the resonance condition for the propagation of these waves. Taking into account the need for three-dimensional analysis, the Finite Element Method (FEM) will be introduced and the basis to carry out simulations of acoustic devices will be given. Finally, the comparison with the one-dimensional model will be made using three-dimensional simulations, in order to find the required 3D simulation conditions, and to finally obtain the complete characterization for the electrical behavior of the BAW resonator which cannot be obtained using one-dimensional models.

Chapter 4 covers the optimization of the performance of BAW resonators, particularly in the different solutions for minimizing or avoiding the presence of spurious modes. With regard to the

[2] www.ist-mobilis.org

apodization technique, a systematic study using different metal electrodes and various shapes is undertaken to show the performance of the BAW resonator. The side effects related to the thickened edge load technique will be accurately modelled and validated using three-dimensional simulations.

The ladder-type filters based on BAW resonators are discussed in Chapter 5. First of all, the working principle of these filters is discussed. The design procedure of this type of filter is then developed, with infinitesimal metal electrodes considered first, and the mass loading effects then included in in the design procedure. Finally, the improvement of OoB rejection in these filters is achieved by including external reactive elements in the topology. The closed-form expressions for these modifications and validation examples are found.

The developed double-ladder dual-band filter is shown in chapter 6. As with the conventional ladder-type filter, the working principle is discussed first, and is very similar to the conventional ladder-type filter. Some of the limitations in the conventional ladder-type filter are therefore also found in the double-ladder filter. However, the design procedure for this filter is presented, and some examples for the GNSS are shown. Finally, a transmission response using measured resonator is presented as a validation of the developed topology.

Finally the conclusions of this work as well as the future line work will be set out.

CHAPTER 2

Modelling Acoustic Resonators in One-dimension

The aim of this chapter is to analyze the propagation of an acoustic wave through a non-piezoelectric slab, which will be later extended to the piezoelectric slab. In a first approach, the piezoelectric slab is considered to be infinite in its lateral dimensions which means that only waves propagating in the thickness direction are present. One-dimensional equivalent circuits can therefore be obtained from the given analysis which are a very good approach to the correct characterization of the electrical behavior of the BAW resonator in terms of resonant frequencies, static capacitance and electromechanical coupling constant. The structure of these equivalent circuits leads us to state a series of analogies between the electromagnetic and mechanical plane, which will be very useful for a better understanding of the underlying phenomenon governing the behavior of the acoustic resonator.

Using the models obtained, the problem is extended to the case of loading the piezoelectric slab with arbitrary mechanical loads. This leads to an analysis of the mass loading effect, in which frequency shifting and variations of the electromechanical coupling constant are involved. The development of the one-dimensional mechanical wave as well as the derived electrical models comes from the works in [28, 33, 46].

2.1 One-dimensional Mechanical Equation of Motion

In Newton's basic laws, a given force applied to a rigid body traditionally results in an acceleration of the body. This is the case because the body is assumed to be rigid, and the force transmits instantaneously to all the internal parts of the body. However, this is not exactly true in deformable bodies, in which internal effects are very important. In this case, when some force is applied to this kind of body, internal forces, called *stresses*, and deformations, called *strains*, appear in the atomic structure of the body. Stress does not cause strain, and strain does not cause stress, but the presence of one requires the presence of the other, as is the case with the magnetic and electric field in the electromagnetic plane.

Because of the elasticity of the body, internal deformations and strains occur under a certain applied force. In this case, internal particles of the body will suffer some mechanical displacement, leading to the definition of the strain,

$$S = \frac{\partial u}{\partial z} \tag{2.1}$$

where u is the particle displacement. At the same time, the linear relation between stress and strain by means of the stiffness constant c is given by the Hooke's law,

$$T = cS \tag{2.2}$$

Figure 2.1 shows a general volume which is assumed to be isotropic. In this case, the orientation of the area is defined with its normal vector. Using this reference, the stress can be longitudinal when the components are parallel to the area vector $\vec{A}$, and shear when the components are transversal to $\vec{A}$. Significantly, the stress components usually appears in opposite pairs, which are not always equal. In other words, a traction force T_1 will lead to an opposite traction force $-T_1$. The relation between the applied force and the stress components can be expressed as,

$$dF = \frac{\partial T}{\partial z} dz dA \tag{2.3}$$

Based on the previous definitions, the Newton law can then be rewritten as

$$\frac{\partial T}{\partial z} dz A = \rho A \Delta z \frac{\partial^2 u}{\partial t^2} \quad \Rightarrow \quad \frac{\partial T}{\partial z} = \rho \frac{\partial^2 u}{\partial t^2} \tag{2.4}$$

where the left-hand term in the equation (2.4) is the applied force, the product of the density ρ and the volume, given in terms of area A and z increment, corresponds to the mass, and the second derivative of the displacement with respect z corresponds to the acceleration. Taking into account that the particle velocity is the time derivative of the particle displacement,

$$v = \frac{\partial u}{\partial t} \tag{2.5}$$

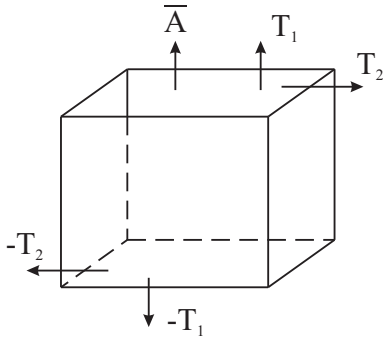

Figure 2.1: Orientation traction forces in an isotropic volume.

all the constitutive equations needed for the one-dimensional mechanical wave equation have been obtained (2.1)-(2.5). If the partial derivative for time is applied to (2.1) and (2.2), the expression obtained results in,

$$\frac{\partial S}{\partial t} = \frac{\partial^2 u}{\partial t \partial z} \;\Rightarrow\; \frac{\partial v}{\partial t} = \frac{1}{c}\frac{\partial T}{\partial t} \tag{2.6}$$

Now, differentiating (2.4) with respect z, and (2.6) with respect time, and equaling the cross derivatives, the one-dimensional mechanical wave equation can be obtained,

$$\frac{1}{\rho}\frac{\partial^2 T}{\partial z^2} = \frac{1}{c}\frac{\partial^2 T}{\partial t^2} \tag{2.7}$$

where the phase velocity of the mechanical wave, v_a, is easily obtained as,

$$v_a = \sqrt{\frac{c}{\rho}} \tag{2.8}$$

However, it is more interesting to express the one-dimensional mechanical wave equation in terms of dependence on the mechanical displacement u for further developments. To do this, using the Newton's and Hooke's laws, and equaling the terms with cross derivatives, the mechanical displacement can be finally expressed as,

$$\frac{\partial^2 u}{\partial z^2} = \frac{\rho}{c}\frac{\partial^2 u}{\partial t^2} \tag{2.9}$$

2.2 Solution of the One-dimensional Mechanical Wave in a Non-Piezoelectric Slab

In this section, the mechanical wave is going to be analyzed when it is propagating in a non-piezoelectric slab, in order to obtain the solution to the wave equation obtained in (2.9). The scenario to be analyzed is shown in Figure 2.2 in which a non-piezoelectric slab with thickness $d_p = z_2 - z_1$ and infinite lateral dimensions is found. Considering the slab as a lossless, isotropic

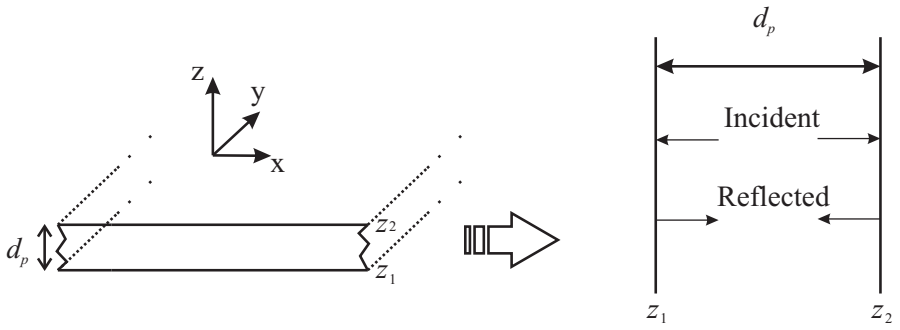

Figure 2.2: Scenario where the propagation of the one-dimensional mechanical wave will be analyzed.

and free-charge medium, two different mechanical waves thus propagates through the structure which are solution of the equation (2.9), the incident and the reflected wave. In this case, the mechanical wave can be expressed as the solution consisting of both waves in its phasor notation,

$$u(z) = A^{+}e^{-jkz} + A^{-}e^{+jkz} \tag{2.10}$$

where A^{+} is the amplitude of the progressive wave while A^{-} is the amplitude of the regressive wave. The term k is the wave number defined as $k = \omega/v_a$, with ω being the angular frequency. If the derivative with respect to t is applied to the expression in (2.10), the particle velocity can be obtained and also be computed in the slab limits z_1 and z_2. In this case the particle velocity results in,

$$\begin{aligned} v_1 &= j\omega\left(A^{+}e^{-jkz_1} + A^{-}e^{+jkz_1}\right) \\ v_2 &= j\omega\left(A^{+}e^{-jkz_2} + A^{-}e^{+jkz_2}\right) \end{aligned} \tag{2.11}$$

Multiplying the first equation in (2.11) with e^{jkz_2} and the second equation with e^{-jkz_2}, means that the second equation can be substituted for the first one. Finally, after some trigonometric transformations, the progressive and regressive waves can also be expressed as,

$$\begin{aligned} j\omega A^{+} &= \frac{v_1 e^{jkz_2} - v_2 e^{jkz_1}}{2j\sin(kd_p)} \\ j\omega A^{-} &= \frac{v_2 e^{-jkz_1} - v_1 e^{-jkz_2}}{2j\sin(kd_p)} \end{aligned} \tag{2.12}$$

The acoustic impedance of the mechanical wave can be defined as $Z = -T/v_p$, where the minus sign is included so that the impedance will be positive because T and v_p are 180° out of phase. Thus, since in the one-dimensional case under study we can consider that $F = -AT$ and we obtain,

$$Z = \frac{-T}{v_p} = \sqrt{\rho c} = \rho v_p = \frac{ck}{\omega} \rightarrow F = \frac{Ackv_p}{\omega} \tag{2.13}$$

The Hooke's law can be rewritten as a function of the applied force leading to,

$$T = c\frac{\partial u}{\partial z} \rightarrow F = Ac\frac{\partial u}{\partial z} \rightarrow F = jAck\left(A^{+}e^{-jkz} - A^{-}e^{jkz}\right) \tag{2.14}$$

Table 2.1: Mechanical and electrical plane analogies. [28]

One-Dimensional Mechanical Equations	Maxwell Equations
Fundamental Physical Laws	
$\frac{\partial T}{\partial z} = \rho \frac{\partial v}{\partial t}$	$\nabla x \vec{E} = -\frac{\partial \vec{B}}{\partial t}$
$S = \frac{\partial u}{\partial z}$	$\nabla x \vec{H} = \frac{\partial \vec{D}}{\partial t} + \vec{J}$
Constitutive Equations	
$T = cS$	$\vec{D} = \varepsilon \vec{E}$
$v = \frac{\partial u}{\partial t}$	$\vec{B} = \mu \vec{H}$

Finally, by substituting the solutions of (2.12) in (2.14), the solution of the mechanical wave in a non-piezoelectric slab as a function of the applied force F, the particle velocity v_p and the acoustical impedance Z is finally obtained,

$$\begin{aligned} F_1 &= \frac{Z}{j \sin(kd_p)} (v_1 - v_2) + jZ \tan\left(\frac{kd_p}{2}\right) v_1 \\ F_2 &= \frac{Z}{j \sin(kd_p)} (v_1 - v_2) - jZ \tan\left(\frac{kd_p}{2}\right) v_2 \end{aligned} \tag{2.15}$$

The way that the relations between the mechanical parameters are given in the set of equations in (2.15) enable a simple circuit representation. To do this, two different loops must be present in the circuit model - one for the applied force F_1 with a particle velocity v_1, and the other in which the force F_2 is applied, with the corresponding particle velocity v_2. Note the dependence with the term $v_1 - v_2$ in both equations, which can be represented as an element contained in both loops. Therefore, the circuit model is found in Figure 2.3. The model obtained may be related with the classic distributed T-impedance equivalent network for a transmission line, which can be found in [107]. It is therefore possible to consider the non-piezoelectric slab as an acoustic transmission line if the applied force F is related to the electrical voltage V and the particle velocity to the intensity current I.

Meanwhile, we can also validate the analogy between the electrical and mechanical plane by analyzing the transverse electromagnetic (TEM) waves. The wave impedance of a TEM wave can be obtained as the ratio between transverse electric and magnetic fields. In the mechanical plane, we have defined the acoustic impedance of the medium as the ratio between the stress T and the particle velocity v_p with the minus sign. However, after some transformations, the acoustic impedance can be also defined as [28],

$$Z = j \frac{c\omega \vec{u}}{\vec{v} v_p} \tag{2.16}$$

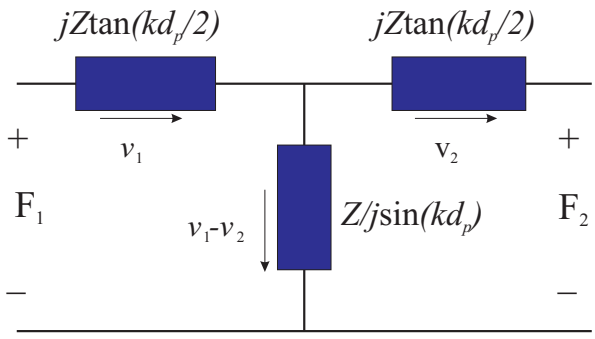

Figure 2.3: T impedance equivalent circuit for an acoustical non-piezoelectric transmission line.

which in this case is expressed as a function of the ratio between the particle displacement and the particle velocity, which are orthogonal to each other.

Taking into account the considerations above, the analogies between the electric and mechanical plane are summarized in Table 2.1 as analogies between the one-dimensional acoustic equations and the traditional Maxwell equations. It must to be pointed out that further developments related with the piezoelectric effects are based on the analogies discussed.

2.3 Solution of the One-dimensional Mechanical Wave in a Piezoelectric Slab

The distributed model for an acoustic non-piezoelectric transmission line was obtained in the previous section. The model obtained can be related with the distributed T-impedance transmission line equivalent network, which allows some analogies between the electric and mechanical plane to be affirmed. In this section, we are therefore going to analyze the piezoelectric slab in order to obtain an equivalent circuit, as in the previous section.

2.3.1 The piezoelectric effect

In order to analyze the propagation of the acoustic wave through a piezoelectric slab, we first briefly review the concept of piezoelectricity. The developments due to the effect of the piezoelectricity on the mechanical and electrical properties are extensively discussed in [28].

Piezoelectricity involves the coupling between the electric and mechanical properties of a crystal. The relation between both planes is given by means of the polarization vector. This is proportional to the electric field in the form,

$$\vec{P} = \epsilon_0 \mathbf{k} \vec{E} \tag{2.17}$$

where ϵ_0 is the permittivity of free space and $\mathbf{k}$ is the electric susceptibility matrix. Meanwhile, the displacement vector $\vec{D}$ can be related with the polarization vector as,

$$\vec{D} = \varepsilon_0 \vec{E} + \vec{P} = \varepsilon_0 \vec{E} + \varepsilon_0 \mathbf{k} \vec{E} \tag{2.18}$$

The displacement vector can also be described in sum notation as,

$$D_i = \varepsilon_{ij} E_j \quad i = 1...3 \ , \quad j = 1...3 \tag{2.19}$$

where

$$\varepsilon_{ij} = \varepsilon_0 (1 + k_{ij}) \tag{2.20}$$

If the medium is isotropic, the $\boldsymbol{\varepsilon}$ matrix reduces to a scalar. In this case, $\varepsilon_{ij} = \varepsilon_r \varepsilon_0$ where ε_r is the relative dielectric constant. In the free space $\varepsilon_r = 1$ and $\mathbf{k} = 0$. Unlike a non-piezoelectric material, in a piezoelectric medium, the polarization vector is created not only by the effect of an external electric field, but also by a stress or strain since a crystal deformation also causes charge separation. Continuing with the double subscript notation, the equation that relates the polarization vector with the stress and piezoelectric strain matrix can be also expressed as,

$$P_i = d_{ij} T_J \quad i = 1...3 \ , \quad J = 1...6 \tag{2.21}$$

where the subscript J denotes two different dimensions in the space, as will be discussed in the next chapter.

As discussed above, the fact that a stress or strain produces an electrical response involves the inverse piezoelectric effect, and thus, the electrical variables (E, D and P) and mechanical variables (T and S) are also involved. The inverse piezoelectric effect can be defined by means of the ratio between the strain and the electric field,

$$S_J = d'_{iJ} E_i \tag{2.22}$$

where d'_{ij} is the transposal of the piezoelectric strain matrix. After some transformations that have been meticulously developed in [28], the direct and inverse piezoelectric effect can be expressed by means of the piezoelectric stress matrix $\mathbf{e}$ leading to the well-known constitutive equations in matrix notation,

$$\begin{aligned} \mathbf{T} &= -\mathbf{e} : \mathbf{E} + \mathbf{c}^{\mathbf{E}} : \mathbf{S} \\ \mathbf{D} &= \boldsymbol{\epsilon}^{\boldsymbol{S}} : \mathbf{E} + \mathbf{e} : \mathbf{S} \end{aligned} \tag{2.23}$$

The superscript E denotes that the mechanical properties have been measured under a constant electric field in order to prevent charge buildup, while the superscript S denotes that the electrical properties have been measured under a constant strain. The " : " operator corresponds to the matrix product.

A more in-depth study of the effect of piezoelectricity on crystals is found in [28], where the electromagnetic wave equation is modified by the presence of a mechanical perturbation term using the Christoffel equation. In this case, for our purposes, we can summarize this effect in a correction term applied to the stiffness constant, and specifically in the term c_{33}, which is related to the stiffness constant in the thickness direction. Taking into account this consideration, c_{33} must be modified as follows,

$$c'_{33} = c_{33} + \frac{e_{33}^2}{\varepsilon_{r_{33}}} \tag{2.24}$$

where c'_{33} is called stiffened stiffness constant. This correction is very important since the mechanical parameters related with the stiffness constant will be also modified. The phase velocity in (2.8) must be redefined as,

$$v'_a = \sqrt{\frac{c'^E_{33}}{\rho}} = \sqrt{\frac{c^E_{33} + \frac{e_{33}^2}{\varepsilon_{r_{33}}}}{\rho}} \tag{2.25}$$

When the term $[e]$ is avoided, i.e. when the piezoelectric effect is not taken into account, the equations above remains in their classical form for a non-piezoelectric medium.

2.3.2 Propagation of the acoustic wave through the piezoelectric slab: The Mason model

The analysis of the propagation of the acoustic wave through the piezoelectric slab will follow the same development as the one seen in section 2.2. However, in the piezoelectric slab, the correction terms due to the piezoelectric effect must be applied to the mechanical parameters. Hooke's law must be therefore rewritten as,

$$T = c^E \frac{\partial u}{\partial z} - eE \tag{2.26}$$

where the piezoelectric contribution is given by the second term of the equation.

Figure 2.4 shows the scenario in which the propagation of the acoustical wave through the piezoelectric slab will be analyzed. Here, a piezoelectric slab is excited by means of an electric field in the thickness direction. For a thickness excitation, the displacement vector $\vec{D}$ remains constant in the thickness direction because in the piezoelectric medium there is no free charge density ρ_e, leading to,

$$\nabla \cdot \vec{D} = \rho_e = 0 \tag{2.27}$$

If the piezoelectric slab was laterally excited, the electric field $\vec{E}$ would remain constant instead of $\vec{D}$ [28], but this is a different situation which will not be discussed in this work.

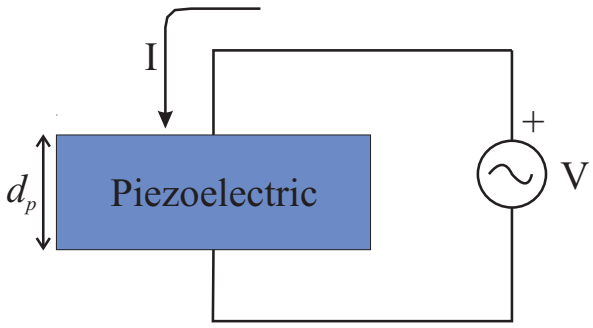

Figure 2.4: Thickness excitation of a piezoelectric slab.

The goal of the analysis is to obtain the current-voltage I-V characteristic. Since the piezoelectric slab is a dielectric material, it may initially be considered that the current through a piezoelectric medium is purely a displacement current which corresponds to an electron flow due to the presence of an external electric field $\vec{E}$. However, as discussed below, this is not exactly true. This displacement current is expressed as,

$$J = \frac{\partial D}{\partial t} = j\omega D \Rightarrow I = j\omega DA \tag{2.28}$$

where J is the displacement current density. In order to obtain the voltage, the electric field must be integrated along the piezoelectric slab, as is also suggested for the case of TEM waves in [107]. The electric field in the one-dimensional case can be defined as,

$$E = \frac{D}{\epsilon^S} - \frac{e}{\epsilon^S}\frac{\partial u}{\partial z} \tag{2.29}$$

where the first term is the external electric field and the second term in the equation is the internal electric field generated by the acoustic wave. The voltage can therefore be expressed as the integral of the electric field between the limits of the piezoelectric slab z_1 and z_2,

$$V = \int_{z_1}^{z_2} E d_p z = \frac{D d_p}{\varepsilon^S} - \frac{e}{\varepsilon^S}\left(u\left(z_1\right) - u\left(z_2\right)\right) \tag{2.30}$$

Substituting the term D of (2.28) and using that the particle velocity is the derivative of the mechanical displacement with respect time, the voltage can be expressed as,

$$V = \frac{d_p}{\varepsilon^S}\frac{I}{j\omega A} + \frac{h}{j\omega}\left(v_1 - v_2\right), \quad h = \frac{e}{\varepsilon^S} \tag{2.31}$$

Finally, from the previous development, we can obtain that,

$$I = j\omega C_0 V + hC_0\left(v_1 - v_2\right), \quad C_0 = \frac{\varepsilon^S A}{d_p} \tag{2.32}$$

where C_0 is the static capacitance given between the electrodes of the piezoelectric slab. The current through the piezoelectric slab is given by the contribution of two different terms. The

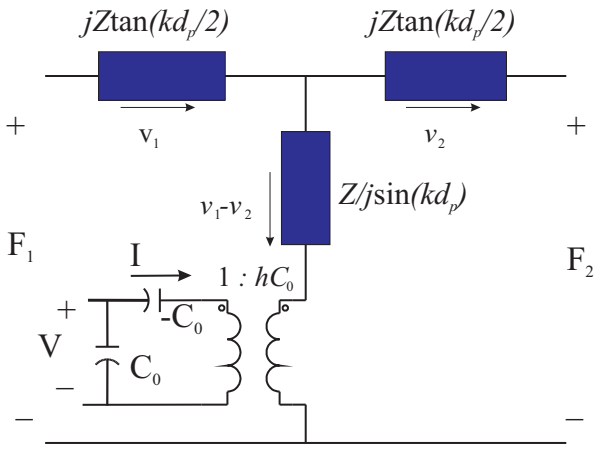

Figure 2.5: Equivalent Mason model for a piezoelectric slab.

first is due to the displacement current through a capacitance; and the second term is due to the conversion between mechanical and electrical energy, i.e. due to the piezoelectric effect. This is the reason why the current in a piezoelectric medium is not exactly a pure displacement current. The set of equations for the non-piezoelectric slab in (2.15) can therefore be modified by adding the current term due to the piezoelectric effect which results in,

$$\begin{aligned} F_1 &= \frac{Z}{j\sin\left(kd_p\right)}\left(v_1 - v_2\right) + jZ\tan\left(\frac{kd_p}{2}\right)v_1 + \frac{h}{j\omega}I \\ F_2 &= \frac{Z}{j\sin\left(kd_p\right)}\left(v_1 - v_2\right) - jZ\tan\left(\frac{kd_p}{2}\right)v_2 + \frac{h}{j\omega}I \end{aligned} \tag{2.33}$$

Figure 2.5 shows the Mason model, an equivalent electrical circuit. The model consists of two mechanical ports where a certain mechanical forces F_1 and F_2 are applied, and one electrical port, defined by V and I. The transformer is modelling the mechanical to electrical energy conversion and viceversa. The turn ratio of the transformer can be easily derived by applying the voltage Kirchoff's voltage law in both loops of the transformer resulting in a ratio of hC_0. Another interesting point is the negative capacitor. Due to the definition of V and I, we can state that I is directed away from the node to the transformer, then, the voltage drop in the capacitor must be negative. The capacitor behaves as a capacitor, where its reactance varies inversely with the frequency, however, the magnitude of its reactance is positive, as an inductance.

2.4 Analysis of the Electrical Input Impedance for a Piezoelectric Slab

The one-dimensional Mason model has been obtained from the analysis of the propagation of the acoustic wave through a piezoelectric slab in the thickness direction. The electrical input

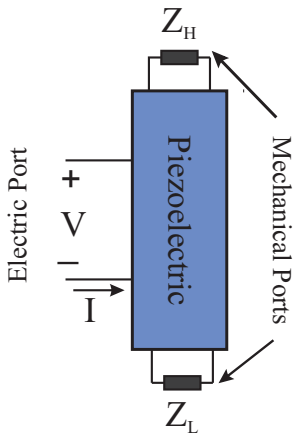

Figure 2.6: Piezoelectric Slab loaded with arbitrary load impedances in the mechanical ports.

impedance for a piezoelectric slab with arbitrary load impedances in the mechanical ports is therefore going to be obtained at this point.

Taking into account the situation shown in Figure 2.6, the equations in (2.33) become,

$$\begin{aligned} -Z_H v_1 &= Z_p \left(\frac{v_1}{j\tan(kd_p)} - \frac{v_2}{j\sin(kd_p)} \right) + \frac{h}{j\omega} I \\ -Z_L v_2 &= Z_p \left(\frac{v_1}{j\sin(kd_p)} - \frac{v_2}{j\tan(kd_p)} \right) + \frac{h}{j\omega} I \end{aligned} \tag{2.34}$$

where Z_p is the piezoelectric acoustic impedance, Z_H is the top mechanical impedance and Z_L is the bottom mechanical impedance. By developing the previous set of equations mathematically, the V/I characteristic is found,

$$\begin{aligned} \frac{v_1}{I} &= \left(\frac{h}{\omega}\right) \left(\frac{Z_p(\cos(kd_p)-1)+jZ_L\sin(kd_p)}{(Z_p^2+Z_H Z_L)\sin^2(kd_p)-j(Z_H+Z_L)Z_p\sin(kd_p)\cos(kd_p)} \right) \sin(kd_p) \\ \frac{v_2}{I} &= \left(\frac{h}{\omega}\right) \left(\frac{-Z_p(\cos(kd_p)-1)-jZ_L\sin(kd_p)}{(Z_p^2+Z_H Z_L)\sin^2(kd_p)-j(Z_H+Z_L)Z_p\sin(kd_p)\cos(kd_p)} \right) \sin(kd_p) \end{aligned} \tag{2.35}$$

and taking into account that the electrical impedance can be written as,

$$Z = \frac{V}{I} = \frac{h}{j\omega}\left(\frac{v_1}{I} - \frac{v_2}{I}\right) + \frac{1}{j\omega C_0} \tag{2.36}$$

we can finally obtain the expression of the electrical impedance for the piezoelectric slab with arbitrary loads in the mechanical ports after applying some mathematical transformations,

$$Z = \frac{1}{j\omega C_0}\left(1 - \frac{k_t^2}{kd_p}\frac{\tan(\phi)}{\phi}\frac{\left(\frac{Z_H+Z_L}{Z_p}\right)\cos^2(\phi) + j\sin(2\phi)}{\left(\frac{Z_H+Z_L}{Z_p}\right)\cos(2\phi) + j\left(1+\frac{Z_H Z_L}{Z_p^2}\right)\sin(2\phi)}\right) \tag{2.37}$$

being $\phi = kd_p/2$, and k_t the electromechanical coupling constant which is defined with the piezoelectric material properties as,

$$k_t^2 = \frac{e^2}{Z_p \epsilon_0 \epsilon_r v_p} \tag{2.38}$$

The expression obtained for the input electrical impedance in (2.37) is worthy of particular mention due to its importance in further discussions. This expression relates the electrical behavior of a piezoelectric slab for any impedance load connected in the mechanical ports. As in the electromagnetic plane, we can therefore consider a situation in which several layers are mechanically coupled to the piezoelectric slab, and we can then translate the mechanical impedance of these layers to obtain the resulting Z_H or Z_L mechanical equivalent impedance and then, to carry out the corresponding electrical analysis.

2.4.1 Electrical input impedance for a piezoelectric slab without mechanical loads

The first situation that can be analyzed is the simplest one, in which there is no mechanical loads, i.e. there is air on the upper and lower surfaces of the piezoelectric slab. The force that the air exerts on the piezoelectric slab is null, and we can therefore consider the mechanical loads Z_H and Z_L to behave as a shortcircuit since $F_1 = F_2 = 0$. In this case, the acoustic wave is confined to the piezoelectric cavity. Thus, the expression in (2.37) is reduced to a more simplified expression,

$$Z_{in} = \frac{1}{j\omega C_0}\left(1 - k_t^2 \frac{\tan\left(kd_p/2\right)}{kd_p/2}\right) \tag{2.39}$$

The magnitude and phase of the electrical input impedance as a function of the frequency for a given electromechanical coupling constant k_t^2 and piezoelectric thickness d_p can be found in Figure 2.7. As briefly discussed in the introduction section, two different resonances can be clearly distinguished: the resonance and mechanical or antiresonance frequency. The former occurs when the magnitude of the electrical input impedance tends to 0 Ω, while the latter occurs when the magnitude is maximum.

By analyzing the electrical input impedance for the case of the antiresonance frequency, the next relation between the thickness d_p and the propagation velocity v_p in the piezoelectric layer can be stated,

$$Z_{in} \to \infty \Rightarrow \tan\left(kd_p/2\right) = \infty \quad \Rightarrow \quad \frac{kd_p}{2} = \frac{\pi}{2} \quad \Rightarrow \quad f_a = \frac{v_p}{2d_p} \tag{2.40}$$

Thus, at the antiresonance frequency the piezoelectric thickness is equal to half of the acoustic wavelength in the case of infinitesimal metal electrodes. For the case of the resonance frequency the electrical input impedance can be also analyzed providing the relation between the electromechanical coupling constant which is directly related to the frequency separation between resonant frequencies,

$$Z_{in} \to 0 \Rightarrow k_t^2 \frac{\tan\left(kd_p/2\right)}{kd_p/2} = 1 \quad \Rightarrow \quad k_t^2 = \frac{\pi}{2}\frac{f_r}{f_a}\cot\left(\frac{\pi}{2}\frac{f_r}{f_a}\right) \tag{2.41}$$

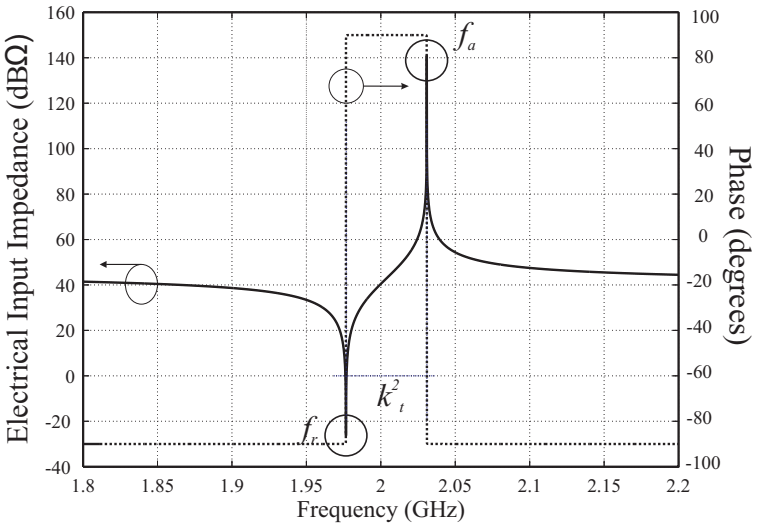

Figure 2.7: Electrical Input Impedance of a BAW resonator.

This can be approximated using the Taylor series to,

$$k_t^2 = \frac{\pi^2}{4}\left(\frac{f_a - f_r}{f_a}\right)\left(\frac{f_r}{f_a}\right) \tag{2.42}$$

The phase is also found in Figure 2.7. It can be seen that between resonant frequencies, the piezoelectric slab behaves as an inductance with phase of 90°, while out of these frequencies, the behavior is purely capacitive with a phase of -90° given by the static plate capacitance C_0.

Next, the piezoelectric slab will be considered to be loaded with a certain mechanical loads. These mechanical loads are usually a metal electrodes in the upper and bottom surfaces of the piezoelectric layers, but different layers conforming the Bragg reflector under the bottom electrode can also be present as in the SMR configuration. Loading the piezoelectric slab with metal electrodes entails a certain effects on the mechanical and electrical plane which are called mass loading effects. The importance of these effects warrants a specific section discussing them.

2.4.2 Electrical input impedance of a piezoelectric slab with arbitrary mechanical loads: The mass loading effect

Among others, the mass loading effects are those ones associated with the deposition of metal electrodes in a piezoelectric slab. These effects can be related with the shifting of resonant frequencies, which are also known as inertial effects, with the concept of energy trapping, and with the stress in the structure [108, 109].

The previous section showed that, if no mechanical loads are present, the antiresonance frequency can be directly related with the thickness of the piezoelectric layer. However, in this case,

Table 2.2: Mechanical and electrical properties of non-piezoelectric materials.

Material	Young Modulus[GPa]	Poisson ratio	ρ[Kg/m^3]	V_p[m/s]	Z_a[Kg/m^2s]
Al	63.61	0.362	2695	6330	1.71e7
Mo	324.054	0.31	10200	6636	6.77e7
Pt	144.79	0.38	21500	3550	7.63e7
W	344.738	0.28	19300	4776	9.21e7
SiO_2	70	0.17	2200	5848	1.28e7

when metal electrodes are present, since the thickness of the structure is higher, the allocation of the resonant frequencies will be different. This also entails variations in the electromechanical coupling constant obtained from (2.42). As a result, when metal electrodes are present in the structure the intrinsic k_t it will be recalled as k_{eff}, the effective electromechanical coupling constant.

The most commonly used metal electrodes are Aluminum (Al), Molybdenum (Mo), Platinum (Pt) and Tungsten (W). The main mechanical properties of them and also other non-piezoelectric materials are summarized in Table 2.2. The propagation velocity and the acoustic impedance have been calculated using the Young modulus E, the Poisson ratio σ and the mass density ρ as,

$$\begin{aligned} v_p &= \sqrt{\frac{E\,(1-\sigma)}{\rho\,(1+\sigma)\,(1-2\sigma)}} \\ Z_a &= \rho v_p \end{aligned} \tag{2.43}$$

We can consider the metal electrodes as an acoustic transmission line of length t_e, which corresponds to the electrode thickness, and characteristic impedance the acoustic impedance for each one of them. In this case, as it was suggested above, we can obtain the values of Z_H and Z_L by moving the mechanical loads found at the input and output mechanical ports along the acoustic transmission line given by the electrodes, as occurs in the traditional microwave networks analysis.

Using the expression in (2.37), one of the most important results that can be extracted is the relation between the effective electromechanical coupling constant k^2_{eff} and the thickness ratio between the electrode and piezoelectric layer t_e/d_p. In order to carry out the appropiate analysis, Table 2.3 shows the main electrical and mechanical parameters for the piezoelectric materials used, Zinc Oxide (ZnO) and Aluminum Nitride (AlN).

If the antiresonance frequency f_a is maintained at a fixed value, the piezoelectric and electrode thickness can be swept, which leads to a certain resonance frequency f_r, and thus, a certain k^2_{eff}. Figure 2.8 shows the dependence of the effective electromechanical coupling constant on a certain ratio between the thickness of the electrode and piezoelectric layer. These results have

Table 2.3: Mechanical and electrical properties of piezoelectric materials.

Material	c_{33}[N/m^2]	ρ[Kg/m^3]	e_{33}[C/m^2]	ϵ_r	V_p[m/s]	Z_a[Kg/m^2s]
AlN	395	3260	1.5	10.5	11340	3.70e7
ZnO	211	5680	1.32	10.2	6370	3.61e7

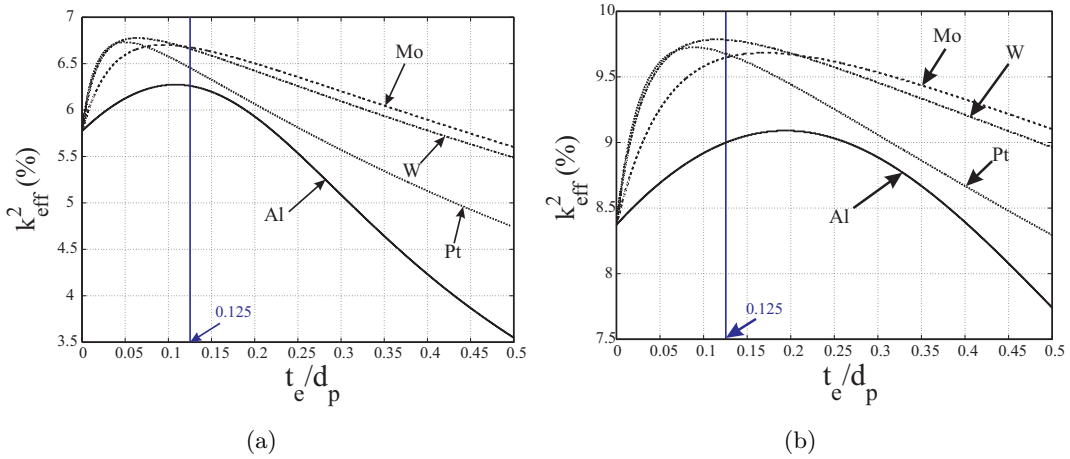

Figure 2.8: Effective electromechanical coupling constant as a function of the thickness ratio for: (a) Aluminum Nitride Piezoelectric material. (b) Zinc Oxide Piezoelectric material.

been calculated for the case of ZnO, and AlN, and the metal electrodes defined in each case.

First, it can be seen that for a single piezoelectric slab without metal electrodes, that is, $t_e = 0$, the observed value of the k^2_{eff}, corresponds to k^2_t as expected. As the ratio t_e/d_p becomes greater, the curve present a maximum in the value of k^2_{eff}. The conductor material with the highest acoustic impedance, in this case W, leads to the maximum achievable value for k^2_{eff}. As discussed below, since the bandwidth of the filters is usually related with the value of k^2_{eff}, a common design rule consists of choosing the ratio corresponding to the maximum achievable k^2_{eff}. Furthermore, a certain value of k^2_{eff} is given by two different t_e/d_p ratios. This is also useful from the point of view of the manufacturing process since, in the event of a limitation on the thickness, the layers can be redesigned to overcome this.

When discussing the behavior of the effective electromechanical coupling constant, and why the achieved value is higher with some metals, we can use the definition of k_t given by Berlincourt in [110]. In this work, the development is based on the definition of the internal energy for a piezoelectric body with volume V. This is also studied in [111].

$$k_t = \frac{U_m}{\sqrt{U_e U_d}} \tag{2.44}$$

where U_m is the called mutual energy, U_e is the elastic energy and U_d is the electric energy.

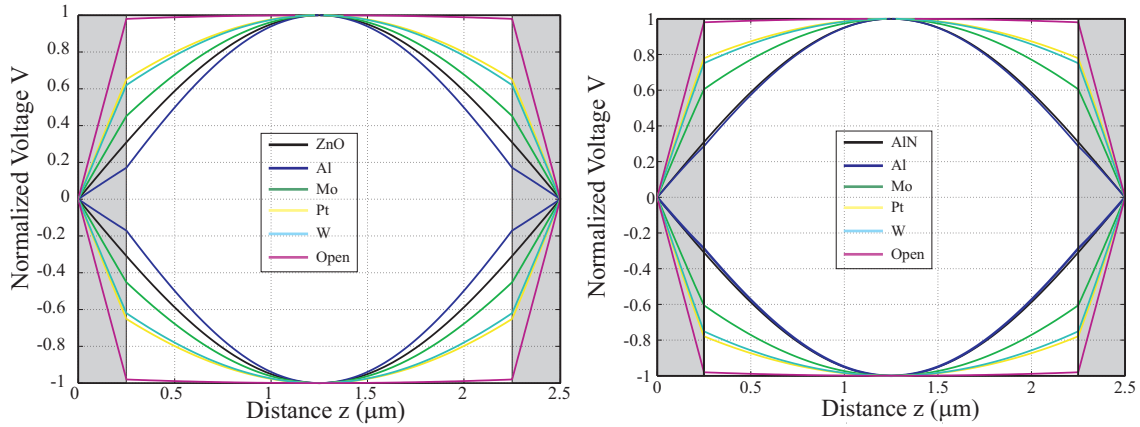

Figure 2.9: Distribution of the electrical voltage along the BAW resonator with metal electrodes of Al, Mo, Pt and W, and also special cases where the mass loading is done with a material with the same properties as the piezoelectric, and a fictitious material with an infinite acoustic impedance (Open). In this figures, d_p=2 μm and t_e=0.25 μm. (a) Zinc Oxide piezoelectric material. (b) Aluminum Nitride piezoelectric material.

These are defined as,

$$\begin{aligned} U_e &= \tfrac{1}{2}\int_V T_i S^E_{ij} T_j dV \\ U_m &= \tfrac{1}{2}\int_V T_i d_{ni} E_n + E_n d_{ni} T_i dV \\ U_d &= \tfrac{1}{2}\int_V E_m \epsilon^T_{mn} E_n dV \end{aligned} \tag{2.45}$$

where $m, n = 1, 2, 3$ and $i, j = 1, 2, 3, ..., 6$. The value of the electromechanical coupling constant will therefore be maximized when U_m is maximized. In a parallel plate capacitor the electric field can be assumed to be constant. Considering only the thickness dimension, the term d_{33} is also constant, and the mutual energy will therefore basically depend on the distribution of the component T_{33} of the stress. Using the analogies described between the electric and mechanical plane, and since the stress is proportional to the applied force, for a qualitative study, the stress distribution for a given electrode material can be obtained by means of the distribution of the voltage across the piezoelectric slab. For a piezoelectric slab with thickness $d_p = 2$ μm, and electrode thickness $t_e = 0.25$ μm, the distribution of the voltage along the structure is shown in Figure 2.9 using Al, Mo, Pt and W as the metal materials for ZnO in (a) and AlN in (b). "Fictitious" materials have been also used: these are materials with the same properties as the piezoelectric material, and a material with an acoustic impedance tending towards infinity, since they are cases of special interest.

When the properties of the electrode are the same as the piezoelectric material (v_p and Z_a), the first derivative of the distribution of the voltage through the structure is continuous. In this case, the standing wave can be written as $V(z) = A\cos(kz)$ as it is discussed in [21] and

Table 2.4: Obtained effective electromechanical coupling constant k^2_{eff} [%].

	ZnO/AlN	Al	Mo	Pt	W	Open-circuit
ZnO	9.30	9.03	9.74	9.62	9.82	10.52
AlN	6.45	6.23	6.64	6.47	6.63	7.01

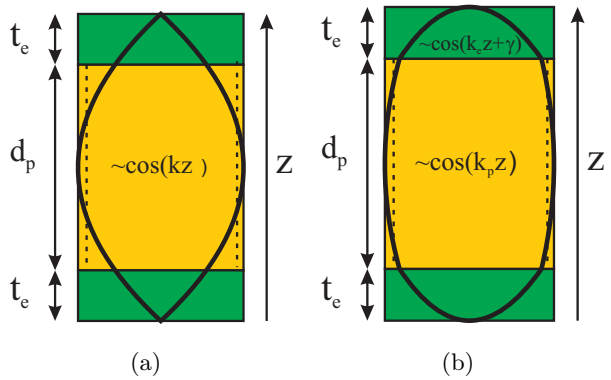

Figure 2.10: Stress field distribution for: (a) Equal acoustic impedance in the piezoelectric and electrodes (b) Different acoustic impedance in the piezoelectric and electrodes.

represented in Figure 2.10(a).

In the case of the used metal electrodes, it can be seen that the distribution of the voltage through the piezoelectric and electrode layer is different, which is of course, due to the different acoustic impedance and propagation velocity in each layer. This situation is represented schematically in Figure 2.10(b). For each metal electrode, the values obtained for k^2_{eff} are shown in Table 2.4. It can be seen that the highest values for k^2_{eff} occur when the distribution of the voltage becomes more parallel to the thickness direction. The obvious case is found for the open-circuit load. In this case, the distribution is almost flat in the whole piezoelectric layer parallel to the thickness direction. Taking into account that the electric field is constant as well as the piezoelectric strain constant d_{33}, we can conclude that the mutual energy U_m, and therefore k^2_{eff}, will be maximized in event of a flat distribution of the stress in the piezoelectric layer in the thickness direction. Note that for the specific case under study in which $t_e/d_p = 0.125$, the material with the highest acoustic impedance does not necessarily lead to the highest k^2_{eff}. This is shown in Figure 2.8, in which the blue line shows the specific ratio.

There is also a second effect arising from the presence of the metal electrode, which is the electrode's resistance. Let us take the Al as an example which is the conductor with the higher conductivity. In the frequency range of 2 GHz, the calculated skin depth is approximately 2 μm. Taking into account that the thickness to achieve the optimum value of k^2_{eff} is around 200 nm, a current flow may be present through the electrode thickness leading to power losses. There

is therefore a trade-off between thin metal electrodes which lead to resistive losses, and thick metal electrodes which lead to mechanical losses. This situation is represented in Figure 2.11 where the Q-value at the resonance frequency has been plotted against the thickness of the metal electrodes using Au, Al and Mo at the frequency of 10 GHz. For low values of t_e, the obtained Q-value is low due to the electric losses associated as it has been previously commented. As the value of t_e is increased the maximum Q-value is achieved when the electric and mechanical losses are equal. Beyond that point, mechanical losses are the dominant with the consequent degradation of Q.

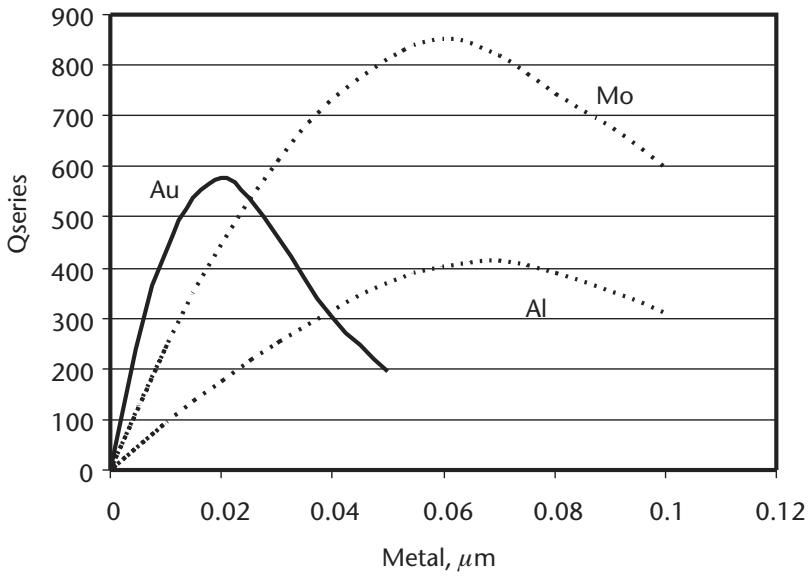

Figure 2.11: Dependence of the Q-value of the series resonance with the electrode thickness for Au, Al and Mo as a metal electrodes [67].

One solution in front of the decision in front of thin or thick metal electrodes is the use of composite electrodes. This consists of using a metal electrode composed of Al and W layer, taking advantage on the high acoustic impedance, and thus the high value of k^2_{eff}, of the W, and the high conductivity of the Al for a better conduction.

Finally, some considerations related with the analysis of the BAW resonator warrant discussion in order to obtain the position of the resonant frequencies, and thus the value of k^2_{eff}. For a symmetrical structure in the thickness direction, i.e. a piezoelectric slab with the same thickness and electrode material, the BAW resonator can be considered as the classical electromagnetic stepped impedance resonator (SIR) [112].The methodology applied to the analysis of these structures can therefore be also applied to the case of the BAW resonator, using the symmetry of the structure at the reference point $z = d_p/2$. The results obtained are completely equivalent to the results obtained from equation (2.37), and for this reason the complete analysis

of the BAW resonator with the commented technique has been included in Appendix A.

2.5 Other important one-dimensional models

As seen in the previous section, the Mason model was obtained from the analysis of the propagation of the mechanical wave in the thickness direction. The equivalent electrical circuit is considered an acoustic transmission line in a T-impedance configuration loaded with an arbitrary mechanical load Z_H and Z_L. However, two more one-dimensional models must be described in this section, due to their importance in the field of acoustic resonators: the KLM and the Butterworth-Van Dyke (BVD) model. The former is a modification of the Mason model which retains its distributed nature. The latter is based on the representation of the main fundamental mode as well as higher harmonics by means of lumped elements. The BVD model will be widely used in further developments.

2.5.1 The KLM model

The KLM model was developed by Krimholtz, Leedom and Matthaei in 1970 [113]. Like the Mason model, the KLM model present also a distributed nature in which the piezoelectric slab is modelled as an acoustic transmission line in its classical form, i.e. using two different conductors of length $d_p/2$ each, unlike the T-impedance network form, which is found in Figure 2.12. Likewise, as in the Mason model, the KLM model can be loaded with arbitrary mechanical loads which can be cascaded at the mechanical ports. The difference between the Mason and KLM models is given by the removal of certain lumped elements, between the top of the transformer and the acoustic transmission line, in the latter. The transformer is placed at the central point between the two transmission lines. In this case, the negative static capacitance $-C_0$ is removed, while the series branch in the electrical port now consists of the positive static C_0 in series with a reactance X_1 which is described as,

$$X_1 = Z_0 M^2 \sin\left(\frac{d_p \omega}{v_p}\right) \Rightarrow M = \frac{h_{33}}{\omega Z_0} \tag{2.46}$$

The turn ratio of the transformer Φ is defined as,

$$\Phi = \left(\frac{1}{2M}\right) \csc\left(\frac{d_p \omega}{2v_p}\right) \tag{2.47}$$

With this electrical equivalent circuit, the analysis of the input electrical impedance is very easy. We only need to displace the acoustic loads Z_L and Z_H through the transmission line with characteristic impedance Z_p. In this case, at the central point between both transmission line,

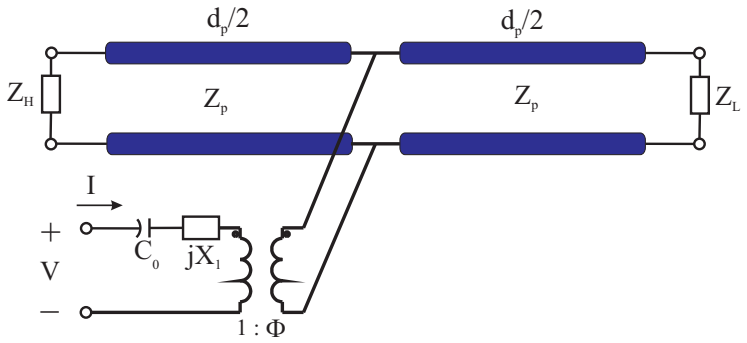

Figure 2.12: KLM equivalent electrical model

the equivalent acoustic impedance will be,

$$Z'_A = \frac{Z'_L Z'_H}{Z'_L + Z'_H} \tag{2.48}$$

where

$$Z'_{L,H} = \frac{Z_{L,H} + jZ_p \tan(\beta d_p/2)}{Z_p + jZ_{L,H} \tan(\beta d_p/2)} \tag{2.49}$$

The equivalent impedance Z'_A can be now translated to the electrical port taking the turn ratio into account. The input electrical impedance using the KLM model is therefore,

$$Z_{in} = \frac{V}{I} = \frac{1}{j\omega C_0} + jX_1 + \frac{Z'_A}{\Phi^2} \tag{2.50}$$

The comparison of the obtained results using the Mason and KLM mode has been studied widely in [114]. There, the agreement between both models for the thickness mode is total, regardless of the boundary conditions used.

2.5.2 The Butterworth-Van Dyke model

Unlike the Mason and KLM model described above, the BVD model is an equivalent electrical circuit made up of lumped components. This equivalent circuit has become as a very suitable equivalent circuit for the BAW resonator for the fundamental operating mode, but also, higher harmonics can be modelled by adding motional arms in shunt configuration with the static capacitance. The equivalent circuit is found in Figure 2.13, where C_0 corresponds to the static capacitance, R_p is the associated material losses resistance, R_m is the resistance associated with mechanical losses [15], and L_m and C_m are the motional inductance and capacitance. Also other $L_m - C_m$ in shunt configuration can be added to model higher harmonics or other present modes.

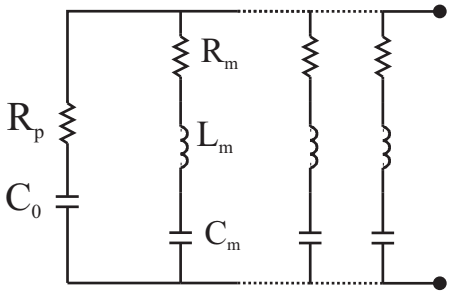

Figure 2.13: BVD equivalent electrical model

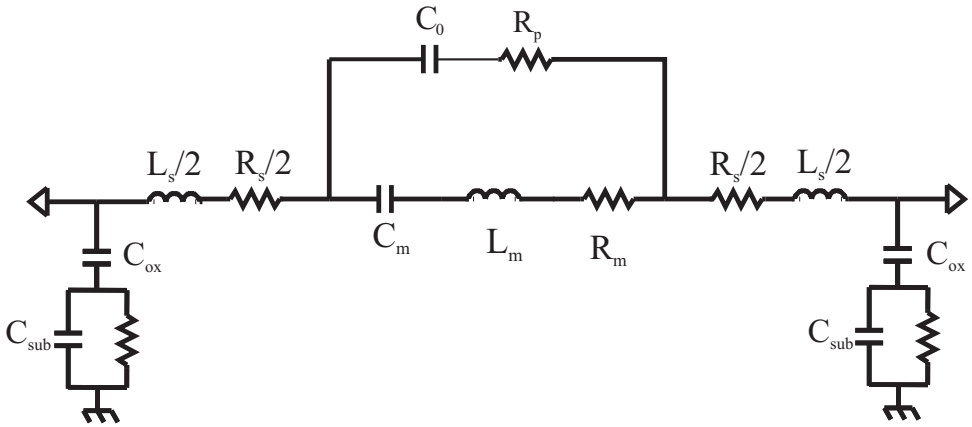

Figure 2.14: BVD equivalent electrical model

By one hand, the simplicity of the model, due to the fact that it only contains lumped elements makes it to be very suitable for obtaining electrical models for more sophisticated structures as will be shown in later chapters. This model is also very suitable for obtaining the electrical characterization of a BAW resonator from a given measurement. In [115], a modified BVD model is presented in order to extract the value of the various lumped components from the measurement of a BAW resonator. The modified BVD model is shown in Figure 2.14. In this case, in addition to the basic equivalent in Figure 2.13, the effects arising from the losses of the access line represented by a series resistance and inductance with respective values $R_s/2$ and $L_s/2$, the effects of the parasitic capacitance due to the oxide layer with value C_{ox}, which is usually present in the structure in order to isolate the resonator from the substrate, and the losses due to the substrate represented by the $R-C$ tank with values R_{sub} and C_{sub}, have been also taken into account. Taking into account the modified BVD model, Appendix B contains the automated parameter extraction algorithm used, as well as the results obtained with measured resonators.

2.6 Chapter Summary

In this chapter, the analysis and the solution to the wave equation of the mechanical wave in one dimension has been carried out, i.e. in the thickness direction, with lateral dimensions assumed to be infinite. In this case, before the piezoelectric effect is taken into account, a generic slab can be considered as an acoustic transmission line, since the electric equivalent circuit which describes the propagation of the mechanical wave is completely analogous to the T-impedance network transmission line on the electromagnetic plane. This analogy also means that the propagating mechanical wave can be considered analogous to the TEM wave on the electromagnetic plane. At the same time, the applied force F is assumed to be analogous to the electric voltage V and the phase velocity of the mechanical wave v_p to the current intensity I.

The piezoelectric effect has been described as a property of certain materials, in which a certain applied mechanical force results in a generated electric field in the structure and viceversa. When the piezoelectric effect is taken into account, analysis of the propagation of the mechanical wave through the piezoelectric slab provides the well-known one-dimensional Mason model. This is an equivalent electric circuit, which is composed of one electrical port and two mechanical ports. The Mason model describes the electric behaviour of the piezoelectric slab for any mechanical load condition. The conversion between electrical and mechanical energy is modelled by means of a transformer which links the mechanical and electric port.

The simplest situation is when the piezoelectric slab is considered to have infinitesimal metal electrodes and thus air as a mechanical load. In this case, the expression of the input impedance for a piezoelectric slab is considerably reduced. In the electrical input impedance for a BAW resonator, there are two clearly different resonances: the resonance, when the magnitude of the input electrical impedance tends to a shortcircuit behavior, and the antiresonance or also known as the mechanical resonance, in which the magnitude of the electric input impedance tends to its maximum value. The phase of the BAW resonator shows that between resonances the BAW behaves as a pure inductance. This is an inductive phenomenon with mechanical origin. Since in this case there are not associated losses due to the metal conductivity, as it occurs in the electric inductors, the obtained quality factor in a BAW resonator is very high. Out of the resonant frequencies, the BAW resonator behaves as a pure capacitance given by C_0.

When the metal electrodes are taken into account, a series of effects appear in the electrical behavior of the BAW resonator. These are called mass loading effects and are mainly related with the resonant frequencies shifting and the consequent variation in the effective electromechanical coupling constant. As has been seen, depending on the thickness of the metal electrode and its mechanical properties, a maximum value of k^2_{eff} can be achieved. It must also be taken into account that the conductor material with the highest acoustic impedance leads to have a maximum value for k^2_{eff}.

Finally, although the Mason model is the reference model for analysis of the BAW resonator, other one-dimensional models have also been described in this chapter due to their importance in further developments. First, there is the KLM which is a modification of the Mason model. This is also a distributed model, in which the transmission line appears in its classical form, i.e. by means of two different conductors, unlike the T-impedance network present in the Mason model. Using this model, some of the lumped components present in the Mason model can be removed, and particularly the negative static capacitance in the electric port of the transformer. Second, there is the Butterworth-Van Dyke model, which is an electric circuit conisiting lumped elements which is used to model the fundamental mode of a BAW resonator. The lumped nature of this model makes it very suitable for obtaining electrical equivalent circuits of more sophisticated structures, as will be discussed in subsequent chapters.

CHAPTER 3

Modelling Acoustic Resonators in Three-dimensions

In the previous chapter, the BAW resonator was studied using infinite lateral dimensions. Using the analysis of the propagation of the acoustic wave in the thickness direction, the one-dimensional Mason model and the KLM, and the Butterworth-Van Dyke equivalent circuit can thus be obtained. This is a very good approach to the electrical behavior of the BAW resonator for its fundamental mode operation and higher harmonics. However, the BAW resonator is composed of different layers, mainly metal electrodes and piezoelectric material, with a finite lateral dimensions. This means that not only the thickness can be excited in the BAW resonator, but so can the lateral modes.

Taking the considerations above into account, the one-dimensional wave equation will first be extended to the three-dimensional case. After this, since also lateral waves can propagate along the structure, the origin and the resonance conditions of these modes for certain boundary conditions will be analyzed. This leads to the introduction of the very important concepts of energy trapping and acoustic dispersion, which are linked to the coupling between thickness and lateral wave modes.

When characterizing the electrical behavior of the BAW resonator when lateral effects are also considered, the need for a 3D simulator becomes evident. With this in mind, the finite element method will be discussed, as well as the simulation strategy. The effect of lateral standing waves on the electrical behavior of the BAW resonator will also be extensively discussed, from both the electrical and the mechanical point of view. The discussions and results will be carefully compared with various works related to these topics.

3.1 Three-dimensional study of the piezoelectric slab

3.1.1 3D equation of the mechanical wave

The development of the one-dimensional equation of the mechanical wave was briefly discussed in the previous chapter, with the lateral dimensions assumed to be infinite. However, BAW resonators are finite structures, in which the finite lateral dimensions must also be taken into account when analyzing the propagation of the mechanical wave in a BAW resonator. With this in mind, a brief review of the 3D mechanical parameters must first be included, in order to extrapolate the one-dimensional equation of motion to the 3D case. This development has been widely studied, and it can be found in [28] and [46].

The 3D form of the strain **S** can be expanded from its one-dimensional form and can be written as,

$$S = \begin{bmatrix} S_{xx} & S_{xy} & S_{xz} \\ S_{yx} & S_{yy} & S_{yz} \\ S_{zx} & S_{zy} & S_{zz} \end{bmatrix} \tag{3.1}$$

where ,

$$S_{ij} = \frac{1}{2}\left(\frac{\partial u_i}{\partial r_j} + \frac{\partial u_j}{\partial r_i}\right) \tag{3.2}$$

being i and j the directions x, y and z. At this point we can assume that the strain tensor is reciprocal due to the atomic structure of the piezoelectric materials ($6mm$ hexagonal class), leading to the matrix **S** to be symmetric.

From Hooke's law, we can ascertain the ratio between the strain and stress by means of the stiffness coefficient, as mentioned in the previous section. As a result, it is reasonable to extend the 3x3 matrix form in the strain definition to the stress definition. Taking this into account, the 3D form of the stress tensor can be defined by means of a symmetric 3x3 matrix,

$$T = \begin{bmatrix} T_{xx} & T_{xy} & T_{xz} \\ T_{yx} & T_{yy} & T_{yz} \\ T_{zx} & T_{zy} & T_{zz} \end{bmatrix} \tag{3.3}$$

Using the 3D form of the Hooke's law, it can be seen that the existence of a stress in some direction will cause a certain strain not only in the same direction but also in the perpendicular directions. Furthermore, depending on the material properties, the coupling between the stress and strain in different directions may be different. If the material is isotropic, the stress and strain will couple in the same way in the three directions. The developed form of the 3D Hooke's

Table 3.1: 3D indices nomenclature.

I,J	i,j
1	xx (11)
2	yy (22)
3	zz (33)
4	yz (23), zy (32)
5	zx (31), xz (13)
6	xy (12), yx (21)

law developed for an isotropic material can be written as,

$$\begin{aligned} T_{xx} &= c_{xxxx}S_{xx} + c_{xxyy}S_{yy} + c_{xxzz}S_{zz} \\ T_{yy} &= c_{yyxx}S_{xx} + c_{yyyy}S_{yy} + c_{yyzz}S_{zz} \\ T_{zz} &= c_{zzxx}S_{xx} + c_{zzyy}S_{yy} + c_{zzzz}S_{zz} \\ T_{xy} &= c_{xyxy}S_{xy} \\ T_{xz} &= c_{xzxz}S_{xz} \\ T_{yz} &= c_{yzyz}S_{yz} \end{aligned} \tag{3.4}$$

If we deal with anisotropic materials, a given stress can couple to the six possible shear strains. Due to the complexity involved in writing the Hooke's law for an anisotropic materials, a reduced form can be used,

$$T_{ij} = \sum_{k=1}^{3}\sum_{k=1}^{3} c_{ijkl}S_{kl} \tag{3.5}$$

where i, j, k and l represents the various directions x, y and z. However, this nomenclature is still tedious and that is why the next compact notation can be used: $c_{ijkl} \rightarrow c_{IJ}$, $I = 1...6$, $J = 1...6$. This notation is clarified in Table 3.1.

Once the nomenclature has been clarified, the 3D Hooke's law in its expanded form is finally written as,

$$\begin{bmatrix} T_1 \\ T_2 \\ T_3 \\ T_4 \\ T_5 \\ T_6 \end{bmatrix} = \left[\begin{array}{ccc|ccc} c_{11} & c_{12} & c_{13} & c_{14} & c_{15} & c_{16} \\ c_{21} & c_{22} & c_{23} & c_{24} & c_{25} & c_{26} \\ c_{31} & c_{32} & c_{33} & c_{34} & c_{35} & c_{36} \\ \hline c_{41} & c_{42} & c_{43} & c_{44} & c_{45} & c_{46} \\ c_{51} & c_{52} & c_{53} & c_{54} & c_{55} & c_{56} \\ c_{61} & c_{62} & c_{63} & c_{64} & c_{65} & c_{66} \end{array}\right] \begin{bmatrix} S_1 \\ S_2 \\ S_3 \\ S_4 \\ S_5 \\ S_6 \end{bmatrix} \tag{3.6}$$

The **c** matrix in (3.6) has been blocked in four different regions. The upper left region represents the coupling between the longitudinal stresses and strains. Here, the diagonal terms couple both parameters in the same direction, while the off-diagonal terms couple the stresses and strains in orthogonal directions. These terms are given by Poisson's ratio σ, which is a dimensionless constant of the material that gives the ratio between orthogonal components of

the stress and the strain. The upper left region will be always filled regardless of the type of material.

The lower right region represents the coupling between shear stresses and shear strains. The diagonal terms are always present in this matrix. However, depending on the material properties, the off-diagonal terms may or may not be present. Finally, the lower left and upper right region of the matrix represents the coupling between shear stresses and longitudinal strains and longitudinal stresses and shear strains. These terms may or may not be present depending on the material properties.

The materials used in this work belong to the class $6mm$ hexagonal systems, where the only terms that are present in the stiffness matrix are those belonging to the upper left region and the diagonal of the lower right region. The stiffness matrix for this material class takes the following form,

$$\begin{bmatrix} c_{11} & c_{12} & c_{13} & 0 & 0 & 0 \\ c_{12} & c_{11} & c_{13} & 0 & 0 & 0 \\ c_{13} & c_{13} & c_{33} & 0 & 0 & 0 \\ 0 & 0 & 0 & c_{44} & 0 & 0 \\ 0 & 0 & 0 & 0 & c_{44} & 0 \\ 0 & 0 & 0 & 0 & 0 & c_{66} \end{bmatrix}, \quad c_{66} = \frac{c_{11} - c_{12}}{2} \tag{3.7}$$

where it can be seen that there are five independent terms. Also note the symmetry properties of this matrix where $c_{12} = c_{21}$, $c_{13} = c_{31}$ and $c_{22} = c_{11}$. Taking into account the 3D definition of the mechanical parameters related with the wave equation, the mechanical equation expanded to the 3D case can thus be derived from the Newton's and Hooke's law as,

$$\frac{\partial T_{ij}}{\partial x_j} = \rho \frac{\partial^2 u_i}{\partial t^2} \tag{3.8}$$

$$T_{ij} = c_{ijkl} S_{kl} \tag{3.9}$$

Finally, related with the piezoelectric effect, the piezoelectric stress matrix $\mathbf{e}$, in its 3D form, for a 6mm hexagonal class piezoelectric material is expressed as,

$$\begin{bmatrix} 0 & 0 & 0 & 0 & e_{15} & 0 \\ 0 & 0 & 0 & e_{15} & 0 & 0 \\ e_{31} & e_{31} & e_{33} & 0 & 0 & 0 \end{bmatrix} \tag{3.10}$$

3.2 Propagation of Mechanical Waves in the Lateral Dimension

As it was briefly discussed in the introduction to this chapter, the structure of the BAW resonator is finite in its thickness direction but also in its lateral dimensions. Mechanical waves propagating in the lateral directions of the structure may thus also be present in the electrical behavior of the BAW resonator. Taking into account that several mechanical waves may be propagating in the

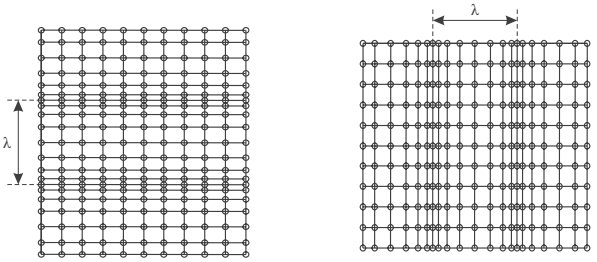

(a) Longitudinal waves

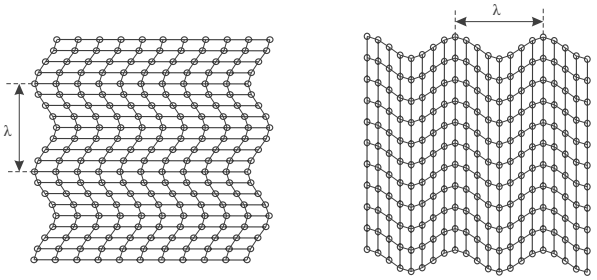

(b) Transversal waves

Figure 3.1: Particle displacement and propagation direction for longitudinal and transversal waves [67]. Vertical definition of the wavelength denotes waves propagating in the thickness direction while horizontal definition of the wavelength denotes waves propagating in the lateral direction.

structure, it is worth of clarifying the nomenclature used for them. In the one-dimensional case, the wave propagates in the thickness direction and the particle displacement was also assumed to be in the same direction. These kind of waves are represented in Figure 3.1(a) on the left side, and we use to refer to them as thickness modes. They are sometimes also called longitudinal. However this may lead to confusion since waves propagating in the lateral dimension with the particle displacement also in the lateral dimension are also longitudinal as seen on the right side in Figure 3.1(a). On the other hand, we use the term shear waves to refer to the kind of waves in which the propagation direction and the particle displacement direction are orthogonal. This case is represented on the left side in Figure 3.1(b). The literature also includes the term thickness shear (TS), which is related with waves propagating in the lateral direction with the particle displacement in the thickness direction as seen on the right side in Figure 3.1(b). These kind of waves will be widely discussed along this chapter since the origin of the main lateral spurious resonances are associated to them. They are also referred to as Lamb waves [46] since they are lateral waves propagating in a finite plate with a finite thickness dimension.

In order to analyze the origin and the resonance conditions for lateral standing waves, we are going to use the scenario found in Figure 3.2, which shows the cross section of the BAW resonator. It clearly distinguishes between two different regions: the electroded region, i.e. the

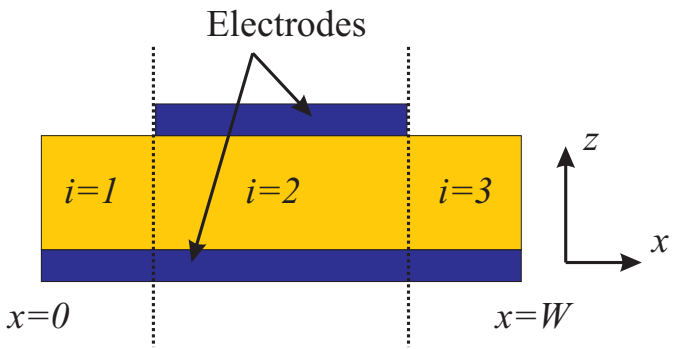

Figure 3.2: Definition of the different region in an acoustic resonator.

area consisting of the piezoelectric material between metal electrodes at $i = 2$, and the non-electrode region, which is the surrounding area at $i = 1$ and $i = 3$. The resonance condition will be obtained by analyzing the mechanical displacement in the structure, taking the boundary conditions into account.

3.2.1 Resonance condition for Lamb waves

For isotropic materials, the independent elastic stiffness constants are represented by c_{11} and c_{44}. On the other hand, in this kind of materials, the Lame's constants, λ and μ, are used as the quantities equivalent to two elastic stiffness constants. The relation between stiffness and the Lame's constants is given by $c_{11} = \lambda + 2\mu$ and $c_{44} = \mu$ [46]. Using the Helmholtz's theorem, also known as a Fundamental theorem of vector calculus, which states that every vector field can be considered to be generated by a scalar function ϕ and a vector function $\vec{A}$, the displacement vector $\vec{u}$ can be decomposed in,

$$\vec{u} = \nabla\phi + \nabla \times \vec{A} \tag{3.11}$$

where

$$-\omega^2\rho\phi = (\lambda + 2\mu)\,\nabla^2\phi \tag{3.12}$$

$$-\omega^2\rho\vec{A} = \mu\nabla^2\vec{A} \tag{3.13}$$

Taking the above equations into account, it can be stated that the scalar function ϕ is related with the longitudinal wave and the vector function $\vec{A}$ is related with the shear waves. The solutions for ϕ and $\vec{A}$ are $\phi = A_L e^{j\vec{k}\cdot\vec{r}}$ and $\vec{A} = \vec{A_S} e^{j\vec{k}\cdot\vec{r}}$ where A_L and A_S are amplitude constants, $\vec{r}$ is the position vector and $\vec{k}$ is the wave vector. The solution to the equation for the displacement vector in (3.11) therefore consists of the sum of a displacement component related with the longitudinal wave and a displacement component related with the shear wave. For the sake of simplifying the development, the structure is considered to be infinite in the $y-$direction.

Considering, then, the wave propagating in the lateral $x-$ and the longitudinal $z-$ direction, the wave vector is defined as $\vec{k} = k_x\vec{u_x} + k_z\vec{u_z}$. The displacement on the surface of the plate $z = 0$ becomes,

$$\vec{u}(z=0) = \nabla A_L e^{jk_x x} + \nabla \times \vec{A_S} e^{jk_x x} = \vec{C} e^{jk_x x} \tag{3.14}$$

where $\vec{C}$ is the constant amplitude vector. The form of the previous equation shows that the wave behaves like a travelling harmonic wave on the surface of the plate.

The vibration on a plate can be described by the interaction of two harmonic waves travelling in opposite directions. In this case, the displacement of a Lamb wave is given by a scalar function $\Psi(x)$ as,

$$\Psi(x) = Ae^{-jkx} + Be^{jkx} \tag{3.15}$$

However, in the piezoelectric resonator, at least, there are two different regions (electroded and non-electroded), making the values of A, B and the wave number k to be different in each region i. Therefore, the previous equation may be rewritten as,

$$\Psi_i(x_i) = A_i e^{-jk_i x_i} + B_i e^{jk_i x_i} \tag{3.16}$$

The mechanical boundary conditions in a semi-infinite crystal are extensively described in [33], section 5.1.2. Here, the stress on the surfaces of the crystal is said to be zero, and thus this situation can be expressed as,

$$j\omega \frac{\partial u_z}{\partial z} = 0 \tag{3.17}$$

At the same time, due to the continuity condition between regions, the mechanical displacement must be continuous and the stress must be equal on both sides of the interface resulting in the next equalities,

$$\begin{aligned} &\Psi_i\left(x_i = W_i\right) = \Psi_{i+1}\left(x_{i+1} = 0\right) \\ &\left.\frac{d\Psi_i}{dx}\right|_{x_i=W_i} = \left.\frac{d\Psi_{i+1}}{dx}\right|_{x_{i+1}=0} \end{aligned} \tag{3.18}$$

Taking into account the boundary conditions that must be fulfilled, the relation between the progressive and regressive wave amplitude at region $i = 2$ becomes [62],

$$\frac{A_2}{B_2} s = e^{jk_2 W_2} \tag{3.19}$$

where $s = 1$ for the symmetric solutions of the displacement, and $s = -1$ for the antisymmetric solutions. Figure 3.3 shows both types of wave solution, while Figure 3.4 shows the particle displacement for the first symmetric and antisymmetric modes. By inserting the ratio between

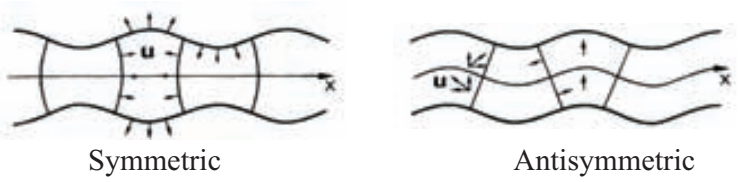

Figure 3.3: Symmetric and Antisymmetric Lamb waves [33].

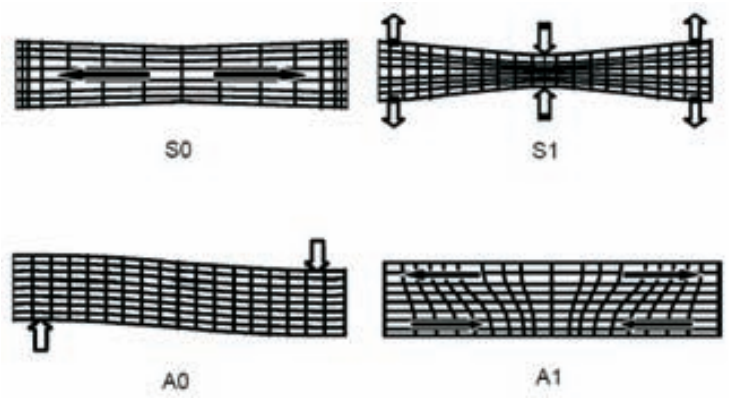

Figure 3.4: Particle displacement for the first four Lamb modes. S refers to symmetric modes and A to asymmetric modes .

A_2 and B_2 in the set of equations related with the continuity of the mechanical displacement, and equaling the real and imaginary parts, the resonance condition can finally be obtained,

$$\sin\left(k_2 W_2\right) = s\frac{2K_1/k_2}{1+\left(K_1/k_2\right)^2} \tag{3.20}$$

where $K_1 = jk_1$.
The piezoelectrically generated voltage can be calculated as the integral of the mechanical displacement over the electroded region W_e as,

$$V = h\int_0^{W_e} \Psi\, dx \tag{3.21}$$

where h is a proportionality constant. In this case, we can therefore express the piezoelectrically generated voltage as a function of the obtained values A_2 and B_2 as,

$$V = \frac{h}{jk_2}(s+1)(A_2 - B_2) = \frac{-hjk_1\Psi_0}{k_2^2}(s+1) \tag{3.22}$$

where it can be seen that the antisymmetric solutions ($s = -1$) cannot be piezoelectrically generated, unlike the symmetric solutions.

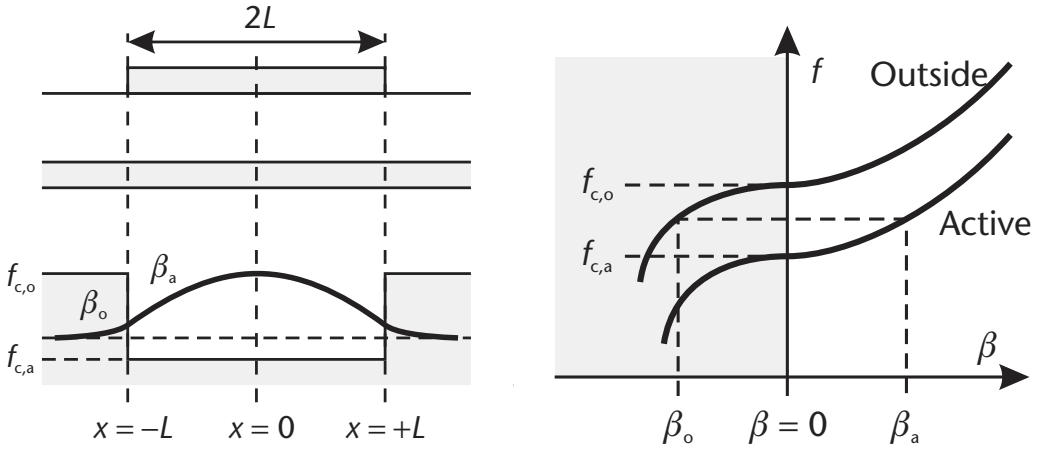

Figure 3.5: (a) Cut-off frequency diagram for a BAW resonator with dispersion type I. (b) Dispersion curves for the thickness extensional TE1 mode in the active and outside regions. [67]

3.2.2 Acoustic dispersion

Before talking about the acoustic dispersion, it is required to introduce the energy trapping concept. This concept enables the lateral effects in a BAW resonator to be studied in more depth. The concept was introduced by Shockley in [48], who says that: If the portion of the surrounding region in a BAW resonator ($x < -L$ and $x > L$ in Figure 3.5(a)), in our case $i = 1, 3$, presents a higher cut-off frequency than the exciting frequency, the resulting vibratory energy is essentially confined to the active region ($-L < x < L$), in our case $i = 2$, with an energy distribution decreasing exponentially with the distance away from the resonator. In other words, the oscillating energy is trapped within a confined region.

The lateral propagation constant β can be pure real, pure imaginary or complex leading to a sinusoidal propagating wave, to an exponentially decreasing wave or to an attenuating sinusoidal propagating wave respectively. The BAW resonator can be also understood as an acoustic waveguide with a certain cut-off frequency, where the lateral wave number β can be related with the cut-off frequencies as,

$$\beta = \sqrt{\alpha(\omega_i^2 - \omega_c^2)} \tag{3.23}$$

However, it can be seen that β also depends on the parameter α. This is a dispersion type parameter which is $\alpha > 0$ for materials with dispersion type I, and $\alpha < 0$ for materials with dispersion type II [62].

Let us first consider a dispersion type I BAW resonator. The cut-off frequenciy diagram is shown in Figure 3.5(a). For a certain frequency between the cut-off frequency of the active region

denoted as $f_{c,a}$, and the outside cut-off frequency $f_{c,o}$, the lateral propagation constant is real in the active region ($\beta \in \Re$), leading to a propagating sinusoidal wave; and purely imaginary in the outside region ($\beta \in \Im$), and thus an exponentially attenuating propagating wave. Figure 3.5(b) shows the dispersion relation curves for the fundamental thickness mode in the active and outside region, where the situation discussed here is clarified. The gray shading denotes purely imaginary β values. The dispersion curves give a response to the kind of waves characterized by the lateral propagation constant β can be supported by the BAW resonator at a given frequency. The dispersion curves are usually obtained by means of matrix methods, some of which are reviewed by Lowe in [51].

Also very useful is the analysis in [28], in which as previously assumed, the BAW resonator is an acoustic waveguide. Here, after some mathematical transformations, the eigenfrequencies which are the solution of the wave equations, with reflecting walls at the top, bottom, and lateral boundaries, are expressed as,

$$f_{NM} = \frac{v_a N}{2d_p}\left[1 + \left(\frac{1}{2}\frac{Md_p}{WN}\right)^2\right] \tag{3.24}$$

where v_a is the acoustic velocity for the lateral wave, W is the width of the top electrode, with $M, N = 1, 3, 5, ...$ In other words, for a given mode N, there are a series of harmonic modes given by $M = 1, 3, 5, ...$ which represent the spurious resonances that are generally present in the electrical behavior of the BAW resonator. It must to be pointed out that this result is valid for longitudinal lateral propagating waves. If we are interested, the lateral standing waves come from the interaction between thickness and shear modes. That is why more sophisticated matrix methods are required to predict the position of the lateral spurious modes.

With respect to dispersion type II resonators, the situation is the inverse of that discussed above. In this case $\alpha < 0$, and frequencies above the cut-off frequency of the active region will thus present a pure imaginary propagation constant leading to an exponentially attenuating wave, while frequencies below the cut-off frequency of the active area will present a real propagation constant leading to sinusoidal propagating waves. As will be discussed in subsequent chapters, the spurious modes in the dispersion type I resonators are present above the resonance frequency of the BAW resonator, while for dispersion type II they are present below this frequency.

The presence of lateral spurious resonances in the electrical behavior of the BAW resonator is due to shear modes which, under the proper boundary conditions, are coupled to the thickness mode. The nature of the dispersion type in a BAW resonator is given by the relation between the resonance frequency of the thickness and shear modes. Figure 3.6 shows the dispersion curves including both the thickness and shear branches. It must to be pointed out that the thickness shear TS1 mode occurs at very low frequencies, making the effects at the fundamental resonant frequencies of the BAW resonator almost negligible, and this is therefore not shown in the Figure. However, the TS2 mode is closer to the fundamental thickness mode frequency. In dispersion type

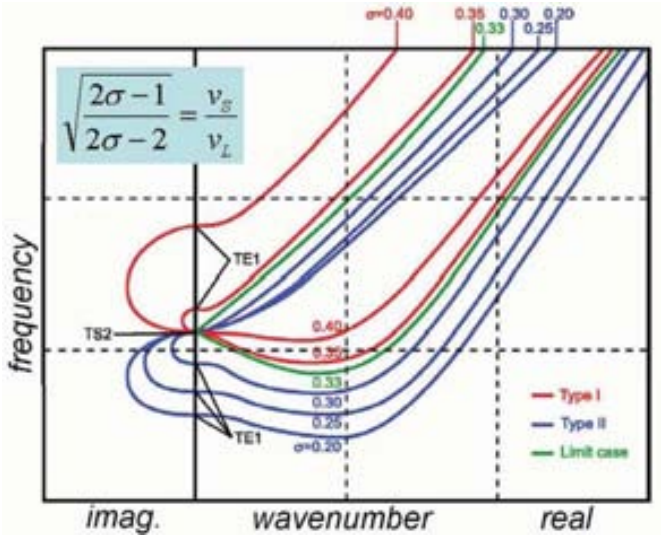

Figure 3.6: Dispersion curves showing the thickness and shear branches for different materials with a specific Poisson ratio σ [63].

I resonators, the TS2 resonance frequency of this mode is below the TE1 resonance frequency. For dispersion type II resonators the situation is the opposite, as the resonance frequency of the TS2 mode is above the TE1 resonance frequency. That is, using the dispersion relations, we can predict the frequencies at which the fundamental TE mode couples with the different harmonics of the TS2. It can also be seen that the Poisson ratio is obtained by means of the relation between longitudinal and shear acoustic velocities.

The origin and the resonance condition for lateral standing waves have been considered in this chapter. It has also been seen that predicting the position of spurious resonances in the electrical behavior of the BAW resonator is not an easy task, since it requires sophisticated matrix methods. The need for a 3D analysis tool in order to characterize the electrical behavior of the BAW resonator is therefore obvious. To this end, the Finite Element Method (FEM) will be used to simulate the BAW resonator from the electrical and mechanical point of view.

3.3 Finite Element Method

The BAW resonator performance has been widely described by means of the Mason and the KLM one-dimensional models. As discussed in chapter 3, the Mason model arises from the propagation of the acoustic wave in the thickness dimension, and lateral dimensions are therefore considered infinite. However, BAW resonators present a finite lateral dimension, which must be considered in the study of their electrical behaviour, due to the presence of lateral standing waves as seen in the previous section. A 3D simulator must be used for this purpose and,

of course, it must be capable of analyzing coupled-fields (Electro-mechanical fields). The 3D simulators use various techniques: Momentum, Finite Difference Time Domain (FDTD) and the Finite Element Method. The software chosen for this work was ANSYS Release 11.0, which uses the FEM method, since a solution for the coupled-fields analysis is also provided. The Finite Element Method was originally introduced by Turner in 1956 [116], in order to provide approximate solutions to a wide variety of engineering problems with complex domains subjected to general boundary conditions. The basis of FEM relies on the decomposition of the domain, which is a continuum with a known boundary, into a finite number of subdomains, which will be called elements, for which the systematic approximate solution is constructed by applying the variational or weighted residual methods. The ability to discretize the irregular domains with finite elements makes the method suitable for this study.

Taking into account the basis of the FEM method, the BAW resonator will be discretized in a finite number of elements to carry out the coupled-fields analysis. Each element of the discretized structure is connected to each other by their common nodes. A node specifies the coordinate's location in space containing certain degrees of freedom. This situation is shown in Figure 3.7.

Depending on the geometry of the problem, the domain can be discretized in line, area or volume elements, where each of those elements, identified with an element number, is identified by a given number of nodes. Due to the nature of the structure of the BAW resonator, volume elements are the most suitable for the discretization process. The type of element to use must be chosen taking into account the degrees of freedom available in the nodes contained in the element, and the reaction solution.

The nature of the structure under study requires two different types of element for its full characterization: a structural element for the non-piezoelectric layers (metal electrodes, coupling layers, Bragg reflector layers), and a coupled-field element for the piezoelectric layers, in order to solve the constitutive equations governing the piezoelectric effect. For the former, the element type is the "SOLID95", while for the latter it is the "SOLID226". Both elements are 20-node

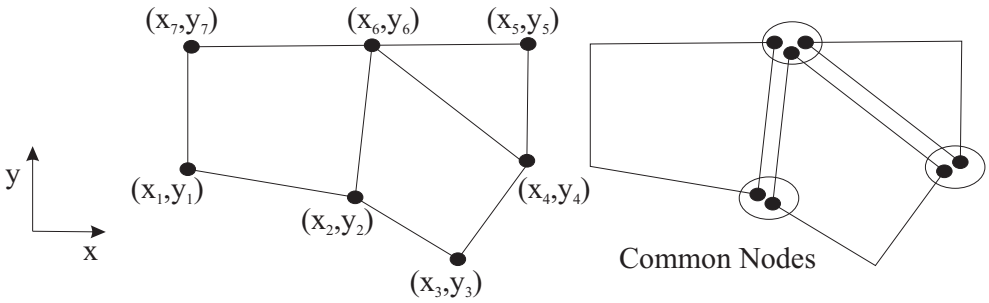

Figure 3.7: Division of the domain into elements.

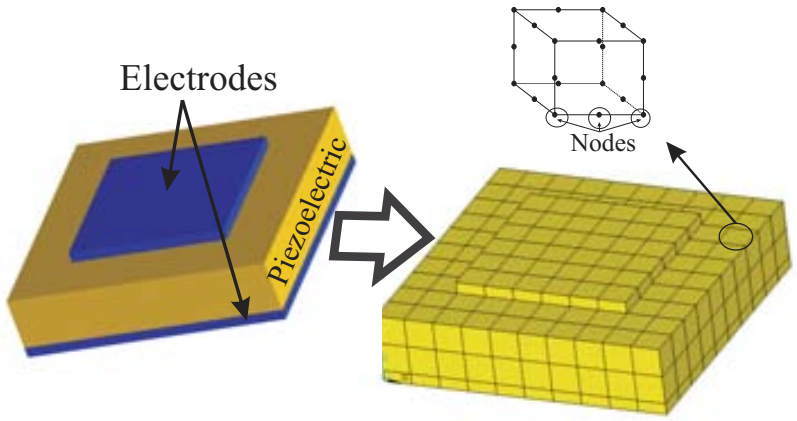

Figure 3.8: Basic BAW resonator discretized in elements.

Table 3.2: Element type definition.

	Degrees of Freedom	Reaction Solution
SOLID95	u_x, u_y, u_z	Force
SOLID226	u_x, u_y, u_z, V	Force, Electric Charge Q_e

hexahedral brick elements. Figure 3.8 shows the discretized BAW resonators in these elements. The degrees of freedom and reaction solutions for each element type are listed in Table 3.2. The element type referred to in the non-piezoelectric layer contains the mechanical displacements u_x, u_y, u_z as degrees of freedom, and the force as a reaction solution. For the piezoelectric element, the degrees of freedom are u_x, u_y, u_z, the electrical voltage V, and the reaction solutions are the mechanical force and electric charge Q_e with negative sign, since this is a reactive solution.

3.3.1 Simulation strategy

This section provides the basis for carrying out a 3D simulation of a BAW resonator using the FEM method. The various steps used in the simulation can be summarized as:

1. **Define the geometry of the structure**. First of all, the different variables related with the physical geometry of the structure are defined.

2. **Define the elements in which the structure must be discretized**. In this case, as mentioned above, the elements used are SOLID226 for the piezoelectric layer and SOLID95 for the non-piezoelectric layers. Note that different options must be set for the SOLID226 element, since not both electro-mechanical analysis and different coupled field analysis is possible.In our case we must therefore specify the type of degrees of freedom that the element must contain in order to carry out the desired analysis.

3. **Define the material parameters**. At this point, once the element type has been defined for each layer of the structure, the material parameters must be defined. The piezoelectric material is defined with the density ρ, the electric relative permittivity matrix $[\epsilon_r]$, the piezoelectric coupling matrix $[e]$, the stiffness matrix $[c]$ and, if required, the losses of the material in the form of the damping ratio ξ, which is directly related with the quality factor of the materials. The non-piezoelectric layers are usually defined with the density of the material ρ, the Young modulus matrix $[E]$, the Poisson's ratio σ and the shear module matrix $[G]$. As is the case with the piezoelectric material, losses in the form of a damping ratio can also be set.

4. **Create the structure using volumes**. In this step, using the definition of the structure in step 1, the structure must be created using volumes with the corresponding size. Once the structure has been created, a boolean operation called $VGLUE$ must be applied to the structure. The result of "gluing" the full structure is a structure where each area which is in contact with another one belonging to a different volume shares the same boundaries and nodes, i.e. this operation provides mechanical and electrical continuity between different volumes.

5. **Assign element type and material to the different volumes of the structure**. In order to mesh the structure, the type of elements and materials must be linked to the different volumes composing the structure.

6. **Mesh the structure** At this point, the size of the elements must be set in order to mesh the structure. There are various ways to mesh the structure. The kind of elements that can be used to mesh the structure are: tetrahedral, hexahedral or a mixed mesh, using the previous shape. The suitability of each mesh element depends on the nature of the structure. In our case, since the geometry is formed with square blocks, the most suitable type is the hexahedral mesh, since the final meshed structure presents a perfect symmetry in each direction, thereby reducing numerical errors. As discussed below, this is a critical point since depending on the mesh size, the results may not converge to the desired solution.

7. **Set the boundary conditions**. Due to the finite character of the structure, certain boundary conditions must also be applied to it. In the case under study, the boundary conditions are of two different types: electrical and mechanical boundary conditions. The electrical boundary conditions are related with the definition of the electric voltage in the structure. As can be seen in Figure 3.9, the interface between the piezoelectric layer and the top electrode has been set at a certain value of V, usually $V = 1$ V, and the interface between the piezoelectric layer and the bottom electrode has been grounded, i.e. $V = 0$ V. Note that the electric voltage is applied to the piezoelectric layer since the elements which

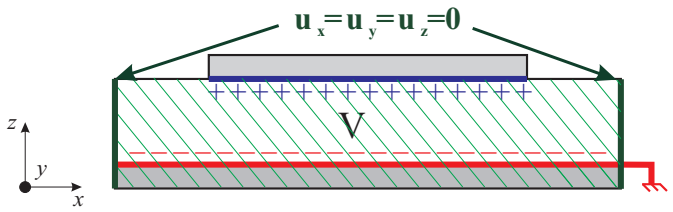

Figure 3.9: Definition of the electrical and mechanical boundary conditions in the BAW structure.

conform this layer contain it as a degree of freedom. As regards the mechanical boundaries, the BAW structure will be assumed to be clamped, i.,e. the mechanical displacement at the edges of the structure will be null, i.e. $u_x = u_y = u_z = 0$. What is usually done in this kind of analysis is all the nodes are coupled with some degree of freedom -in this case with the same electric potential- to a single node, in order to obtain the final result easily.

8. **Simulate the structure**. ANSYS provides various types of simulation: Static, Modal, Harmonic, Transient, Spectrum, Eigen Bucking and Substructuring. When simulating BAW resonators, two of them are of great interest: the static and the harmonic. With the former, the value of the static capacitance C_0 can be computed and compared against the theoretical value. The latter allows us to obtain the frequency response of the BAW resonator.

   In order to carry out the harmonic analysis, different methods can be used: Full, Reduced and Mode Superposition method. In this work, different harmonic analysis have been carried out by means of the Full method. This is the easiest of the three methods. It uses the full system matrices to calculate the harmonic response, i.e. there is no matrix reduction. The advantages of this method can be summarized as:

   - There no need to choose master degrees of freedom or mode shapes, as occurs with the Reduced Method.

   - It uses full matrices, and there is therefore no mass approximation involved in the analysis.

   - This kind of method allows symmetric and unsymmetrical matrices, which are typical of acoustic applications.

   - It accepts all the available load types.

   - It allows effective use of solid-model loads.

   The disadvantage compared to other methods is that this kind of analysis is more time-consuming.

   Once the computation method, the frequency range and the number of steps have been set, the harmonic analysis can be carried out.

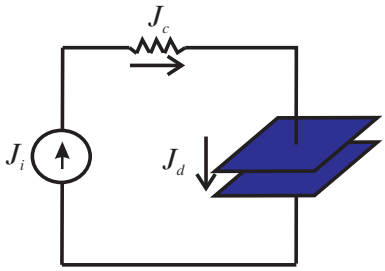

Figure 3.10: Electric current density in a dielectric slab.

9. **Post-process the results**. The results available using the piezoelectric analysis are the mechanical force and the electric charge Q_e with a negative sign (because it is a reaction solution). However, the aim is to obtain the electrical input impedance in order to study the electrical behaviour of the BAW resonator. In order to compute the electrical input impedance, we can first consider the BAW resonator as a dielectric slab as done in [117].

   Figure 3.10 shows a current source connected to a resistor and a parallel-plate capacitor, which is equivalent to a piezoelectric slab. The electric current density can be understood as the sum of the conduction current density J_c through the resistor, and the displacement current density J_d through the dielectric material. In addition to Maxwell's equation, the called "continuity equation" refers to the current density J_{ic}, where $J_{ic} = J_i + J_c$, with the charge density q_{ev}. It relates the net flow of current out of the small volume to the rate of decrease of the charge, and takes the form,

$$\nabla \cdot J_{ic} = -\frac{\partial q_{ev}}{\partial t}, \quad \nabla \cdot J_{ic} + j\omega q_{ev} = 0 \tag{3.25}$$

   By integrating both terms in a certain volume we can write,

$$\iiint_V \nabla \cdot \mathrm{J_{ic}} dv + \iiint_V j\omega q_{ev} dv = 0 \tag{3.26}$$

   Taking into account that the integral of the charge density in a certain volume results in the total electric charge, and the divergence theorem,

$$\oiint_S \vec{A} d\vec{s} = \iiint_V \vec{A} dv \tag{3.27}$$

   the continuity equation can be rewritten as,

$$\oiint_S J_{ic} dS = -j\omega Q_e, \quad I = -j\omega Q_e \tag{3.28}$$

   The minus sign in the second term of the equation indicates the opposite direction between the electric charge and the current intensity. As we have set the voltage in the top surface of the piezoelectric slab, the electrical impedance can be obtained by means of the Ohm's law.

For the purposes of this work, we are interested in the electrical characterization of the BAW resonator. That is why the post-process step has been focused on this area. However, the 3D simulator used enables us to go beyond observation of the electrical behavior. The mechanical phenomena governing the BAW resonator can also be studied, and in most cases, this can be very useful for full understanding of the various effects observed. As discussed in subsequent sections, we are going to use both the electric and mechanical behavior to describe the origin of unwanted modes and thus the degradation of the expected performance of the BAW resonator.

The source code for carrying out the simulation of a conventional BAW resonator can be found in Appendix C.

3.4 3D Simulation of Acoustic Resonators

In this section, we are going to carry out the 3D simulation of the BAW resonator, once the basis for carrying out this simulation has been stated. First, we need to state the required conditions in the 3D simulator in order to obtain an accurate solution. To do this, we expect the 3D simulation of the BAW resonator to converge with the obtained results by means of one-dimensional models of the resonant frequencies position, and therefore the value of the effective electromechanical coupling constant, but also the static capacitance C_0. In the first step, we are therefore going to simulate a piezoelectric slab, neglecting the effect of the electrodes, and setting the lateral dimension as much larger than the thickness dimension, i.e. similar to the one-dimensional scenario. Afterwards, the BAW resonator will be simulated with the presence of the metal electrodes.

3.4.1 3D simulation of a piezoelectric slab with infinitesimal electrodes

Figure 3.11 shows the piezoelectric slab which is going to be analyzed in this section, where as has been discussed, the metal electrodes are considered to be infinitesimal. The corresponding dimensions of the piezoelectric slab are shown in Table 3.3, where the piezoelectric material is ZnO. Note that the lateral dimensions are much bigger than the thickness dimension, making the BAW resonator behave like a one-dimensional structure. As mentioned above, although the lateral dimensions of the piezoelectric slab are finite, the convergence with the Mason model for the fundamental longitudinal mode and successive harmonics must be accomplished, as well as the value of C_0. To do so, the mesh density must be fine enough for an accurate result to be obtained.

In order to obtain the response of the fundamental mode, somehow, the size of the used elements in the discretization of the structure must be small enough to converge to the expected result. Therefore, we can directly relate the wavelength of the fundamental mode with the mesh

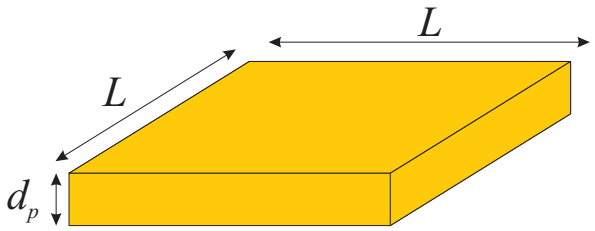

Figure 3.11: Definition of the piezoelectric slab.

Table 3.3: Dimensions of the piezoelectric slab in Figure 3.11.

Material	Thickness dimension d_p	Lateral dimension L
Zinc Oxide	1.52 μm	130 μm

size. When the electrodes are infinitesimal the wavelength of the fundamental longitudinal mode is related with the piezoelectric thickness as $d_p = \lambda/2$. In [61], the number of elements used in the thickness dimension is 2, the same as $\lambda/4$ in terms of the acoustic wavelength. Some other techniques, such as the method of moments are a good approach for using an element size for meshing of $\lambda/10$.

The lateral dimensions must also be taken into account in order to set the mesh size. Relating the mesh size with the lateral dimension entails a very large number of elements in the thickness dimensions. In our case, the ratio between lateral and thickness dimension is around 85:1. Using 10 elements in the thickness direction entails an element size of $L_m = 0.152$ μm. We can easily calculate the number of equations that the simulator tool should solve: the number of elements present in the surface with area L^2 is $n = L^2/L_m^2 = 731.475$ elements. This means that the number of elements in the whole structure is $n = 7.31 \cdot 10^6$. Finally, each of the elements contains 20 nodes, where the corresponding constitutive equations are solved. It is clear that this would lead to a very expensive cost-time simulation.

The proposed solution for overcoming this problem consists of meshing the structure independently in the lateral, X- and Y-dimension, and the thickness Z-dimension. To do so, there is a very simple method that consists of forming the piezoelectric layer by using as many layers as there are number of elements in the Z-dimension. If the desired number of elements is $N = 10$, then the piezoelectric layer will be composed of a stack of 10 independent piezoelectric layers of thickness $d_p' = d_p/N$. In this case, since the BAW resonator is physically truncated in the thickness dimension, a single element will be considered on each layer, although the size of the element is bigger than the thickness of each single piezoelectric layer. The mesh size can be thus directly related with the lateral dimensions, regardless of the number of layers in the thickness.

The first step is to establish the required number of thickness elements in order to achieve

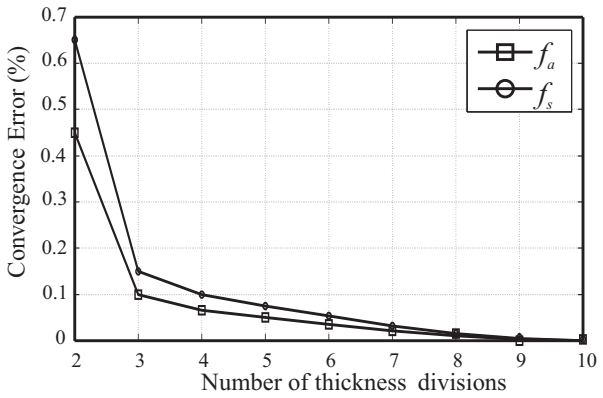

Figure 3.12: Convergence for the resonance and antiresonance frequency with the Mason model.

convergence in terms of the Mason model response. To do so, different simulations have been carried out for different numbers of divisions in the thickness dimension. The result is shown in Figure 3.12, where it can be seen that the convergence is achieved for a number of thickness divisions starting at $N = 10$ which is $\lambda/20$. It must be pointed out that these simulations were carried out for the fundamental thickness mode. For higher harmonics, the wavelength decreases. This means that the number of elements must be increased in order to converge with the expected result.

Figure 3.13 shows the resulting electrical input impedance obtained by means of the 3D simulator and compared with the Mason prediction for the fundamental mode 3.13(a), and the first harmonic allocated at $3f_a$ in 3.13(b). The 3D simulation has been carried out using $N = 10$ divisions in the thickness dimensions, and using a size element of $L_m = 5$ μm, which leads to 25 elements in the lateral dimension. It can be seen that the agreement between both responses for each case is very good in terms of resonant frequencies, and also in terms of the static capacitance out of the resonant frequencies C_0.

As mentioned above, both the electrical and the mechanical behavior of the BAW resonator can be obtained. For our purposes, we are interested in the distribution of the mechanical displacement in the thickness direction in order to see how the BAW resonator is vibrating and deformed. The distribution of the mechanical displacement in the thickness direction is shown in Figure 3.14 for the resonance and antiresonance frequencies. It is apparent that the distribution is uniform in the center of the structure, but this is not fully extended to the whole surface. This is due to the fact that we have imposed that the BAW resonator is clamped at the edges, that is, $u_x = u_y = u_z = 0$, otherwise, the distribution would be extended to the full surface of the BAW resonator. It can also be seen that in the case of the antiresonance frequency, the displacement is maximum, while in the case of the resonance frequency it is minimum. As discussed in Appendix A, due to the symmetry of the BAW resonator, a vertical symmetry

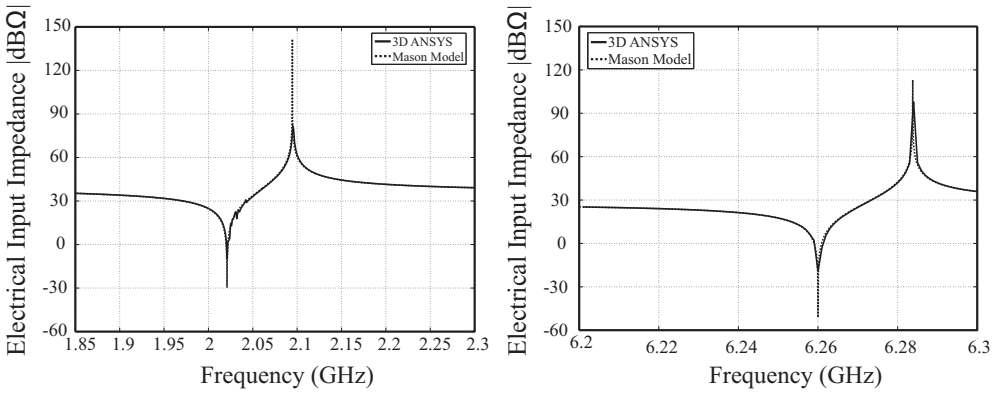

Figure 3.13: Electrical input impedance comparison between the Mason model and the 3D simulation for: (a) Fundamental mode and (b) the first harmonic mode.

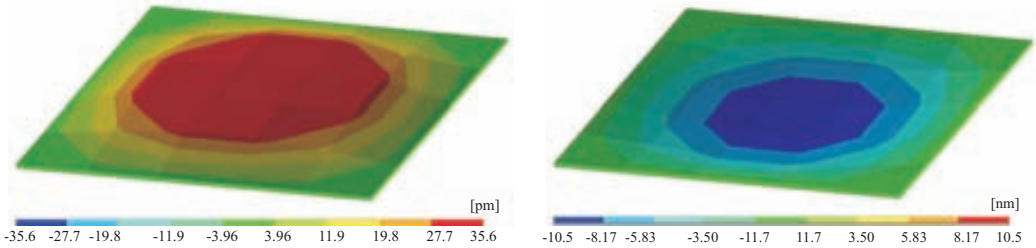

Figure 3.14: Mechanical Z-displacement distribution : (a) Antiresonance frequency and (b) resonance frequency.

arises at $d_p/2$. At this point, in the case of the antiresonance frequency, the excitation mode is even, which means that at this point the equivalent impedance corresponds to an open-circuit. In the case of the resonance frequency, the excitation mode is odd, which means that at $d_p/2$ the equivalent impedance corresponds to a shortcircuit. That is why, the mechanical behavior of the BAW resonator at the two frequencies is the opposite.

In Figure 3.15, the magnitude of the mechanical displacement in the longitudinal direction is also shown for the fundamental mode in 3.15(a), and the first harmonic in 3.15(b). In the former, it can be seen that the wavelength of the mechanical wave along the piezoelectric layer is $\lambda/2$ as predicted, while for the latter, the wavelength corresponds with $3\lambda/2$. In other words, the BAW resonator present a periodic behavior with the odd multiples of the fundamental frequency. We can state that the BAW resonator is deformed in a compression/expander way, as can also be seen in Figure 3.4 for the S1 mode, i.e. the fundamental symmetric thickness mode.

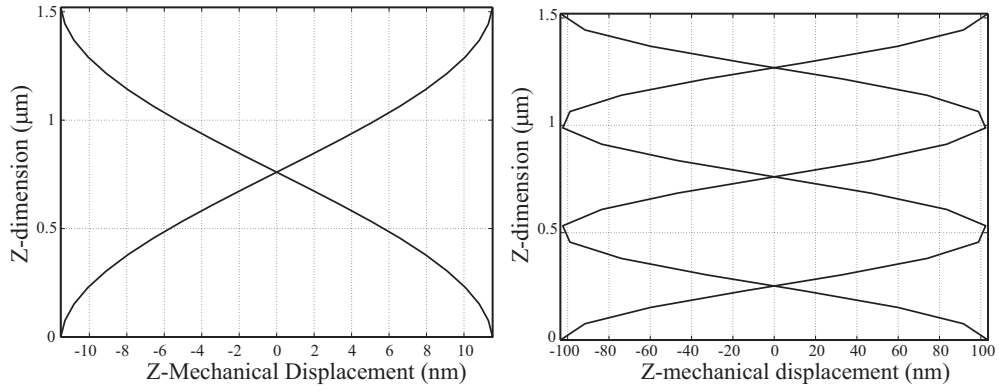

(a) (b)

Figure 3.15: Mechanical Z-displacement in the piezoelectric layer : (a) Fundamental mode and (b) the first harmonic.

Thickness Mode Condition

As it has been seen, the lateral dimensions of the piezoelectric slab are large enough to converge with the one-dimensional Mason model response. In this situation, the so-called thickness mode condition is accomplished. That is, the lateral dimensions are large enough to make the resonance frequency of lateral waves to be far away from the fundamental mode, or even to be evanescent if losses in the piezoelectric slab are included. Some works have presented the ratio needed between lateral and thickness dimension (L/d_p) to have a pure thickness mode resonating in the BAW resonator [118, 119]. As the lateral dimensions of the BAW resonator becomes comparable to the thickness dimension, lateral modes are strongly coupled to the thickness mode [119]. Part of the energy contained in the thickness mode thus leaks to the lateral mode making the electromechanical coupling constant to be degraded. This also results in a decrease in the quality factor Q of the BAW resonator. In this situation, the antiresonance frequency is still directly related with the thickness dimension of the BAW resonator. If the value of the electromechanical coupling constant is degraded, the resonance frequency will therefore be shifted to higher values, that is, the frequency difference between the resonance and antiresonance frequency will be lower.

In order to analyze this, several simulations have been carried out for different ratios between lateral and thickness dimensions. The results are found in Figure 3.16. Here four different BAW resonators with a thickness $d_p = 0.5$ μm, 1 μm, 1.5 μm and 3 μm have been simulated decreasing the lateral dimensions. It can be seen that as the ratio between the lateral and thickness dimension becomes smaller, the convergence error compared to Mason model becomes greater. Using the results obtained, it can therefore be stated that for a ratio of 40:1, the error convergence in the resonance frequency is below 0.1%, making the value of the electromechanical coupling constant remain at the expected value.

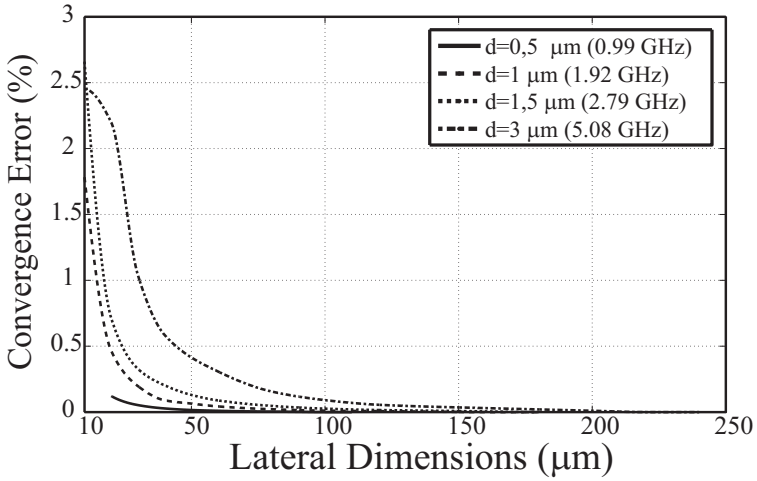

Figure 3.16: Convergence for the resonance frequency to the Mason model for different ratio between lateral and thickness dimension.

In order to validate the results above, Figure 3.17 shows the convergence error of the resonance frequency as a function of the lateral dimensions for different resonators provided by Triquint Semiconductors. As expected, as the lateral dimensions of the resonator becomes larger, the error in the resonance frequency becomes closer to zero. The value of the effective electromechanical coupling coefficient is also plotted. In this case, as the resonance frequency moves towards its predicted value, the value of k^2_{eff} tends to higher values. This is due to the fact that for small lateral dimensions, lateral modes couples strongly with the thickness extensional mode, leading to a leak of the energy of the main mode with the consequent degradation of the effective electromechanical coupling coefficient and the Q-value.

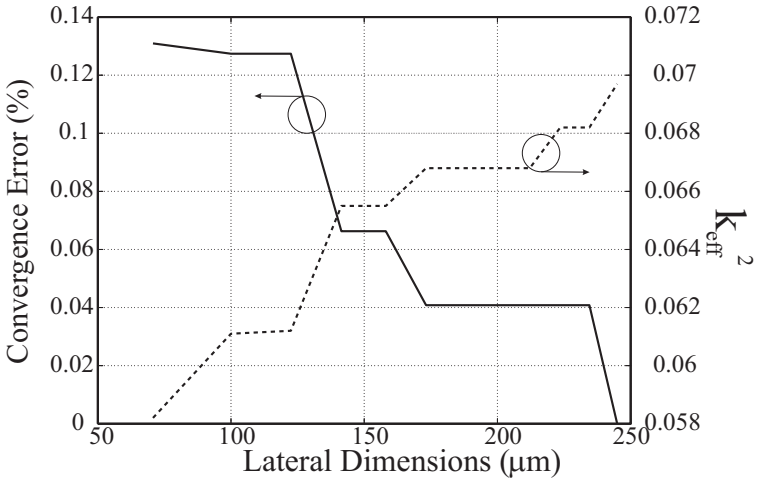

Figure 3.17: Convergence error in the resonance frequency and effective electromechanical coupling factor as a function of the lateral dimensions for measured BAW resonators.

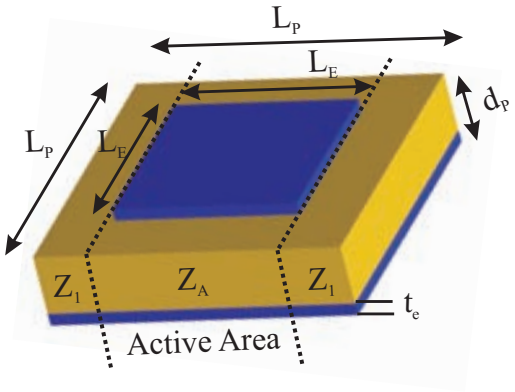

Figure 3.18: Definition of the electroded BAW Resonator.

Table 3.4: Dimensions and materials of the BAW resonator in Figure 3.18.

Layer	Material	Thickness dimension	Lateral dimension
Top electrode	Aluminum	100 nm	100 μm
Piezoelectric	Zinc Oxide	1.52 μm	130 μm
Bottom electrode	Aluminum	100 nm	130 μm

3.4.2 3D simulation of an electroded BAW resonator

The requirements in the 3D simulation in order to converge with the one-dimensional Mason model have been stated for the BAW resonator with infinitesimal electrodes in terms of the number of thickness elements, and the ratio between the lateral and thickness dimensions. However, in the previous section, since there was no region distinction (electroded and non-electroded region) the presence of lateral unwanted modes was not evident. In this section, the BAW resonator is going to be analyzed with the presence of metal electrodes. To that end, the BAW resonator to be analyzed is shown in Figure 3.18, and the materials and dimensions of the different layers are shown in Table 3.4.

Figure 3.19 shows the resulting electrical input impedance of the BAW resonator using the 3D simulation compared to the one-dimensional Mason model. The result shows a very large number of spurious resonances in the electrical response. The spurious resonances present in the electrical response can be classified in two different groups depending on their origin: cavity modes and lateral standing wave modes. The origin of the cavity modes comes from the artificial boundary conditions considered in the structure. The mechanical displacement has been set to zero in the lateral edges, making the BAW resonator to be clamped. As a result, the mechanical wave is reflected at this interface, making the mechanical wave to propagate along the whole structure. In order to avoid these modes, PML (Perfectly Matched Layers) can be used at these edges of the structure. This is an artificial absorbing layer which is designed so that incident

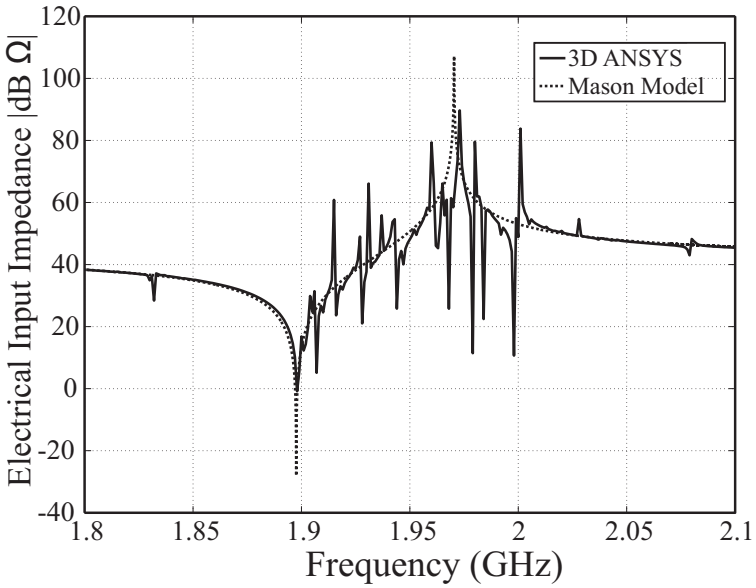

Figure 3.19: Electrical response for a BAW with no losses.

waves upon the PML from a non-PML layer do not reflect at the interface. However, the solution used in order to avoid this kind of spurious resonances is the inclusion of material losses in the form of mechanical damping in the piezoelectric layer. The value of the damping ratio is related with the quality factor of the BAW resonator as,

$$Q = \frac{1}{2\zeta} \tag{3.29}$$

In order to clearly observe the distribution that the modes mentioned above present in the electrical behavior of the BAW resonator, and specifically the cavity modes, the lateral dimension of the whole structure L_p has been set to a higher value. Figure 3.20(a) shows the mechanical displacement distribution for the fundamental thickness mode. It can be seen that this presents a uniform distribution which is confined in the electroded region as it was discussed in Figure 3.14. Figure 3.20(b) shows the sum of the mechanical displacement distribution for the cavity modes, where the mechanical displacement is distributed along the whole structure, electroded and non-electroded region, as it was previously discussed. Finally, Figure 3.20(c) shows the mechanical distribution for the lateral standing waves. In this case, unlike cavity modes, the distribution is confined in the electroded region due to the trapping energy concept.

In order to minimize the cavity modes, a damping ratio of 0.03% has thus been included in the piezoelectric layer. In Figure 3.21, the electrical response of the BAW resonator of Figure 3.19 is compared with to a lossy BAW resonator. In this case, the quality factor Q of the BAW resonator is affected by the mechanical damping ratio according to the expression in (3.29), obtaining a value of $Q \simeq 1500$. The strength of the different spurious modes has therefore been

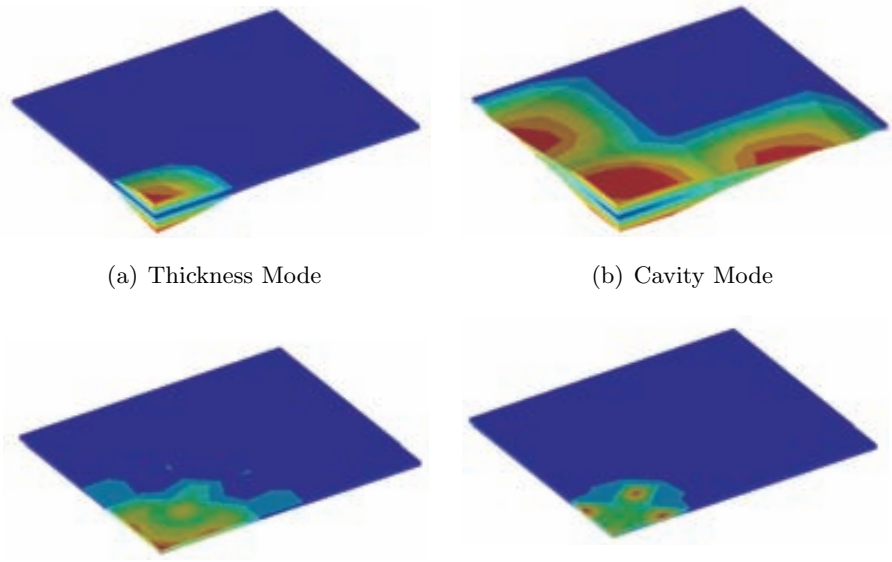

(a) Thickness Mode (b) Cavity Mode

(c) Standing Wave Modes

Figure 3.20: Sum of the mechanical displacement distribution for the resonant modes present in a BAW resonator.

Table 3.5: ANSYS parameters for the 3D simulation.

Mesh size	Thickness divisions	Damping ratio ζ
5 μm	10	0.03%

substantially decreased and the presence of the cavity modes has been minimized. Table 3.5 summarizes the main parameters used in the 3D simulation of the proposed structure, which has been meshed using 26 elements in the lateral direction, and 12 elements in the thickness dimension. Note that numerical errors could be present in the form of unwanted modes in the electrical behavior of the BAW resonator depending on the simulation conditions, that is, the number of elements in the lateral dimensions and the step frequency used in the harmonic analysis.

3.4.3 Lateral standing waves

As discussed in the previous section, the presence of cavity modes can be avoided or minimized by means of a PML layer, or by including the mechanical damping ratio in the piezoelectric layer. In this section, the aim is to study the lateral standing waves arising from the trapping energy concept, the origin and resonant condition of which was extensively discussed in section 3.2. For this purpose, we use the BAW resonator in Figure 3.18, with the corresponding materials. Note that Aluminum Nitride could be also chosen for the analysis. However, as discussed above, the allocation of the lateral standing waves occurs below the resonance frequency due to the type

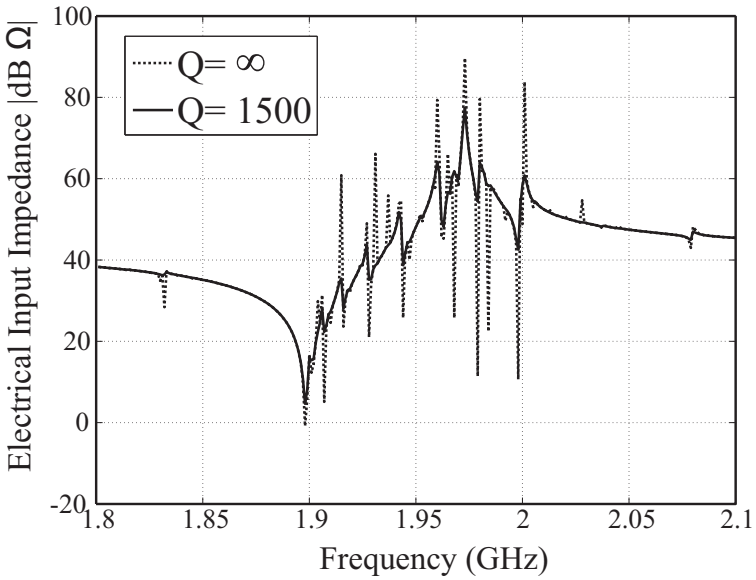

Figure 3.21: Comparison of the electrical input impedance of the lossless BAW resonator, and a BAW resonator with $Q = 1500$.

II dispersion. Unlike the case of Aluminum Nitride, when Zinc Oxide is used as a piezoelectric material, the allocation of the lateral unwanted modes occurs between resonant frequencies which could lead to negative effects in a microwave device response.

The origin of lateral unwanted modes is given by the excitation of Lamb waves by means of the coupling with the fundamental thickness mode. The dispersion relation for the first four Lamb modes in a dispersion type I piezoelectric material is found in Figure 3.22, which is very useful since, in a first approach, the allocation of the unwanted modes can be predicted. The particle displacement for each mode is also given, and the mechanical displacements obtained can therefore be compared with the expected theoretical results. With regard to the antisymmetric modes An, they cannot be piezoelectrically generated, and we are therefore not going to consider them.

The first Lamb mode of interest is the mode $S0$. This mode is found at a very low frequency, and thus, the electrical behavior of the BAW resonator in frequencies close to the resonant frequencies is not affected. The resonant frequency of this mode is directly related with the lateral dimension of the top metal electrode and it can be calculated as [59],

$$f_N = \frac{v_s N}{2L_E} \tag{3.30}$$

where v_s corresponds to the shear velocity of the lateral propagating mode, N corresponds to the number of harmonic and L_E is the width of the top electrode in which lateral modes are trapped.

Figure 3.23(a) shows the electrical input impedance of the BAW resonator at very low fre-

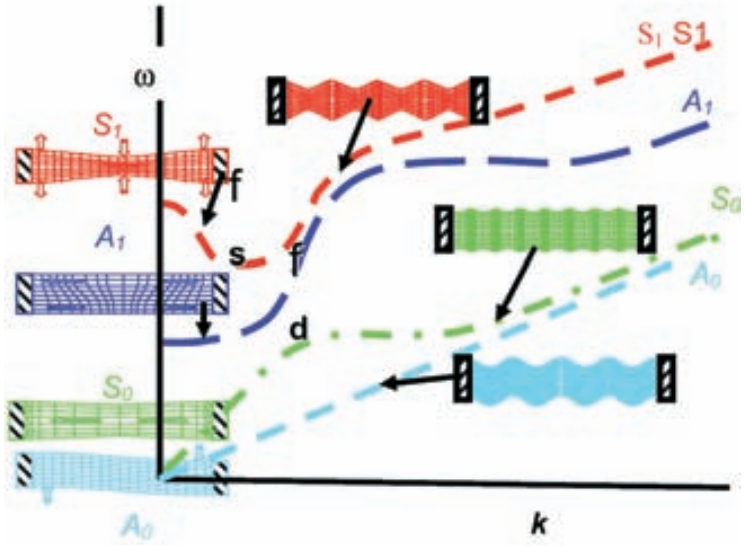

Figure 3.22: Particle displacement for the first four Lamb modes at low and high frequency and acoustic dispersion relation [52].

quencies, where the $S0$ mode is found at approximately 42 MHz. For this mode we can therefore also obtain the distribution of the mechanical displacement. Figure 3.23(c) shows the distribution of the mechanical displacement in the lateral dimension. The magnitude of the mechanical displacement in the lateral direction is two magnitude orders higher than the displacement in the thickness direction since in this case, the particle displacement and propagation direction occur in the lateral dimension. We can therefore state that for this mode, the BAW resonator is deformed in a compression/expansion way in the lateral dimension. Of course, this also entails some deformation in the thickness dimension and that is why we see the result in Figure 3.23(b). This result is consistent with the theoretical particle displacement found in Figure 3.22. Higher harmonics of this mode can also be found, but their frequency allocation is not equally spaced due to the non-linearity of the $\omega - k$ dispersion relation curve.

At higher frequencies, the $S1$ mode is the mode with the strongest contribution to the presence of lateral standing waves in the electrical behavior of the resonator, since as mentioned above, these are allocated between resonant frequencies. Figure 3.24 shows the 3D simulation of the BAW resonator compared with the one-dimensional simulation result. The agreement between both responses is very good in terms of static capacitance and resonant frequencies. However, as expected, different standing waves are found in the 3D response which cannot be predicted by one-dimensional models. As it occurs with the $S0$ mode, the harmonic modes are not equally spaced due to the non-linearity of the $\omega - k$ dispersion relation. The distribution of the mechanical displacement in the thickness dimension is also plotted for the first three harmonic modes. A pattern in the mechanical distribution given by the position of the maximum and

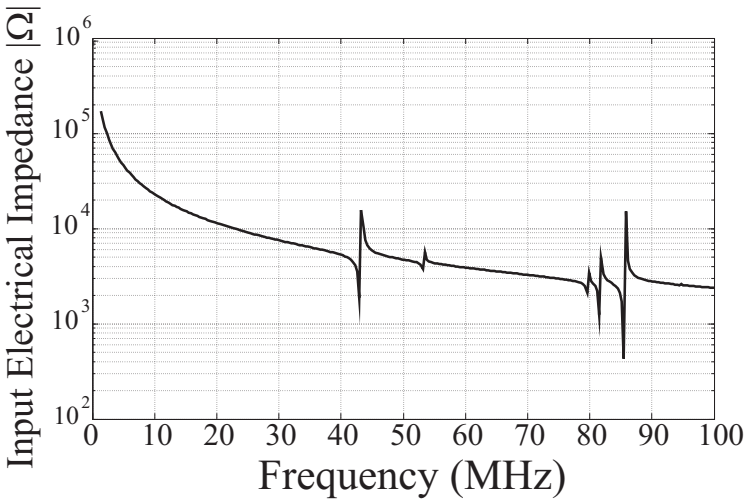

(a) Magnitude of the input electrical impedance of the BAW resonator at low frequencies.

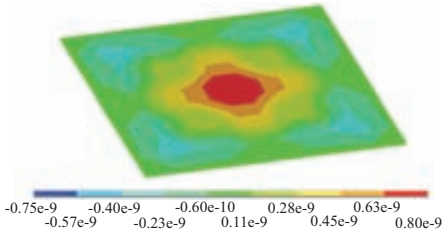

(b) Distribution of the mechanical displacement in the Thickness direction

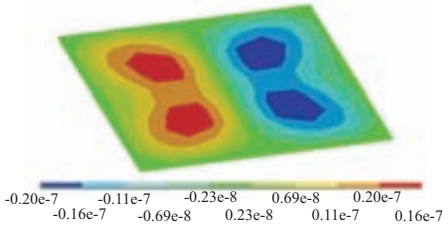

(c) Distribution of the mechanical displacement in the X-Lateral direction

Figure 3.23: Electrical behavior of the BAW resonator at low frequencies.

minimum mechanical displacement points can be observed. In this case, the mechanical wave is propagating in the lateral dimension and, at the same time, the particle displacement occurs in the thickness dimension. This is the typical behavior of the thickness shear TS waves as it was discussed in section 3.2 in this chapter. As a result, a more detailed study of the different present spurious modes in the electrical behavior of the BAW resonator must take place.

Figure 3.25 shows the mechanical displacement distribution in the thickness direction for the fundamental mode at the resonance frequency at 1899 MHz, and the next standing modes placed at 1903, 1909 and 1917 MHz. The phenomena occurring at the resonance frequency is a special case. As constantly mentioned on various occasions throughout this chapter, plate wave modes are always combinations of longitudinal and shear wave modes. However, at the resonance frequency we have a special case because here, $\beta = 0$, that is, the lateral dependence of the mechanical displacement disappears. In this situation, the whole structure vibrates in phase either as a longitudinal compression/expansion way for the thickness extensional TE mode, or for the TS mode. As will be discussed below, this is called the piston mode. At the

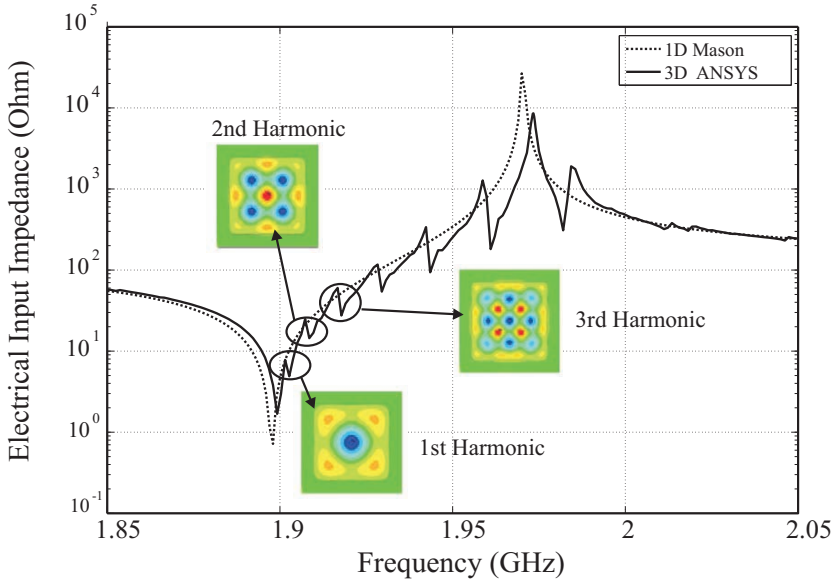

Figure 3.24: Comparison of the one- and 3D simulation of the electrical input impedance for the BAW resonator.

resonance frequency we will therefore always find a lateral standing wave with wavelength $\lambda/2$, with the particle displacement in the thickness direction.

For the consecutive modes, the mechanical displacement in the thickness direction is plotted on the $X-Y$ plane in the diagonal direction. It is apparent that we found mechanical displacements consistent with the consecutive wavelengths $3\lambda/2$, $5\lambda/2$ and $7\lambda/2$, that is, odd multiplies of the fundamental mode. The distribution pattern of each of these spurious modes has been compared with the distributions obtained in [120]. Here, the technique used to measure the displacement profiles is Laser-Interferometric Probing. To do this, a particular frequency range is selected. The optical scanning interferometer sweeps the sample surface at each frequency, recording the time-averaged amplitude of the motion in the thickness dimension of the surface and the intensity of the reflected light for each point in x and y. More information about the technique can be found in [54, 55, 56]. The mechanical displacement distribution pattern is then obtained. As can be seen, the agreement between 3D simulations and the patterns obtained using Laser-Interferometric Probing is very good. This is a very promising result since, first, we have the certainty that the previous assumptions related with the 3D simulation environment were correct taking into account the results obtained; second, due to this certainty, we can consider the performance of a conventional BAW resonator and carry out the study of more complex structures, as will be discussed in further chapters. Finally, note that the presence of lateral standing waves out of the resonant frequencies is not as evident as between resonant frequencies. This is because out-of-band, the BAW resonator behaves as a parallel capacitor plate, with a very low quality factor making the amplitude of the lateral standing waves to be weak.

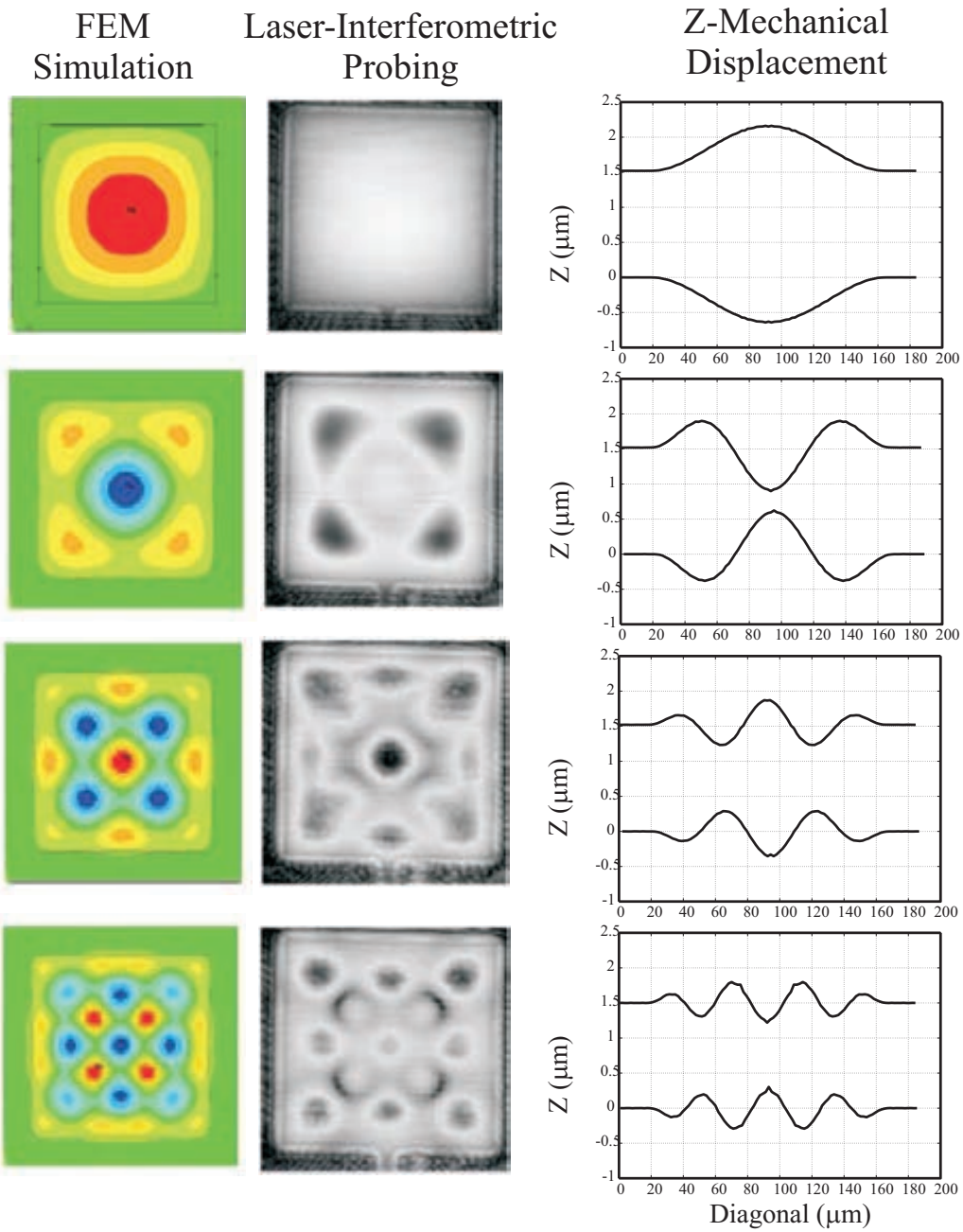

Figure 3.25: Comparison between the obtained results using the 3D simulation and the results using Laser-Interferometric probing in [120].

3.5 Chapter Summary

In this chapter, we have extended the solution of the mechanical wave in one dimension, i.e. considering infinite lateral dimensions, to the three-dimensional case, where lateral dimensions are also considered to be finite. This means that not only thickness modes can propagate in the structure, but also lateral modes, which are usually called Lamb waves. When metal electrodes are present in the structure of the BAW resonator, a distinction must be made between two different regions: the electroded and non-electroded region. The former is the area covered by all the layers making up the structure, while the latter is the outside or surrounding region. Taking this into account, the propagation of Lamb waves can be analyzed and, for some boundary conditions at the interface between the two regions, lateral standing waves can be excited in the BAW resonator.

In order to predict the specific lateral modes that can be excited in the BAW resonator, we can use the dispersion relations curves, which relate the acoustic wave frequency with the lateral propagation constant. For a given ,frequency and depending on the cut-off of the different regions, the lateral propagation constant can therefore be real, which leads to a sinusoidal propagating wave, or may be purely imaginary which leads to an exponentially attenuating wave, or may also be complex, which leads to a sinusoidal attenuating wave. These considerations give rise to the well-known concept of energy trapping.

The need for a 3D simulator becomes evident when lateral waves, which cannot be predicted by the one-dimensional models, are also present in the electrical behavior of the BAW resonator. That is why the finite element method is introduced in this chapter, where the simulation strategy is widely discussed. However, before the simulation of a BAW resonator, the mesh element size in the simulator environment must be set. Some partial results are obtained using 3D simulations. The most important refers to the thickness mode condition, and this establishes the required ratio between the lateral and thickness dimensions needed for a weak coupling between the lateral and thickness waves. This would otherwise lead to the degradation of the effective electromechanical coupling constant.

Finally, the BAW resonator has been simulated using the 3D simulator. The origin of the various unwanted modes in the electrical behavior of the BAW resonator has been studied extensively, but also from the mechanical point of view. The results have been compared against various works in which measured resonators are discussed, and very good agreement with the 3D results has been achieved. These results encourage us to move beyond the simulation of a conventional BAW resonator in the next chapters, where more sophisticated structures are discussed.

CHAPTER 4

Optimization of the Electrical Behavior of a Bulk Acoustic Wave Resonator

As seen in the previous chapter, the conventional BAW resonator presents lateral standing waves which degrades its electrical performance. The need for 3D simulations therefore becomes evident in order to predict the allocation and the effect of these lateral modes. The next question is therefore: is it possible to design a BAW resonator with the aim of avoiding or minimizing the presence of the spurious lateral modes? There are basically two different techniques, which when applied to the BAW resonator design lead to an improvement in its performance: apodization and the thickened edge load solution.

Apodization consists of designing the top electrode in such a way that non-parallel edges are found. In this case, the standing paths which create the lateral standing waves are larger, which means that the strength of the lateral modes are minimized. However, this also leads to more standing paths, and more lateral modes are thus present in the electrical behavior of the BAW resonator, although they are not as strong as the BAW resonator with a square top electrode. The presence of these unwanted modes therefore also entails the consequent degradation of the Q quality factor. Meanwhile, the thickened edge load consists of the presence of a border ring which forces certain boundary conditions that makes lateral standing waves unable to propagate in the structure. This means that the Q quality factor obtained in the BAW resonator is higher than the one in the apodization technique. Taking into account these considerations, both techniques will therefore be described in this chapter. Although the apodization technique is described and discussed by means of 3D simulations, this chapter is mainly focused on the thickened edge solution, since the performance obtained from the BAW resonator is better than from the apodization technique.

It must be pointed out that, for the purposes of this work, ZnO has been chosen as a piezoelectric material since the lateral standing modes will be present between resonant frequencies (dispersion type I), unlike AlN where they are found below the resonance frequency f_r (dispersion type II).

4.1 Apodized BAW Resonator

The first discussed technique for minimizing the presence of lateral standing waves in a BAW resonator is the apodization technique which is described in [57, 59].

The piezoelectric layer can be understood as an acoustical cavity in which lateral standing waves can be present. These modes occur due to the resonant paths in which the wave is travelling parallel to the electrodes, bounces off the electrode edges a certain number of times and finally returns to the same point on the wall of the cavity. In the conventional structure of the BAW resonator with a squared top electrode with a length of W, the modes will be placed at the frequencies [59],

$$f_N = \frac{v_S N}{2W} \qquad N = 1, 2, ... \tag{4.1}$$

where v_S corresponds to the shear acoustic propagation velocity in the piezoelectric layer taking into account the effect of the metal electrodes. The strength of the spurious mode will be thus increased by the number of the points having the same resonant path.

The primary idea of apodization is to design a BAW resonator containing a top electrode with non-parallel edges. By doing so, the resonant path becomes greater leading to a more attenuated mode. The apodized resonator geometry can be seen in Figure 4.1. In (a), the idea is to design a shape with non-parallel edges, while in (b) all the sides of the top electrode are curved [60]. In this work we are going to focus on the former solution. One of the parameters that defines the apodization shape is the angle α_a as seen in the figure. The blue line shows the theoretical path for a given propagating wave. Thus, depending on the apodization angle, the path that the propagating wave must travel will be longer than the standing path for a square electrode. Since material losses have been assumed in the piezoelectric material, the longer the standing path, the more attenuated the spurious mode will be.

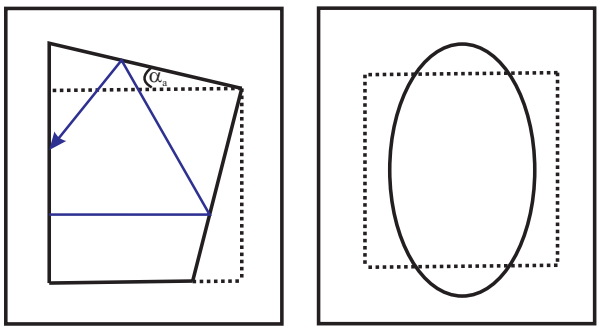

(a) Non-parallel edges (b) Curved sides

Figure 4.1: Schematic view of the apodized electrode.

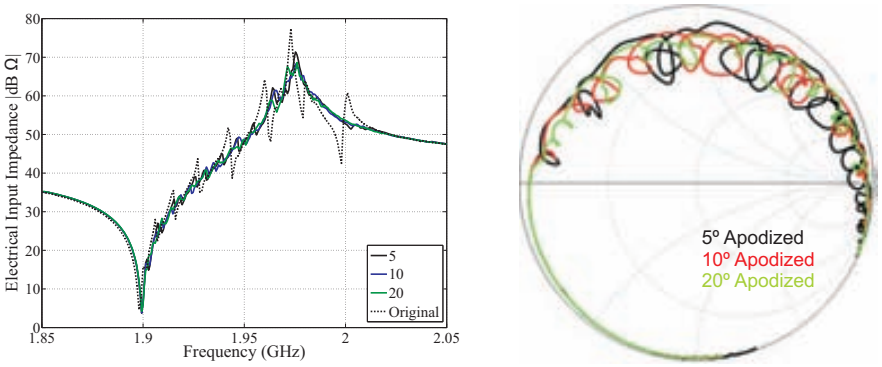

(a) (b)

Figure 4.2: (a) Electrical impedance of the BAW resonator for different apodization angle. (b) Smith Chart representation for the apodized BAW resonator.

In order to study this technique, several 3D simulations have been carried out for BAW resonators with ZnO as a piezoelectric material, and with different electrode materials and also different apodization angles α_a. In this sense, the discussion is focused on the electrical performance of the BAW resonator in terms of presence of spurious modes and also the obtained quality factor.

First of all, in order to determine the limit apodization angle, Figure 4.2(a) shows the electrical input impedance for a 5°, 10° and 20° values for α_a using ZnO as a piezoelectric material, and Al as a metal electrode. Analysis of the possible standing paths for a different apodization angle shows that a maximum apodization is approximately $\alpha_a \simeq 22°$, which is the equidistant angle between 0° and 45°. This is because standing paths with $22° < \alpha_a < 45°$ are equivalent to the standing paths with $0° < \alpha_a < 22°$. 3D simulations have shown that for a given apodization angle above 25°, the electrical performance of the BAW resonator is not improved compared to the 22° situation.

Some conclusions can be from Figure 4.2(a). It is clear than that apodized BAW resonators present an electrical response where the spurious modes are clearly attenuated. However, the number of spurious modes is higher than the original situation. The non-parallel edge will lead to many more standing wave paths than the square one, since more possible paths can be found.

The presence of more lateral standing waves also entails that part of the energy associated with the fundamental thickness mode will leaks to these modes making the Q quality factor of the BAW resonator to be degraded. This can be clearly seen in Figure 4.2(b), where the reflection coefficient for each value of α_a is shown. As predicted with the electrical input impedance, it can be seen that the radius of each of these loops is decreased as the apodization angle becomes greater, i.e. the modes are more attenuated. It can also be seen that the number of the present

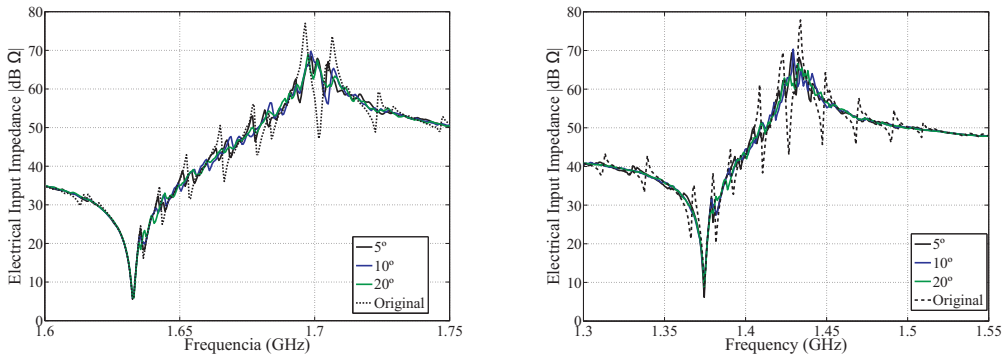

(a) Molybdenum electrodes.

(b) Platinum electrodes.

Figure 4.3: Electrical input impedance for different apodization angle using: (a) Molybdenum electrodes and (b) Platinum electrodes.

loops is higher. Finally, when the apodization angle is increased, the radius of the curve which is described in the Smith chart also becomes smaller. This is related with the quality factor Q of the BAW resonator, which tends towards lower values when the apodization angle is increased, as mentioned above.

In order to study the electrical behaviour of the BAW resonator with other type of metal electrodes, the same simulations have been carried out for heavier metals such as Molybdenum and Platinum. Figure 4.3(a) and 4.3(b) shows the electrical input impedance of the BAW resonator for Molybdenum and Platinum metal electrodes. As with Aluminum electrodes, the attenuation of the spurious modes is evident, but the number of modes is now higher. Meanwhile, the quality factor of the BAW resonator also seems to be degraded, as can clearly be seen in the Smith Chart representation in Figure 4.4 due to the number of lateral standing modes, where part of the energy of the fundamental thickness mode is leaked.

Figure 4.4(a) and 4.4(b) shows the Smith Chart representation of the reflection coefficient for the apodized BAW resonator with Molybdenum and Platinum electrodes. As with Aluminum, the number of modes have been increased although they are not as strong as the original situation. The quality factor is degraded as the apodization angle increases, as can be observed in the radius of the circle which describes the input impedance. However, this degradation also depends on the acoustic impedance of the metal electrodes used. For the heaviest material - in this case Platinum - the degradation of the quality factor Q seems to be stronger. This is due to the fact that the higher is the acoustic impedance of the metal electrode the stronger are the reflected wave modes at the interface, and thus, the higher coupling between thickness and shear modes which entails greater degradation of the Q quality factor.

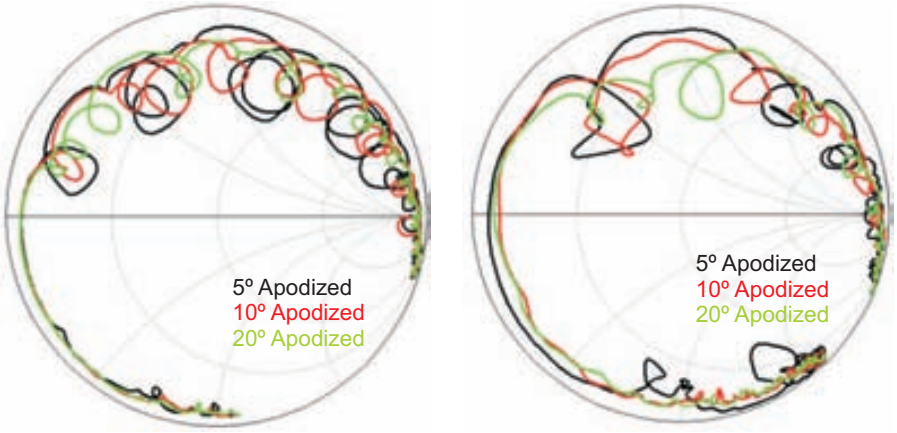

(a) Molybdenum electrodes. (b) Platinum electrodes.

Figure 4.4: Smith chart representation of the reflection coefficient for: (a) Molybdenum electrodes and (b) Platinum electrodes.

The statement above can be validated by means of the mechanical results obtained in the 3D simulations. Figure 4.5 shows the distribution of the mechanical displacement in the thickness direction for the BAW resonator with different metal electrodes and apodization angle at the antiresonance frequency f_a. In the case of Aluminum, which is the metal with the lowest acoustic impedance and also a mass density ρ, for each of the values of α_a, the distribution is uniformly confined in the active are of the resonator. In the case of Molybdenum with an acoustic impedance and mass density are higher than that of Aluminum, it can be seen that, as the apodization angle α_a increases, the distribution of the mechanical displacement is less uniform. This is also seen in the electrical input impedance, where unlike the original situation, the antiresonance frequency is not a clear frequency point as with f_r, i.e. the quality factor is clearly degraded. Finally, the worst case occurs with Platinum electrodes which is the metal material with the highest acoustic impedance and mass density of the materials used for this analysis. In this case, for $\alpha_a = 5°$, it can be seen that the distribution of the mechanical displacement is non-uniform along the active area. As the value of α_a is increased the distribution becomes more non-uniform, a situation in which predicting the antiresonance frequency becomes a very hard task.

In the literature is found that high acoustic impedance metal electrodes are preferred in a filter configuration due to the high effective electromechanical coupling constant associated with them. However, these conductor materials also present high resistivity. The resistivity of the metal electrodes can be modelled by means of a series resistance as it was done in the modified Butterworth-Van Dyke equivalent using R_s. The value of R_s, as seen in [27] is related with the

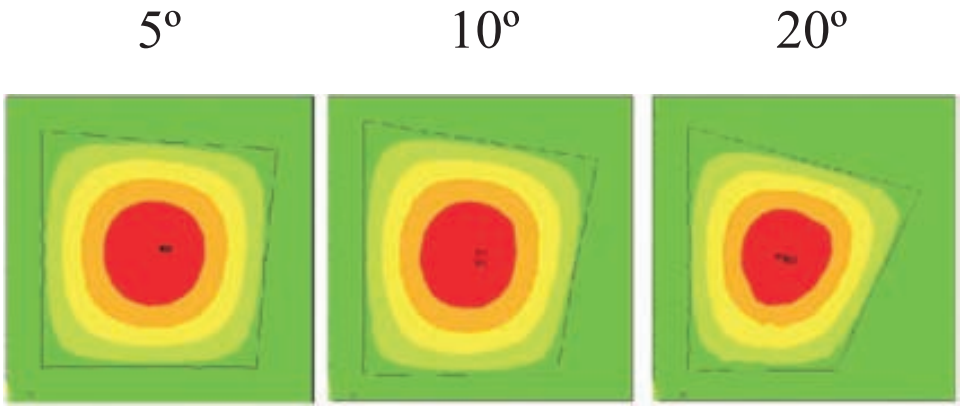

(a) Aluminum electrodes.

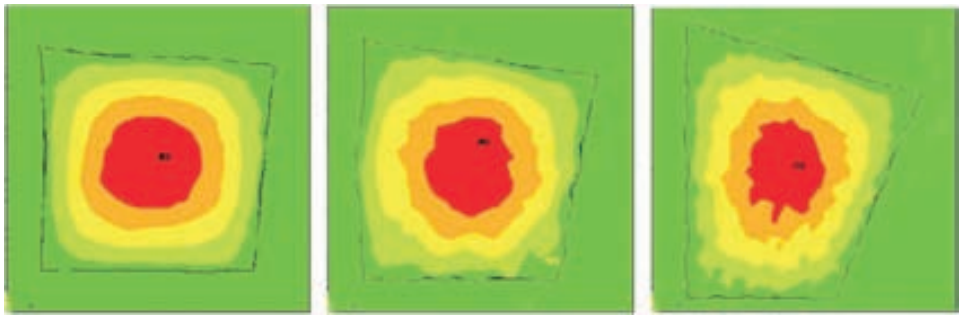

(b) Molybdenum electrodes.

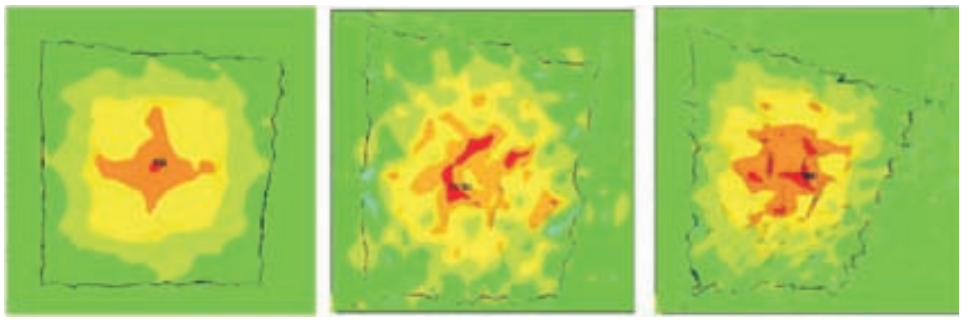

(c) Platinum electrodes.

Figure 4.5: Distribution of the mechanical displacement in the thickness direction for a BAW resonator with different metal electrodes and apodization angle α_a: (a) Aluminum electrodes. (b) Molybdenum electrodes. (c) Platinum electrodes.

quality factor of the series resonance as,

$$Q_s = \frac{\omega_s L_1}{R_s + R_m} \tag{4.2}$$

where as it was discussed in chapter 2, L_1 corresponds to the parasitic inductance of the metal contacts, and R_m is associated with the acoustic losses in the motional arm of the BVD model. The resistive loss mechanism is thus most pronounced near the operating frequencies where the electrical currents are largest.

Meanwhile, resistive effects arise from non-uniform stress distributions over the area of the electrodes as it is discussed in [121]. This is clear by looking at the distributions of the mechanical displacement in Figure 4.5. As the acoustic impedance is higher, as is the resistivity associated to this material, the distribution becomes less uniform. In this case, if the distribution is not flat, there are areas of the resonator vibrating at different amplitudes or phases which leads to redistributions of currents associated with them. In other words, non-uniform distribution of the mechanical displacement entails points of the metal electrode being at different voltages. Therefore, so-called eddy currents [27], will flow between points of the electrode with local maximum and minimum displacement. Since the electrode is not a perfect conductor, there will be $I^2 R_s$ losses associated with these eddy currents.

We can conclude that in order to improve the BAW resonator performance by means of the apodization technique, lighter metals are advisable to be used to try to obtain a reasonably good quality factor since they present a lower metal resistivity. From the point of view of the shape of the top electrode, low values of α_a are desirable for a greater possible uniform distribution of the mechanical displacement in the active area of the BAW resonator, and thus the better performance. However this also entails stronger lateral resonances since there are fewer standing paths.

4.2 Thickened Edge Load solution

The previous section showed that using the apodization technique, the spurious modes in the electrical behavior of the BAW resonator can be minimized. However, they are still present in the electrical response leading to the quality factor to be degraded. On the other hand, high acoustic impedance metals are usually desired in the BAW resonator since it enables the highest value of k^2_{eff} which offer a very good performance in a filter configuration. However, these metals also present high resistivity which entails a significant loss mechanism, and the consequent degradation of the Q value, due to the non-uniform distribution of the mechanical displacement.

The solution proposed in this section consists of including a perimetric thickened edge load in the top electrode which forces the required boundary conditions to not generate these un-

wanted modes. This is accomplished when the distribution of the mechanical displacement in the active area of the resonator is flat. As discussed in the previous chapter, any non-perpendicular longitudinal waves affecting a material interface will become reflected and transmitted in form of longitudinal and shear waves. The lateral boundaries require the same continuity of displacement and stress as the vertical boundaries. On the outside region side, the vertical stress must equal zero, but on the active area side it does not generally have to. An additional mechanism is therefore needed in order to facilitate this mismatch. The additional mechanism is thickened edge in the perimeter of the top electrode mentioned above. This solution was patented by Kaitila in [62]. In this section, the side effects will also be analyzed using an in-depth knowledge of the proposed solution. This will lead to a one-dimensional equivalent circuit, which takes the side effects mentioned above into account.

4.2.1 Theoretical development for the thickened edge load solution

In Figure 4.6(a), the 3D view of the BAW resonator is shown where the thickened edge load has been included. The two-dimensional cross section in Figure 4.6(b) shows five different regions with characteristic propagation and mass loading condition, unlike the situation shown in Figure 3.2 in the previous chapter, with only three regions. In order to develop the theoretical development, as it was discussed in section 3.2, longitudinal and transverse waves can be studied separately. Due to the symmetry of the structure in the x-direction, regions 1 and 5 and 2 and 4 are assumed to be equal since the mechanical and electrical conditions are the same.

The mechanical displacement Ψ at regions $i = 2, 3, 4$ can be expressed as,

$$\Psi_i(x_i) = A_r e^{-jk_i x_i} + B_r e^{jk_i x_i} \tag{4.3}$$

while in regions $i = 1, 5$ this is expressed as $\Psi_1 = A_1 e^{K_1 x_1}$ and $\Psi_5 = A_5 e^{-K_5 x_5}$ being K_1 and K_5 real numbers in order to make the propagating wave in this region to be evanescent. Thus, the resonance condition in region $r = 3$ can be expressed using the boundary conditions, that

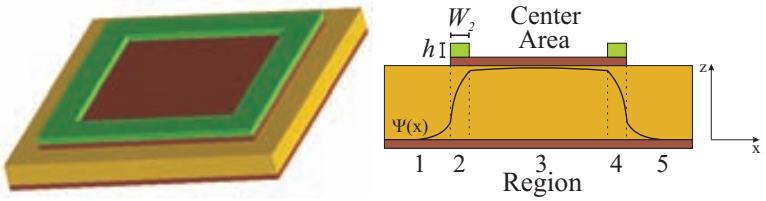

(a) (b)

Figure 4.6: (a) 3D view of a BAW resonator with the thickened edge load. (b) BAW resonator two-dimensional section with the mechanical distribution.

is, continuity of displacement Ψ and its differential $\nabla\Psi$. This results in,

$$\begin{aligned} &\Psi_3(x_3=0) = s\Psi_3(W_3) \\ &\left.\frac{d\Psi_3}{dx}\right|_{x_3=0} = -s\left.\frac{d\Psi_3}{dx}\right|_{x_3=W_3} \end{aligned} \tag{4.4}$$

where W_3 is the width of the region $r=3$. As it occurred in the development in section 3.2, the symmetry of the solutions is expressed for $s=\pm 1$. The set of equations in 4.4 and the resonance condition for this mode, the piezoelectrically generated voltage can be obtained as,

$$\begin{aligned} &V = \frac{h}{jk_3}(s+1)(A_3-B_3), k_3 \neq 0 \\ &V = hW_3(A_3+B_3), k_3 = 0 \end{aligned} \tag{4.5}$$

where as is the case with the conventional BAW resonator, antisymmetric modes are not piezoelectrically generated. In the case of $k_3=0$, the operating mode in the BAW resonator is called the piston mode, which present a flat distribution of the mechanical displacement. Resonances occurring near the piston mode operation frequency are therefore often weakly coupled, which enhances the electrical performance of the BAW resonator.

It is therefore straightforward to state that in this case $\nabla\Psi=0$. Therefore, in order to satisfy the continuity of the differential of the displacement between regions $i=2$ and $i=3$, the next relation must be accomplished,

$$\left.\frac{d\Psi_2}{dx}\right|_{x_2=W_2} = jk_2(-A_2e^{-jk_2W_2} + B_2e^{jk_2W_2}) = 0 \tag{4.6}$$

so, the width W_2 at region $r=2$, that is the thickened edge region, in order to achieve a piston mode in the active region $i=3$ must be,

$$W_2 = \frac{\arctan\frac{K_1}{K_2} + n\pi}{K_2}, \quad n=0,1,...,N \tag{4.7}$$

which has been obtained by equating the real and imaginary parts. Note that $k_1 = jK_1$ is the wave number at region 1, with K_1 being a real number, and $k_2 = jK_2$ is the wave number in region 2. The width presents a periodical solution with n due to the periodicity of the trigonometrical functions. Due to the symmetry of the structure, the width of region $r=4$ is exactly the same as the calculated for region $r=2$, that is, $W_2 = W_4$. In this case, since one of the lateral dimensions in this development has been considered to be infinite, the obtained results are not the optimal results which may be found experimentally, but they are a very good approach. On the other hand, in order to ensure that $W_2 > 0$, the number K_2 must be real. Regarding with the continuity conditions at the different interfaces, if a piston mode operating mode is considered in region $i=3$, with a flat displacement, that is, $\nabla\Psi_3=0$, it must be the case that,

$$\left.\frac{d\Psi_3}{dx}\right|_{x_3=0} = -jk_3A_3 + jk_3B_3 = 0 \Rightarrow \left.\frac{d\Psi_2}{dx}\right|_{x_2=W_2} = 0 \tag{4.8}$$

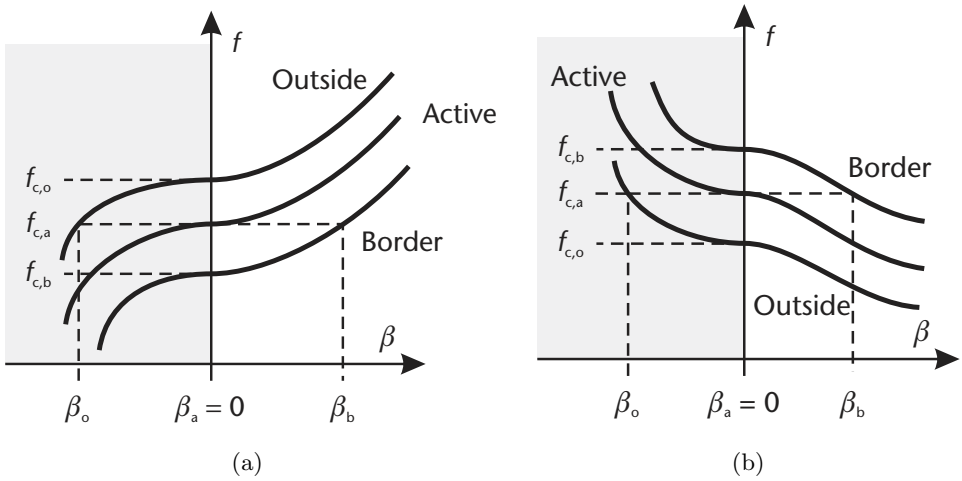

Figure 4.7: Dispersion relation curves in the outside, active and thickened edge region for a material with: (a) dispersion type I and (b) dispersion type II [67].

which means that $A_3 = B_3$. Thus, the piezoelectric coupling which is proportional to $A_3 - B_3$ in equation (4.5) is weak, leading at the same time to the coupling to spurious modes modes to be also weak as was anticipated above.

Depending on the material's properties and the operating mode of the BAW structure, it is possible to distinguish between acoustic dispersion type I or II. If the Poisson's ratio for a given material is above 1/3, the dispersion is type I, while if the ratio is below 1/3, it is type II. This situation was seen in Figure 3.6. The dispersion curves for type I and II in the outside, active and thickened edge regions are shown in Figure 4.7(a) for the former and 4.7(b) for the latter. As discussed above, the presence of the thickened edge enables the mismatch between the active and outside region to be avoided. To do so, the lateral propagation constant must be real, while it must be pure imaginary in the outside region. In dispersion type I materials this is achieved when the cut-off frequency of the thickened region is below the cut-off frequency of the active region. An additional mass loading must therefore be included in the top electrode. As discussed at length in chapter 3, in a dispersion type II material the behaviour is the opposite, and the cut-off frequency of the thickened edge region must therefore be higher than the active area. To achieve this, some of the metal electrode must be removed, which entails a very complicated fabrication process. In order to overcome these limitations, some works propose including as much as dispersion type I in the stack which changes the material dispersion from type II to type I, and the thickened edge load can thus be included [63].

The structure of the BAW resonator under study presents an Aluminum electrode with a Poisson's ratio equal to 0.362, and Zinc Oxide as a piezoelectric material with a Poisson's ratio equal to 0.39, leading to a dispersion type I [63]. Taking into account that the BAW resonator

Table 4.1: Dimensions for the thickened edge load in the BAW resonator in Figure 4.6.

n-solution	height h	width W_2
10	300 nm	11.65 μm

can be understood as an acoustic waveguide, the thickness of each region will set the cut-off frequency of this region ω_{ci}. Therefore, the wave number at each region k_i can be related with the cut-off frequency of the region and the dispersion parameter α [62],

$$k_i = \sqrt{\alpha\left(\omega_i^2 - \omega_c^2\right)} \tag{4.9}$$

where ω_c is the cut-off frequency of the center area at region $i = 3$, where as it was discussed in the previous chapter $\alpha = 10^8$ for dispersion type I and $\alpha = -10^8$ for dispersion type II [62].

Figure 4.8(a) shows the comparison between the electrical impedance in the conventional non-optimized resonator, and the resonator in which the thickened edge load is included. Using the expression in 4.7, the geometry characterization of the thickened edge load is summarized in Table 4.1. It can be seen that the presence of lateral resonant modes using the thickened edge load is almost avoided. Note that this is not the optimum solution, but it is much better in comparison with the conventional case. There is also a side effect which is related to the allocation of the antiresonance frequency. This effect will be extensively discussed in the following section.

The Smith chart representation of the reflection coefficient is shown in Figure 4.8(b). In this case we have compared the conventional with the optimized BAW resonator by means of the apodization technique and the presence of the thickened edge load. As expected, the conventional BAW resonator presents several loops between resonant frequencies corresponding to the lateral standing waves. If the top electrode is apodizated, in this case with $\alpha_a = 5°$, the strength of the lateral modes is reduced, but there are more resonant modes. In terms of the quality factor Q, both resonators present almost the same performance. Finally, in the case of the thickened edge load solution, very few loops are present between resonant frequencies, and thus, since there is no leak of energy to these modes, the quality factor of the BAW resonator presents a very good performance.

4.2.2 Side effects coming from the thickened edge load in the BAW resonator

Taking into account the dispersion type and depending on the materials to be used, the height h of the thickened edge load is set to accomplish the relation between the cut-off frequencies of the different regions in (4.9). Afterwards, the equation in (4.7) can be solved in order to obtain the width of the thickened edge. There is therefore a freedom degree when setting the height h, and there is another freedom degree when the n-solution must be chosen to obtain the width

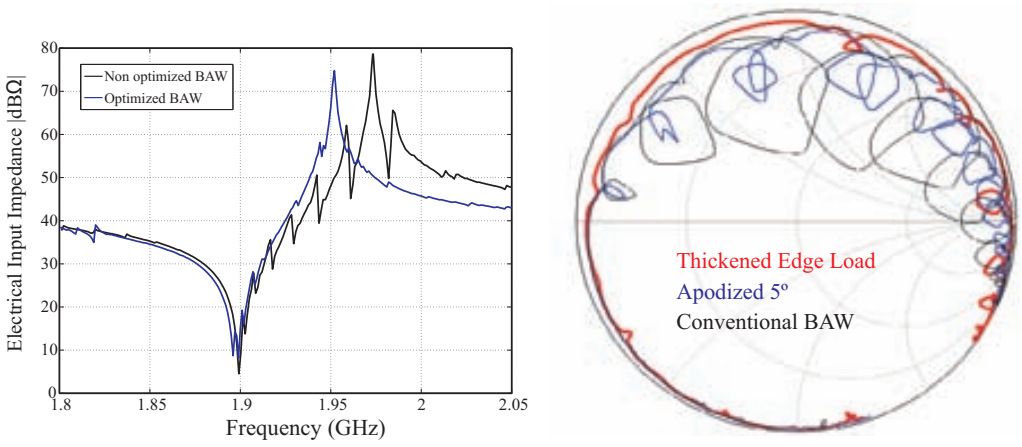

(a) (b)

Figure 4.8: (a) 3D simulation for a conventional BAW resonator compared with the BAW resonator with the thickened edge load. (b) Comparison of the reflection coefficient for the thickened edge load, apodized and conventional BAW.

W_2. Both parameters, h and W_2, are going to be discussed in this section, and how they affect the electrical behavior of the BAW resonator will be seen.

Resonant mode due to the thickened edge load

The fundamental mode operation of the BAW resonator can be modelled by means of the Butterworth-Van Dyke (BVD) equivalent circuit considering infinitesimal electrodes. This circuit consists of a static capacitance C_0, which is the parallel plate capacitor, in a shunt configuration with a series L-C circuit corresponding to the motional arm [122]. However, when the thickened edge load is included, a distinction must be made between two different regions in which the mass loading conditions are different, meaning that the application of the one-dimensional BVD equivalent circuit to the full structure is not a valid approach.

Figure 4.6(b) shows the cross-section of the BAW resonator with the thickened edge load where two different areas can be distinguished: the center area, confined between the thickened edge load, corresponding to region 3; and the thickened edge load area corresponding to region 2 and 4. For our purposes, the structure can therefore be understood as two different BAW resonators that are electrically connected in a shunt configuration due to the different mass loading conditions. Each of the regions with the same boundary conditions can be modelled using an independent Butterworth-Van Dyke equivalent, as shown in Figure 4.9. The BAW corresponding to the central area is characterized by the static capacitance C_{01} and the motional arm consisting of C_1 and L_1, while the BAW resonator of the thickened edge load is characterized with C_{02}, C_2 and L_2. The values for the mechanical and the electrical arm of each BAW resonator,

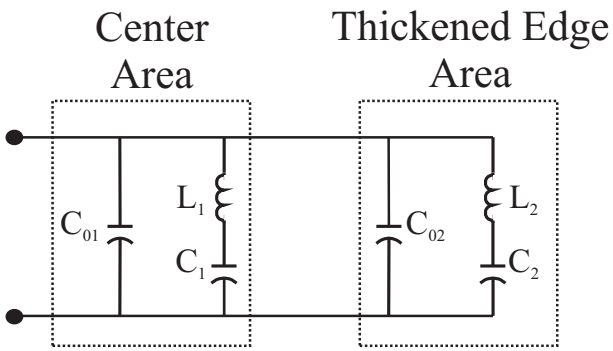

Figure 4.9: Equivalent electrical circuit for the thickened edge configuration using the Butterworth-Van Dyke equivalent.

according to the Butterworth-Van Dyke model, can be expressed as [122],

$$\begin{aligned} C_{0x} &= \frac{A_x \varepsilon_r \varepsilon_0}{d_p} \\ C_x &= \frac{8 C_{0x} k_{eff_x}^2}{\pi^2 - 8 k_{eff_x}^2} \qquad x = 1, 2 \\ L_x &= \frac{\pi^2}{8 k_{eff_x}^2 \omega_{a_x}^2 C_{0x}} \end{aligned} \tag{4.10}$$

The set of equations in (4.10) shows that each BAW resonator is completely defined with $\omega_a = 2\pi f_a$, the antiresonance frequency that is directly related with the thickness of the structure, the effective coupling coefficient k_{eff} which depends on the mass loading effect, and the static capacitance C_0 of each resonator, with d_p being the thickness of the piezoelectric slab. Thus, the input electrical impedance can be then obtained by analyzing the electrical equivalent circuit in Figure 4.9, leading to (4.11), where $C_0 = C_{01} + C_{02}$.

$$Z(\omega) = \frac{(w^2 L_1 C_1 - 1)(w^2 L_2 C_2 - 1)}{w^4 (L_1 C_1 L_2 C_2 C_0) + w^2 (-C_0 (L_1 C_1 L_2 C_2) - C_1 C_2 (L_1 + L_2) + C_0 + C_1 + C_2} \tag{4.11}$$

By analyzing (4.11), it can be seen that the magnitude of the electrical impedance is zero for,

$$\begin{aligned} \omega_{r1} &= 1/\sqrt{L_1 C_1} \\ \omega_{r2} &= 1/\sqrt{L_2 C_2} \end{aligned} \tag{4.12}$$

that is, each BAW resonator contributes with a resonance frequency that only depends on the mechanical arm of each resonator. In the case of the antiresonance frequency f_a, the magnitude of the electrical impedance must be infinite. Solving the roots of the denominator, two antiresonance frequencies occur at,

$$\begin{aligned} \omega_{a1} &= \tfrac{1}{2A} \sqrt{-2A \left(B + \sqrt{B^2 - 4AC} \right)} \\ \omega_{a2} &= \tfrac{1}{2A} \sqrt{-2A \left(B - \sqrt{B^2 - 4AC} \right)} \end{aligned} \tag{4.13}$$

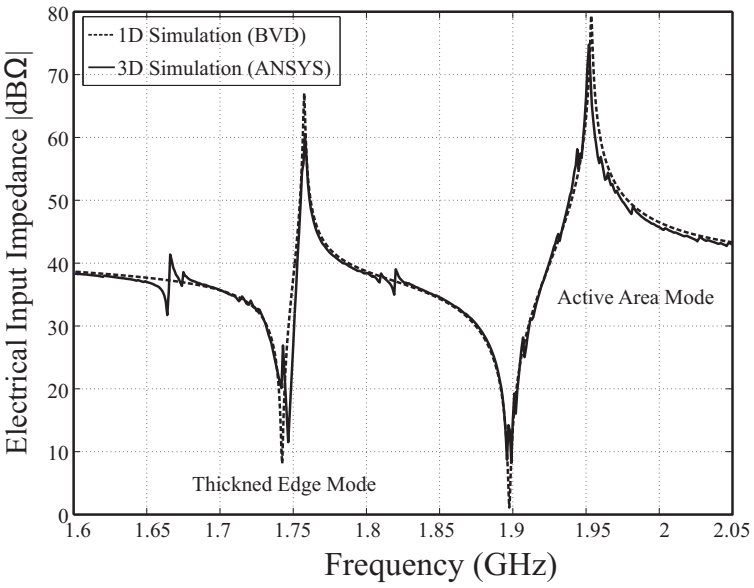

Figure 4.10: Electrical impedance using the one- (dashed line) and the 3D simulation (solid line).

where, $A = L_1C_1L_2C_2C_0$, $B = -C_0(L_1C_1 + L_2C_2) - C_1C_2(L_1 + L_2)$ and $C = C_0 + C_1 + C_2$ corresponding to the shunt equivalent capacitance of the equivalent model.

Figure 4.10 shows the comparison between the one-dimensional equivalent using Butterworth-Van Dyke and the 3D simulation using the ANSYS finite element simulator. The first resonant mode is at a round 1.75 GHz is found, which is due to the thickened edge load. As discussed above, the thickened edge load region can be understood as an independent BAW resonator, since the mechanical boundary conditions are not the same as the active area. The thickness in this region was also designed to have a lower cut-off frequency, which contributes to a resonant mode at this frequency. However, note the the slight difference in the allocation of the resonance frequency f_r between both simulations. The lateral dimension of the width compared with the thickness dimensions leads to a ratio of approximately 8:1. The thickness mode condition is therefore not accomplished, with the resulting shift of the resonance frequency to higher values, as predicted in Figure 3.16 in the previous chapter. Moving to higher frequencies, at 1.9 GHz, the main fundamental mode of the structure is found as expected. It can be seen that the agreement between the proposed one-dimensional equivalent circuit and the 3D simulations is very good.

Meanwhile, the contribution of each region in the structure can be observed from the mechanical point of view. Figure 4.11 shows the distribution of mechanical displacement in the frequencies of interest. In 4.11(a), the distribution has been obtained at the frequency of the mode due to the thickened edge load. In this case, the distribution is confined to the thickened edge region, while in 4.11(b), the distribution is obtained for the fundamental mode, with the distribution confined to the central area of the structure as expected.

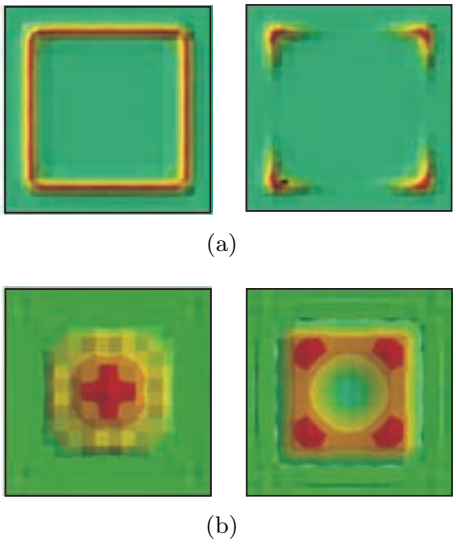

(a)

(b)

Figure 4.11: Mechanical distribution at the resonance (Right) and antiresonance (Left) frequency in the Z-direction for each of the modes present in Fig.4.10. 4.11(a) is the mechanical distribution of the mode due to the thickened edge load around 1.75 GHz. 4.11(b) is the mechanical displacement of the main mode between 1.9 and 1.95 GHz. In this case, the mechanical distribution is confined to the central area of the BAW resonator.

Effective coupling coefficient degradation

It has been previously discussed that the thickened edge load contributes with a resonant mode placed at its own cut-off frequency, which depends on the used height h. The comparison between the 3D simulation agrees perfectly with the proposed model shown in Figure 4.9, where the active and thickened edge region can be modelled as an independent resonators electrically connected in shunt configuration. This is accomplished in terms of resonance frequency since w_{r1} and w_{r2} only depends on the mechanical arms of each BAW resonator. However, in the case of the antiresonance frequency ω_{ax}, (4.13) shows that the position of these frequencies are function of ω_{ax} and k_{eff_x} of each resonator. This was seen in Figure 4.8(a), where the resonant frequency f_r was found at the predicted value, while the antiresonance frequency f_a had shifted down. This is due to the fact of the presence of the thickened edge mode, which takes energy from the main resonant mode making the effective electromechanical coupling coefficient to be degraded. Since the resonance frequency f_r is fixed, the degradation of the value of k^2_{eff} makes the antiresonance frequency to shift down. When the width W_2 is so small that it is almost negligible, the value of C_{02} is also very small leading to approximate $C_0 \approx C_{01}$, and the $C_2 - L_2$ branch behaving like an open circuit, turning back to the non-optimized BAW resonator.

In order to validate these results, the effective electromechanical coupling constant of two different groups of BAW resonators provided by Triquint Semiconductors has been measured. The first group consist of resonators with f_r=1.907 MHz, while the second group present a

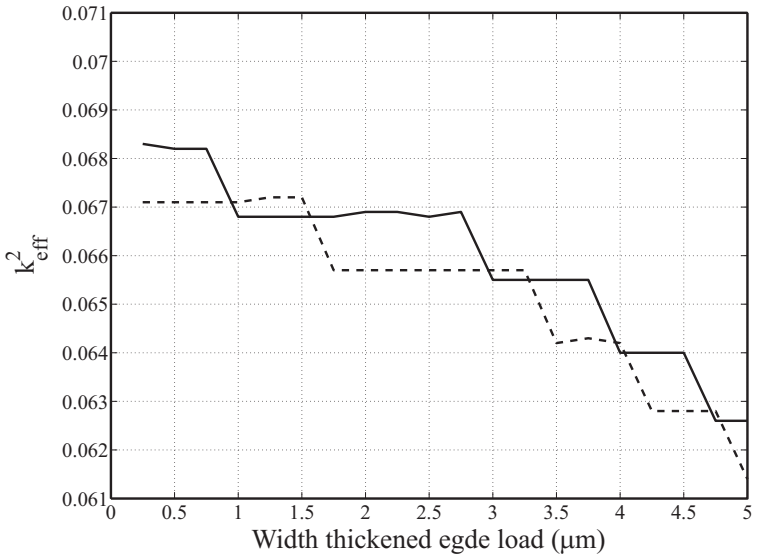

Figure 4.12: Effective electromechanical coupling constant values obtained for various width of the thickened edge load in measured BAW resonators.

resonance frequency of f_r=1.963 MHz. In both groups, a thickened edge load was included where the value of the width was designed from 0.25 μm to 5 μm in steps of 0.25 μm. The variation of the effective electromechanical coupling constant as a function of the width W_2 is shown in Figure 4.12. It can be clearly seen that as the width W_2 becomes greater, the value of the effective electromechanical coupling becomes more degraded. These results are in agreement with the results obtained by means of the one- and three-dimensional simulation.

4.3 Chapter Summary

Before the presence of lateral standing wave modes, basically, two different techniques had been developed in order to minimize or even prevent the effects of these modes on the electrical performance of the BAW resonators: the apodization and the thickened edge load solution. In this chapter, both techniques have been studied by means of the 3D simulations and their limitations have been discussed, although the attention has been focused on the thickened edge solution due to its better performance compared to the apodization technique.

The apodization technique consists of designing the top electrode in such a way that it contains non-parallel edges. By doing so, the resonant paths in the structure become larger, which entails a higher attenuation of the propagating mode. However, with an apodized electrode, there are more standing paths which leads to a larger number of spurious resonances. Taking this into account, the performance of the apodized BAW resonator has been evaluated for various top electrode shapes and metal materials. It has been seen that there is a limit of $\alpha_a = 22^\circ$ at which the standing paths obtained are equivalent. It therefore makes no sense to go further than 22°. As

the apodization angle is increased, as mentioned above, more standing paths are possible, which means more spurious modes are present, although their amplitude is considerably attenuated. This leads to the degradation of the quality factor Q of the BAW resonator, since part of the energy contained in the fundamental thickness mode leaks to these modes. The performance of the apodized BAW resonator also depends on the metal electrode. It has been seen that metals with high acoustic impedance also present high resistivity. Using these materials, the distribution of the mechanical displacement in the thickness direction along the surface of the top electrode becomes non-uniform. In this case, there are local points in the top electrode at a different voltage and eddy currents are therefore generated, with the associated losses.

The second technique consists of the presence of a border region on the perimeter of the top electrode in a BAW resonator. This creates certain boundary conditions and makes the BAW resonator operate in the so-called piston mode. The piston mode present a flat distribution of the mechanical displacement in the active region, which makes the coupling with shear modes very weak. In this case, lateral standing waves are not excited. This results in very high Q free-spurious resonators. Using this technique, we have gone further, and the one-dimensional equivalent circuit has been developed. With this in mind, we assume the full structure to be two independent BAW resonators in a shunt configuration due to the differences in the mass loading and boundary conditions between the active and thickened edge region. The Butterworth-Van Dyke model has been applied to this situation and the agreement with the 3D simulations is very good. This result is worthy of mention, since more sophisticated asymmetric acoustic structures can be modelled using the proposed strategy.

CHAPTER 5

Ladder-Type Filters Based on Bulk Acoustic Wave Resonators

Filters based on BAW resonators have become vital in the exponential growth of communications systems and microwave devices. This is basically due to the small size of the resulting device, and compatibility with the standard integrated circuits (IC) technologies, unlike filters based on surface acoustic wave (SAW) resonators, which are not compatible.

Filters based on BAW resonators can be classified in two major families, depending on how the different BAW resonators are connected. There are Ladder and Lattice topologies, in which the BAW resonators are electrically coupled; and coupled resonator filters and stacked crystal filters, in which the BAW resonators are acoustically coupled.

This chapter is focused in filters based on electrically coupled resonators, more specifically in Ladder-type filters. First of all the working principle operation of this class of filters will be analyzed. After this, a design procedure applied to the ladder-type filters will be widely discussed. This design procedure can be used when the effects of the electrodes are not considered, but also, when these are present. In the latter case, the drawback is that the value of k^2_{eff} is not a-priori known. To overcome this, we propose an iterative method which allows obtaining the physical dimensions of the piezoelectric and electrodes.

On the other hand, Ladder-type filters are characterized by a very selective transmission band due to the presence of a pair of transmission zeros. However, the natural capacitive voltage divider out of the resonant frequencies entails a poor out-of-band rejection. With the aim to improve the out-of-band performance, external reactive elements are included in the BAW resonator, and latter in the conventional topology.

5.1 Working Principle of Ladder-type Filters

The configuration of a conventional ladder-type filter topology is shown in Figure 5.1. It consists of consecutive series and shunt resonators, usually called L configuration, being all the series and shunt resonators equal. The single cell is composed of one series and one shunt BAW resonator. However, another configuration is also possible where the first element in the topology corresponds to a shunt resonator. In both topologies the order N of the filter is given by the number of resonators making up the structure.

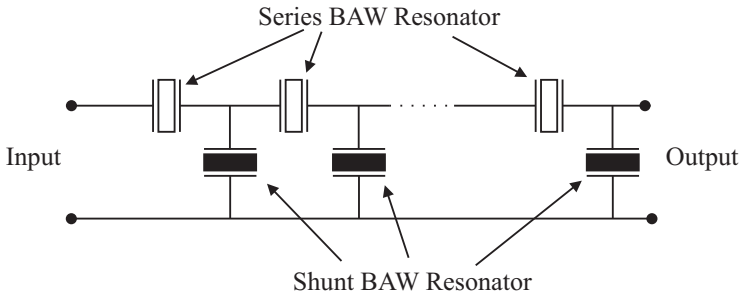

Figure 5.1: General configuration for a Ladder-type Filter.

As mentioned above, ladder-type filters present a pair of transmission zeros or notches which somehow define the bandpass in its transmission response. The lower transmission zero is given by the resonance frequency f_r of the shunt resonators. In this case, the electrical input impedance tends towards 0 Ω, i.e. the BAW resonator behaves as a shortcircuit, making the signal grounded, as shown in Figure 5.2(a). The upper transmission zero occurs at the antiresonance frequency of the series BAW resonators f_a^P. At this frequency, the series BAW resonator behaves as an open circuit, since the electrical input impedance tends to a very high value, preventing the propagation of the signal from the input to the output port as shown in Figure 5.2(b).

Figure 5.3 shows the lossless transmission response for a Ladder-type filter with order $N = 6$, and the electrical input impedance for the series and shunt resonators. It can be seen that the presence of the transmission zeros means that this topology offers a very good selectivity, but

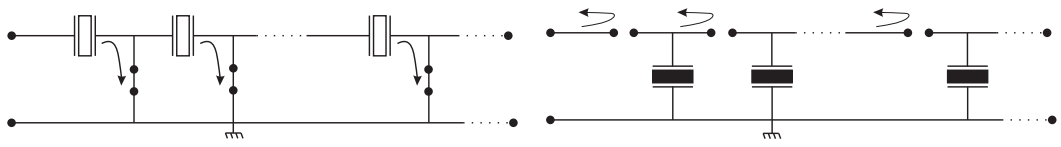

(a) Lower Transmission Zero. (b) Upper Transmission Zero.

Figure 5.2: Behavior of the BAW resonators at the frequencies of the lower and upper transmission zero.

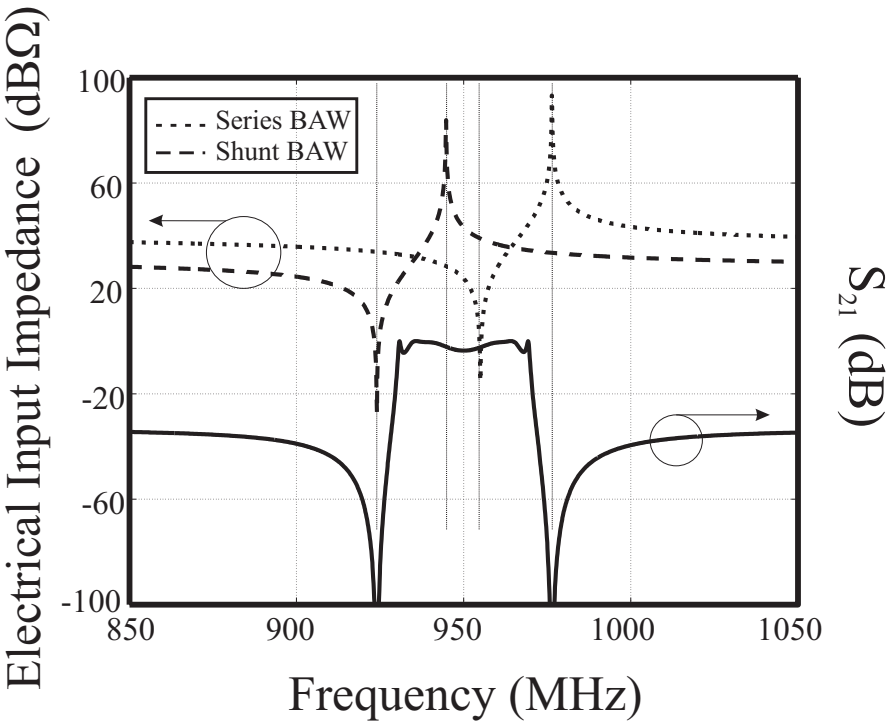

Figure 5.3: Transmission response for a Ladder-type filter with order $N = 6$ and the electrical input impedance for the series and shunt BAW resonators.

also a poor out-of-band rejection. Out of the resonant frequencies, the BAW resonator behaves as a pure capacitor, and the out-of-band rejection is thus given by the natural capacitor divider. Taking this into account, it is straightforward to state that improving the out-of-band rejection, initially entails increasing the order of the filter.

Meanwhile, the bandpass is characterized by a certain ripple and the presence of two spikes at the limits of the band. These spikes are only given for high values of N and lossless BAW resonators. The ripple in the bandpass is due to the unfulfillment of the image impedance condition but also to the topology itself. The image impedance is the image of the single L-network at the input and output ports Z_{I1} and Z_{I2}. In order to avoid reflections, both image impedances are required to be equal to the source and load impedance, usually 50 Ω, in the whole bandpass of the transmission response. As it will be lately discussed, this can be partially achieved resulting in some mismatch losses at the center of the band. This situation is represented in Figure 5.4(a), where as seen, the resonant loop in the reflection coefficient is not centered with respect the real axe in the Smith Chart.

On the other hand, the ripple is also due to the topology itself. As it will be discussed in the design procedure, the BAW resonators are designed in such way in the bandpass $|Z_s| << |Z_p|$. However, part of the signal will be grounded which also contributes to the ripple in the bandpass.

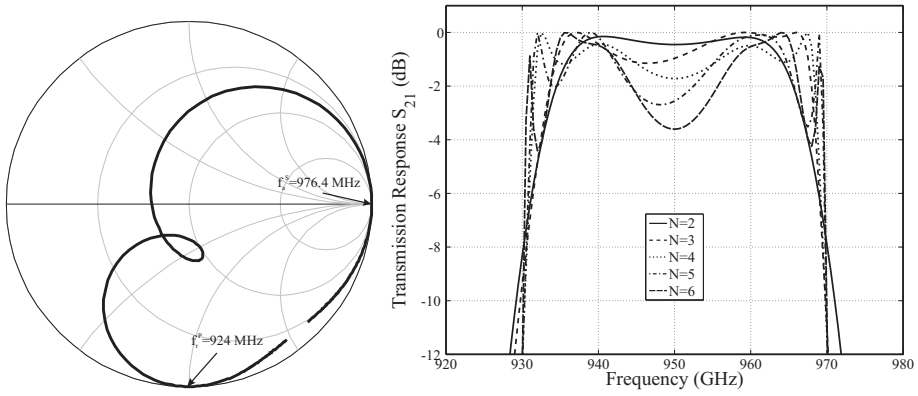

(a) (b)

Figure 5.4: (a) Reflection coefficient S_{11} for a ladder-type filter with order $N = 2$. (b) Detail of the bandpass of the ladder-type filter for different values of N.

This effect is more pronounced as the order of the filter increases since more ground paths are found. This situation is represented in Figure 5.4(b), where the valley at the center of the band is more pronounced as the order of the filter is increased.

5.2 Design Procedure for Ladder-type Filters

The design of a BAW resonator entails characterizing C_0 and f_a, which are directly related to the resonator's physical dimensions: On the one hand, like in any parallel plate capacitor $C_0 = \varepsilon_0 \varepsilon_r A/d_p$ is fulfilled, where A is the resonator area and d_p the piezoelectric thickness. On the other hand, the mechanical resonant frequency f_a is mainly determined by the piezoelectric thickness, but also by the thickness of the electrodes [20, 123]. In a first approach, we are considering the electrode thickness to be infinitesimal. In this case, the piezoelectric thickness corresponds to a half acoustic wavelength and the electromechanical coupling coefficient is given by the intrinsic k_t^2.

In this section the design procedure developed in [76] will be described. The specifications of the filter are: the bandwidth Bw_c, the Out-of-Band (OoB) rejection and the allocation of the lower and upper transmission zeros f_0^L, f_0^U. One of the difficulties in the design of such a filter arises from the dependence of the bandwidth of the filter $B_{w(-3dB)}$ on the order N as seen in Figure 5.4(b). Thus, for the sake of simplicity of the design procedure, Bw_c is defined as the frequency difference given by the frequency points where the electrical input impedance for the series and shunt resonators are equal, that is $|Z^s(f_i)| = |Z^p(f_i)|$ for $i = 1, 2$, which is not dependent on the order of the filter N. Taking into account the previous considerations, the design procedure can be summarized in the following steps:

1. **Determine $\mathbf{f_a^S}$ and $\mathbf{f_r^P}$.** As seen in Figure 5.3, it is straightforward to state that $f_a^S = f_0^U$ and $f_r^P = f_0^L$, where the S and P upper scripts are referred to the series and shunt resonators, and L and U are referred to the lower and upper transmission zeros.

2. **Determine $\mathbf{f_r^S}$ and $\mathbf{f_a^P}$.** The frequency difference between the resonance and antiresonance frequency is given by the electromechanical coupling factor as it was discussed in Chapter 2. In this case, we are considering infinitesimal electrode thickness, leading to the electromechanical coupling constant being expressed as,

$$k_t^2 = \frac{\pi^2}{4}\left(\frac{f_r}{f_a}\right)\left(\frac{f_a - f_r}{f_a}\right) \tag{5.1}$$

   Using the definition for the electromechanical coupling constant, which is an inherent property of the piezoelectric material, both frequencies can be obtained for each resonator since k_t is known. However, in order to obtain a reasonable bandwidth it must be accomplished that $f_r^S \geq f_a^P$. This condition can be directly related with the transmission zeros, which must fulfill,

$$f_0^U \geq \left(\frac{\pi}{2k_t}\right)^2 \left(\frac{\pi - \sqrt{\pi^2 - 16k_t^2}}{\pi + \sqrt{\pi^2 - 16k_t^2}}\right) f_0^L \tag{5.2}$$

3. **Determine the capacitance ratio $\mathbf{\Psi = C_0^S/C_0^P}$.** The definition given for the bandwidth depends on the resonant frequencies and the static capacitances of both series and shunt resonators. As a result, using the next approximation for the electrical input impedance of the BAW resonator,

$$Z(f) = \frac{1}{j2\pi f C_0}\left(\frac{f^2 - f_r^2}{f^2 - f_a^2}\right) \tag{5.3}$$

   the capacitance ratio can be expressed as,

$$\Psi = \frac{C_0^S}{C_0^P} = \frac{-f_i^4 + f_i^2 f_a^{P^2} + f_i^2 f_r^{S^2} - f_r^{S^2} f_a^{P^2}}{f_i^4 - f_i^2 f_a^{S^2} - f_i^2 f_r^{P^2} + f_a^{S^2} f_r^{P^2}} \tag{5.4}$$

   where f_i can be either f_1 or f_2 since, in this case, it has been considered that both frequencies are considered symmetrically spaced around the central frequency of the filter bandpass f_0. Therefore, $f_1 = f_0 - Bw_c/2$ and $f_2 = f_0 + Bw_c/2$. It is also important to point out that in order to obtain values for $\Psi > 0$, the Bw_c must fulfill,

$$f_0 - f_a^P < \frac{Bw_c}{2} < f_0 - f_r^P \tag{5.5}$$

4. **Determine the capacitance product $\mathbf{\Theta = C_0^S C_0^P}$.** In the previous step the capacitance ratio was ascertained. However, another equation is needed in order to obtain the static capacitances of both series and shunt resonators. The required equation comes from the image impedance matching condition [79], which relates the input and output impedances,

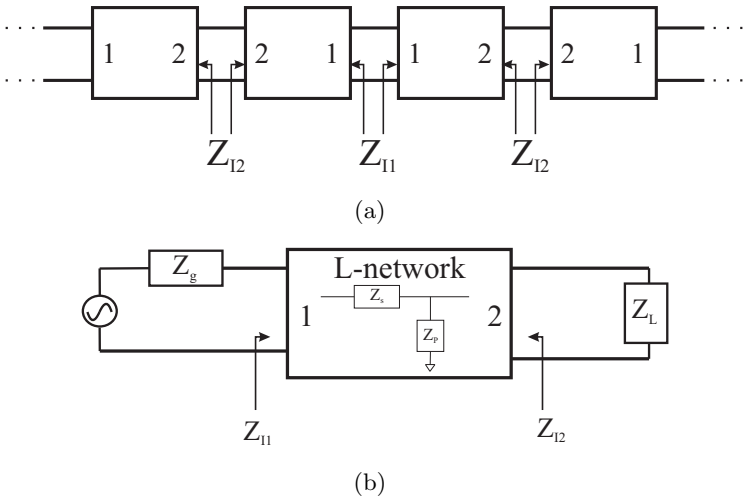

Figure 5.5: (a) Periodic structure composed by N L-networks. (b) L-Network with the terminations which must be matched to Z_{I1} and Z_{I2}

in a network composed of a series of cascaded sub-networks, with the source and load impedances.

Figure 5.5(a) shows the cascade of N L-networks so that at each junction either port 1 or port 2 are connected together. All the composing networks are therefore perfectly matched. The impedances Z_{I1} and Z_{I2} are the so-called image impedances. Figure 5.5(b) shows a single network with the corresponding terminations Z_g and Z_L at the input and output ports. The image impedances for the L-network are defined as,

$$\begin{aligned} Z_{I1} &= \sqrt{Z_S\left(Z_S + Z_P\right)} \\ Z_{I2} &= \frac{Z_S Z_P}{\sqrt{Z_S(Z_S+Z_P)}} \end{aligned} \tag{5.6}$$

To have transmission between input and output ports requires $Z_{I1} = Z_g$ and $Z_{I2} = Z_L$. At the same time $Z_g = Z_L = Z_0$ leading to obtain the needed product capacitances equation required in the design procedure,

$$C_0^S C_0^P = \frac{1}{\left(2\pi f_0 Z_0\right)^2} \tag{5.7}$$

At this point it is straightforward to compute the values for C_0^S and C_0^P. It must to be pointed out that the asymmetry in the L-network makes $Z_{I1} \neq Z_{I2}$, what give cause to a certain mismatch losses at the center of the band f_0 as it was briefly discussed in the introduction section.

5. **Determine the order of the filter N**. The Ladder-type filter behaves as an out-of-band ladder of capacitances, with the rejection decreasing slowly as the frequency moves away from the central frequency of the filter f_0. The achievable level of attenuation will

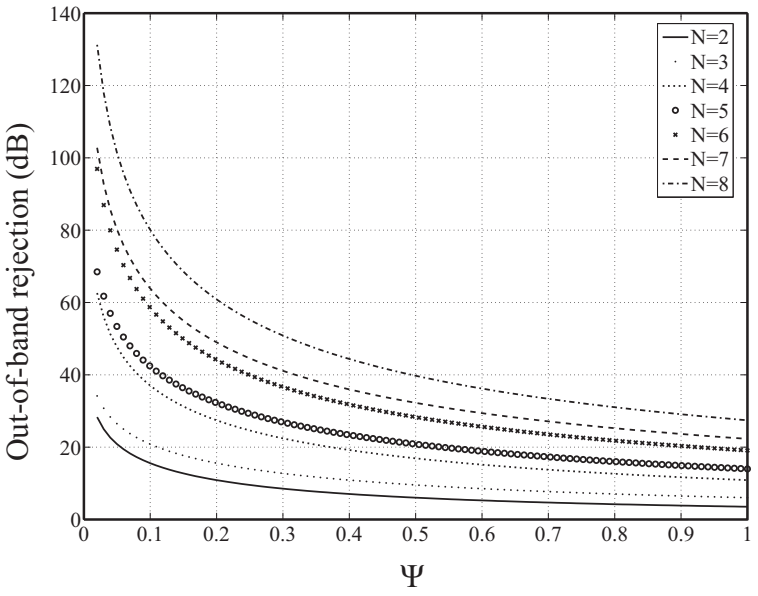

Figure 5.6: Out-of-Band rejection depending on the capacitance ratio Ψ for a given order of the filter N.

Table 5.1: GSM filter specifications.

Bandwidth [MHz]	28.2
Lower transmission zero [MHz]	924
Upper transmission zero [MHz]	976.4
Out-of-band rejection [dB]	35

depend on the capacitance ratio Ψ and the order of the filter N. Once the capacitance ratio has been chosen in order to fulfill the specified Bw_c, only the order of the filter N can be set to achieve the specified OoB rejection. Figure 5.6 shows the out-of-band rejection as a function of Ψ for a given value of N. By one hand, it can be seen that as the order is increased, the OoB rejection is improved, while for a given order of the filter N, as the value of the bandwidth is increased, that is, the value of the capacitance ratio Ψ is increased, the out-of-band rejection becomes lower. Thus, in order to achieve a high out-of-band rejection, the static capacitance C_0^S is desired to be lower than C_0^P.

Design example

In order to validate the proposed design procedure, a ladder-type filter has been designed to fulfill the GSM specifications and compared with the work in [86]. The specifications are listed in Table 5.1. The values obtained for the static capacitances of the series and shunt resonators and

Table 5.2: Values obtained with the design procedure.

Parameter	Series BAW	Shunt BAW
C_0	2.016 pF	5.571 pF
f_r	955 MHz	924 MHz
f_a	976.4 MHz	944.7 MHz

the resonant frequencies for each are listed in Table 5.2. The order of the filter in order to fulfill the out-of-band rejection requirement must be $N = 6$ using the curves in Figure 5.6. Figure 5.7 shows the transmission response of the designed filter and the electrical input impedance of the series and shunt BAW resonators making up this structure. The value for the out-of-band rejection corresponds to the expected value, that is OoB$\simeq$-35 dB. The ripple appearing in the center of the transmission band comes from the topology itself and the non-fulfilment of the image impedance matching condition. In the case under study $Z_{I1} = 52.3\ \Omega$ and $Z_{I2} = 47.5\ \Omega$ at f_0.

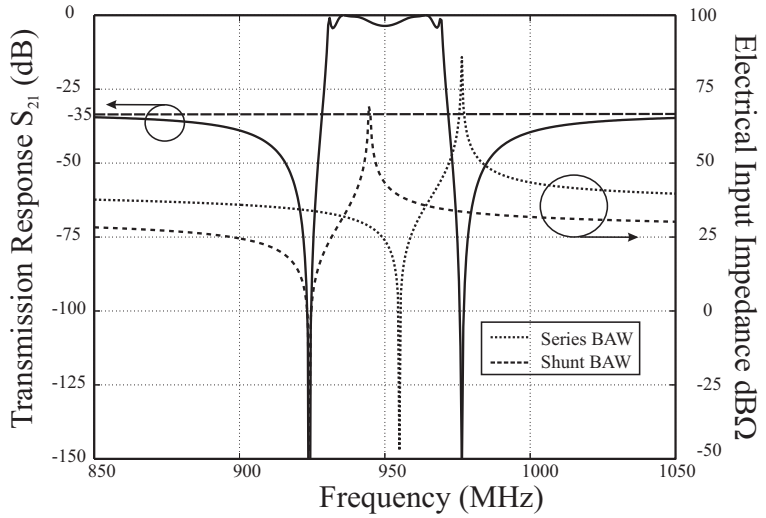

Figure 5.7: Designed ladder-type filter for GSM specifications with order $N = 6$.

In the presented design procedure, the thickness of the electrodes has been considered to be infinitesimal. Thus, from the antiresonance frequency the thickness of the piezoelectric layer can be obtained. However, in a real case, the metal electrodes are also present. In this case, the design procedure only requires to use k^2_{eff} instead of k^2_t. The problem is that we are not able to know a priori the value of k^2_{eff} since it depends on the thickness of piezoelectric and metal electrodes. In order to overcome this, we propose an iterative method. First, the previously developed design procedure is applied using k^2_t. Once the output parameters are obtained, the electrode thickness is fixed and then the piezoelectric thickness can be calculated which give rise

to a new resonance frequency f_r, and thus, a new value of k^2_{eff}. Then, using the new value of k^2_{eff} the design procedure must be again carried out in an iterative way until the convergence between the obtained values of k^2_{eff} is achieved.

5.2.1 Effect of the electrodes in the design procedure of ladder-type filters

In this section, the iterative method to include the effect of the electrodes in the design procedure discussed in the previous section is given. When the metal electrodes are considered to have a certain thickness, k^2_t becomes k^2_{eff} due to the mass loading effect. In this case, the value of the piezoelectric layer can be determined using the following equation, which is derived from the analytical expression of the lossless input electrical impedance of a BAW resonator applying the condition that at frequency f_a this tends to infinity [20, 123]:

$$(z_1 + z_2)\cos\gamma + j(1 + z_1 z_2)\sin\gamma = 0, \tag{5.8}$$

where $\gamma = 2\pi f_a d_p/v_p$, and $z_1 = Z_1/Z_p$ and $z_2 = Z_2/Z_p$ are the lossless input acoustic impedances at frequency f_a looking into the top and bottom of piezoelectric boundaries that are normalized to the piezoelectric characteristic impedance. The impedances Z_1 and Z_2 can easily be obtained by modelling the single or multi-layer electrodes as acoustic transmission lines [123]. It should be noted that Z_1 and Z_2 are always purely imaginary numbers since it is assumed that both electrodes are acoustically short-circuited [75].

Once the resonator has been designed, it is important to ascertain its effective coupling coefficient k^2_{eff}. To do so, it is necessary to determine the frequency f_r. This can be determined using the following equation, which is derived from the analytical expression of the lossless input electrical impedance applying the condition that at frequency f_r this tends to zero [20, 123]:

$$\cos\gamma + j\left(\frac{1 + z_1 z_2}{z_1 + z_2}\right)\sin\gamma = \frac{k^2_t}{\gamma}\left(\sin\gamma + 2j\frac{1 - \cos\gamma}{z_1 + z_2}\right), \tag{5.9}$$

where $\gamma = 2\pi f_r d_p/v_p$, and $z_1 = Z_1/Z_p$ and $z_2 = Z_2/Z_p$ are the lossless input acoustic impedances at frequency f_r looking at the top and bottom of piezoelectric boundaries that are normalized to the piezoelectric characteristic impedance. As in the previous case Z_1 and Z_2 are always purely imaginary numbers. Once the frequency f_r has been determined, it is straightforward to obtain k^2_{eff} by applying that,

$$k^2_{eff} = \frac{\pi^2}{4}\left(\frac{f_r}{f_a}\right)\left(\frac{f_a - f_r}{f_a}\right). \tag{5.10}$$

The design procedure discussed in the previous section is based on a series of closed-form expressions that make possible, without any optimization work, to relate the number of resonators N and the characteristics of series (f^s_a, C^s_0) and shunt (f^p_a, C^p_0) resonators with the desired filter specifications: Bandwidth, out-of-band rejection, and frequency allocation of the

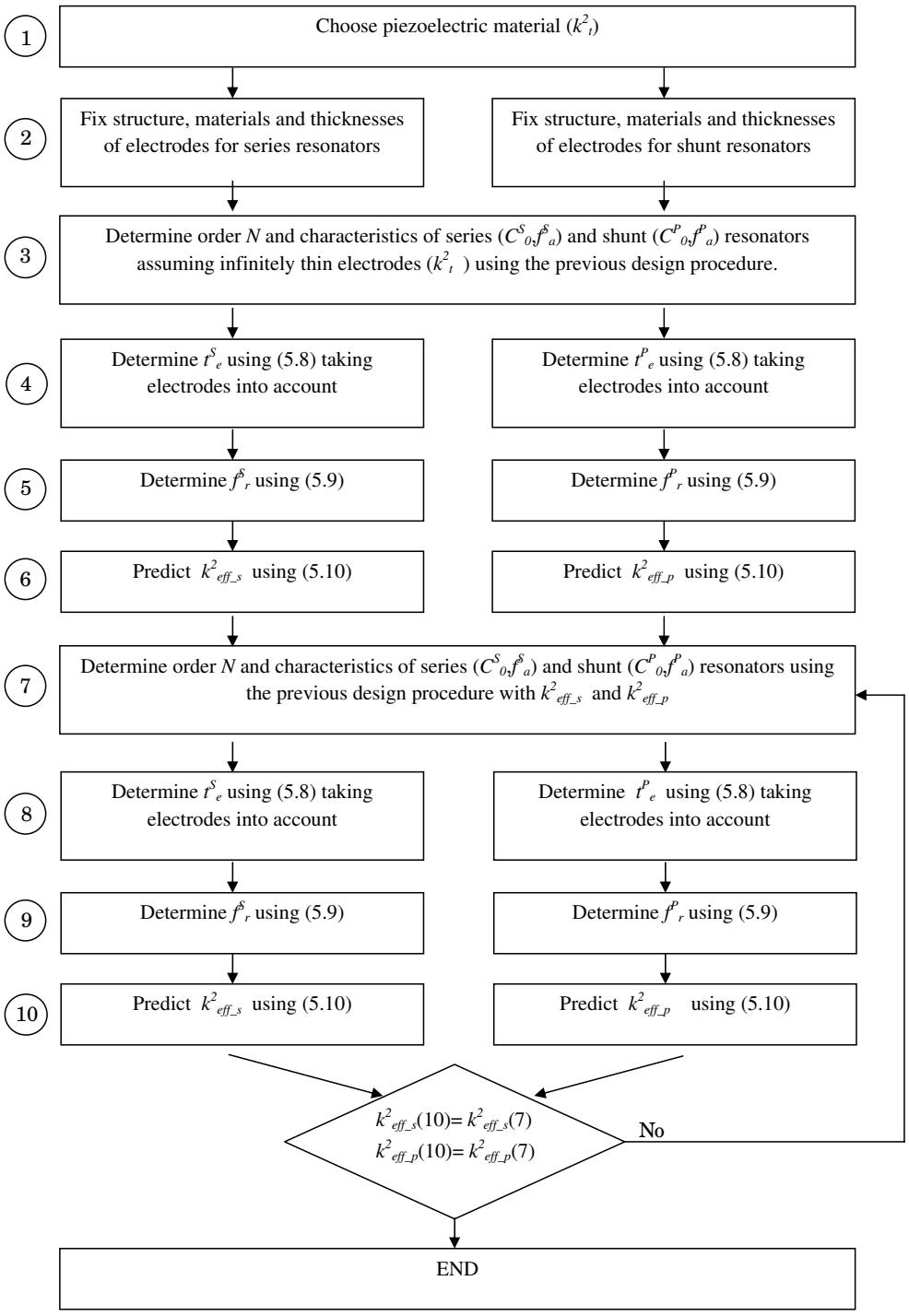

Figure 5.8: Flowchart of the proposed design procedure.

upper and lower transmission zeros. The limitation of this design methodology is that infinitely thin electrodes are assumed. In order to take the thickness of the electrodes into account the coupling coefficient of the piezoelectric material k_t^2 must be replaced by the effective coupling coefficient k_{eff}^2 in the closed-form expressions presented in the previous section. The drawback is that k_t^2 only depends on the piezoelectric properties and can be obtained from the inherent piezoelectric parameters,

$$k_t^2 = \frac{e^2}{Z_p \epsilon_0 \epsilon_r v_p} \tag{5.11}$$

However, k_{eff}^2 is not, a priori, known since it not only depends on the piezoelectric properties but also on the properties of the electrodes and the electrode-to-piezoelectric thickness ratio [123]. To overcome this obstacle, the following design procedure, the flowchart of which is shown in Figure 5.8, must be used:

1. Decide on piezoelectric material and calculate its intrinsic coupling coefficient k_t^2 using (5.11).

2. Decide on structure (single or multi-layer) of the electrodes and set their materials and thickness for both series and shunt resonators.

3. Determine the order N and the characteristics of series (f_a^s, C_0^s) and shunt (f_a^p, C_0^p) resonators assuming infinitely thin electrodes using the design methodology presented in section 5.2.

4. Determine, from (5.8), the piezoelectric thickness for each type of resonator taking electrodes into account in order to obtain the frequencies f_a calculated in the previous step.

5. Determine the frequencies f_r for the designed series and shunt resonators using (5.9).

6. Predict k_{eff}^2 for each type of resonator using (5.10). It should be noted that k_{eff}^2 of the series resonators will be different to k_{eff}^2 of the shunt resonators, and in general both will be different from k_t^2 and therefore the results obtained in step 3 are not accurate.

7. Repeat step 3 but now replacing k_t^2 with the predicted effective coupling coefficients.

8. Repeat steps 4, 5 and 6. If the predicted effective coupling coefficients in step 10 are not the same as those used in step 7 then steps 7-10 must be repeated but now using in step 7 the predicted effective coupling coefficients obtained in step 10. It should be noted that in each iteration the predicted effective coupling coefficients obtained in step 10 will tend towards those in step 7. In general, carrying out steps 7-10 once is enough to obtain a difference of less than 0.1%. When the predicted effective coupling coefficients are close enough to those used in step 7 then the procedure is complete and the filter is designed since the thickness

of the electrodes for the series and shunt resonators was set in step 2, the piezoelectric thickness for each type of resonator was determined in step 8, and finally the area for each type of resonator is obtained by applying the corresponding piezoelectric thickness and static capacitance between electrodes, determined in step 7, in $A = C_0 d_p / \varepsilon_0 \varepsilon_r$.

In order to validate the procedure presented we will use the work published by other authors. The drawback is that the most of the published and manufactured ladder filters were designed by means of an optimization process and therefore, in general, all the resonators are different. Moreover, this optimization usually entails the inclusion of additional lumped elements such as inductors [86, 124]. In [125] several ladder BAW filters without additional elements and with all series resonators equal, and all shunt resonators also equal to each other are presented. The only difference between the presented filters is the order N. Table 5.3 shows the different layers, materials, thicknesses and areas for the series (S) and shunt (P) resonators of these filters.

Table 5.4 shows the properties of the different materials. The aim is to design one of these filters using the presented procedure. We assume that electrodes are composed as shown in Table 5.3, and therefore that design consists of determining the order N and specially the piezoelectric thickness and the area of each type of resonator from the filter specifications. For our purpose the filter order is secondary, as a result of the different orders presented in [125] we have chosen a single-stage ladder filter ($N = 2$), the specifications of which are shown in Table 5.5.

Table 5.6 shows the designed piezoelectric thickness d_p and area A of each type of resonator after applying the presented design procedure. This table also shows the results obtained in each step. The excellent performance of the procedure presented is demonstrated by comparing the designed piezoelectric thicknesses and areas with the original ones (Table 5.3). We could remark that the order is also perfectly determined, but as mentioned earlier this is secondary in this section. The transmission response of the designed filter is shown in Figure 5.9. This has been obtained using the well-known Mason Model implemented in a commercial microwave design simulator (Advanced Design System) [45].

Table 5.3: Characteristics of series and shunt resonators.

Layer	Material	Thickness [nm]	Area [μm$\times\mu$m]
Top electrode	Mo	308	Series Resonators
Piezoelectric	ZnO	2147	225×225
Bottom electrode 1	Mo	308	Shunt Resonators
Bottom electrode 2	SiO_2	90(S)/360(P)	352×352

Table 5.4: Material properties.

	Z [10^7 Ns/m^3]	v [m/s]	e [C/m^2]	ε_r
ZnO	3.61	6370	1.32	10.2
Mo	6.56	6408	NA	NA
SiO_2	1.31	5270	NA	NA

Table 5.5: Filter specifications.

Bandwidth [MHz]	38.4
Lower transmission zero [MHz]	917.4
Upper transmission zero [MHz]	987.4
Out-of-band rejection [dB]	6.5

Table 5.6: Predicted results using the design procedure.

Step	Series Resonator	Shunt Resonator
1	$k_t^2 = 8.393\%$	$k_t^2 = 8.393\%$
3	$f_a = 987.400$ MHz	$f_a = 950.932$ MHz
	$C_0 = 2.225$ pF	$C_0 = 5.027$ pF
4	$d_p = 2146.984$ nm	$d_p = 2164.710$ nm
5	$f_r = 947.068$ MHz	$f_r = 912.327$ MHz
6	$k_{eff}^2 = 9.666\%$	$k_{eff}^2 = 9.610\%$
7	$f_a = 987.400$ MHz	$f_a = 956.219$ MHz
	$C_0 = 2.149$ pF	$C_0 = 5.205$ pF
8	$d_p = 2146.984$ nm	$d_p = 2147.006$ nm
9	$f_r = 947.068$ MHz	$f_r = 917.404$ MHz
10	$k_{eff}^2 = 9.666\%$	$k_{eff}^2 = 9.609\%$
d_p [nm]	2146.984	2147.006
A [μm$\times\mu$m]	226.083 $\times$ 226.083	351.839 $\times$ 351.839

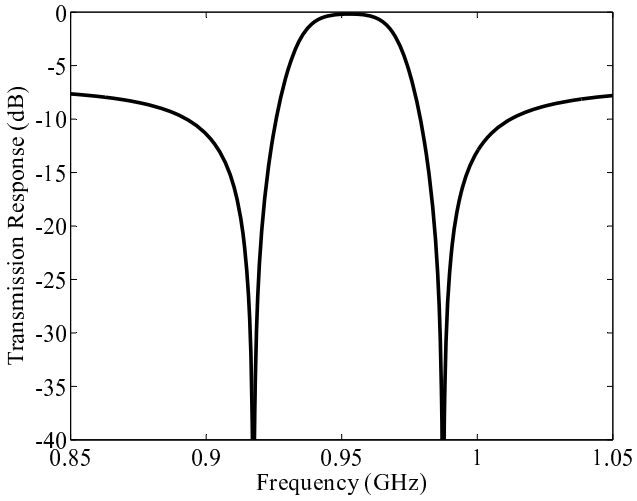

Figure 5.9: Transmission response of the designed filter [87].

5.3 Improvement of the Performance of Ladder-type Filters by Including External Reactive Elements

At this point, the closed-form expressions for the design of ladder-type filters have been developed. The proposed methodology has also been modified in order to take into account the effect of the electrodes that were supposed to be infinitesimal in a first approach.

As discussed in previous sections, ladder-type filters present a poor out-of-band rejection. In order to overcome this limitation, we propose including external reactive elements in this section. First of all, the performance of the single BAW resonators when reactive elements (inductances and capacitors) are included will be analyzed. On this basis, the modified BAW resonators will be applied to the ladder-type filter configuration in order to improve the performance of the filter.

5.3.1 Modification of a BAW resonator by including external reactive elements

The resonance and antiresonance frequencies in a BAW resonator are determined by the motional arm in the BVD equivalent circuit and the effective electromechanical coupling constant. In this section, the electrical performance of the conventional BAW resonator will be modified by including external reactive elements (inductance and capacitance). Depending on the configuration, the allocation of the resonant frequencies can therefore be modified which can be useful in some applications. Thus, in this section the four different possibilities found in Figure 5.10 will be studied. For the analysis of each configuration, a ZnO-BAW resonator with $f_r = 955$ MHz

and $f_a = 976.4$ MHz has been used to analyze each configuration. First of all, the analysis of the input electrical impedance will be analyzed. Therefore, using the obtained closed expressions, the tunability range of the resonant frequencies depending on the value of the reactive element will be exhibited.

Inductance in shunt configuration

The proposed topology when the inductance is included in shunt configuration is shown in Figure 5.10(a). The electrical input impedance of the proposed circuit can be calculated which results in,

$$Z(f) = \frac{\frac{1}{j2\pi f C_o}\left(\frac{f^2-f_r^2}{f^2-f_a^2}\right) j2\pi f L_{tun}}{\frac{1}{j2\pi f C_o}\left(\frac{f^2-f_r^2}{f^2-f_a^2}\right) + j2\pi f L_{tun}} = \frac{j2\pi f L_{tun}\left(f^2-f_r^2\right)}{f^2-f_r^2-4\pi^2 f^4 L_{tun}C_o + 4\pi^2 f^2 f_a^2 L_{tun}C_o} \tag{5.12}$$

where L_{tun} corresponds to the external inductance included. In this case, the resonance frequency f_r of the modified resonator remains at its original value. Therefore, the included inductance will affect to the allocation of the antiresonance frequency. For our purposes, we can express the value of the included inductor as having the antiresonance frequency in a desired allocation. This results in,

$$L_{tun} = \frac{f_r^2 - f_d^2}{4\pi^2 C_o f_d^2\left(f_a^2 - f_d^2\right)} \tag{5.13}$$

where f_a and f_r are the resonant frequencies of the BAW resonator, and f_d is the desired allocation of the new antiresonance frequency.

Figure 5.11 shows the dependence of the new antiresonance frequency as a function of the external inductance L_{tun}. It can be seen that for high values of this inductance, the value for f_a' tends to its original value f_a since the reactance is very high. Meanwhile, the tuning over the antiresonance frequency is almost 100% for a difference of 20 nH in the value of the external inductance.

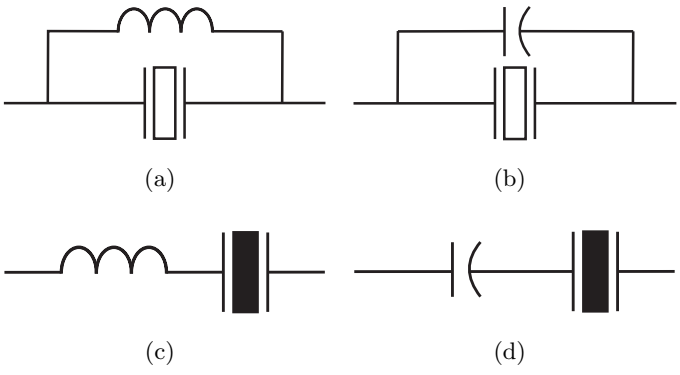

Figure 5.10: Different configurations using reactive elements.

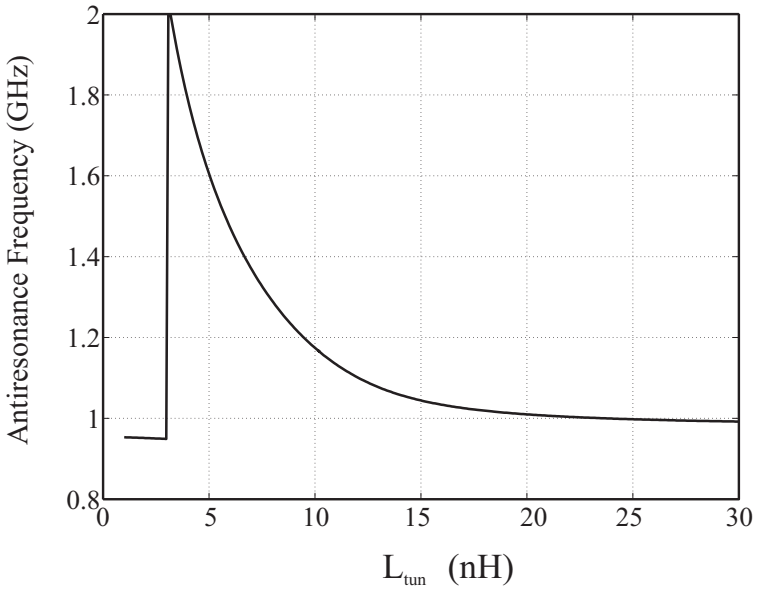

Figure 5.11: Dependence of the antiresonance frequency as a function of the value of the external inductance L_{tun}.

Capacitance in shunt configuration

If an external capacitance C_{tun} is placed in shunt configuration with the BAW resonator as shown in Figure 5.10(b), the total electrical input impedance is then,

$$Z(f) = \frac{\frac{1}{j2\pi f C_o}\left(\frac{f^2-f_r^2}{f^2-f_a^2}\right)\frac{1}{j2\pi f C_{tun}}}{\frac{1}{j2\pi f C_o}\left(\frac{f^2-f_r^2}{f^2-f_a^2}\right)+\frac{1}{j2\pi f C_{tun}}} = \frac{\left(f_r^2-f^2\right)}{j2\pi f\left(C_{tun}\left(f_r^2-f^2\right)+C_o\left(f_a^2-f^2\right)\right)} \tag{5.14}$$

In this case, it can be seen that the value of the resonance frequency remains at its original value, while the allocation of the antiresonance frequency is affected by the capacitance. In this case, as it has been done in the previous configuration, we can express the value of C_{tun} required to allocate the new antiresonance frequency in the desired position,

$$C_{tun} = C_o \frac{f_d^2 - f_a^2}{f_r^2 - f_d^2} \tag{5.15}$$

Figure 5.12 shows the dependence of the antiresonance frequency as a function of the value of the external capacitance C_{tun}. As expected, for a low values of the capacitance, the value of the antiresonance remains at its original value, since the capacitance behaves as an open circuit. As C_{tun} moves to higher values, the antiresonance frequency tends to lower values. However, it must be taken into account that in this case, unlike the case with the inductance, the range of tunability in the antiresonance frequency is low.

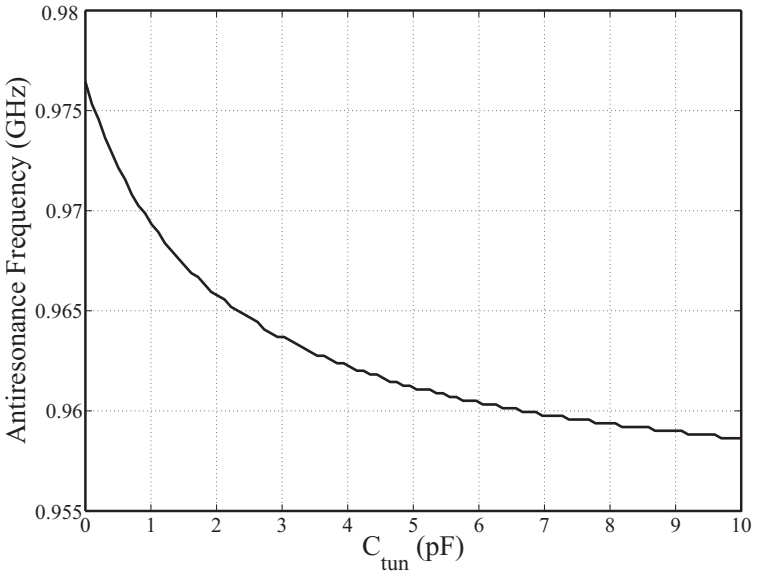

Figure 5.12: Dependence of the antiresonance frequency as a function of the value of the external capacitance C_{tun}.

Inductance in series configuration

The total impedance for the configuration in 5.10(c) can be computed resulting in,

$$Z(f) = \frac{1}{j2\pi f C_0}\frac{f^2 - f_r^2}{f^2 - f_a^2} + j2\pi f L_{tun} \Rightarrow Z(f) = \frac{f^2 - f_r^2 - 4\pi^2 f^2 L_{tun} C_0 (f^2 + f_a^2)}{j2\pi f C_0 (f^2 - f_a^2)} \tag{5.16}$$

When the resulting impedance is analyzed, it can be concluded that the antiresonance frequency will occur for $f = f_a$, i.e. for the natural antiresonance frequency, while the resonance frequency will depend on the value of the inductance L_{tun}. However, for the purposes of this study, it is preferable to obtain the value of the inductance for a given desired frequency. When looking for the new resonance values, we therefore also obtain the equation in (5.13). In this case, Figure 5.13 shows the dependence between the new resonance frequency f_r' compared the value of the external inductance L_{tun}. As expected, for lower values of L_{tun}, the new resonance frequency f_r' tends to its original position at f_r. In this case, as in the previous case, a wide range of values for f_r' can be achieved by small variations in L_{tun}.

Capacitance in series configuration

The last configuration corresponds to the one shown in Figure 5.10(d), where the external capacitance C_{tun} is placed in series with the BAW resonator. Thus, as the previous cases, analyzing the input electrical impedance we obtain,

$$Z\left(f\right) = \frac{1}{j2\pi f C_o}\left(\frac{f^2 - f_r^2}{f^2 - f_a^2}\right) + \frac{1}{j2\pi f C_{tun}} = \frac{C_{tun}\left(f_r^2 - f^2\right) + C_o\left(f_a^2 - f^2\right)}{j2\pi f C_o C_{tun}\left(f_a^2 - f^2\right)} \tag{5.17}$$

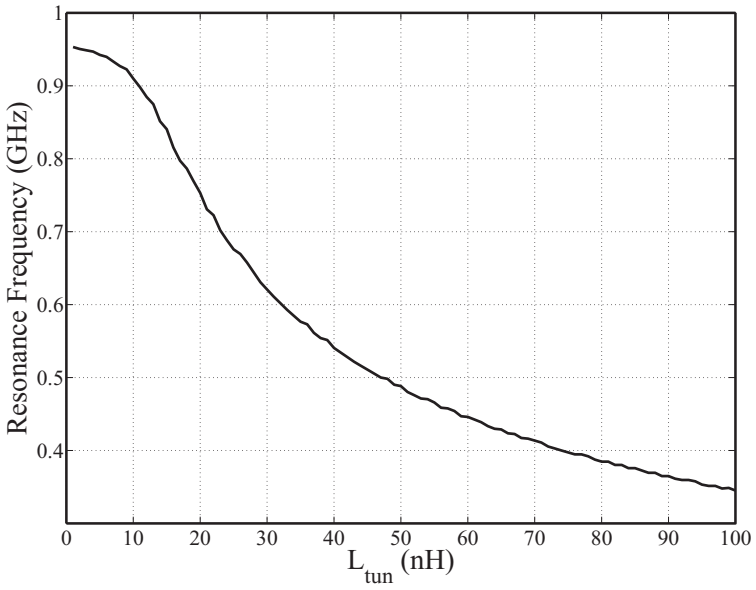

Figure 5.13: Dependence of the resonance frequency as a function of the value of the external inductance L_{tun}.

In this case, the antiresonance frequency f_a remains at the original value while the resonance frequency is modified by the action of the external capacitance C_{tun}. As with all the previous configurations, we can relate the value of C_{tun} with the desired new resonance frequency using,

$$C_{tun} = C_o \frac{f_d^2 - f_a^2}{f_r^2 - f_d^2} \tag{5.18}$$

Figure 5.14 shows the dependence of the resonance frequency as a function of the external capacitance C_{tun}. In this case, f_r' tends to its original value for high values of C_{tun} since in this situation, the capacitance behaves as a shortcircuit. As the capacitance assumes lower values, the resonance frequency tends to higher values. As it occurred in the configuration with the capacitance in shunt configuration, the range of tunability of the resonance frequency is not as high as the case with the inductance L_{tun}.

Table 5.7 shows the tends of the resonance and antiresonance frequency depending on the external reactive element and its configuration with the BAW resonator. It must to be also pointed out that, as it has been previously discussed, the inductance L_{tun} allows a higher tunability range of the resonance and antiresonance frequency than the capacitance C_{tun}. It can be seen that the inductance makes the resonance frequency to go to lower values, or the antiresonance frequency to shift to higher. Somehow, the inductance makes the effective electromechanical coupling constant to be increased.

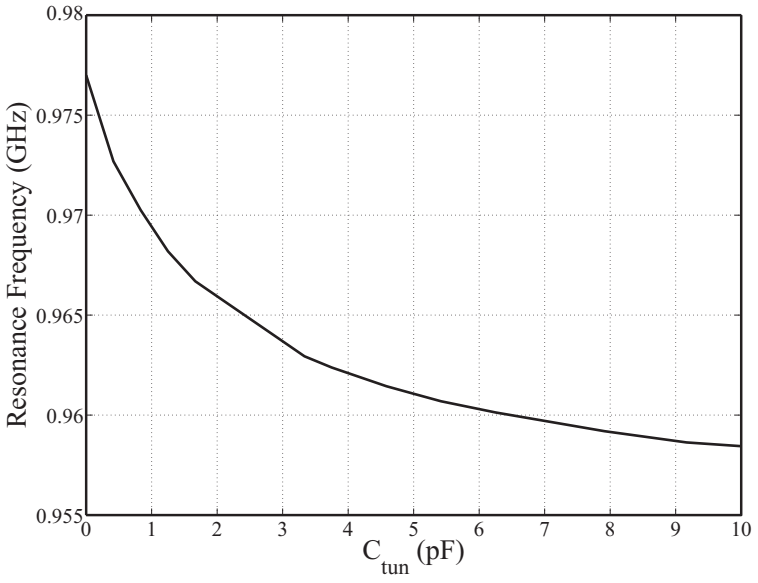

Figure 5.14: Dependence of the resonance frequency as a function of the value of the external capacitance C_{tun}.

Table 5.7: Resonance and antiresonance frequency tends of a modified BAW resonator with reactive elements.

Element	Configuration	Resonance Frequency	Antiresonance Frequency
Capacitance C_{tun}	Shunt (Figure 5.10(b))	$f_r' = f_r$	$f_a' < f_a$
	Series (Figure 5.10(d))	$f_r' > f_r$	$f_a' = f_a$
Inductance L_{tun}	Shunt (Figure 5.10(a))	$f_r' = f_r$	$f_a' > f_a$
	Series (Figure 5.10(c))	$f_r' < f_r$	$f_a' = f_a$

This solution was also discussed by Lakin in [75]. Taking this into account, in the next section, the presence of the external reactive element, mainly the inductance L_{tun}, will be used to introduce new transmission zeros in the frequency response of a ladder-filter which increases the out-of-band rejection.

5.3.2 Improvement of the performance of ladder-type filters using modified BAW resonators

The dependence of the out-of-band rejection on both the order of the filter N and the bandwidth Bw_c was discussed in the design procedure. Thus, for a given capacitance ratio, the OoB rejection will be given by the order of the filter, and if this is not fulfiled, N must be increased. However, a solution for improving the OoB rejection without increasing the order of the filter is discussed in this section. The solution consists of using the previous modified BAW resonators to modify the allocation of the transmission zeros. The idea is to use modified and non-modified BAW

resonators in the same topology. This will provide, two pairs of transmission zeros due to the modified and non-modified BAW resonators.

In order to validate the proposed solution, the conventional ladder-type filter for the GSM application shown in the previous section will be modified by means of the presence of a new pair of transmission zeros. The specifications for the GSM applications are shown in Table 5.1. The allocation for the new transmission zeros has been chosen at $f'_{0L} = 910$ and $f'_{0U} = 990$ MHz, which implies that $f'_r < f_r$ for the shunt, and $f'_a > f_a$ for the series resonators. Looking at Table 5.7, it can be seen that this is achieved by adding a series inductance in the first case, and a shunt inductance for the second case. The value of the inductors can be calculated using the expression in (5.13). In this case, we obtain $L_1 = 2.2$ nH and $L_2 = 32$ nH. At the same time, the position of the new transmission zeros are also a determinant parameter which influences the out-of-band rejection. Figure 5.15 shows the comparison of the transmission response of the conventional ladder-type filter with $N = 6$, the proposed modified filter with the transmission zeros at 910 and 990 MHz, and an optimized configuration in terms of the allocation of the new transmission zeros.

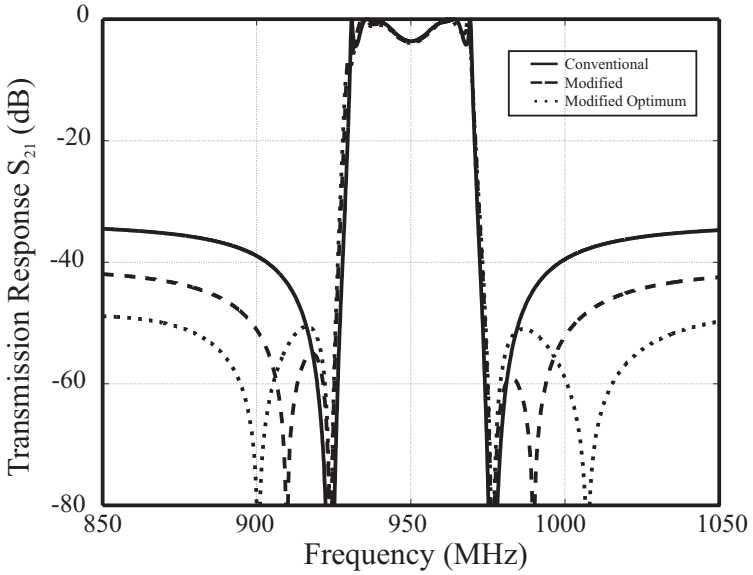

Figure 5.15: Comparison between the conventional ladder-type filter with $N = 6$ (solid line), the non-optimized modified (dashed line) and the modified optimized filter (dotted line).

Introducing the new pair of transmission zeros causes an OoB rejection improvement of about 7 dB, whereas the allocation of the original transmission zeros is not modified, and the filter bandpass is not significantly affected. As mentioned above, the allocation of the new pair of transmission zeros affects the OoB rejection. Here, there is a trade-off since as the distance between the original and new transmission zeros is increased, the minimum rejection between the two zeros is decreased but the OoB rejection is increased. There is therefore an optimum

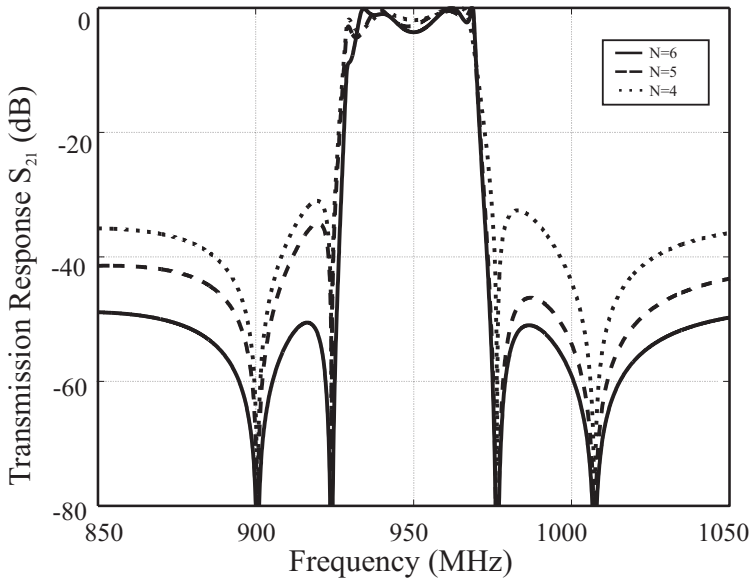

Figure 5.16: Comparison between the modified ladder-type filter with $N = 6$ (solid line), $N = 5$ (dashed line) and $N = 4$ (dotted line).

allocation of the new transmission zeros, and this occurs when the OoB rejection is the same as the minimum rejection between the new and original transmission zeros. In our case, the optimum situation occurs when the new transmission zeros are placed at $f'_{0L} = 901$ MHz ($L_1 = 20.5$ nH) and $f'_{0U} = 1008$ MHz ($L_2 = 2.9$ nH). In this case, the OoB rejection improvement as regards the conventional ladder-type filter is about 15 dB, as shown in Figure 5.15. These results suggest that it is possible to continue to fulfil the required rejection specification shown in Table 5.1 with a lower order.

Using the optimum configuration, if the last shunt resonator is eliminated, then the lossless transmission response shown in Figure 5.16 is obtained being $N = 5$. Compared to the transmission response with six resonators, it can be seen that neither the allocation of the original and new transmission zeros nor the filter bandpass is substantially modified. However, since the filter order is decreased, then the rejection -both OoB and between zeros- is also decreased but continues to fulfill the rejection specification shown in Table 5.1. It is important to point out that this transmission response is more asymmetrical due to the fact the number of series resonators is greater than shunt resonators. Naturally, as series resonators affect to the upper transmission zeros then the rejection in this band is higher than the rejection in the low band. Finally, for a $N = 4$ order filter, then the rejection between zeros does not fulfil the specifications in 4 dB as shown in Figure 5.16.

As seen above, by modifying the conventional ladder-type filter structure it is possible to increase the OoB rejection, which entails a possible reduction in number of resonators in order to fulfil the required specifications. However, this is achieved by introducing a pair of reactive ele-

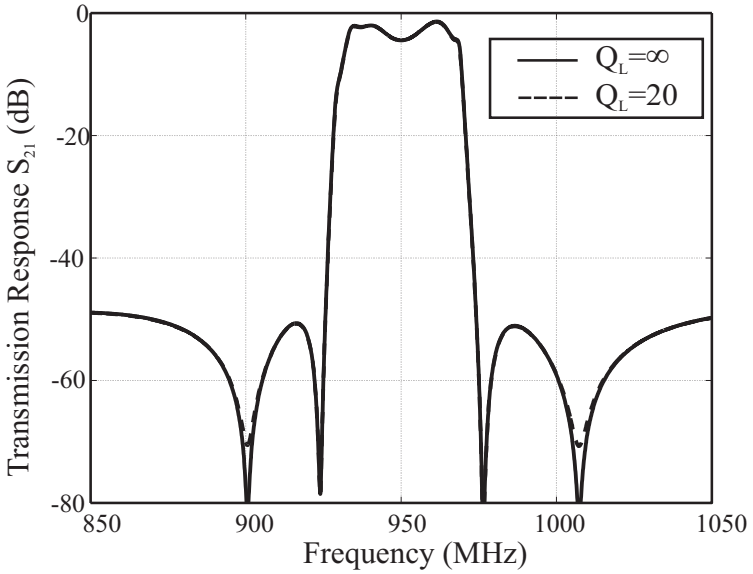

Figure 5.17: Comparison between the modified ladder-type filter with $N = 6$ and $Q = 1000$ considering an inductor with infinite quality factor (solid line) and $Q = 20$ (dashed line)

ments - inductors in this case - with a quality factor that is much lower than the BAW resonator quality factor [126].A priori, these new elements should therefore considerably increase the filter insertion loss. Using the optimum configuration with six resonators, the lossless transmission response of which is shown both in Figure 5.15 and Figure 5.16, various simulations have been performed taking losses into account in the form of a finite value for the quality factor Q. In Figure 5.17 the transmission response, only taking the losses for BAW resonators (Q = 1000 [85]) into account, is compared to the transmission response, considering account the losses both for resonators and inductors (Q = 20 [126]). This figure shows that the low quality factor of the reactive elements only significantly affects the bandwidth of the new pair of transmission zeros, since this is increased. The reason why the high losses of a reactive element only affect the bandwidth of the corresponding new transmission zero and not the filter insertion loss is because this only modifies one of the previously defined resonance frequencies, as shown in Table 5.7. In the configurations studied - a reactive element in series with a shunt resonator or in shunt with a series resonator - the high losses of the reactive element only reduce the quality factor of either the resonance frequency of the modified shunt resonator or the anti-resonance frequency of the modified series resonator, and these frequencies are directly related to the allocation of the new transmission zeros. Finally, it is possible to add more than one pair of new transmission zeros, or to modify more than just one series resonator and one shunt resonator, without increasing the filter insertion loss significantly.

5.4 Chapter Summary

Ladder-type filters are one of the most straightforward topologies that can be implemented due to their simplicity. The common topology is composed of consecutive series and shunt resonators. This type of filter presents a very high selectivity due to the presence of a pair of transmission zeros or notches, but also has a poor out-of-band rejection.

This chapter has considered the design procedure for designing ladder-type filters. The specifications of these filters are the allocation of the transmission zeros, the bandwidth B_{wc}, defined as the frequency distance in which the electric impedance of series and shunt resonators is equal, and the out-of-band rejection. Taking these considerations into account, the closed-form expressions for the design of this filter are revealed. However, the effect of the electrodes is not taken into account in an initial approach. The proposed design procedure is therefore modified slightly in order to incorporate these effects.

As discussed above, one of the limitations of ladder-type filters is their poor out-of-band rejection. In order to overcome this limitation, in this chapter, we propose modifying the BAW resonators in terms of the allocation of the resonant frequencies using reactive elements. The four possible configurations using inductances and capacitors have been discussed. To achieve this, the input electrical impedance is obtained by considering the value of the external reactive element. We thus obtain a closed-form expression that relates the new allocation of the resonance or antiresonance frequency, depending on the configuration, with the value of the included reactive element.

Finally, we have used the modified BAW resonators in a ladder-type filter topology. Having both types of resonators in the topology - modified and non-modified - means that the filter response presents a new pair of transmission zeros which leads to a better out-of-band rejection. The order of the filter can therefore be decreased for a certain out-of-band rejection specification. Note that increasing the order of the filter entails more insertion losses.

CHAPTER 6

Dual-Band Filter Based on Bulk Acoustic Wave Resonators

The growth of wireless communications applications in the recent past requires the design of more efficient equipment and devices, but multi-frequency receivers are also required, as is the case with positioning systems. In order to reduce the size of this equipment, the various devices which are contained inside this equipment must also have a dual-band behaviour. Since devices based on BAW resonators are becoming consolidated in these applications, filters based on BAW resonators exhibiting a dual-band response are therefore required. It must be also taken into account that the dual-band filter can also be incorporated in systems with different bandpass filters, with the corresponding size reduction and improvement in performance, since no external elements are needed for the connection between single-band filters.

As an example of the expected developed multi-standard applications, in 2006 the European project MOBILIS[1] was launched. One of the objectives of the project was to try to develop and implement a multi-standard transmitter architecture based on digital RF signal generation, use of BAW filters and BAW duplexers for the DCS/UMTS applications.

In this chapter, we present a configuration based on the conventional ladder-type filter, which is called the double-ladder type filter. It achieves a dual-band transmission response in which each bandpass is allocated to the desired frequencies. Initially, there are no restrictions on the frequency separation between transmission bands; however, as discussed below, high frequency separation could lead to degradation of the filter's performance. The procedure for designing dual-band filters based on BAW resonators using the double ladder topology will therefore be extensively discussed in this chapter. The design strategy is based on the strategy discussed for conventional ladder-type filters.

[1] www.ist-mobilis.org

6.1 Introduction

The rapid development of wireless communication equipment at microwave frequencies require the design and production of high quality miniature devices with efficient use of more and more frequency channels. Multi-bandpass components (antennas, amplifiers and filters) have been developed to reduce the volume and weight of these devices [127, 128, 129].

It is well-known that technology based on bulk acoustic wave (BAW) resonators has recently emerged as the advantageous alternative for filter designs based on both surface acoustic wave (SAW) resonators and ceramic resonators, due to its capacity for integration in a standard microelectronics process and miniaturization, its high quality factor, and its higher power-handling capability [67, 88]. However, most of the known BAW configurations present a single band response [67, 88]. In [130], a dual band filter is presented in which the BAW resonators comprise two piezoelectric layers with an opposite orientation. However, in this case, the design of the piezoelectric layers are dependent on each other because they exert a mass loading effect on each other.

A double-ladder topology is proposed to obtain a dual-band response using BAW resonators based on the conventional ladder-type topology. The general configuration proposed for the double-ladder configuration consists of m-single stages as shown in Figure 6.1, where all the m-stages are identical. It can be seen that this configuration is very similar to the ladder-type configuration, but in this case, two BAW resonators are placed in the series path, and two BAW resonators are placed in the shunt path at each stage. A general dual-band response using the proposed structure is shown in Figure 6.2. The lower band (Band 1) is achieved by the interaction between one series and one shunt resonator (BAW_{1s} and BAW_{1p}), while the upper band (Band 2) is achieved by the interaction of the remaining pair of BAW resonators (BAW_{2s} and BAW_{2p}). The order N of ladder-type filters is usually determined by the number of single resonators that make up that structure. In this case, due to the dual behavior of the structure, the order of the filter will be determined by the number of pairs of series and shunt resonators. The main

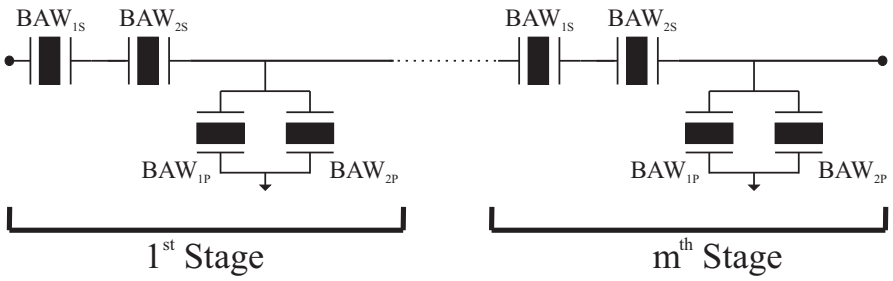

Figure 6.1: General configuration for the Double-Ladder dual-band filter using BAW resonators.

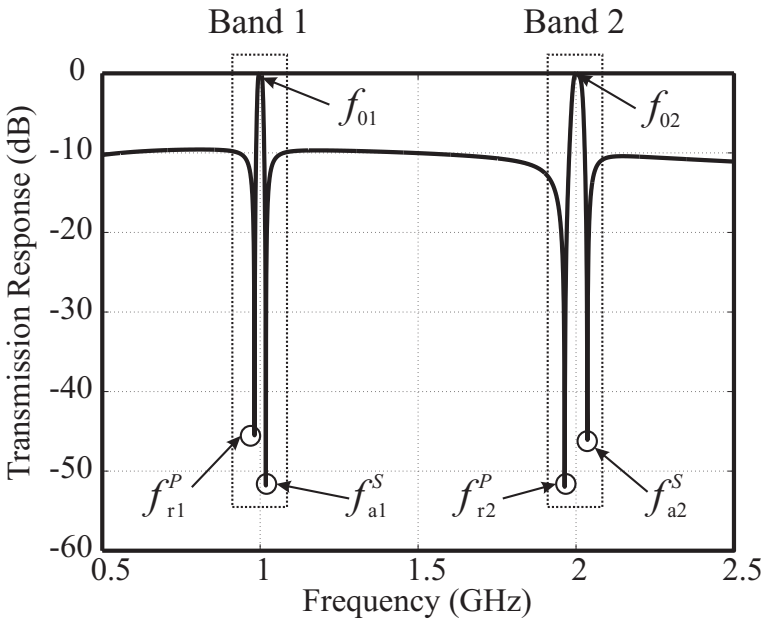

Figure 6.2: Generic dual-band response of a double-ladder filter using BAW resonators.

consideration that must be applied to the design procedure in the double-ladder configuration is known as the transmission condition: at the center frequencies of each band (f_{01} and f_{02}), the signal is desired to travel between the input and output electrical ports freely, which forces the resultant impedance of the series path to be zero, that is, to behave as a shortcircuit. This is achieved by the inductive behavior of the BAW resonator between the resonant frequencies being cancelled by the capacitive behavior out of these frequencies at each band.

6.2 Working Principle of the Double-Ladder topology

The working principle behind the proposed structure is very similar to the conventional ladder-type filter one. The lower transmission zeros at each band will be located at the resonance frequency of the shunt resonators (f^P_{r1} and f^P_{r2}), since at these frequencies the signal will find a direct ground path. The upper transmission zeros in both bands are given by the antiresonance frequency of series resonators (f^S_{a1} and f^S_{a2}), since the series resonators will behave as an electrical open-circuit at these frequencies.

The consideration that must be used in the double-ladder topology is the fulfillment of the transmission condition: at the center frequency of each band (f_{01} and f_{02}), the resultant electrical impedance of the series resonators must be zero. The electrical behavior of the BAW resonator between f_r and f_a is inductive while out of these frequencies, the electrical behavior is purely

capacitive. Based on the approach of the electrical impedance of the BAW resonator [85],

$$Z\left(f\right)=\frac{1}{j2\pi fC_0}\left(\frac{f^2-f_r^2}{f^2-f_a^2}\right) \tag{6.1}$$

with $C_0 = A\epsilon/d_p$, the transmission condition can be expressed as,

$$\begin{array}{c}\frac{1}{j2\pi f_{01}C_{01}^S}\left(\frac{f_{01}^2-f_{r1}^2}{f_{01}^2-f_{a1}^2}\right)+\frac{1}{j2\pi f_{01}C_{02}^S}=0\\ \frac{1}{j2\pi f_{02}C_{01}^S}+\frac{1}{j2\pi f_{02}C_{02}^S}\left(\frac{f_{02}^2-f_{r2}^2}{f_{02}^2-f_{a2}^2}\right)=0\end{array} \tag{6.2}$$

where the first and second terms in the equations in (6.2) correspond to the electrical impedance of the series resonator BAW_{1S} and BAW_{2S}, respectively, at the center frequencies f_{01} and f_{02}. Thus, the ratio between the series static capacitances C_{01}^S and C_{02}^S is given by,

$$\begin{array}{c}\frac{\mathrm{C_{01}^S}}{\mathrm{C_{02}^S}}=\left|\frac{f_{01}^2-f_{r1}^2}{f_{01}^2-f_{a1}^2}\right|\\ \frac{\mathrm{C_{01}^S}}{\mathrm{C_{02}^S}}=\left|\frac{f_{02}^2-f_{a2}^2}{f_{02}^2-f_{r2}^2}\right|\end{array} \tag{6.3}$$

It must be taken into account that the transmission condition in (6.3) cannot be accomplished with freely chosen resonators. This will be dealt with in the design procedure section.

6.3 Design Procedure of the Dual-band Filter

The output parameters of the proposed design procedure are: C_{01}^S, C_{01}^P, C_{02}^S, C_{02}^P and f_{ri}^S and f_{ai}^P since the remaining frequencies are given by the allocation of the transmission zeros as seen in Figure 6.2. The filter response will be described by the center frequency of each transmission band f_{0i}, considering that the transmission zeros are symmetrically spaced around the center frequency of each band, the allocation of the upper f_{zi}^U and lower f_{zi}^L transmission zeros to each band, and the out-of-band (OoB) rejection. The subscript $i = 1, 2$ refers to each of the frequency bands.

Taking the considerations above into account, we can define a design procedure that is summarized as follows:

1. **Determine the value of the resonance frequency $\mathbf{f_{r1}^S}$ using $\mathbf{f_{z1}^U = f_{a1}^S}$.** To carry out this step, the value of the effective electromechanical coupling constant k_{eff1S}^2 for the series BAW related with band 1 must be set. This value is related with the resonant frequencies as,

$$k_{eff}^2=\left(\frac{\pi^2}{4}\right)\left(\frac{f_r}{f_a}\right)\left(\frac{f_a-f_r}{f_a}\right) \tag{6.4}$$

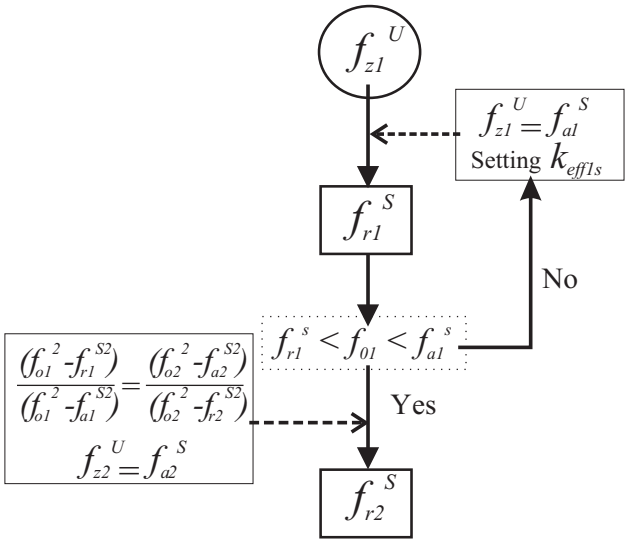

Figure 6.3: Flow diagram for obtaining of the resonant frequencies of the series resonators .

There is a freedom degree in setting the value of k_{eff}^2, but two conditions must be fulfilled: the value of k_{eff1}^S must be lower than the maximum achievable value with the materials used, and the resonant frequencies obtained for this resonator must accomplish,

$$f_{r1}^S < f_{01} < f_{a1}^S \tag{6.5}$$

to ensure that the series BAW resonator presents an inductive behavior at the center frequency. A good approach for defining the value of k_{eff1}^S consist of relating this value with the transmission zeros distance as,

$$k_{eff1}^{S2} = \left(\frac{\pi^2}{4}\right)\left(\frac{f_{r1}^P}{f_{a1}^S}\right)\left(\frac{f_{a1}^S - f_{r1}^P}{f_{a1}^S}\right) \tag{6.6}$$

In this case, the resonance frequency of the series and shunt resonators is equal. Otherwise, for a different value, both frequencies will be allocated to close positions as shown in Figure 6.4, which also shows the effects on the transmission response for the pass band 1 depending on the chosen value of k_{eff1}^S. It can be seen that for a random value, a certain losses appear in the transmission response. This is due to the fact that for the resonance frequency of the series resonator f_{r1}^S, at which the signal must travel freely along the series path, the electrical input impedance of the shunt resonators is low, leading to part of the energy being grounded and resulting in some insertion losses. The value obtained using (6.6) is $k_{eff1}^{S2} = 3.67$ %, while the random value used is $k_{eff1}^{S2} = 4.5$ %.

2. **Determine the resonance frequency $\mathbf{f_{r2}^S}$ using $\mathbf{f_{z2}^U = f_{a2}^S}$ and the frequency relation in the transmission condition in (6.3).** Once this frequency is obtained, the value

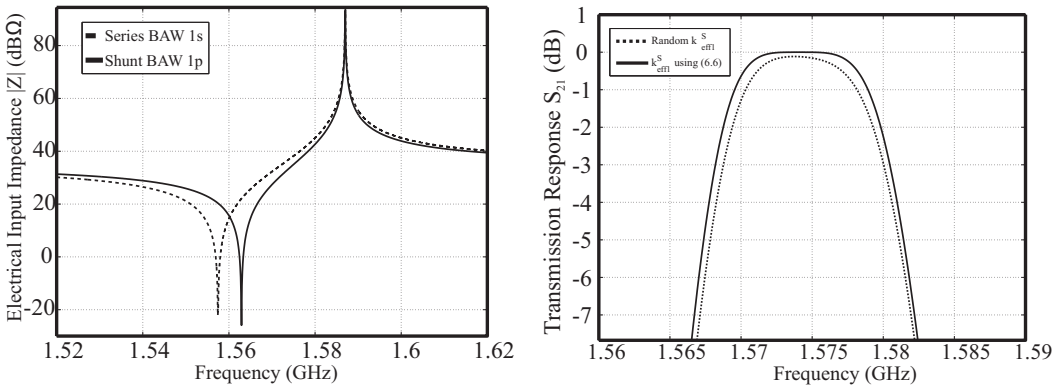

(a) Input electric impedance for random value of k^S_{eff1}

(b) Detail of the bandpass for random and calculated value of k^S_{eff1}

Figure 6.4: Effects of the chosen value of k^S_{eff1} on the transmission response

of k^2_{eff2S} can be calculated using (6.4). This value is also subject to the same limitations as the previous case.

At this point, the series resonators are fully characterized in terms of resonant frequencies and the effective electromechanical coupling constant needed. In order to clarify the design procedure, the flow diagram required for obtaining these parameters is shown in Figure 6.3. For the shunt resonators, the design procedure does not require as many restrictions. The only one which must be ensured is the allocation of the resonance frequency f_r to the position of the lower transmission zeros at both bands. The design procedure is therefore:

3. **Set the values for antiresonance frequency of the shunt resonators $\mathbf{f^P_{ai}}$.** The only restriction on setting these values is the resulting value for the k^2_{effiP}, which must be obtainable with the used materials as above. In this case, for the sake of simplicity these values can be set to the same values as the values of f^S_{ai}.

4. **Determine the static capacitances $\mathbf{C^{S/P}_{0i}}$ of each resonator.** In this case, it can be assumed that $C^S_{01} = C^P_{01} = C_{01}$ and $C^S_{02} = C^P_{02} = C_{02}$. As seen in [76], one of the conditions for finding the static capacitance that the filter must accomplish is the image impedance matching condition. This condition is accomplished at a single frequency and is defined as,

$$C^S_0 C^P_0 = \frac{1}{(2\pi f_0 Z_0)^2} \tag{6.7}$$

where $Z_0 = 50\ \Omega$ is the impedance of the source and load. Note that as discussed extensively in the previous chapter, the asymmetry in the structure means that $Z_{i1} \neq Z_{i2}$, and some mismatch losses must therefore be assumed. On the other hand, if there are two different frequencies with a separation, the condition will not be accomplished at both frequencies

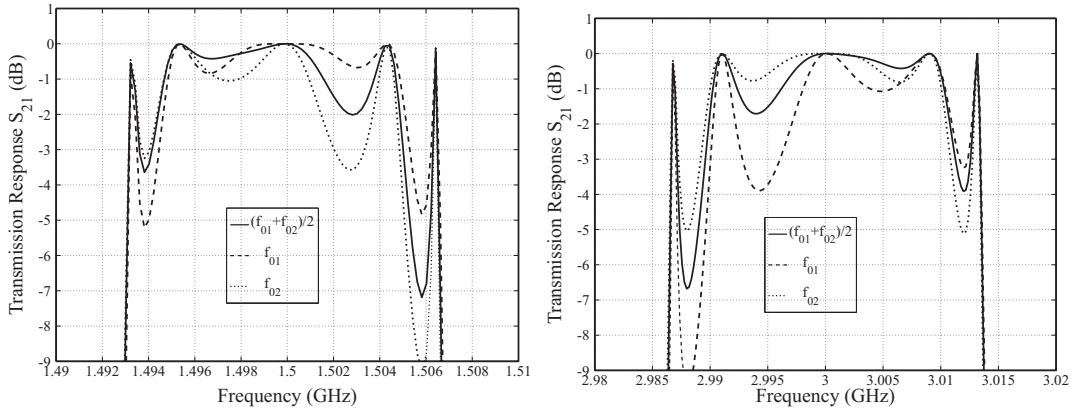

(a) Transmission band 1 (b) Transmission band 2

Figure 6.5: Detail of both transmission bands depending on the chosen frequency for calculating the value of the static capacitance C_{01}^S and C_{02}^S

at the same time. In this case, there are three different ways of obtaining the values of C_{01} and C_{02}:

-Applying the image impedance matching condition to the central frequency of the lower band f_{01} to obtain C_{01}, and find C_{02} using the capacitance relation in (6.3). In this case, some mismatch losses will appear in the upper band.

-Applying the image impedance matching condition to the central frequency of the upper band f_{02} to obtain C_{02}, and find C_{01} using the capacitance relation in (6.3). In this case, some mismatch losses will appear in the lower band.

-Calculating the capacitance C_{01} at the frequency between both center frequencies $(f_{01} + f_{02})/2$ in order to minimize the mismatch losses in both bands, then using the ratio in (6.3) to find C_{02}.

In order to validate the assumptions above, a filter response has been designed at the central frequencies $f_{01} = 1.5$ GHz and $f_{02} = 3$ GHz, which entails a big frequency separation between bands. The static capacitance for the series resonators has been calculated using the three possibilities and the order of the filter has been set to $N = 4$ since, as discussed in the conventional ladder-type filter, the higher the order, the higher the insertion losses. The results in Figure 6.5 confirm that the optimum way of calculating the value of the static capacitances is the one with frequency at the center frequency between transmission bands. With the other possibilities, the final result has very few mismatch losses in one of the bands, in which the image impedance condition is applied, and higher mismatch losses in the other one. As seen in Figure 6.5, this is 1 dB in the matched band, and 4 dB in the other band.

5. **Determine the OoB rejection.** As it occurs with the conventional ladder-topology,

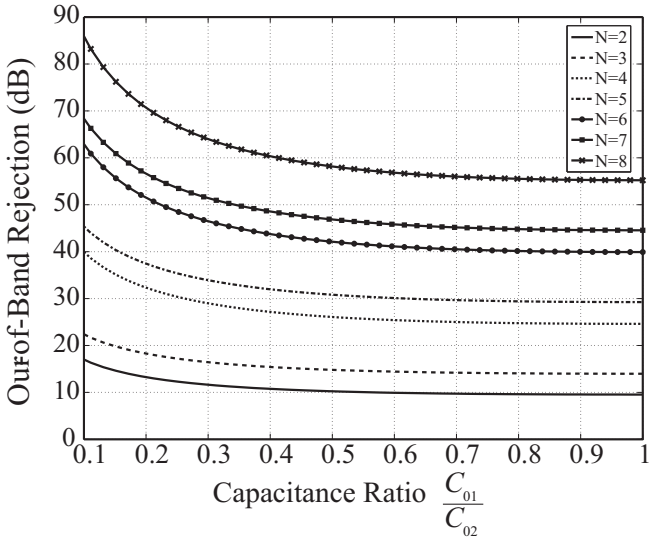

Figure 6.6: Out-of-band rejection depending on the capacitance ratio for a given order N of the filter.

the out-of-band rejection will be determined by the order of the filter [76]. The relation between the order N and the OoB rejection is shown in Figure 6.6 when $C_{01}^S = C_{01}^P = C_{01}$ and $C_{02}^S = C_{02}^P = C_{02}$. Otherwise, the OoB rejection might be calculated for each case.

6.4 Application of the Dual-Band BAW Filter to the GNSS System

One of the most straightforward applications in which the dual-band BAW filter can be included is the RF receiver for global navigation satellite systems (GNSS) signals. This system usually contains the general positioning system (GPS), which is operated by the United States; the global orbiting navigation satellite systems (GLONASS), which is operated by the Russian Federation and the projected Galileo system which is going to be built by the European Union. The common feature in all these systems is their multi-frequency nature. The receivers are currently designed to work using one single band for a specific system. However, it has been shown that using various bands to obtain the information minimizes the position errors due to the ionosphere [131]. However, receivers have also been developed which work with a single band of two different systems as in [132], in which a GPS/Galileo receiver is discussed. The center frequency of the different multi-standard applications in the GNSS, the required bandwidth and the availability of the service are shown in Table 6.1. Note the presence of interferer signals which are listed in Table 6.2 as well as the frequency range and the power associated with each one [133].

Table 6.1: GNSS signals [133].

Signal	Center Frequency [MHz]	Bandwidth [MHz]	Service
GPS L1	1575.420	20.46	Open
GPS L2	1227.600	20.46	Open
GPS L5	1176.450	24	Open
Gal L1	1575.420	4	Open
Gal E1L1E2	1575.420	32	Open
Gal E5a	1176.450	20.46	Open
Gal E5b	1207.140	20.46	Open/Encrypted
Gal E6	1278.750	10.23	Encrypted
Gal E6	1207.140	40	Encrypted
Gal E5ab	1191.795	51.15	Open/Encrypted
GLO L1	1603.41	12.27/20.92	Open
GLO L2	1247.09	9.77/18.52	Open

Table 6.2: Interferer signals [133].

Signal	Frequency Range [MHz]	Power
Satellite communication 1	1544.5	Medium
Satellite communication 2	2200-2300	Medium
UHF TV	500-860	Strong
CT2/+ cordless phones	864-948	Weak
DAB	1452-1492	Strong
GSM cell-phones	824-960/1710-1990	Medium
TDMA, IS-54 cell-phones	854-894/1850-1990	Medium
CDMA, IS-95 cell-phones	824-894/1850-1990	Medium
DECT phones	1880-1900	Weak
PHS phones	1895-1918	Weak
PDC cell-phones	810-956/1429-1501	Medium
UMTS/WCDMA phones	1900-2170	Medium
Bluetooth	2402-2495	Weak
WLAN (IEEE802.11b)	2410-2483	Medium
UWB	1000-3000	Weak

Table 6.3: Obtained values with the design procedure for resonators associated to Band 1 and Band 2 for the GPS L1/L5 application.

Parameter	Band 1	Band 2
C_0	2.31 pF	2.35 pF
f_a	1195.7 MHz	1591.8 MHz
f_r	1157.3 MHz	1558.6 MHz

6.4.1 Dual-band filter for the GPS system

The first design is for the GPS L1 and L5 bands simultaneously. As described in Table 6.1, the chosen central frequencies and Bandwidths are $f_{01} = 1176.45$ MHz and $f_{02} = 1575.42$ MHz, and $B_{w1} = 24$ MHz and $B_{w2} = 20.46$ MHz. Taking into account the required bandwidth, the allocation of the transmission zeros has been set to $f_{01}^L = 1157.3$ MHz, $f_{01}^U = 1195.7$ MHz, $f_{02}^L = 1559.1$ MHz and $f_{02}^U = 1591.8$ MHz. In this case, we have chosen the order of the filter to be $N = 4$ which entails and OoB higher than 25 dB. The static capacitances and resonant frequencies obtained using the design procedure are shown in Table 6.3. Note that series and shunt resonators has been designed to be equal and that is why there is no distinction between them in the summary.

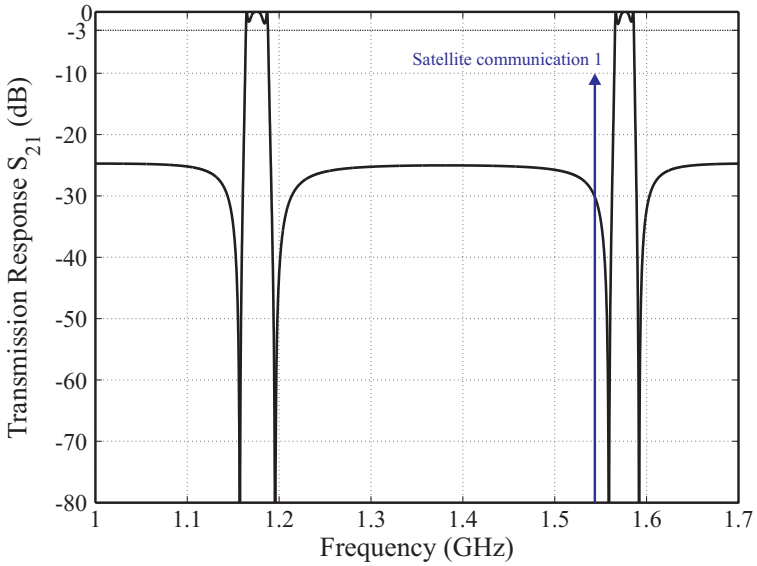

Figure 6.7: Simulated lossless transmission response for the GPS L1 and L5 frequency bands and the Satellite communications 1 interferer signal.

As it was done with the conventional ladder-type filter, from the resonant frequencies and the static capacitances, the thickness of the electrode and piezoelectric layer, as well as the

Table 6.4: Dimensions of the BAW resonators for the GPS L1-L5 Dual Band Filter.

	BAW_{1S}	BAW_{1P}	BAW_{2S}	BAW_{2P}
Metal Electrode [μm]	0.63	0.63	0.59	0.59
Piezoelectric layer [μm]	1.82	1.82	0.99	0.98
Area [μm x μm]	216.5x216.5	216.5x216.5	160.9x160.9	160.9x160.9
k^2_{eff}[%]	7.67	7.67	5.04	4.97

Table 6.5: Modification of the dimensions of the BAW resonators for the GPS L1-L5 Dual Band Filter.

	BAW_{1S}	BAW_{1P}	BAW_{2S}	BAW_{2P}
Metal Electrode [μm]	0.59	0.59	0.59	0.59
Piezoelectric layer [μm]	1.90	1.90	0.99	0.99
Area [μm x μm]	216.5x216.5	216.5x216.5	160.9x160.9	160.9x160.9

required area are needed. In order to obtain these results, the equations (5.8,5.9) developed in the previous chapter must be used.

The values obtained for the resonators of the structure as well as the effective electromechanical coupling constant obtained are found in Table 6.4. The materials used are Aluminum for the electrodes and ZnO for the piezoelectric layer. The transmission response is shown in Figure 6.7. The two transmission bands where the transmission zeros are allocated to the expected frequencies are clearly shown. The simulation has been carried out considering lossless BAW resonators. At the same time, the interferer signal coming from the satellite communications 1 at $f = 1544.5$ MHz is shown, where as can be seen, the rejection for this signal is 30 dB.

Some modifications can be made to the dimensions obtained for the designed filter in Table 6.4, for the sake of greater simplicity in the fabrication process. It can be seen that the thickness of the electrodes is very similar for the two pairs of resonators. The value of the effective electromechanical coupling constant for BAW_{2S} and BAW_{2P} is almost the same, with the difference being a slight variation in the thickness of the piezoelectric layer. The designed filter has therefore been modified in order to use the same electrode thickness. To do so, the thickness has been equaled to the one referred to in band 2. Since the electrode to piezoelectric thickness ratio in this case is lower, a slight variation strongly affects than variations over the electrode for the pair of resonators associated with band 1. On the other hand, the thickness of the piezoelectric layer in the resonators associated to band 2 has also been equaled. The resulting dimensions are shown in Table 6.5. The variation in the thickness of the electrodes entails a slight shift in the allocation of one of the transmission zeros in band 1 since the metal electrode to piezoelectric

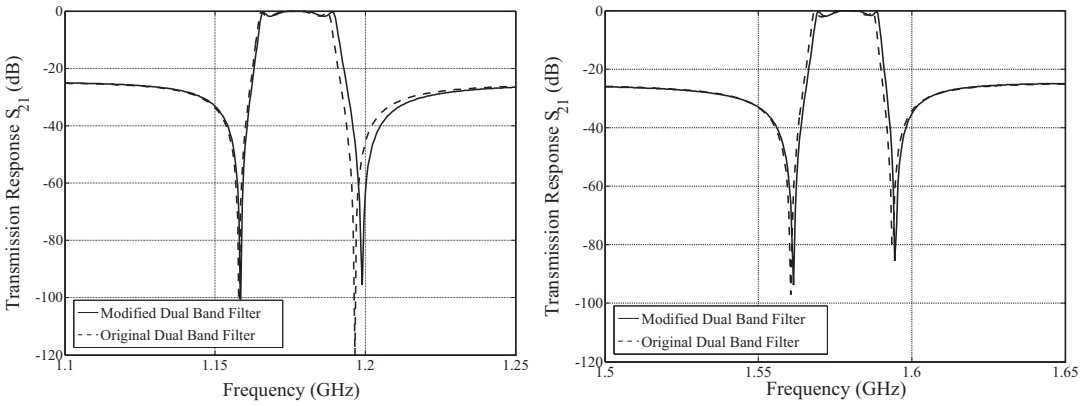

(a) Transmission band 1 (b) Transmission band 2

Figure 6.8: Detail of both transmission bands for the original (dashed line) and modified (solid line) dual-band filter for GPS L1 L5.

thickness ratio has also been slightly modified. As it is expected, the band 2 remains as its original situation. The detail of both transmission bands are seen in Figure 6.8.

6.4.2 Dual-band filter for the Galileo System

The frequency distance between both bands of the designed filter for GPS L1 - L5 is 400 MHz. For this distance, the behavior of the filter for the frequencies between both bands can be easily obtained since at these frequencies, all the resonators making up the structure present a capacitive behavior. In order to check the proper behavior of the proposed structure when both transmission bands are allocated close together, a dual band filter for Galileo E5a and E5b has been designed.

The central frequencies of each bands are $f_{01} = 1176.450$ MHz and $f_{02} = 1207.140$ MHz, as shown in Table 6.1, which entails a frequency distance of only 30 MHz. For this design, the transmission zeros have been allocated at $f_{01}^{L} = 1166.3$ MHz, $f_{01}^{U} = 1187.7$ MHz, $f_{02}^{L} = 1197.3$ MHz and $f_{02}^{U} = 1217.8$ MHz. As in the previous design, the materials used are Aluminum for the electrodes and ZnO for the piezoelectric layer. The resulting output parameters from the design procedure are summarized in Table 6.6. In this case, also the series and shunt resonators associated to each band has been designed to be equal.

As it was done in the GPS L1/L5 application, with the static capacitance and the resonant frequencies, applying the equations (5.8,5.9) in the previous chapter, the physic dimensions of the BAW resonators can be extracted which are summarized in Table 6.7. As it occurred in the previous design, the value of $k_{eff1}^{S} = k_{eff1}^{P}$, but $k_{eff2}^{S} \neq k_{eff2}^{P}$. This is due to the fact that the capacitance ratio C_{01}^{S}/C_{02}^{S} is not exactly one. The transmission response for the designed filter

Table 6.6: Obtained values with the design procedure for resonators associated to Band 1 and Band 2 for the Galileo E5a/E5b application.

Parameter	Band 1	Band 2
C_0	2.67 pF	2.69 pF
f_a	1186.7 MHz	1217.4 MHz
f_r	1166.2 MHz	1196.7 MHz

Table 6.7: Dimensions of the BAW resonators for the Galileo E5a - E5b dual band filter.

	BAW_{1S}	BAW_{1P}	BAW_{2S}	BAW_{2P}
Metal Electrode [μm]	0.83	0.83	0.82	0.82
Piezoelectric layer [μm]	1.16	1.16	1.11	1.11
Area [μm x μm]	185.2x185.2	185.2x185.2	182.4x182.4	181.9x181.9
k^2_{eff}[%]	4.18	4.18	4.11	4.08

can be seen in Figure 6.9, where both bands are clearly distinguished with the corresponding transmission zeros allocated at the expected frequencies.

As in the case above, some modifications in the geometry of the composing resonators can be made in order to simplify the fabrication process further. In this case, unlike in the design above, the thickness of the piezoelectric layers of the resonators associated with band 1 and 2 are very similar, since the transmission bands are allocated to very close frequencies. In this case, the frequency shift of the transmission band can be assumed by the thickness of the electrode. The modification consists of forcing all the piezoelectric layers to have the same thickness. Of course, the thickness of the electrodes will have to be modified in order to correct this deviation. The resulting dimensions are shown in Table 6.8.

Figure 6.10 shows the comparison in the transmission response with the original resonators obtained using the design procedure, and using modified resonators in order to simplify the

Table 6.8: Modification of the dimensions of the BAW resonators for the Galileo E5a - E5b dual band filter.

	BAW_{1S}	BAW_{1P}	BAW_{2S}	BAW_{2P}
Metal Electrode [μm]	0.83	0.83	0.80	0.80
Piezoelectric layer [μm]	1.16	1.16	1.16	1.16
Area [μm x μm]	185.2x185.2	185.2x185.2	182.4x182.4	181.9x181.9

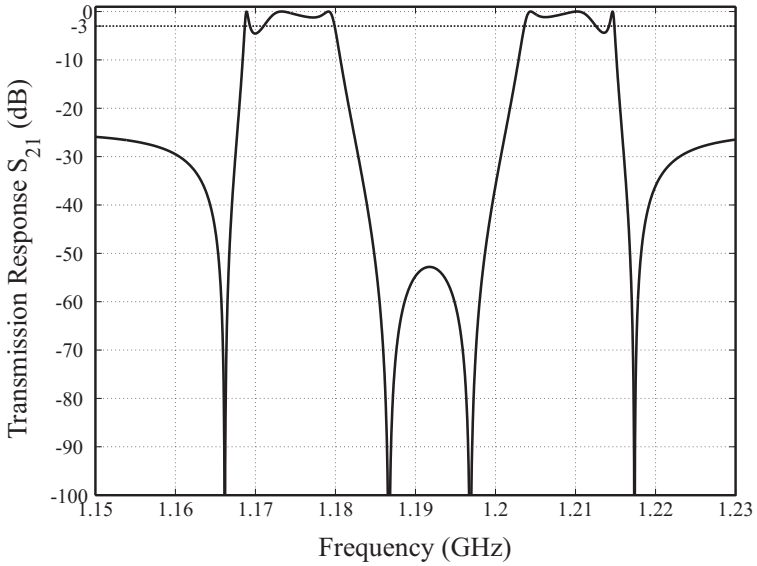

Figure 6.9: Simulated lossless transmission response for the Galileo E5a and E5b frequency bands.

fabrications process. It can be seen that since the piezoelectric thickness has been equaled to the one belonging to the resonators associated with band 1, the slight difference occurs in band 2. In this case, the rectification in the electrode thickness entails a small modification in the value of the effective electromechanical coupling constant, and thus in the frequency distance between the transmission zeros. However, the agreement between both responses can be assumed to be accurate enough.

With respect the in-band losses, it is seen that these are higher than the GPS L1/L5 application. By one hand, the matching impedance condition is better accomplished since both bands are closer. However, on the other hand, as the bands are closer, at the center of each band, the behavior of the resonators is not as expected, that is, pure inductive or capacitive depending on the band.

6.5 Topology Validation Using Measured BAW Resonators

In order to validate the proposed topology, different measured resonators have been electrically connected using the electrical simulator Agilent ADS. The measured resonators present resonant frequencies f_{r1}=1.877 MHz and f_{a1}=1.931 GHz for the pair of resonators associated with the lower band, and f_{r2}=1.962 MHz and f_{a2}=2.017 GHz for the pair of resonators associated with the upper band, forming a double-ladder with order $N = 2$. In this case, BAW_{1s}=BAW_{1p} and BAW_{2s}=BAW_{2p}, and the capacitance ratio is approximately $C_{01}/C_{02} \simeq 1$.

The transmission response and the return loss of the filter are shown in Figure 6.11. The

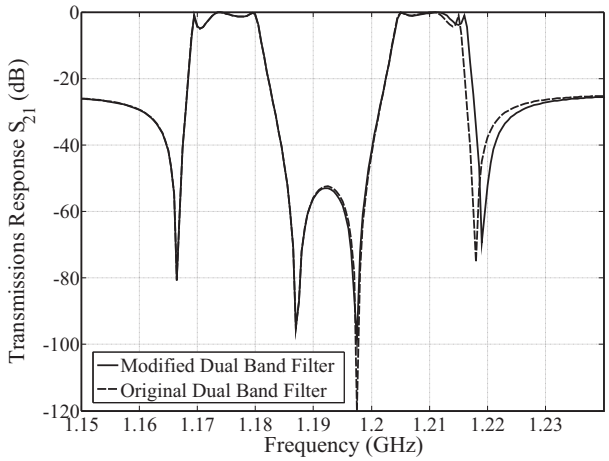

Figure 6.10: Simulated lossless transmission response for the Galileo E5a and E5b frequency bands using the original (dashed line) and modified resonators (solid line).

transmission response clearly shows both transmission bands, with the transmission zeros placed at the expected frequencies. The lower band has a ripple in the bandpass, which is due to the presence of spurious modes in its electrical behavior. Unlike the pair of resonators associated with the upper band, these resonators are not optimized to avoid or minimize the presence of these spurious modes. The OoB rejection is about 10 dB, which is the expected value considering Figure 6.6 and taking into account the capacitance ratio. Note also, that the rejection between transmission bands is even higher, in this case higher than 20 dB.

6.6 Chapter Summary

This chapter presents the double-ladder type filter. With this topology, a dual band transmission response can be achieved, in which each of the transmission bands can be allocated at the desired frequencies. Using the design procedure for the conventional ladder-type BAW filter, we discus a design procedure for the double-ladder filter.

The single cell of the proposed topology is composed of two series and two shunt resonators, where one of the series and shunt resonators are associated with one of the transmission bands, while the remaining pair of resonators is associated with the second transmission band. In order to achieve the desired response, the transmission condition must be fulfiled. This means that at the center frequencies of each of the transmission bands, the resulting impedance of the series branch must be 0 Ω. Using the capacitive behavior of the BAW resonator outside the resonant frequencies and inductive behavior between resonant frequencies, this condition can therefore be easily accomplished.

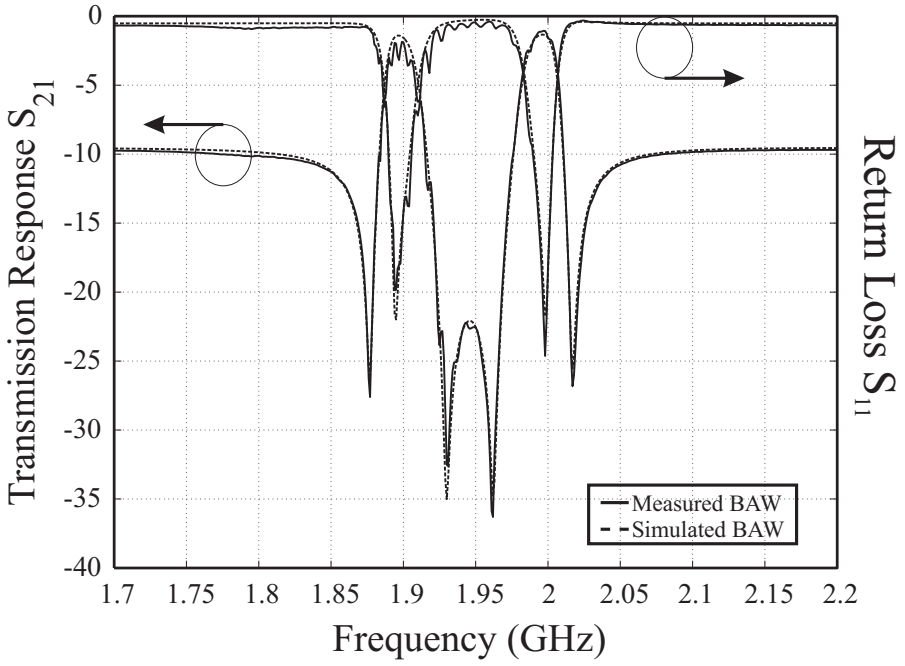

Figure 6.11: Simulated transmission response for the dual-band filter using measured BAW resonators.

On the other hand, the dual nature of the structure limits the fulfillment of the image impedance matching condition. As it was also developed in the previous chapter, this condition is only fulfilled at a single frequency. The unfulfillment of such condition entails mismatch losses in the transmission bandpass. Thus, there is a trade-off in which is the frequency where the image impedance condition must be applied. It seems that the optimum solution is to apply such condition in the equidistant frequency from both transmission bandpass. Therefore, as the frequency distance between the transmission bandpass is higher, the mismatch effects will be stronger. On the other hand, when both transmission bands are closely allocated, the behavior of the BAW resonators is not the expected, that is, pure capacitive or inductive, giving rise to a higher ripple in the bandpass.

With regards the proposed design procedure, two different issues must be pointed out related with the effective electromechanical coupling constant. The value of the k^2_{eff} has been traditionally set to the maximum achievable value which results in a decrease of the insertion losses. However, in this case, we have considered this parameter as a design parameter which gives the required degree of freedom to achieve the desired responses. The fact of reducing the value of k^2_{eff} does not imply that the quality factor of the resonator will be degraded. However, the insertion losses will be increased since the resistance of the series resonance is inversely proportional to k^2_{eff} and the resistance of the parallel resonance is proportional to k^2_{eff} [27].

Finally, the proposed design procedure has been applied to the GPS and Galileo applications. In GPS L1-L5, the frequency distance between transmission bandpass is around 400 MHz, while in the Galileo E5a-E5b, the distance is around 20 MHz, which allows studying the proposed topology as a function on the frequency distance between transmission bands.

CHAPTER 7

Conclusions and Future Work

As discussed at length in the introduction to this work, BAW technology seems to be the key to overcoming the limitations presented by other technologies that are mainly related with their size and ability to integrate devices based on these technologies. The driving forces behind the development of the BAW technology can be summarized as size reduction, high performance and integration.

In recent years, much of the effort in this area has focused on the control and improvement of the various processes for manufacturing acoustic devices. However, there is still much work yet to be done in the study of BAW resonators, as well as their application to microwave devices. The conclusions of the work proposed in this thesis can be summarized in the following points for each chapter:

1. In chapter 2, analysis of the propagation of the acoustic wave through a piezoelectric layer shows certain analogies with the electromagnetic plane that are very useful for understanding the physical phenomena underlying the working principle of BAW resonators. Several one-dimensional models have also been proposed in order to characterize the electrical behavior of these resonators. However, the three-dimensional nature of a BAW resonator makes the various one-dimensional models insufficiently accurate for full electrical characterization. This is due to the fact that lateral effects cannot be predicted by these models.

2. In order to overcome the limitations of the one-dimensional models, the one-dimensional study of the BAW resonator is expanded to the three-dimensional case in chapter 3. In order to obtain the full electrical characterization, the strategy for carrying out the three-dimensional simulation was introduced. The results were compared with various studies using laser interferometry in the characterization of such resonators, in which the agree-

ment was very good. The degradation of the electrical performance of BAW resonators - basically the quality factor of the BAW resonator - is mainly due to the presence of lateral standing waves. At the same time, this also leads to a strong ripple in the bandpass filter response.

3. Chapter 4 tries to answer the question arising from chapter 3: how can the electrical performance of the BAW resonator be improved? There are basically two different techniques that focus on this issue: the apodization solution and the thickened edge load solution. The former consists of designing the top electrode in such a way that non-parallel edges are found. In this case, the standing paths present in the structure are larger, which makes the lateral standing waves more attenuated. However, more standing paths are present, and therefore more lateral standing waves. Furthermore, since lateral modes are still present, the quality factor of the BAW resonator is still degraded because part of the energy of the fundamental mode leaks to the lateral standing waves. The thickened edge solution consists of the inclusion of a border region in the top electrode. By doing so, boundary conditions are created in which lateral modes cannot propagate through the structure. In this case, the quality factor of the BAW resonator obtained is much better than when using the apodization technique.

   An equivalent electrical circuit has been developed using one-dimensional models in order to model side effects using this solution. When the border is included, the structure can be understood as two independent BAW resonators since the mechanical boundary conditions are different in the active and thickened edge region. In this case, a new resonant mode appears due to the thickened edge load. The frequency allocation of this mode can be controlled by means of the height of this region. On the other hand, due to the presence of this mode, the total amount of energy of the fundamental mode is reduced since part of the energy leaks to the thickened edge mode, with the corresponding degradation of the effective electromechanical coupling constant.

4. After studying the BAW resonators in terms of their electrical behavior and optimization, but also from the mechanical point of view, the ladder-type filters were introduced in Chapter 5. The design procedure for this type of filter was discussed, considering infinitesimal electrodes first, and then including the mass loading effects in the design procedure. Ladder-type filters are characterized by a high selectivity due to the presence of a pair of transmission zeros, but also by a poor out-of-band rejection due to the natural capacitor divider. This chapter shows how the OoB rejection can be improved by including reactive elements in the ladder-type topology. The presence of reactive elements can modify the resonant frequencies of the BAW resonators. Doing this, if the ladder-type topology is formed by modified and non-modified BAW resonators, two pairs of transmission zeros will be present in the transmission response with the improvement of the OoB rejection.

With this solution, and depending on the application, the order of the filter could even be decreased.

5. Most of the known filter topologies based on BAW resonators only present one transmission band. There are some works containing a dual band filter is found, but the resulting performance is very poor or the bands cannot be allocated to the desired frequencies. In this work, we have developed a double-ladder topology which enables a dual-band transmission response in which each of the bands can be allocated to the desired frequencies. The only limitation of this topology is that the image impedance condition can be only fulfiled at a single frequency. As a result, for very widely spaced transmission bands, some mismatch losses may occur in the form of insertion losses in the bandpass. This can be minimized by applying this condition in the center frequency between transmission bands.

Future Work

This work includes a great deal of theoretical content in the description of the electrical performance of the BAW resonator, and also in its application to microwave filters. The most pressing task for the immediate future is therefore to manufacture BAW resonators in order validate all the results provided in this work; and to manufacture ladder-type and double ladder-type filters for a given specification. Note that manufacturing acoustic devices entails a complex process in which the design must be determined by the fabrication process requirements in terms of layer thickness limitation, the mechanism for confining the acoustic wave, the design of the access lines and so on.

Fabrication is a further step needed in the research on the FBAR field to validate all the results shown in this work. However, the research can also focus on the following points:

1. Most of the equivalent circuits proposed for the various acoustic structures are given from the electrical point of view. However, in more complex structures such the coupled resonator filter, electrical models, despite being accurate, do not provide all the information needed for comprehensive knowledge of the working principles of these structures.

   Acoustic resonators have been also explained from the mechanical point of view by means of the spring-mass model, in which the mechanical properties of the resonator can be directly related with the frequency response. Mechanical models can also be developed in order to model more complex structures, as with coupled resonator filters. The coupling mechanisms must be investigated in depth in this kind of structure, and mechanical models could be a very useful tool for obtaining more information about the working operation underlying these structures.

2. As microwave applications are constantly increasing, the demand for microwave filters with more sophisticated responses is evident. As with the asymmetrical coupled resonator filter [105], various filter architectures must be developed in order to fulfil the requirements mentioned above. Although most work has focused on bandpass filters, bandstop filters are also required.

3. In the most modern communication systems, wireless applications are added as stand-alone features in which the integration only occurs at software level. However, future systems are expected to have optimized flexible digital signal processors and reconfigurable RF system-in-package (SiP) radios that can be used for various wireless applications. This scenario requires advanced SiP technologies in order to reduce the size and the cost of the final device, as well as the performance. Passive components usually account for more than 80% of the total amount of components in a microwave system. Therefore, as seen in the recent works published in this field, the integration and package is one of the issues were the future lines should be put on.

As in the introduction, areas for future work can be summarized as having three strong driving forces: high performance, minimum size and low cost. These driving forces sparked off research in acoustic devices, and these are the driving forces which the most of the scientific community specialising in this field is working on.

APPENDIX A

Transcendental Equations for the Resonance and Antiresonance Condition

As it was briefly discussed in Chapter 2, the BAW resonator can be also understood as the stepped impedance resonator (SIR), of course, without taking into account the piezoelectric effect. This is because the observed symmetry of the BAW resonator in the thickness dimension when the thickness and material of top and bottom electrodes are the same.

In this appendix, the fundamental equations for the resonance and antiresonance conditions will be obtained by means of the analysis of the SIR in the electromagnetic plane. Taking this consideration into account, an horizontal symmetry plane can be observed in the BAW structure at $z = d_p/2$. For the sake of simplicity, the mechanical load at top and bottom electrodes will be air. The piezoelectric material is ZnO and the metal electrodes are considered to be Aluminum.

A.1 Antiresonance frequency condition

The antiresonance frequency is given when the total thickness of the structure corresponds to the half acoustic wavelength. At this point, taking into account the electrical boundary conditions at the top and bottom surfaces of the structure, is straightforward to state that the fields along the structure are symmetric, leading to the resonator to behave as an open circuit at the center of the structure. This situation is represented in the Figure A.1(a).

To accomplish the antiresonance condition, the relation between the impedances, looking into the opposite directions from the interface between the electrode and piezoelectric layer, must be Z_{sce}=Z^*_{ocp} as it occurs with the stepped impedance resonators [134], which lead us to

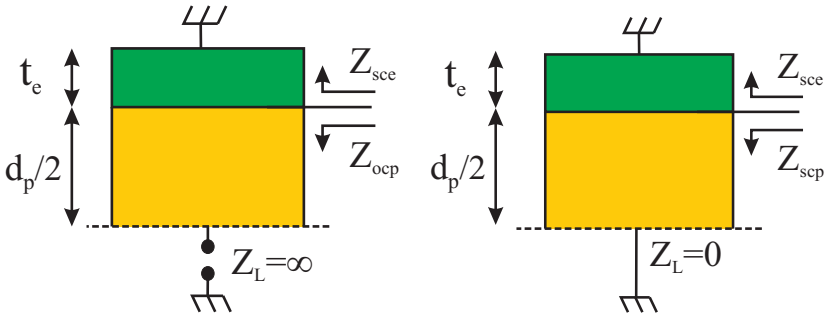

(a) Even mode for the antiresonance condition

(b) Odd mode for the resonance condition

Figure A.1: Symmetry analysis for a BAW resonator.

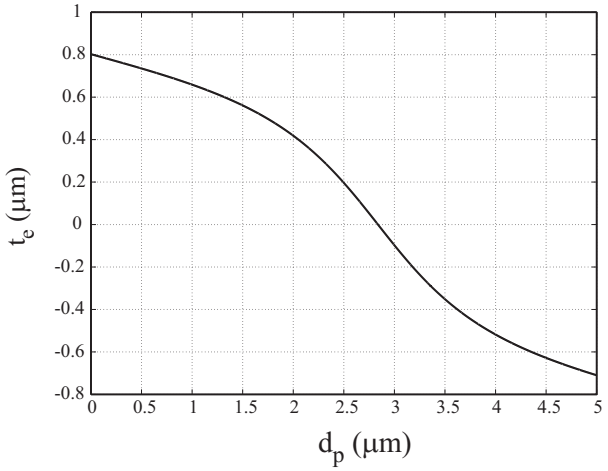

Figure A.2: Pairs of solution of d_p and t_e for the transcendental equation (A.1).

have,

$$\frac{Z_p}{Z_e} = \tan\theta_e \tan\theta_p \tag{A.1}$$

with $\theta_e = k_e t_e$, $\theta_p = k_p d_p/2$ and $k = \omega/v_p$. In order to solve the transcendental equation in (A.1), we will fix the antiresonance frequency, and we will sweep the piezoelectric thickness for a given value of the electrode thickness. Solving the equation numerically we obtain the solution shown in Figure A.2.

From the results in Figure A.2 we can see how from a certain value for the thickness of the piezoelectric layer we obtain negative values for the electrode thickness. In the case of $t_e = 0$, the thickness of the piezoelectric layer corresponds to the half of acoustic wavelength. If we increase the thickness of the piezoelectric layer, the results tend to negative values to try to reach the fixed antiresonance frequency, which is physically not possible.

A.2 Resonance frequency condition

In the case of the resonance frequency, the fields in the structure are antisymmetric, situation that lead us to set the impedance at the center of the piezoelectric layer as a short circuit. As previously, the relation between the impedances, looking into the opposite directions from the interface between the electrode and piezoelectric layer, must be Z_{sce}=Z^*_{scp}. Taking this into account, and the condition for the resonance frequency from the electrical impedance of a BAW resonator, that is the input electrical impedance is zero at this frequency, we can obtain the transcendental equation for the resonance frequency as,

$$Z_p \left(\frac{1}{\tan \theta_p} - \frac{k_t^2}{\theta_p} \right) = Z_e \tan \theta_e \tag{A.2}$$

Using the pair of electrode and piezoelectric thickness which are solution of equation (A.1) for a given antiresonance frequency, and using equation (A.2), we can obtain the solution for the resonance frequency. Once the resonance and antiresonance frequencies have been obtained and using the relation with the electromechanical coupling coefficient,

$$k_{eff}^2 = \frac{\pi^2}{4} \left(\frac{f_a - f_r}{f_a} \right) \left(\frac{f_r}{f_a} \right) \tag{A.3}$$

we could also obtain the curves that relates the achievable effective electromechanical coupling constant as a function of the ratio between the piezoelectric and the electrode thickness for a given material.

APPENDIX B

Automated FBAR Parameter Extraction Based on the Modified Butterworth-Van Dyke Model

In this appendix, the used automatic FBAR parameter extraction method is going to be discussed, which is based on the minimum least square method. Specifically, due to the nature of the problem to be solved, the more suitable method is the Gauss-Newton algorithm, which is used to minimize the sum of squared function values, due to the nonlinear nature of the data. In this case, which is minimized is the sum of the squared of the residuals as,

$$\min_x f(x) = \frac{1}{2}\sum_{i=1}^{m} f_i(x)^2 = \frac{1}{2}F(x)^T(x) \tag{B.1}$$

where F is the residual vector and F^T its transpose. Taking advantage of the Hessian $\nabla f(x)$, and the Jacobian $\nabla^2 f(x)$, and doing some mathematical transformations, we can obtain the Gauss-Newton formula given by,

$$\nabla F(x)\nabla F(x)^T p = -\nabla F(x)F(x) \tag{B.2}$$

where $p = -f(x_k)/f'(x_k)$ evaluated at the point x_k. Somehow, p can be understood as an increment, thus, the next solution will be evaluated at x_{k+1} or equivalently $x_k + p$.

Taking advantage of the modified Butterworth-Van Dyke equivalent circuit, the objective is to find the different parameters of the model that fit the measured response of a BAW resonator. The general working principle of the used algorithm is:

1. State the initial conditions. In this case the initial conditions are the different parameters in the model.
2. Compare the measurement with the response of the model. If the error between them is large enough, to look for the next solution.

Table B.1: Consecutive steps to obtain the parameters of the modified BVD equivalent circuit.

Step	Parameter	S-parameter fitted	Error function
1	C_0	S_{12}	$\|S_{12}\|(C_0)$
2	L_m, C_m	S_{11}	$\|S_{11}\|(L_m, C_m)$
3	C_{ox}	S_{11}	$\|S_{11}\|(C_{ox})$
4	R_s	S_{11}	$\angle S_{11}(R_s)$
5	R_p	S_{12}	$\angle S_{12}(R_p)$
6	R_m	S_{11}	$\|S_{11}\|(R_m)$
7	R_{sub}	S_{11}	$\angle S_{11}(R_{sub})$
8	C_0	S_{12}	$\|S_{12}\|(C_0)$
9	C_{sub}	S_{11}	$\|S_{11}\|(C_{sub})$
10	C_0	S_{12}	$\angle S_{12}(C_0)$
11	L_m, C_m	S_{12}	$\|S_{12}\|(L_m, C_m)$
12	C_{ox}	S_{11}	$\angle S_{11}(C_{ox})$

3. For a given error below a specified value, the algorithm will be finished.

The used method is an iterative multistep algorithm, thus, each one of the steps results in a specific BVD model. On the other hand, the information of the measure is given in the S-parameter format, that is, $|S_{11}|$, $\angle S_{11}$, $|S_{21}|$ and $\angle S_{21}$. Therefore, a sensitivity study of the different parameters of the BVD model with respect the S-parameters is needed.

The used algorithm in [115] is a valid approach for free-spurious resonators, however, when also spurious modes are present in the electrical behavior of the BAW resonator, the convergence to the solution is not achieved. To overcome this, one solution could be to extract the model in a frequency range limited by the resonant frequencies. This entails that, by one hand, the convergence of the static capacitance C_0 value may present some error since this is better optimized out of the resonant frequencies. On the other hand, it must be notice that parasitic elements present a stronger effect at high frequencies.

The solution that we propose can be used also with the presence of spurious modes. First of all, the main fundamental mode must be identified. To do this, we take advantage on the magnitude of the reflection and transmission coefficient $|S_{11}|$ and $|S_{12}|$, since at the resonance frequency f_r $|S_{11}|$ tends to its minimum value, while at the antiresonance frequency f_a is the magnitude $|S_{12}|$ what tends to its minimum value.

Taking into account the previous considerations, the order of the different parameters to be optimized is shown in Table B.1. A different order could result in a non-convergence of the proposed algorithm. It must to be pointed out that, by one hand, since it is an optimization

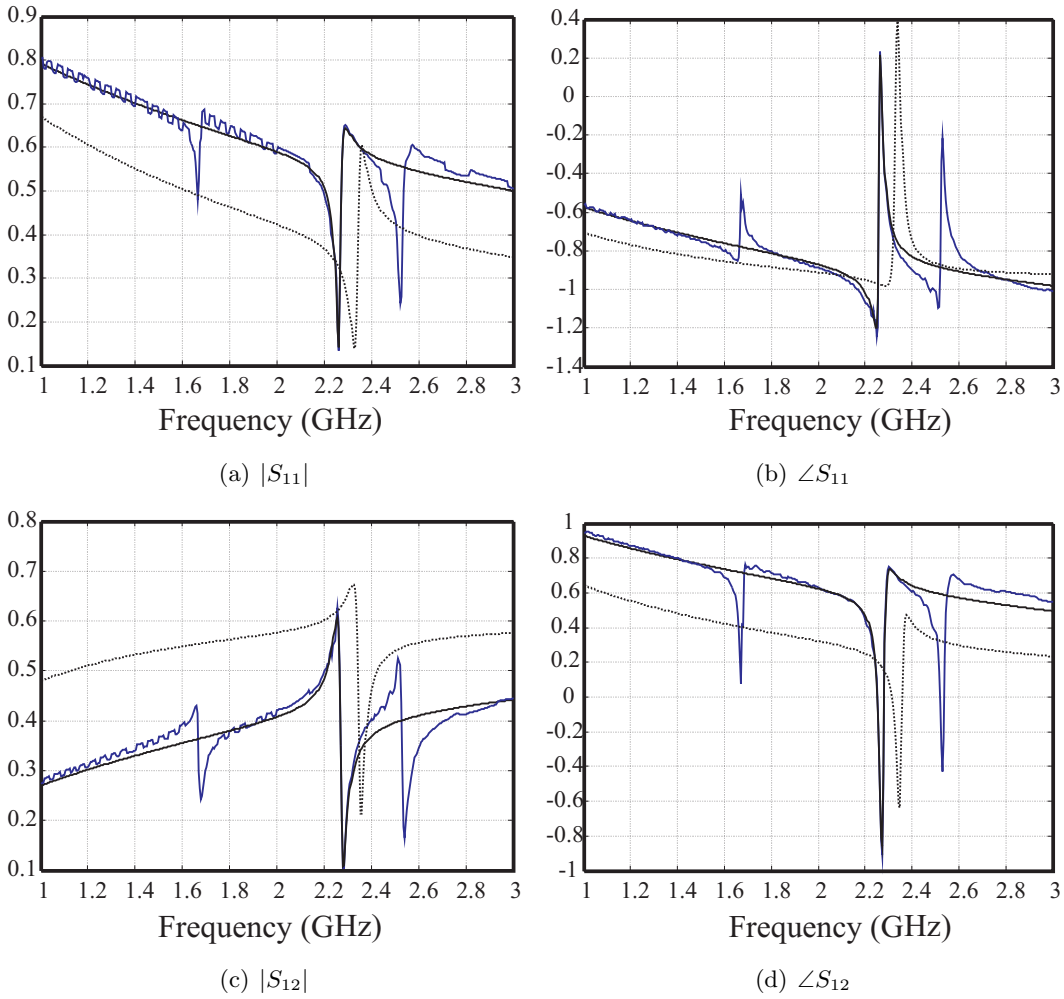

(a) $|S_{11}|$ (b) $\angle S_{11}$

(c) $|S_{12}|$ (d) $\angle S_{12}$

Figure B.1: Comparison between the measurement (blue solid line), the initial prediction (dotted black line) and the final response (solid black line) for a measured BAW resonator presenting spurious modes.

algorithm, different solutions to the implementation of the code are possible. On the other hand, it can be seen that there are some parameters that requires to be optimized in the same iteration more than one time. This is due to the fact that some of the parasitic elements exert a stronger influence on them. Finally, in order to run the algorithm, the number of iterations and the error convergence are required.

Figure B.1 shows the comparison between the measurement of the BAW resonator with the initial prediction of the different parameters and the final result. It can be seen that with the obtained values of the different parameters, the model fits the measurement for the fundamental mode. At the same time, it can be seen that the spurious resonances are not taken into account for the optimization algorithm. Also Figure B.2 shows the final result for a measured free-spurious resonator. The result, as the previous case, agrees perfectly with the measurement.

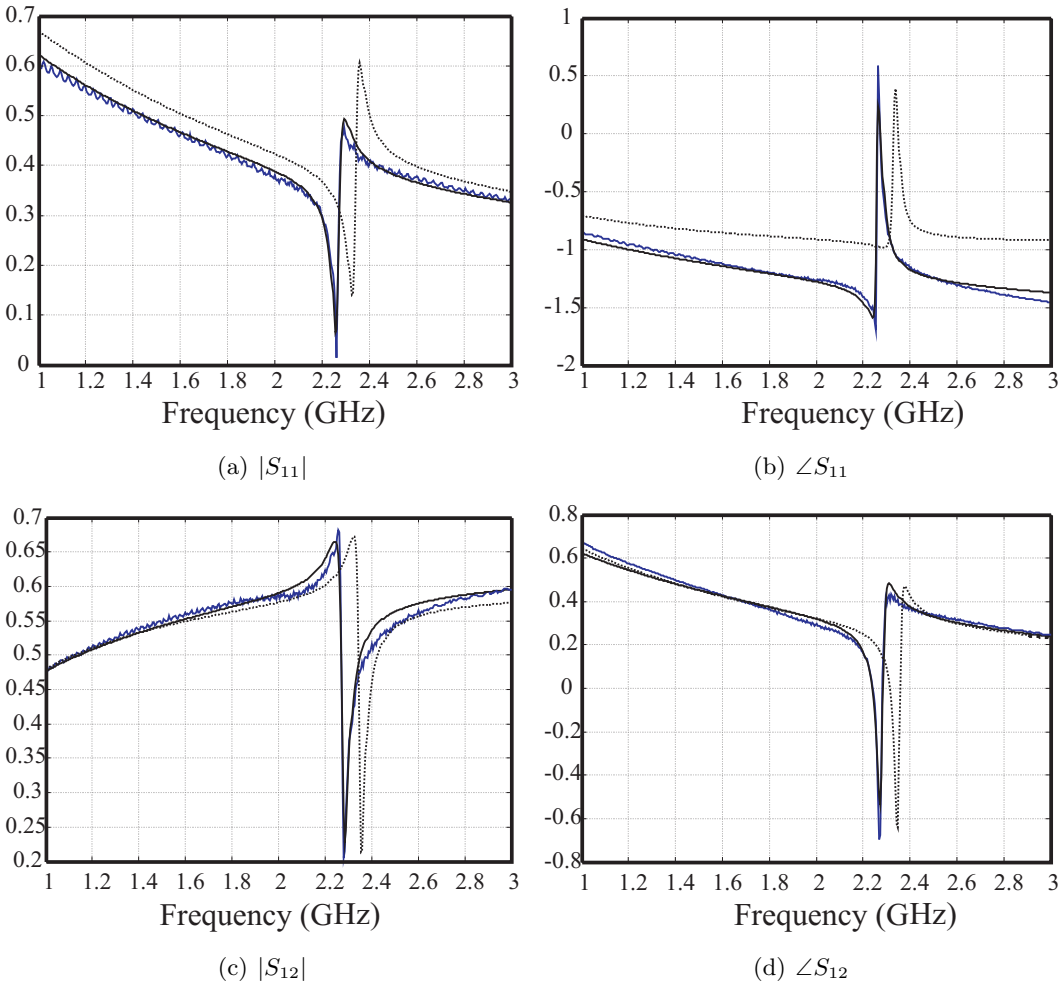

(a) $|S_{11}|$ (b) $\angle S_{11}$

(c) $|S_{12}|$ (d) $\angle S_{12}$

Figure B.2: Comparison between the measurement (blue solid line), the initial prediction (dotted black line) and the final response (solid black line) for a free-spurious measured BAW resonator.

APPENDIX C

ANSYS Routine for the 3D Simulation of a BAW Resonator

In order to clarify the code, the commands provided by the ANSYS simulator have been written in upper case.

```
/clear
/TITLE,Simulation of a conventional BAW resonator

************** Variable definition *************

Substrate definition:

x_subs=200e-6
y_subs=200e-6
z_subs=0.5e-6

Resonator definition:

x_electro_bot=200e-6
y_electro_bot=200e-6
z_electro_bot=260e-9

x_electro_top=150e-6
y_electro_top=150e-6
```

```
z_electro_top=260e-9

x_piezo=200e-6
y_piezo=200e-6
z_piezo=1e-6

************** Element type definition *************

/PREP7
ET,1,solid226,1001
ET,2,solid95
ET,3,solid95

************** Materials parameters definition *************

Aluminum Nitride:

MP,DENS,1,3260

MP,PERX,1,8
MP,PERY,1,8
MP,PERZ,1,10

TB,PIEZ,1
TBDATA,1,0,0,-0.58
TBDATA,4,0,0,-0.58
TBDATA,7,0,0,1.53
TBDATA,10,0,0,0
TBDATA,13,0,-0.48,0
TBDATA,16,-0.48,0,0

TB,ANEL,1
TBDATA,1,345e9,125e9,120e9
TBDATA,7,345e9,120e9
TBDATA,12,395e9
TBDATA,16,110e9
TBDATA,19,118e9
TBDATA,21,118e9
```

```
DMPRAT, 0.0003

Silicon:

MP,DENS,2,2181.5

MP,EX,2,176.52e9
MP,EY,2,176.52e9
MP,EZ,2,176.52e9

MP,PRXY,2,0.22
MP,PRYZ,2,0.22
MP,PRXZ,2,0.22

MP,GXY,2,72.345e9
MP,GYZ,2,72.345e9
MP,GXZ,2,72.345e9

Molybdenum:

MP,DENS,3,10096

MP,EX,3,232.36e9
MP,EY,3,232.36e9
MP,EZ,3,232.36e9

MP,PRXY,3,0.362
MP,PRYZ,3,0.362
MP,PRXZ,3,0.362

MP,GXY,3,85.30e9
MP,GYZ,3,85.30e9
MP,GXZ,3,85.30e9

************** Building geometry *************

BLOCK,0,x_electro_bot/2,0,y_electro_bot/2,0,z_subs
```

```
z0=z_subs+z_electro_bot

BLOCK,0,x_electro_bot/2,0,y_electro_bot/2,z_subs,z0

layers = 10
    *DO,i,1,layers
        BLOCK,0,x_piezo/2,0,y_piezo/2,z0+(i-1)*z_piezo/layers,z0+(i)*z_piezo/layers
    *ENDDO

z1=z0+z_piezo
h1=(y_piezo-y_electro_top)/2
h2=(x_piezo-x_electro_top)/2

BLOCK,h2,h2+x_electro_top/2,h1,h1+y_electro_top/2,z1,z1+z_electro_top

VGLUE,all

************** Assign material and element type to the blocks *************

ALLSEL
VSEL,S,LOC,Z,0,z_subs
VATT,2, ,2,0

ALLSEL
VSEL,S,LOC,Z,z_subs,z0
VATT,3, ,3,0

ALLSEL
VSEL,S,LOC,Z,z_subs+z_electro_bot,z_subs+z_electro_bot+z_piezo
VATT,1, ,1,0

ALLSEL
VSEL,S,LOC,Z,z0+z_piezo,z0+z_piezo+z_electro_top
VATT,3, ,3,0

************** Mesh *************
```

```
size=10e-6
ALLSEL
ESIZE,size
VMESH,all

************** Setting the mechanical boundary conditions *************

ALLSEL
NSEL,R,LOC,x,x_piezo/2 NSEL,R,LOC,y,y_piezo/2
D,ALL,Ux,0
D,ALL,Uy,0

ALLSEL
NSEL,R,LOC,x,x_piezo/2
D,ALL,Ux,0

ALLSEL
NSEL,R,LOC,y,y_piezo/2
D,ALL,Uy,0

ALLSEL
NSEL,R,LOC,x,0,
D,ALL,Ux,0
D,ALL,Uy,0
D,ALL,Uz,0

ALLSEL
NSEL,R,LOC,y,0,
D,ALL,Ux,0
D,ALL,Uy,0
D,ALL,Uz,0

************** Setting the electrical boundary conditions *************

ALLSEL
NSEL,S,LOC,z,z_subs+z_electro_bot
CM,electro_masa_sup,NODE
CP,1,VOLT,ALL
```

```
*GET,electre_masa_sup_number,NODE,,NUM,MIN

ALLSEL
NSEL,R,LOC,z,z_subs+z_electro_bot+z_piezo
NSEL,R,LOC,x,h2,h2+x_electro_top/2
NSEL,R,LOC,y,h1,h1+y_electro_top/2
CM,electrode_top,node CP,2,VOLT,ALL
*GET,electrode_top_numero,NODE,,NUM,MIN

ALLSEL
D,electro_masa_sup,VOLT,0.0
D,electrode_top,VOLT,1.0

************** Harmonic Analysis *************

/SOLU
ANTYPE,HARMONIC
HARFRQ,1100E6,1250E6
NSUB,151
OUTRES,ALL,ALL
KBC,1
SOLVE
FINISH

************** Postprocessing *************

/POST26
RFORCE,2,electrode_top_number,CHRG
FILLDATA,192, , , ,0,0,
FILLDATA,193, , , ,1,0,
FILLDATA,194, , , ,-1,0,
FILLDATA,195, , , ,1,1,
FILLDATA,195, , , ,1,1,
VARNAM,195,NSET
PROD,199,2,194 ADD,3,199,,,CHARGE
```

APPENDIX D

List of Author's Contributions

D.1 International Journals

1. J. Verdú, Ó. Menéndez and P. de Paco, "Ladder-Type Filters Based on BAW resonators with Improved Out-of-band Rejection," *Microwave and Optical Technology Letters.*, Vol. 50, 103–107, 2008.

2. P. de Paco, J. Verdú, Ó. Menéndez and E. Corrales, "A Balanced Branch-Line Coupler based on Edge-Coupled Parallel Lines," *IEEE Microwave Theory and Techniques.*, Vol. 56, 2936–2941, 2008.

3. Ó. Menéndez, P. de Paco, J. Gemio, J. Verdú and E. Corrales, "Methodology for designing microwave acoustic filters with Butterworth/Chebyshev response," *International Journal of Microwave and Wireless Technologies.*, Vol. 1, 11–18, 2009.

4. Ó. Menéndez, J. Verdú, E. Corrales and P. de Paco,"A review of recent patents on bulk acoustic wave resonators and filters," *Recent Patents on Electrical Engineering.*, Vol. 2, 92–108, 2009.

5. Ó. Menéndez, P. de Paco, E. Corrales and J. Verdú, "Procedure for the design of Ladder BAW filters taking electrodes into account," *Progress in Electromagnetics Research Letters.*, Vol. 7, 127–137, 2009.

6. E. Corrales, J. Verdú, P. de Paco and Ó. Menéndez, "Analysis technique for asymmetrically coupled resonator structures," *IEEE Transactions on Ultrasonics, Ferroelectrics, and Frequency Control.*, Vol. 56, 1703–1707, 2009.

7. J. Verdú, P. de Paco and Ó. Menéndez, "Electric equivalent circuit for the thickened edge load solution in a bulk acoustic wave resonator," *Progress in Electromagnetics Research M.*, Vol. 11, 13–23, 2010.

8. J. Verdú, P. de Paco and Ó. Menéndez, "Double-Ladder filter topology for a dual-band transmission response based on bulk acoustic wave resonators," *IEEE Microwave and Wireless Components Letters.*, Vol. 20, 151–153, 2010.

D.2 Chapters Book

1. J. Verdú, Ó. Menéndez and P. de Paco, "Modified Ladder-type BAW filter for an out-of-band rejection improvement," *Recent Developments in MEMS Technologies for Microwave and Millimeter Wave Circuits.*, 127–136, 2008.

2. J. Verdú, P. de Paco, Ó. Menéndez and E. Corrales, "Acoustical structures based on the thickened edge load solution," *New developments in Micro Electro Mechanical systems for radio frequency and millimeter wave applications.*, 221–230, 2009.

3. Ó. Menéndez, P. de Paco, E. Corrales and J. Verdú, "A novel bulk acoustic wave duplexer based on stacked crystal filters for WCDMA handset applications," *New developments in Micro Electro Mechanical systems for radio frequency and millimeter wave applications.*, 231–238, 2009.

4. E. Corrales, P. de Paco, Ó. Menéndez and J. Verdú, "Bulk acoustic wave CRF design," *New developments in Micro Electro Mechanical systems for radio frequency and millimeter wave applications.*, 239–248, 2009.

D.3 International Congress

1. E. Corrales, P. de Paco, Ó. Menéndez and J. Verdú, "Design of three-pole bulk acoustic wave coupled resonators filters," *European Microwave Week.*, 2008.

2. Ó. Menéndez, P. de Paco, M. Ramírez, J. Verdú and E. Corrales, "Design, Fabrication and measurement of a GPS-Galileo dual-passband filter," *10th Annual IEEE Wireless and Microwave Technology.*, 2009.

3. J. Verdú, P. de Paco, Ó. Menéndez and E. Corrales, "Simulation of electromechanical resonators using the finite element method," *10th International symposium on RF-MEMS and RF Microsystems.*, 2009.

4. E. Corrales, P. de Paco, Ó. Menéndez and J. Verdú, "Design of a WLAN 802.11 b/g RF filter based on electrically connected bulk acoustic wave coupled resonator filter," *10th International symposium on RF-MEMS and RF Microsystems.*, 2009.

5. J. Verdú, P. de Paco, Ó. Menéndez and E. Corrales, "Dual bandpass ladder-type filter," *International Microwave Symposium.*, 2010.

6. E. Corrales, P. de Paco, Ó. Menéndez and J. Verdú,"Analysis and Design of Coupled Resonator Filters with a Single Coupling Layer," *European Microwave Week.*, 2010.

7. E. Corrales, O. Menéndez, P. de Paco, M. Ramírez and J. Verdú,"Microstrip Dual-band Bandpass Filter Based on the Cul-de-sac Topology," *European Microwave Week.*, 2010.

D.4 National Congress

1. J. Verdú, Ó. Menéndez, P. de Paco and E. Corrales, "Low order ladder-type filter including reactive elements," *Metamaterials Week.*, 2008.

2. E. Corrales, P. de Paco, Ó. Menéndez, J. Verdú, J. Parrón, R. Villarino and G. Junkin, "Implementation of a dual-band mixer using comnposite right/left handed transmission lines," *Metamaterials Week.*, 2008.

3. E. Corrales, P. de Paco, Ó. Menéndez, J. Verdú,"Modelo circuital de un filtro BAW basado en resonadores acoplados acústicamente," *XXIII Simposium nacional de la unión científica internacional de radio.*, 2008.

4. J. Verdú, P. de Paco, Ó. Menéndez and E. Corrales, "Simulación 3D de estructuras compuestas por resonadores acústicos," *XXIII Simposium nacional de la unión científica internacional de radio.*, 2008.

5. Ó. Menéndez, P. de Paco, M. Ramírez, J. Verdú and E. Corrales,"Diseño, fabricación y medida de un filtro paso-banda dual GPS-Galileo," *XXIII Simposium nacional de la unión científica internacional de radio.*, 2008.

D.5 Patents

1. J. Verdú, P. de Paco and Ó. Menéndez, "Filtro de resonadores de onda acústica con respuesta en transmisión multibanda," *Spanish Patent.*, P200901558, 02/07/2009.

Bibliography

[1] R. Weigel, D.P. Morgan, J.M. Owens, A. Ballato, K.M. Lakin, K. Hashimoto, and C.C Ruppel, "Microwave Acoustic Materials, Devices and Applications," *IEEE Transactions on Microwave Theory and Techniques.*, vol. 50, no. 3, pp. 738–749, March 2002.

[2] F.S. Hickernell, "The Piezoelectric Semiconductor and Acoustoelectronic Device Development in the Sixties," *IEEE Transactions on Ultrasonics, Ferroelectrics and Frequency Control*, vol. 52, no. 5, pp. 737–745, May 2005.

[3] T.R. Sliker and D.A. Roberts, "A thin-film CdS-quartz composite resonator," *Journal of Applied Physics*, vol. 38, no. 5, pp. 2350–2358, 1967.

[4] D.J. Page, "A cadmium sulfide-silicon composite resonator," *Proceedings of the IEEE*, pp. 1748–1749, 1968.

[5] J.D. Maines and E.G. Paige, "Surface-acoustic-wave components, devices and applications," *Proc. IEE*, pp. 1078–1110, 1973.

[6] F.G. Marshall and E.G. Paige, "Mode conversion in surface acoustic wave reflective arrays," *Electronic Letters*, pp. 137–138, 1974.

[7] M.F. Lewis, "Surface acoustic wave oscillators," *Proceedings of microwave conference*, pp. 437–441, 1973.

[8] F.G. Marshall, "Analogue signal processing devices," *7th solid-state devices conference*, pp. 107–131, 1977.

[9] A.J. Pointon, "Piezoelectric Devices," *IEE Proceedings*, , no. 5, pp. 285–307, 1982.

[10] K.M Lakin and J.S. Wang, "UHF composite bulk wave resonators," *Ultrasonics Symposium proceedings*, pp. 834–837, 1980.

[11] K.M Lakin and J.S. Wang, "Acoustic Bulk Wave Composite Resonators," *Applied Physics Letters*, pp. 125–127, 1981.

[12] T.W. Grudkowski, J.F. Black, T.M. Reeder, D.E. Culler, and R.A. Wagner, "Fundamental-mode VHF/UHF miniature acoustic resonators and filters on silicon," *Journal of Applied Physics Letters*, pp. 993–995, 1980.

[13] K.M Lakin andG.R. Kline and K.T. McCarron, "Development of niniature filters for wireless applications," *IEEE Microwave Theory and Techniques*, vol. 43, no. 12, pp. 2933–2939, 1995.

[14] R. Ruby and P. Merchant, "Micromachined thin film bulk acoustic resonators," *IEEE International Frequency Control Symposium*, pp. 135–138, 1994.

[15] J.D. Larson III, P.D. Bradley, S. Wartenberg, and R.C. Ruby, "Modified Butterworth-Van Dyke Circuit for FBAR Resonators and Automated Measurement System," *IEEE Ultrasonics Symposium*, pp. 863–868, 2000.

[16] T. Kojima and H. Obara, "Two-port saw resonator using series connected idts," *Ultrasonics Symposium, 1998. Proceedings., 1998 IEEE*, vol. 1, pp. 81 –86 vol.1, 1998.

[17] M. Ueda and Y. Satoh, "FBAR and SAW techonologies and their applications for mobile communications," *Asia-Pacific Microwave Conference Workshops and Short Courses Digest*, 2006.

[18] Y. Satoh, O. Ikata, and T. Miyashita, "RF SAW Filters," *International Symposium on Acoustic Wave Devices for Future Mobile Communication Systems*, 2001.

[19] S. Mahon and R. Aigner, "Bulk Acoustic Wave Devices - Why, How, and Where They are Going," *CS MANTECH Conference*, pp. 15–18, 2007.

[20] R. Aigner, "MEMS in RF filter applications: Thin-Film bulk acoustic wave technology," *Wiley InterScience: Sensors Update*, vol. 12, pp. 175–210, 2003.

[21] J. Kaitila, "Review of Wave Propagation in BAW Thin Film Devices Progress and Prospects," *IEEE Ultrasonic Symposium*, pp. 120–129, 2007.

[22] K.M Lakin, "Fundamental Properties of Thin Film Resonators," *IEEE 45th Annual Symposium on Frequency Control*, pp. 201–206, 1991.

[23] M. Hara, T. Yokoyama, M. Ueda, and Y. Satoh, "X-band filters utilizing AlN thin film bulk acoustic resonators," *IEEE Ultrasonics Symposium*, pp. 1152–1155, 2007.

[24] T. Yokoyama, M. Hara, M. Ueda, and Y. Satoh, "K-band ladder filters employing air-gap type thin film bulk acoustic resonators," *IEEE International Ultrasonic Symposium*, pp. 598–601, 2008.

[25] T. Nishihara, T. Yokoyama, T. Miyashita, and Y. Satoh, "High performance and miniature thin film bulk acoustic wave filters for 5 GHz," *IEEE Ultrasonics Symposium*, pp. 969–972, 2002.

[26] G. Fattinger, J. Kaitila, R. Aigner, and W. Nessler, "Thin film bulk acoustic wave devices for applications at 5.2 GHz," *IEEE Ultrasonics Symposium*, pp. 174–177, 2003.

[27] R.C. Ruby, "Review and comparison of bulk acoustic wave FBAR, SMR technology," *IEEE Ultrasonics Symposium*, pp. 1029–1040, 2007.

[28] J.F. Rosenbaum, *Bulk Acoustic Wave Theory and Devices*, Artech House, 1988.

[29] J.G. Gualtieri, J.A. Kosiniski, and A. Ballato, "Piezoelectric materials for acoustic wave applications," *IEEE Trans. on Ultrasonics, Ferroelectrics, and Frequency control*, vol. 1, no. 41, pp. 53–59, 1994.

[30] A. Khelif, M. Wilm, V. Laude, S. Ballandras, and B. Djafari-Rouhani, "Guided elastic waves along a rod defect of a two-dimensional phononic crystal," *Physical Review E*, , no. 69, 2004.

[31] G. Carlotti, F.S. Hickernell, H.M. Liaw, L. Palmieriri, G. Socino, and E. Verona, "The elastic constants of sputtered aluminum nitride films," *IEEE Ultrasonics Symposium*, pp. 353–356, 1995.

[32] H. Jaffe and D.A. Berlincourt, "Piezoelectric transducer materials," *Proceedings of the IEEE*, vol. 10, no. 53, pp. 1372–1386, 1965.

[33] D. Royer and E. Dieulesaint, *Elastic Waves in Solids I*, Springer, 1996.

[34] M.H. Francombe and S.V. Krishnaswamy, "Growth and properties of piezoelectric and ferroelectric films," *Journal of vacuum science and technology*, vol. 8, pp. 1382–1390, 1990.

[35] R. Lanz, "Piezoelectric thin films for Bulk Acoustic Wave resonator applications: From processing to microwave filters," *PhD. Thesis*, 2004.

[36] Y. Le, P. Wei, S.K. Eun, and C.T. William, "Single-chip multiple-frequency VHF low-impedance micro piezoelectric resonators," *IEEE Electron Device Letters*, vol. 27, no. 4, pp. 246–248, April 2006.

[37] Y.P. Jae, C.L. Hee, H.L. Kyeong, M.L. Heon, and J.K. Young, "Micromachined FBAR RF Filters for advanced handset applications," *Interantional Conference on Solid State Sensors, Actuators and Microsystems*, pp. 911–914, 2003.

[38] Z. Hao and S.K. Eun, "Air-Backed Al/ZnO/Al Film Bulk Acoustic Resonator without any support layer," *IEEE International Frequency Control Symposium and PDA Exhibition*, pp. 20–26, 2002.

[39] R. Aigner, "Volume manufacturing of BAW-filters in a CMOS fab," *International symposium on acoustic wave devices for future mobile communication systems*, pp. 129–134, 2004.

[40] K.M Lakin, K.T. McCarron, and R.E. Rose, "Solidly Mounted Resonators and Filters," *IEEE Ultrasonic Symposium*, pp. 905–908, 1995.

[41] J. Kaitila, M. Ylilammi, J. Molarius, J. Ellä, and T. Makkonen, "ZnO Based Thin Film Bulk Acoustic Wave Filters for EGSM Band," *IEEE Ultrasonic Symposium*, pp. 803–806, 2001.

[42] R. Aigner, J. Ella, H.J. Timme, L. Elbrecht, W. Nessler, and S. Marksteiner, "Advancement of MEMS into RF-Filter Applications," *IEDM Proceedings*, pp. 897–900, 2002.

[43] S. Marksteiner, J. Kaitila, G.G. Fattinger, and R. Aigner, "Optimization of Acoutic Mirrors for Solidly Mounted BAW Resonators," *IEEE Ultrasonic Symposium*, pp. 329–332, 2005.

[44] S. Marksteiner, J. Kaitila, G.G. Fattinger, R. Aigner, and J. Kaitila, "Acoustic Reflector for a BAW resonator providing specified reflection of both shear waves and longitudinal waves," *US Patent 6933807 B2*, 2005.

[45] W.P. Mason, *Physical acoustics principles and methods*, vol. 1A, Academic Press, 1964.

[46] J. David and N. Cheeke, *Ultrasonic Waves*, CRC Press LLC, 2002.

[47] R.D. Mindlin and D.C. Gazis, "Strong resonances of rectangular AT-cut quartz plates," *4th National Congress of Applied Mechanics*, pp. 305–310, 1962.

[48] W. Shockley, C.R. Curran, and D.J. Koneval, "Energy trapping and related studies of multiple electrode filter crystals," *17th Annual Symposium on Frequency Control*, pp. 88–126, 1963.

[49] D.R. Curran and D.J. Koneval, "Energy trapping and the design of single and milti-electrode filter crystals," *18th Annual Symposium on Frequency Control*, pp. 93–119, 1964.

[50] E.L. Adler, "Matrix methods applied to acoustic waves in multilayered," *IEEE Transactions on Ultrasonics, Ferroelectrics and Frequency Control*, vol. 37, no. 6, pp. 485–490, 1990.

[51] M.J.S. Lowe, "Matrix techniques for modeling ultrasonic waves in multilayered media," *IEEE Transactions on Ultrasonics, Ferroelectrics and Frequency Control*, vol. 42, no. 4, pp. 525–541, 1995.

[52] R.Ruby and S. Fazzio, "Performance degradation Effects in FBAR Filters and Resonators due to Lamb Wave Modes," *Microwave Symposium Digest, IEEE MTT-S International*, 2005.

[53] K.L. Telschow, V. Deason, D. Cottle, and J.D. Larson III, "Full-Field Imaging of GHz Film Bulk Acoustic Resonator Motion," *IEEE Transactions on Ultrasonics, Ferroelectrics and Frequency Control*, vol. 50, no. 10, pp. 1279–1285, 2003.

[54] P.T. Tikka, J. Kaitila, M. Ylilammi, T. Makkonen, J.V. Knuuttila, and M.M Salomaa, "Laser Probing and FEM Modeling of Ultrasonically Vibrating Surfaces," *IEEE Ultrasonics Symposium*, pp. 1143–1146, 1999.

[55] P.T. Tikka, J. Kaitila, J. Ellä, T. Makkonen, J. Westerholm, K. Hashimoto, and M.M Salomaa, "Laser Probing and FEM Modeling of Solidly Mounted Resonators," *IEEE Microwave Symposium Digest MTT-S International*, pp. 1373–1376, 2006.

[56] G.G. Fattinger and P. T. Tikka, "Laser Measurements and Simulatins of FBAR Dispersion Relation," *IEEE Microwave Symposium Digest MTT-S International*, pp. 371–374, 2001.

[57] A. Link, E. Schmidhammer, H. Heinze, M. Mayer, B. Bader, and R. Weigel, "Appropiate methods to suppress spurious FBAR modes in volume production," *Microwave Symposium Digest*, pp. 394–397, 2006.

[58] R. Thalhammer, J. Kaitila, S. Zieglmeier, and L. Elbrecht, "Spurious mode supperssion in BAW resonators," *IEEE Ultrasonics Symposium*, pp. 456–459, 2006.

[59] J.D. Larson III, R.C. Ruby, and P. Bradley, "Bulk acoustic wave resonator with improved lateral mode suppression," *US Patent 6215375 B1*, April 2001.

[60] Doo Yeoul Yang and Hong Wook Kim, "Film bulk acoustic resonator with improved lateral mode suppresion," *US Patent 6693500 B2*, February 2004.

[61] T. Makkonen, A. Holappa, J. Ellä, and M. Salomaa, "Finite Element Simulations of Thin-Film Composite BAW Resonators," *IEEE Transactions on Ultrasonics, Ferroelectrics and Frequency Control*, pp. 1241–1258, 2001.

[62] J. Kaitila, M. Ylilammi, and J.Ellä, "Resonator structure and a filter comprising such a resonator structure," *Patent Number 6812619*, November 2004.

[63] G.C. Fattinger, S. Marksteiner, J. Kaitila, and R. Aigner, "Optimization of Acoustic Dispersion for High Performance Thin Film BAW Resonators," *IEEE Ultrasonics Symposium*, 2005.

[64] L. Jiunn-Horng, Y. Chih-Min, T. Kung-Yu, C. Chih-Wei, and S. Yu-Ching, "Optimization of Frame-like film bulk acoustic resonators for suppression os spurious lateral modes using finite element method," *IEEE Ultrasonics Symposium*, pp. 278–281, 2004.

[65] R.Ruby, J. Larson, C. Feng, and S. Fazzio, "The Effect of Perimeter Geometry on FBAR Resonator Electrical Performance," *Microwave Symposium Digest, IEEE MTT-S International*, 2005.

[66] T. Pensala and M. Ylilammi, "Spurious Resonance Suppression in Gigahertz-Range ZnO Thin-Film Bulk Acoustic Wave Resonators by the Boundary Frame Method: Modeling and Experiment," *IEEE Transactions on Ultrasonics, Ferroelectrics and Frequency Control*, vol. 56, no. 8, pp. 1731–1744, 2009.

[67] Ken-Ya Hashimoto, *RF Bulk Acoustic Wave Filters for Communications*, Artech house, 2009.

[68] Y. Kagawa and T. Yamabuchi, "Finite element simulation of two-dimensional electromechanical resonators," *IEEE Transactions on Sonics and Ultrasonics*, vol. SU-21, pp. 275–283, 1974.

[69] D. Boucher, M. Lagier, and C. Maerfeld, "Computation of the vibrational modes for piezoelectric array transducers using a mixed finite element-perturbation method," *IEEE Transactions on Sonics and Ultrasonics*, vol. SU-28, pp. 318–330, 1981.

[70] R. Lerch, "Simulation of piezoelectric devices by two- and three dimensional finite elements," *IEEE Transactions on Ultrasonics, Ferroelectrics and Frequency Control*, vol. 37, no. 2, pp. 233–247, May 1990.

[71] R.F. Milsom, H-P. Lobl, C. Metzmacher, P. Lok, A. Tuinhout, and F. van Straten, "2D model of solidly-mounted and membrane BAW devices," *IEEE Ultraonics Symposium*, pp. 1802–1807, 2003.

[72] R. Thalhammer, J. Kaitila, R. Aigner, and S. Marksteiner, "Prediction of BAW resonator performance using experimental and numerical methods," *IEEE Ultrasonics Symposium*, pp. 282–285, 2004.

[73] S. Giraud, S. Bila, and D. Cros, "Bulk Acoustic Wave Resonators 3D Simulation," *IEEE Frequency Control Symposium*, pp. 1147–1151, May 2007.

[74] David M. Pozar, *Microwave and RF Wireless systems*, John Wiley & Sons, Inc., 2001.

[75] K.M Lakin, "Thin film resonator technology," *IEEE Trans. on Ultrasonics, Ferroelectrics, and Frequency control*, vol. 52, pp. 707–716, May 2005.

[76] O. Menéndez, P. de Paco, R. Villarino, and J. Parron, "Closed-form Expressions for the Design of Ladder-Type FBAR filters," *IEEE Microwave and Wireless components Letters*, vol. 1, Nov 2006.

[77] J. Verdú, O. Menéndez, and P. de Paco, "Ladder-Type Filter Based on Bulk Acoustic Wave Resonators with Improved Out-of-Band Rejection," *Microwave and Optical Technology Letters*, vol. 50, no. 1, pp. 103–107, January 2008.

[78] M. Handtmann, S. Marksteiner, J. Kaitila, and R. Aigner, "Bulk Acoustic Wave Filters for GPS with Extreme Stopband Attenuation," *IEEE MTT-S Digest*, pp. 371–374, 2004.

[79] G.L Matthaei, E.M.T Jones, and L. Young, *Microwave filters, impedance matching networks and Coupling structures.*, McGraw Hill, 1980.

[80] K.M Lakin, K.T. McCarron, J. Belsick, and R. Rose, "Filter Banks Implemented with Integrated Thin Film Resonators," *IEEE Ultrasonic Symposium*, pp. 852–854, 2000.

[81] J.F. Rosembaum, S. Horowitz, S.V. Krishnaswamy, and R. Moore, "FBAR Filters at GHz Frequencies," *44th annual symposium on frequency control*, pp. 332–336, 1990.

[82] K.M Lakin, G.R. Kline, and D.T. McCarron, "Thin Film Bulk Acoustic Wave Filters for GPS," *IEEE Ultrasonics Symposium*, pp. 471–476, 1992.

[83] L. Mang, F. Hickernell, R. Pennell, and T. Hickernell, "Thin-Film resonator ladder filter," *IEEE International Microwave Symposium*, pp. 887–890, 1995.

[84] K.M Lakin, G.R. Kline, and D.T. McCarron, "High-Q Microwave Acoustic Resonators and Filters," *IEEE Transactions on Microwave Theory and Techniques*, pp. 2139–2146, 1993.

[85] A.A. Shirakawa, J-M. Pham, P. Jarry, E. Kerherve, and E. Hanna, "Ladder-type Filter Synthesis Methodology," *Design of Circuits and Integrated Systems Conference*, pp. 519–523, 2004.

[86] M. Ylilammi, J. Ella, M. Partanen, and J. Kaitila, "Thin Film Bulk Acoustic Wave Filter," *IEEE Transactions on Ultrasonics, Ferroelectrics and Frequency Control*, vol. 49, pp. 535–539, April 2002.

[87] O. Menéndez, P. de Paco, E. Corrales, and J. Verdú, "Procedure for the design of a Ladder BAW Filters Taking Electrodes into Account," *Progress in Electromagnetics Research Letters*, vol. 7, pp. 127–137, 2009.

[88] R. Aigner, K. Kaitila, J. Ella, L. Elbrecht, W. Nessler, M. Handtmann, T.R. Herzog, and S. Marksteiner, "Bulk-Acoustic-Wave Filters: Performance Optimization and Volume Manufacturing," *IEEE Microwave Symposium Digest*, pp. 2001–2004, 2003.

[89] K. Wang, M. Frank, P. Bradley, R. Ruby, W. Mueller, A. Barfknecht, and M. Gat, "FBAR Rx Filters for Handset Front-End Modules with Wafer-Level Packaging," *IEEE Ultrasonics Symposium*, pp. 162–165, 2003.

[90] K.M Lakin, "Thin Film BAW Filters for Wide Bandwidth and High Performance Applications," *IEEE MTT-S Digest*, pp. 923–926, 2004.

[91] A.A. Shirakawa, P. Jarry, J.M. Pham, E. Kerhervé, F. Dumont, J.-B. David, and A. Cathelin, "Ladder-Lattice Bulk Acoustic Wave Filters: Concepts, Design, and Implementation," *International Journal of RF and Microwave Comnputer-Aided Engineering*, vol. 18, pp. 476–484, 2008.

[92] O. Menéndez, J. Verdú, E. Corrales, and P. de Paco, "A review of recent patents on Bulk Acoustic Wave Resonators and Filters," *Recent Patents on Electrical Engineering*, vol. 2, pp. 92–108, 2009.

[93] K.M Lakin, J. Belsick, J.F. McDonald, and K.T. McCarron, "High Performance Stacked Crystal Filters for GPS and Wide Bandwidth Applications," *IEEE Ultrasonic Symposium*, 2001.

[94] K.M Lakin, "Bulk Acoustic Wave Coupled Resonator Filters," *IEEE International Frequency Control Symposium and PDA Exhibition*, 2002.

[95] A. Ballato and T. Lukasek, "A Novel Frequency Selective Device: The Stacked Crystal Filter," *27th Annual Frequency Control Symposium*, pp. 257–262, June 1973.

[96] K.M Lakin, "Equivalent Circuit Modeling of Stacked Crystal Filters," *35th Annual Symposium on Frequency Control*, pp. 257 – 262, 1981.

[97] G.R. Kline, R.S. Ketchma, and K.M. Lakin, "Low insertion loss filters synthesized with thin film resonators," *IEEE Ultrasonic Symposium*, pp. 375–380, 1987.

[98] K.M Lakin, J.R. Belsick, J.P. McDonald, K.T. McCarron, and C.W. Andrus, "Bulk Acoustic Wave Resonators and Filters for Applications above 2 GHz," *IEEE Microwave Symposium Digest*, pp. 1487–1490, 2002.

[99] O. Menéndez, P. de Paco, J. Gemio, J. Verdú, and E. Corrales, "Methodology for designing microwave acoustic filters with Butterworth/Chebyshev response," *International Journal of Microwave and Wireless Technologies*, vol. 1, pp. 11–18, 2009.

[100] K.M Lakin, "Coupled Resonator Filters," *IEEE Ultrasonic Symposium*, 2002.

[101] G.G. Fattinger, J. Kaitila, R. Aigner, and W. Nessler, "Single-to-balanced Filters for Mobile Phones using Coupled Resonator BAW Technology," *IEEE Ultrasonics Symposium*, pp. 416–419, 2004.

[102] P. de Paco, O. Menénedez, and E. Corrales, "Equivalent Circuit Modeling of Coupled Resonator Filters," *IEEE Frequency Control Symposium*, pp. 1147–1151, May 2007.

[103] A. Volatier, E. Defay, A. N'hari, J.F. Carpentier, P. Ancey, and B. Dubus, "Design, elaboration and characterization of Coupled Resonator Filters for WCDMA applications," *IEEE Ultrasonics Symposium*, pp. 829–832, 2006.

[104] E. Corrales, P. de Paco, and O. Menéndez, "Closed-Form expressions for the design of BAW CRF acoustic inverters," *Progress in Electromagnetic Research*, vol. -, pp. –, 2009.

[105] E. Corrales, J. Verdú, P. de Paco, and O. Menéndez, "Analysis Technique for Asymmetrically Coupled Resonator Structures," *IEEE Transactions on Ultrasonics, Ferroelectrics, and Frequency Control*, vol. 56, no. 8, pp. 1703–1707, 2009.

[106] A.A. Shirakawa, J-M. Pham, and E. Kerherve, "Bulk Acoustic Wave Coupled Resonator Filters Synthesis Methodology," *European Microwave Conference*, 2005.

[107] David M. Pozar, *Microwave Engineering*, John Wiley & Sons, Inc., 2005.

[108] M.F. Lewis and C-S. Lu, "Relationship of Resonant Frequency of Quartz Crystal to Mass Loading," *29th Annual Symposium on Frequency Control*, pp. 5–9, 1975.

[109] J. Kosinski, S. Mallikarjun, and A. Ballato, "Mass Loading Measurements of Quartz Crystal Plates," *43rd Annual Symposium on Frequency Control*, pp. 365–371, 1989.

[110] D.A. Berlincourt, D.R. Curran, and H. Jaffe, "Piezoelectric and piezomagnetic materials and their function as transducers," *Physical Acoustics, W.P. Mason, Academic Press*, 1964.

[111] S.H. Chang, N.N. Rogacheva, and C.C. Chou, "Analysis of Mehtods for Detmining Electromechanical Coupling Coefficients of Piezoelectric Elements," *IEEE Transactions on Ultrasonics, Ferroelectrics, and Frequency Control*, vol. 42, no. 4, pp. 630–640, 1995.

[112] M. Makimoto and S. Yamashita, "Bandpass Filters Using Parallel Coupled Stripline Stepped Impedance Resonators," *IEEE Transactions on Microwave Theory and Techniques*, vol. 28, no. 12, pp. 1413–1417, 1980.

[113] R. Krimholtz, D.A. Leedom, and G.L Matthaei, "New Equivalent Circuits for Elementary Piezoelectric Transducers," *Electronic Letters*, vol. 6, no. 13, pp. 398–399, 1970.

[114] S. Sherrit, S.P. Leary, B.P. Dolgin, and Y. Bar-Cohen, "Comparison of the Mason and KLM Equivalent Circuits for Piezoelectric Resonators in the Thickness Mode," *IEEE Ultrasonics Symposium*, 1999.

[115] H. Campanella, P. Nouet, A. Uranga, P. de Paco, N. Barniol, and J. Esteve, "Automated on-wafer extraction of equivalent-circuit parameters in thin-film bulk acoustic wave resonators and substrate," *Microwave and optical technology letters*, vol. 50, no. 1, pp. 4–7, 2008.

[116] M.J. Turner, R.W. Clough, H.C. Martin, and L.J. Topp, "Stiffness and deflection analysis of complex structures," *Journal of Aeronautic Science*, 1956.

[117] Constantine A. Balanis, *Advanced Engineering Electromagnetics*, Wiley, 1989.

[118] H.A. Kunkel, S. Locke, and B. Pikeroen, "Finite-Element Analysis of Vibrational Modes in Piezoelectric Ceramic Disks," *IEEE Trans. on Ultrasonics, Ferroelectrics, and Frequency control*, pp. 316–328, 1990.

[119] K.M Lakin and K.G. Lakin, "Numerical Analysis of thin Film BAW Resonators," *IEEE Ultrasonic Symposium*, pp. 74–79, 2003.

[120] T. Makkonen, T. Pensala, J. Vartianen, V. Knuuttila, J. Kaitila, and M.Salomaa, "Estimating Materials Parameters in Thin-Film BAW Resonators Using Measured Dispersion Curves," *IEEE Transactions on Ultrasonics, Ferroelectrics and Frequency Control*, vol. 51, no. 1, pp. 42–51, 2004.

[121] R. Thalhammer, G. Fattinger, M. Handtmann, and S. Marksteiner, "Ohmic effects in BAW resonators," *IEEE Microwave Symposium Digest MTT-S International*, pp. 390–393, 2006.

[122] J.D. Larson III, R. Ruby, P.D. Bradley, J. Wen, S.-L. Kok, and A.L. Chien, "Power handling and temperature coefficient studies in FBAR duplexers for the 1900 MHz PCS band," *IEEE Ultrasonics Symposium*, pp. 8669–874, 2000.

[123] S. Lee, K. Yoon, and J. Lee, "Influence of electrode configurations on the quality factor and piezoelectric coupling constant of solidly mounted bulk acoustic wave resonators," *Journal of Applied Physics*, vol. 92, pp. 4062–4069, October 2002.

[124] Y. Kim, K. Sunwoo, S. Sul, J. Lee, D. Kim, I. Song, S. Choa, and J. Yook, "Highly miniaturized RF bandpass filter based on thin-film bulk acoustic wave resonator for 5 GHz band application," *IEEE Transactions on Microwave Theory and Techniques*, vol. 54, pp. 1218–1228, 2006.

[125] J. Ella, "Filters and duplexers utilizing thin film stacked crystal filter structures and thin film bulk acoustic wave resonators," *US Patent 5910756*, 1999.

[126] H.J. de los Santos, "On the ultimate limits of IC Inductors - An RF MEMS perspective," *IEEE Electronic components and technology conference*, pp. 1027–1031, 2002.

[127] X. Guan, Z. Ma, P. Cai, Y. Kobayashi, T. Anada, and G. Hagiwara, "Synthesis of dual-band bandpass filters using successive frequency transformations and circuit conversions," *IEEE Microwave and Wireless Components Letters*, vol. 16, no. 3, pp. 110–112, 2005.

[128] J. Lee and K. Sarabandi, "Synthesis method for dualpassband microwave filters," *IEEE Transactions on Microwave Theory and Techniques*, vol. 55, no. 6, pp. 1163–1170, 2007.

[129] C. Puente, J. Romeu, R. Pous, and A. Cardama, "On the behavior of the Sierpinski multiband fractal antenna," *IEEE Transactions on Antennas and Propagation*, vol. 46, no. 4, pp. 517–524, 1998.

[130] J.D. Larson and Y. Oshmyansky, "Acoustic resonator devices having multiple resonant frequencies and methods of making the same," *US Patent 6927651B2*, August 2005.

[131] C. Fernandez Prades and J.A. Fernandez Rubio, "Multi-Frequency GPS/Galileo Receiver Design Using Direct RF Sampling and Antenna Arrays," *IEEE Sensor Array and Multichannel Signal Processing Workshop*, pp. 475–479, 2004.

[132] Jun-Gi Jo, Jong-Ho Lee, Do Jin Park, Young Gun Pu, Sung-Cheol Shin, Kang-Yoon Lee, Seong-Eon Park, Seok-Joong Lee, and Changsik Yoo, "A L1-Band Dual-Mode RF Receiver for GPS and Galileo in 0.18 μm CMOS," *IEEE Radio Frequency Integrated Circuits Symposium*, pp. 21–24, 2008.

[133] Z. Gradincic, R. Materini, P. Orsatti, and F. Piazza, "Multiband gnss receiver," *Patent Number 7358896*, April 2008.

[134] S.Y. Lee, "Optimum Resonant Conditions of Stepped Impedance Resonators," *European Microwave Conference*, 2005.